Universitat Autònoma de Barcelona

Non-Linear Nanoelectromechanical Systems for Energy Harvesting

PhD dissertation

Author
Miquel López Suárez

Supervisors
Gabriel Abadal Berini
Riccardo Rurali

UAB
Universitat Autònoma de Barcelona

Departament d'Enginyeria Electrònica

Edifici Q · Campus de la UAB · 08193 Bellaterra
(Cerdanyola del Vallès) · Barcelona · Spain
Tel. +34 93 581 31 83 · Fax +34 93 581 26 00
d.eng.electronica@uab.cat · www.uab.cat

Dr. Riccardo Rurali, Staff Scientist at the *Institut de Ciència de Materials de Barcelona* of the *Consejo Superior de Investigaciones Científicas*, and Dr. Gabriel Abadal Berini, Associate Professor at the *Departament d'Enginyeria Electrònica* of the *Univesitat Autònoma de Barcelona*

HEREBY CERTIFY THAT

the thesis entitled ***Non-linear Nanoelectromechanical Systems for Energy Harvesting*** presented by Miquel López-Suárez to fulfil part of the requirements to achieve the degree of Doctor in Electronic Engineering, has been performed under their supervision

Bellaterra, March the 18th, 2014

Riccardo Rurali

Gabriel Abadal Berini

AKNOWLEDGEMENTS

I would like to thank all the colleagues from the electronic department of the engineering school because these four years have been a very inspiring time. Special thanks goes to my *godfather* Jordi Agustí and Francesc Torres for his help and active participation in the realization of this work. Thanks to Gabriel Vidal, Eloi Marigó and Xavier Saura because the good moments and for the no-ending recurrent discussions. I would like to thanks Gonzalo Murillo, Albert Crespo, Vanessa Iglesias, Gerard Zamora, Paris Velez, Nuria Ayala, Miquel Durán-Sindreu, and José Luís Muñoz beacause of the good moments. I want also to thank Xiomara Maramoto, Mª Carmen Mesas and Antonia Doroteo from the administrative staff and Javier Hellín for his technical support.

I would like to thank my parents and sister because all of this wouldn't be possible without their support.

I would like to thank my friends because the time spent with them allowed me to keep working hard.

I would like to thank Alba because she knows better than anyone else how hard it could be and for making it much easier. I know I own you more than an aknowledge.

I would like to specially thank Gabriel Abadal and Riccardo Rurali for giving me the opportunity to discover the most intimate nature of research and for their guide.

If you think you should be named in this aknowledgements and you are not, please feel free to write by hand your name below these lines.

INDEX

Paper A: López-Suárez, M.; Agustí, J.; Torres, F.; Rurali, R.; Abadal, G. "Inducing bistability with local electret technology in a microcantilever based non-linear vibration energy harvester". A: Applied Physics Letters (2013).

Paper B: López-Suárez, Miquel, et al. "Nanostructured graphene for energy harvesting". Physical Review B 84.16 (2011): 161401.

Paper C: López-Suárez, M.; Rurali, R.; Abadal, G. "Buckling suspended grahene nanoribbons to harvest energy from noisy vibrations". A: Microelectronic Engineering (2013).

Paper D: López-Suárez, M.; Pruneda, M,; Abadal, G.; Rurali, R. "Piezoelectric layered materials for energy harvesting". Accepted for Nanotechnology (2014).

Paper E: M. López-Suárez, F. Torres, N. Mestres, R. Rurali, G. Abadal. "Fabrication of highly regular suspended graphene nanoribbons through a one-step EBL process". Submitted.

CHAPTER 1

INTRODUCTION

Energy Harvesting (EH) has attracted the attention of the scientific community for the latest years motivated in first place by the interest on reducing the energy consumption at all scales and, secondly, by the trend of developing portable devices: the landscape of a smarter society, where electronic devices provide sensing, actuating and communication capabilities to distributed control systems, will not be reached unless the powering issue is solved.

Several efforts have been mostly directed to attempt satisfying three energy requirements: the need of green energies, the need of powering at any time and wherever the system is and the need of developing low-power electronics.

Photovoltaic and windmills shown in Fig.1.1 are the most well known examples of green energies for the vast majority of the population.

Fig.1. 1. Examples of large scale energy harvesting installations: (a) aerial view of the photovoltaic park in Olmedillas (Alcorcón, Spain) capable of producing up to 85MW, (b) windmill park in Ì resund (Copenhagen, Denmark) capable of producing 40MW.

These installations are designed to generate electric power in a massive way (in the range of tens of MW) in order to supply electricity to entities with very high power needs such as industrial plants, cities, etc. In the example of Fig.1.1.a an aerial view of the Olmedillas photovoltaic park (Alcorcón, Spain) is shown, which generates between 60 and 85 MW, the average power consumption of a set of 40000 houses. Fig.1.1.b show another example of harvesting parks, this one built on 2009 at Ì resund (Copenhagen, Denmark) capable of producing 40 MW. Although these technologies are nowadays a reality, they are not able to satisfy the huge amount of energy demanded by human activity. Yet, they are advanced examples for the first claim. The attention of this work is focused on a sort of devices designed for applications in other using scale.

Actually, EH is a concept closer to battery free self-powered devices and low-power consumption electronics rather than production plants. Due to the low intensity of the energy currently present in the environment, the EH community focuses its efforts on meso, micro and nano-scale devices with low-power consumption requirements.

One commercial and much extended example is represented by SEIKO watches. This company developed two different self-powered engines based on scavenging strategies from sunlight and human body movement. Schematics of these examples are depicted in Fig.1.2.

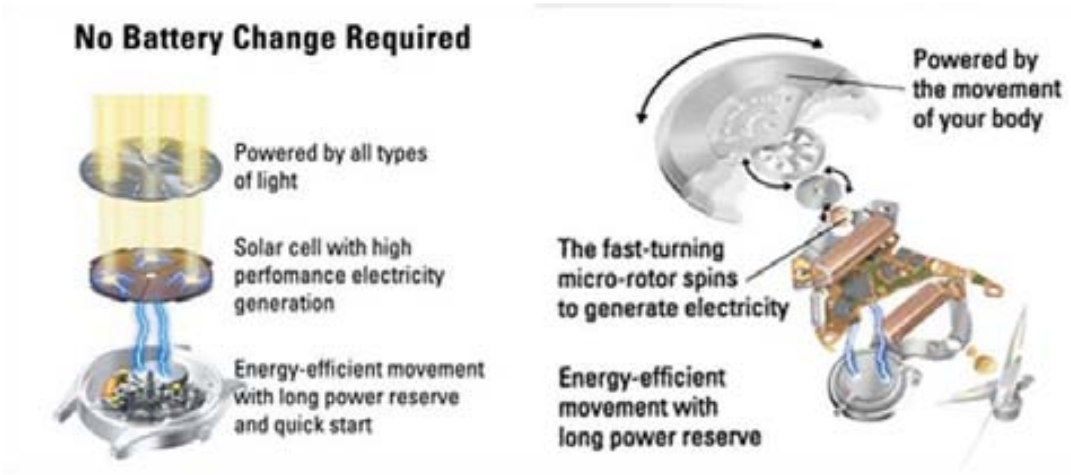

Fig.1. 2. At the left a scheme of the SSC005P1 light-powered watch capable of harvest energy not only from sunlight but from many other light sources. At the right the SNP036P1 designed to be powered by the human body movement.

Regardless of the specific harvesting strategy, there is a key point differentiating the SEIKO engines from the massive generator plants shown in Fig.1.1, which is also present along this thesis dissertation and it is the portability and autonomy of both devices meeting the second claim. Generally speaking, these watches exemplify the need of powering electronics in a ubiquitously manner, as in many applications it is not possible to replace or recharge the battery once it is wasted. Imagine a set of thermal and humidity sensors spread in a forest indicating areas with danger of fire or some health monitoring devices running through a human body alerting of a particular medical threat: battery replacement is unpractical and not realistic as the number of

devices increases and even more if their dimensions are scaled down. Self-powered systems are also useful to track the state of industrial machinery, trains, cars, and other engines as it is currently the case in the London's train net [1]. The possibility of powering sensors capable of sending the obtained data to a control center allows to know in real time the behavior of the engine. This make possible to maintain in an optimal state all the trains from the net without needing to retire periodically the trains from the circulation to check the state of the things.

Electronics and its development were (and still are) a tremendous revolution and they have played a central role in the progress of all kind of scientific and non-scientific fields: fundamental science, computing science, mathematics, geography, among others and can be considered to be a milestone in the development of modern society, even in such important fields as medicine. The trend of increasing the performance of electronics by means of high speed, miniaturization and low heat dissipation among others is a fact [2]. Fig.1.3 represents this improvement for the particular case of laptop components (especially Complementary Metal-Oxide-Semiconductor, CMOS, based technology) but it can be generalized to all kind of microelectronics [3].

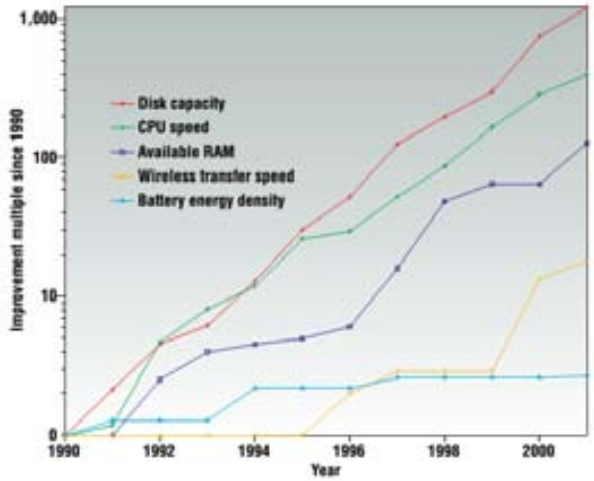

Fig.1. 3. Trend of the improvement on laptop technology. Reference value, improvement=1, corresponds to a 4Mbyte hard-drive space, 16MHz and 8Mbyte RAM capacity computer. While the disk capacity has increased by a factor of approximately 1200, the battery energy density improved only by a factor of 2. Graph extracted from [4].

This trend is called Moore's Law [5-6] and a lot of efforts are dedicated nowadays in order to keep the trend [7]. Generally one can say that these performance improvements are due to the downscaling of the CMOS technology and the resultant decrease of the power consumption covering from transistors to low-power electronics, i.e. active devices as actuators [8], RF-communication nodes [9], sensors [10]. Here it is met the third claim. Moreover, the miniaturization allowed the integration of those active devices in CMOS technology obtaining in a single micro-device the active micro-system and the management electronics. However, quoting from [4]:

"Battery technology is the least likely to change in the 12-month development cycle and could be the most limiting factor in the design with respect to size, weight and cost"

This usually leads the designers to specify the battery first and then design the device electronics under constrictions.

The importance of this topic can be measured in terms of economic investment. Smart Dust, project financed by the US, pursued to bring a complete sensor node with capability for sensing, processing and communicating in a single 1 mm^3 device. The trend of miniaturization also forced the reduction of the dimensions of their powering systems and the autonomy of such ICT devices trying to eliminate the need of batteries. Table 1.1 shows a comparison between ordinary battery strategies and ambient energy sources in terms of power density and its lifetime dependence.

Energy Source	Initial Power per volume unit ($\mu W/cm^3$)	Power per volume unit after one year lifetime ($\mu W/cm^3$)
Solar	*10 – 1000*	*10 – 1000*
Vibrations	*10 – 200*	*10 – 200*
Lithium	*500*	*70*
Alkaline	*200*	*10*
Lithium rechargeable	*200*	*10*
Zinc air	*500*	*0*

Table 1. 1. Lifetime of different common power supply strategies. Solar energy and vibrations are two of the numerous sources of energy which can be harvested presenting infinite lifetime against the finite battery lifetime. Data extracted from [11].

The main advantages for environmental energy sources relies in the high power availability and the infinite lifetime together with their ubiquity.
Beyond this goal, the SINAPS project (*www.sinaps-fet.eu*), financed by the European Commission within the FP7 frame, aims to go further in this path enabling miniaturization below the 1 mm^3 device incorporating an energy harvesting device from electromagnetic radiation. After the reduction in size and energetic autonomy the next step was diminishing the power consumption of ICTs. A remarkable currently ongoing example working in this topic is the Landauer project (*www.landauer-project.eu*), also financed by the European Commission, this last one focused on the reduction of information processing consumption trying to approximate at maximum to the Landauer limit (see textbox).

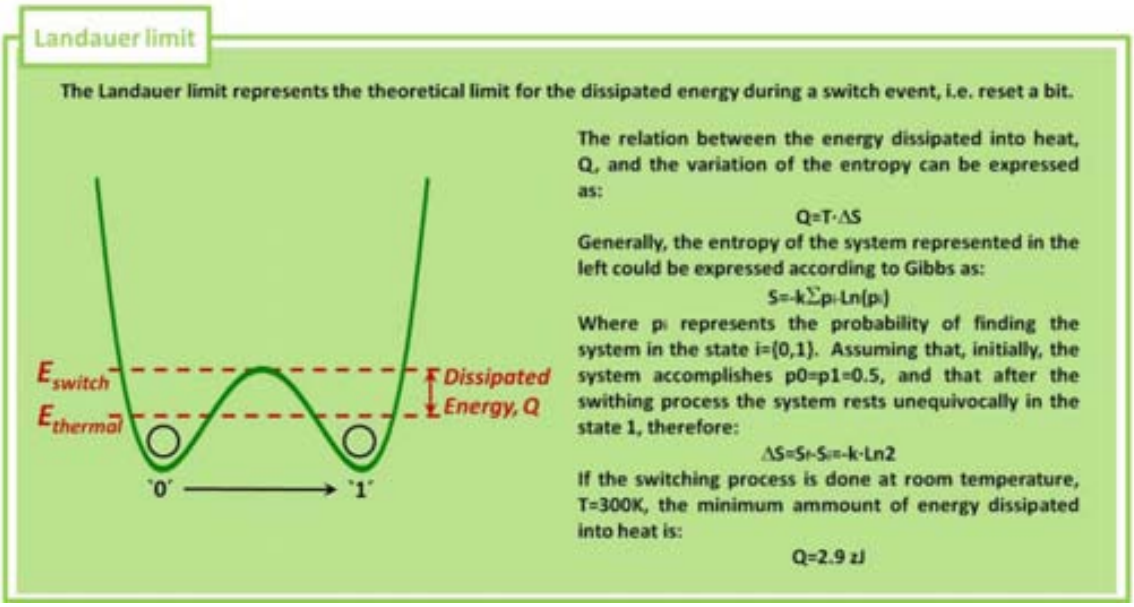

Finally, ICTs have a non negligible impact in the CO_2 footprint. It is considered a contribution of a 3% and continuously increasing. At this point we met again the goals pursued by the green energy strategies presented in Fig. 1.1.

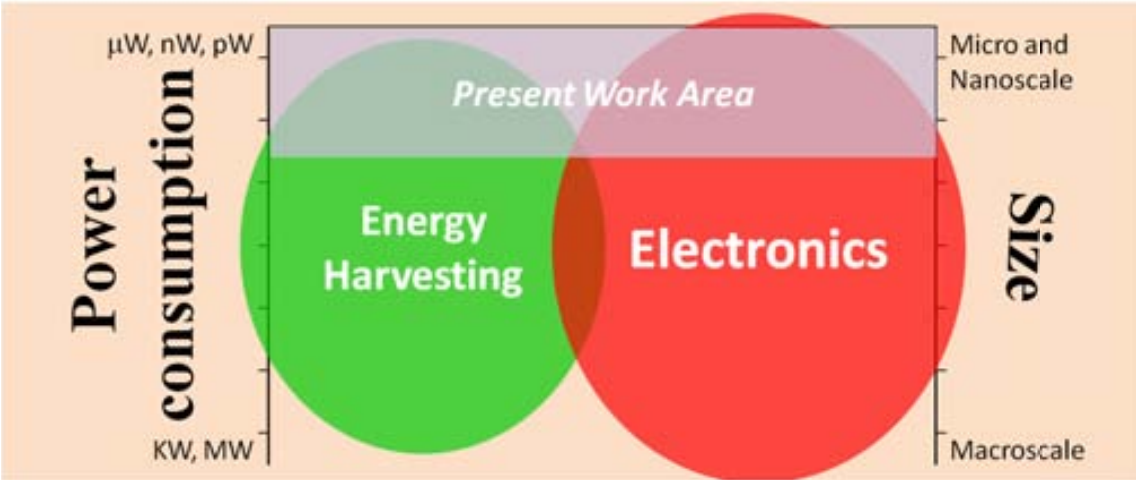

Fig.1. 4. Representation of the scenario in terms of power consumption and size. The shadowed box remarks the part of the graph of interest for this thesis dissertation: ultra-low power consumption technologies at the micro and nano-scale.

EH meets electronics in a vast number of situations, but only that at the micro and nano-scale is the object of this study (Fig.1.4) leaving behind the energy sources and strategies described until this point. An example of a technology working within the shadowed region of Fig.1.4 is the EH-Link™ [12] wireless node: a self powered sensor capable of harvesting energy from ambient sources using as transducing elements a wide range of generators such as piezoelectric, electrodynamic, solar, and thermoelectric generators. Some of its features are an on-board tri-axial accelerometer, relative humidity sensor, temperature sensor, torque sensors, pressure transducers and magnetic sensors, all of them in a miniature package. Then, an energy harvesting device

can solve the problem of the power supply for these kinds of electronics, transferring energy from the environment into usable electric energy to the system. One of these energy sources is what is called mechanical vibrations, to be discussed later on, and it represents the principal target for this work.

Fig.1.5 shows a scheme describing the different parts of an energy harvesting electromechanical device. It takes two transducing steps to convert the environmental energy into the electrical domain each of them with the corresponding losses. In order to store the converted energy it must be rectified to achieve a DC signal which is not a matter of discussion for this work. This thesis dissertation focuses its efforts on both transduction mechanisms of Fig.1.5 with the aim of optimizing the efficiency of the harvester.

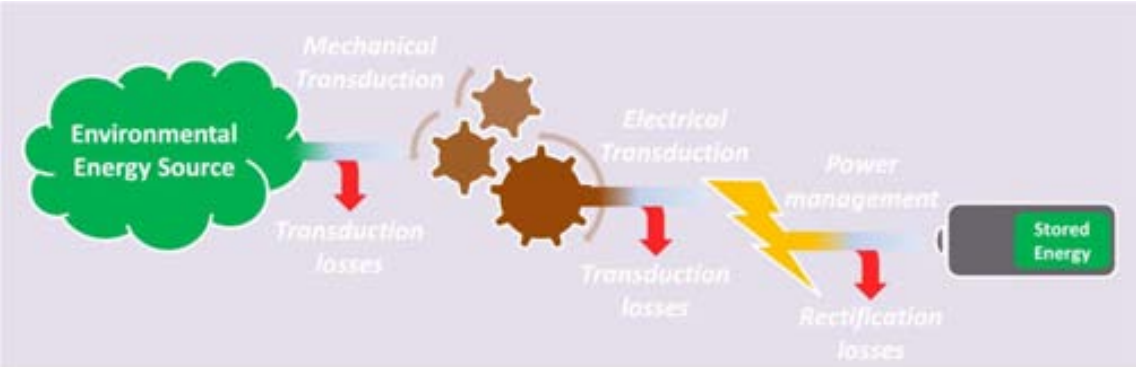

Fig.1.5. Representation of the different parts of a electromechanical harvesting device showing the different transduction steps to take into account. Each transduction carries losses due to the transformation of the energy domain.

Finally, it has to be stressed that the advantage of being autonomous has an unavoidable cost: environmental energy may be a non-constant energy source and the energy harvested in a certain active period could not be enough to power constantly the active block. For this reason some hybrid strategy mixing the potential of different kinds of energy sources should be considered [13].

This section is structured in three parts: first, an introduction to different sources of energy with particular interest in mechanical vibrations and its details accompanied with some numbers is argued. Secondly, a review of the state of the art for different kind of harvesting devices and a justification for the need of downscaling to the micro and nano-scale are provided. Finally, a third part is presented showing the main benefits of the so-called “bistable approach” for EH proposes.

1.1. Vibration energy sources

This section is devoted to give an insight of which energy sources are commonly considered in the EH community and to point out the differences between them. Table 1.2 gives some numbers to compare between different electric power supply strategies in terms of power density and their performance:

Energy source	Maximum power density	Harvested power density	Performance (%)
Solar	*1 mW/cm²*	*100 μW/cm²*	*10*
Thermoelectric		*60 μW/cm²*	
Vibrations*	*200 μW/cm³*	*5 μW/cm³*	*2.5*
Radioactive	*120 μW/cm²*	*2.2 μW/cm²*	*2*

Table 1.2. Typical values for different energy sources [11].

It has been shown that energy scavenging sources, like solar and vibrations, can provide power for an unlimited period of time making the difference with standard power storage devices such as lithium batteries or fuel cells in order to power ICTs technologies. Mechanical vibrations, understood as those energy sources represented by a mechanical movement of a structure, represent a very interesting energy reservoir because of its high power potentiality and its ubiquity. Table 1.3 lists different examples of this kind of reservoirs indicating which frequency contains the majority of the energy and the acceleration it can provide ranging from 10^{-3}g up to 1g. Thus, all these cases present different preferred frequencies but with a common characteristic: the peak is placed at the low frequency range, from 0.1Hz to 500Hz. As a matter of fact, it can be said that mechanical vibrations are found in the low-frequency band.

Vibration source	a (m/s²)	f_{peak} (Hz)
Refrigerator	*0.1*	*240*
Washing machine	*0.5*	*109*
Car instrument panel	*3*	*13*
Window	*0.7*	*100*
Bridge	*0.6*	*20*
Airplane	*1.4*	*30*

Table 1. 3. List of different vibration sources and their acceleration and fundamental frequencies: it can be seen accelerations up to more than 1g and frequency peaks ranging from 0 to 250Hz. Data from [14, 15,16].

Other vibration reservoirs present no peak as those showed in Fig. 1.6. From the Wisepower web site (www.wisepower.it) one can obtain the characterization of a huge number of different real vibrations. Fig.1.6 shows the vibration power spectral density up to 50Hz for a running car (Fig.1.6.a) and for a train upper arm (Fig.1.6.b) in the three Cartesian directions.

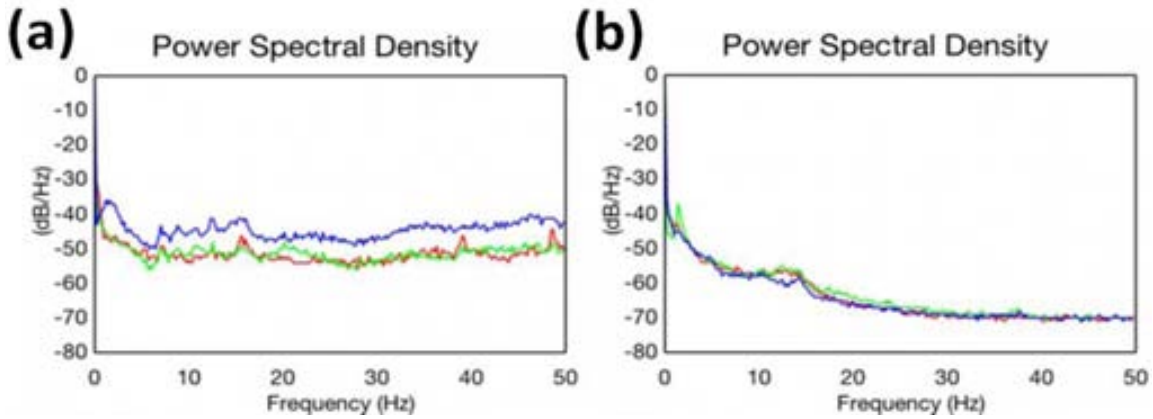

Fig.1. 6. Power spectral densities for a (a) Running BMW x3 and a (b) train upperarm along the three cartesian axis: *x*-axis (blue line), *y*-axis (green line) and *z*-axis (red line). Data extracted from [14].

The three spectral representations shown in Fig. 1.6(a) have a constant level through all the considered frequency range of -45dB/Hz for *x*-axis and -55dB/Hz for *y* and *z*-axis approximately. An increase of the vibration power spectral density in the low frequency range can be seen for the case shown in Fig. 1.6(b) reaching -40 dB/Hz between 0 and 5 Hz and becoming flat for frequencies higher than 30Hz with about -70dB/Hz. However, in both cases no clear peak is observed and the energy is concentrated in the low frequency range as it was pointed out before.

In order to compare the EH devices throughput reported in the literature, there are different options and it is still being a matter of discussion. The power density, PD, in terms of harvested power per unit volume, can provide some information about the goodness of the device but it does not take into account the maximum amount of energy the enviornment can supply for each particular case. Moreover, some strategies would express in a more clarifying way its performance in terms of power per unit area, which makes difficult the comparison with the rest of engines. The normalized power density, NPD, could solve the first of these two problems in the case of vibration EH, introducing to the expression of the PD the acceleration of the main peak in the spectral picture. Unfortunatelly, as it has been showed before, some energy reservoirs do not show a peak, therefore NPD becomes ill defined. With the aim of giving the reader an insight on the state of the art with some numbers, we report both PD and NPD for some exemples taken from the literature in cases where this type of comparison is accepted. The results are showed in Table.1.4 and Fig.1.7.

	P (μW)	f_o (Hz)	a (m/s^2)	V (cm^3)	PD ($\mu W/cm^3$)	NPD ($\mu W/cm^3/g^2$)
Roundy [15]	*275*	*120*	*2.5*	*1*	*275*	*4.5*
White [16]	*2.1*	*80.1*	*2.3*	*0.125*	*16.8*	*0.3*
Elfrink [17]	*17*	*353*	*6.4*	*24.5*	*0.7*	*0.002*
Shearwood [18]	*0.3*	*4400*	*382*	*0.0054*	*55.6*	*3.9*
Perpetuum [1]	*4000*	*100*	*0.4*	*30*	*133.3*	*85*
Wen [19]	*830*	*110*	*95.5*	*1*	*830*	*0.01*
Mitcheson [20]	*3.7*	*30*	*50*	*0.75*	*4.93*	*0.0002*
Despesse [21]	*1052*	*50*	*8.8*	*1.8*	*584.4*	*0.8*
Present work* (chapter 3)	$0.14 \cdot 10^{-6}$	-	-	$7.7 \cdot 10^{-9}$	*12.7**	*11.3***
Present work (chapter 4)	$0.15 \cdot 10^{-6}$	-	-	$9 \cdot 10^{-12}$	$15 \cdot 10^{3}$*	*500***

Table 1. 4. List of different piezoelectric, electromagnetic and electrostatic EH devices reported in the literature comparing the corresponding P, PD and NPD along with the main frequency, acceleration and volume.
*Transduction mechanism not optimized.
**Considering the root mean square of the acceleration instead of the acceleration for the main peak. Without taking into account the volume it would occupy the management electronics but only the harvester's.

Notice that, in terms of PD performance, *Wen* holds the first position while in the NPD representation it falls to the fifth position. The contrary can be appreciated with *perpetuum* which goes from the fourth to the first position. Hence, the throughput for the different harvesters developed by the EH community has not a well established manner to be quantified as it is clear in the light of the results listed in Table 1.4.

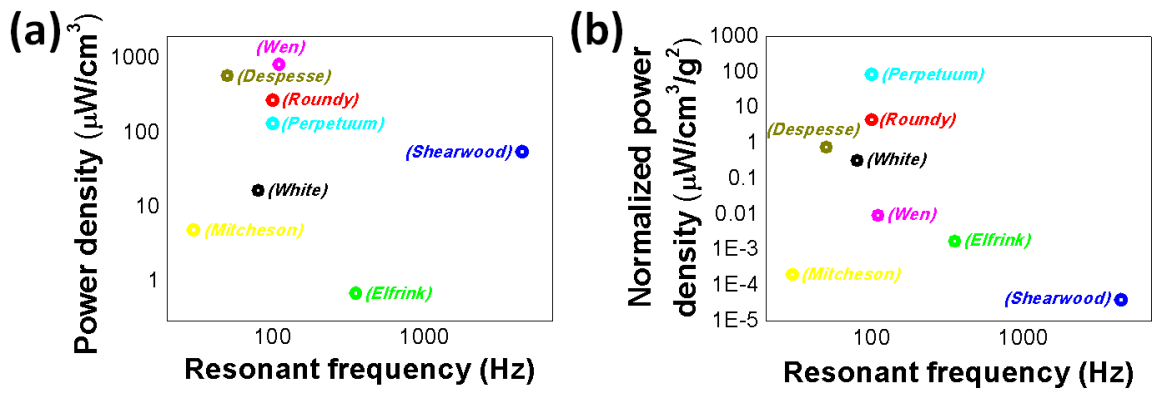

Fig.1. 7. Graphic representation of (a) PD and (b) NPD from the data of Table 1.4 without considering the results achieved for the present work.

At this point it must be stressed that there is an important difference when referring to the "vibration intensity" between inertial and non-inertial vibration forces. The latest have been considered for the results from chapter 3 and 4, while the rest of examples showed in Fig. 1.7 are based on inertial forces. This will be widely addressed during section 1.2.

1.2. The need for downscaling

When designing a harvester device one may need to arrange some parameters to match the specifications of, for instance, the place where it will be installed or thrown, the period of time it should be working, i.e. lifetime or the specific nature of the energy source. When dealing with vibrations, this last constraint becomes really important: the spectral characterization of the source and its intensity are two of the main parameters to take in consideration.

First of all, one should discern if the input vibration shows some preferred frequencies where the majority of the energy is contained or, on the contrary, the energy is spread over a broad band in the frequency domain. In the first case, the most studied one [22], one need to match the resonant frequency of the mechanical structure with the characteristic frequency of the source. The narrower the frequency peak is, the more precise the frequency match needs to be. Under some conditions the maximum output power, $|P|$, achievable for a resonating harvester as a function of the external force frequency, ω, could be expressed as [23]:

$$|P(\omega)| = \frac{m b_e \omega_n \omega^2 \left(\omega/\omega_n\right)^3 Y^2}{2 b_T \, \omega/\omega_n + \left(1 - \left(\omega/\omega_n\right)^2\right)^2} \qquad (1.1)$$

Where m is the mass of the resonator, b_e and b_T are the electrical and viscous damping respectively, ω_n is the natural frequency of the structure and Y represents the input excitation in terms of displacement. Regardless of the specificities of parameters like the moving mass, m, and the damping, b_e and b_T, one can derive directly from this expression that a maximum is achieved when $\omega=\omega_n$.
In second place we should take into account the input intensity. For the simple model given above, the relation between input and output vibration amplitude can be described as follows:

$$|X| = \left| \frac{-\omega^2}{-\omega^2 + 2b_T i\omega\omega_n + \omega_n^2} \right| |Y| \qquad (1.2)$$

Where $|X|$ and $|Y|$ stand for output and input displacement amplitudes respectively. Even if the frequency match is not achieved, an increase of the input intensity is translated to a linear increase of the output displacement, thus of the generated power, showing no saturation. Some practical drawbacks must be considered at this point. On one hand, an increase of the input intensity leads to a greater amount of harvested power, but at some point the mechanical structure will meet the rupture point becoming useless. This means that the designer must adapt the device to the input intensity in the upper band or to the design to limit the maximum vibration amplitude [24]. On the other hand, if $|Y|$ decreases dramatically maintaining the device characteristics it will not be sensitive enough to respond adequately in terms of harvested power density.
In order to illustrate this, consider equation 1.1: assuming the frequency match condition one can express the generated power as:

$$P \propto ma^2\omega_0 \qquad (1.3)$$

Where *a* stands for the acceleration. If a linear downscaling of the device by a factor *h* (*l→hl; w→hw; t→ht; h<1*) is considered, then PD depends on *h* as:

$$\frac{P}{Volume} \propto \frac{1}{h} \qquad (1.4)$$

This indicates that downscaling improves the power performances. Therefore, resonators based energy harvesters work on a two-fold restrictive window: frequency and intensity constraints. After that, one can suggest reducing the device dimensions to increase the sensitivity to an adequate level and, in fact, this is one of the main strategies to increase the device yield. Unfortunately, two problems arise from that: first, the reduction in size carries a reduction of the inertial mass which can provoke the system to reduce its response to the external vibration in some cases, as later will be discussed. Second, this leads to a dramatic increase of the resonant frequency, as it can be seen from the expression corresponding to a cantilever with length *l*, width *w* and thickness *t*:

$$f_r = \frac{1}{2\pi}\sqrt{\frac{k}{m}} \propto {}^{t}/_{l^2} \qquad (1.5)$$

Thereby, when performing a linear downscaling, *h*, the resonant frequency is up-shifted by the same factor *h* as it can be appreciated from Fig.1.8. In some cases, reducing the device dimensions could be done in such a manner that makes possible to keep the

frequency match [25]. However, downscaling becomes generally problematic for what concern the preferred frequencies (Table.1.3), which are far away in terms of MEMS and NEMS specifications with resonant frequencies in the kHz and MHz range.

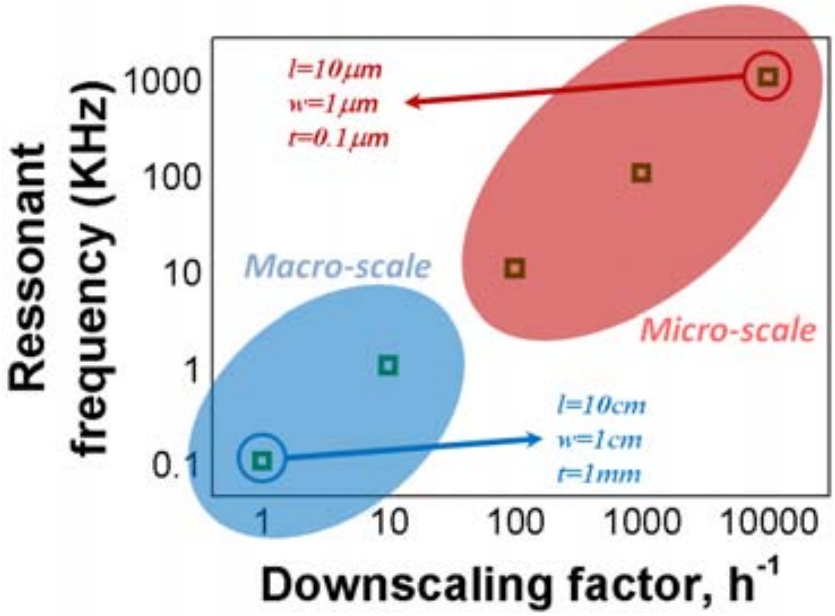

Fig.1. 8. Ressonant frequency as a function of the inverse of the scaling factor, *h*, showing the trend of the miniaturization.

The situation becomes worse if one consider a frequency distribution of the energy where the main source is not concentrated around one specific frequency range, but it is spread all over the low frequency range as pointed out on section 1.1. Even accepting the possibility of downscaling to a micro-structure capable of resonating at the low frequency range, the scenario will demand to adequately respond to a large number of different frequencies, thus revealing the need of using a set of different low frequency micro-systems [26] consisting of an array of MEMS covering the whole frequency band of interest. Although it solves some aspects of the problem, stills being a lost in terms of used area and PD. Actually, this is the most probable scenario when dealing with real applications. The present work is focused on this situation trying to describe the broad-band vibrations in a general frame related with its intensity and spectrum characteristics. Besides the need to design the harvester device depending on the energy source, another motivation for the downscaling could be given by the application itself as it was mentioned before.

m	K	F	x_{rms}	P	PD
h^3	H	h^3	h^2	h^2	$1/h$

Table 1. 5. Dependence of the mass, *m*, elastic constant, *k*, external force, *F*, root mean square of the displacement, x_{rms}, generated power, P, and power density, PD.

Very often vibrations are treated as a source of acceleration. This is the case for example for a resonator attached to a domestic machine: the excitation is transferred to

the moving part of the harvester through the anchor. For this kind of inertial excitations the force suffered by the harvesting device can be expressed as:

$$F = m \cdot a = k \cdot x \qquad (1.6)$$

Consequently, for a given acceleration, the root mean square of the displacement can be expressed as follows:

$$x_{rms} = \frac{m}{k} a_{rms} \qquad (1.7)$$

Therefore, following the dependences shown in Table 1.5, if the system is downscaled by a factor h the ratio m/k decreases in a factor h^2 which means that to maintain the same amplitude of displacement the external acceleration must increase in a factor $1/h^2$. Even if a reduction of the achieved displacement by the same factor is assumed it stills need an increase of $1/h$. This relation between acceleration and displacement constraints the number of inertial vibrations to be considered for EH proposes (see Table 1.5).

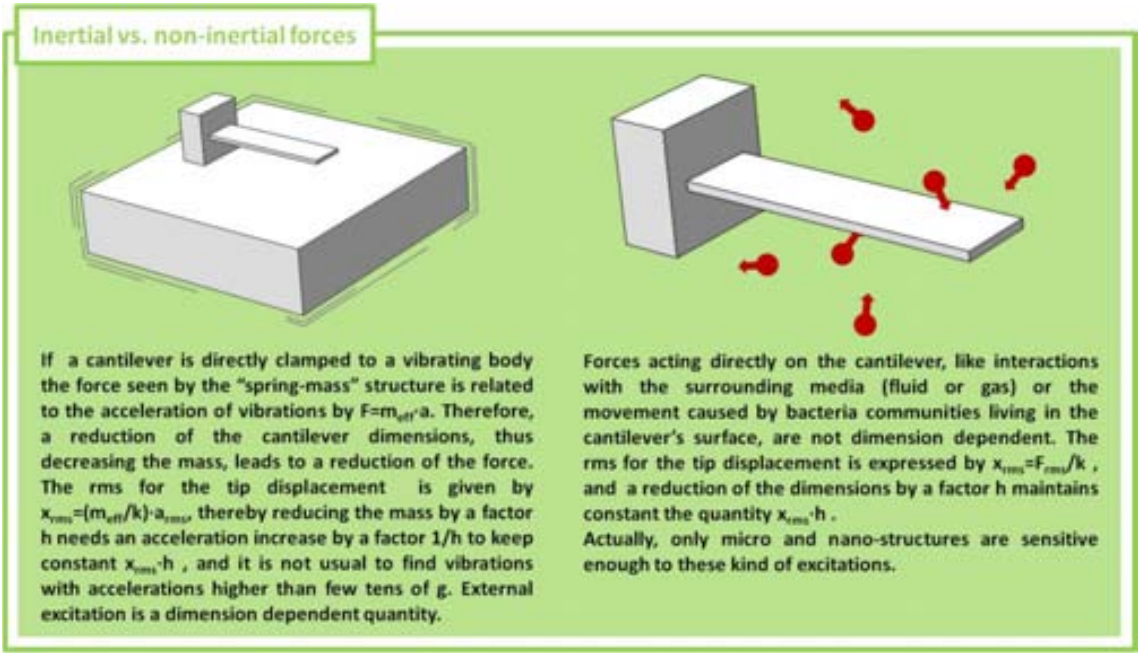

Non-inertial forces are another source of vibrations to take under consideration. Roughly speaking they can be treated as a force source and therefore only the intensity of the force is of interest. One of these representing a very interesting particular case is the vibration induced by the movement of a bacteria population living in the surface of a mechanical structure [27]: a relatively low density bacteria population induces a force of about 0.4nN to the AFM cantilever considered in the referenced work. Taking into account the cantilever's mass, the corresponding acceleration root mean square is 50Š10^{3}m/s^2 which is clearly higher than the values listed in Table 1.2 corresponding to

inertial excitations. Sources of vibrations like acoustic waves [28], fluid turbulences [29], electrostatic forces [30, 31]. actuating directly on the moving part are some excitation reservoirs to take into account.

1.3. The bistable approach

A novel strategy for breaking the need of a frequency match between the mechanical structure and the target was presented on 2009 [32] by the group of L. Gammaitoni at the Universitá di Perugia (Italy). It was based on non-linearizing the resonator response inducing a bistable behavior as it is discussed below. It was demonstrated that the response of a bistable system is improved under some conditions in terms of harvested electrical power when driven by an external force with a white Gaussian noise (WGN) spectrum considered as the most general case of broadband frequency excitation.

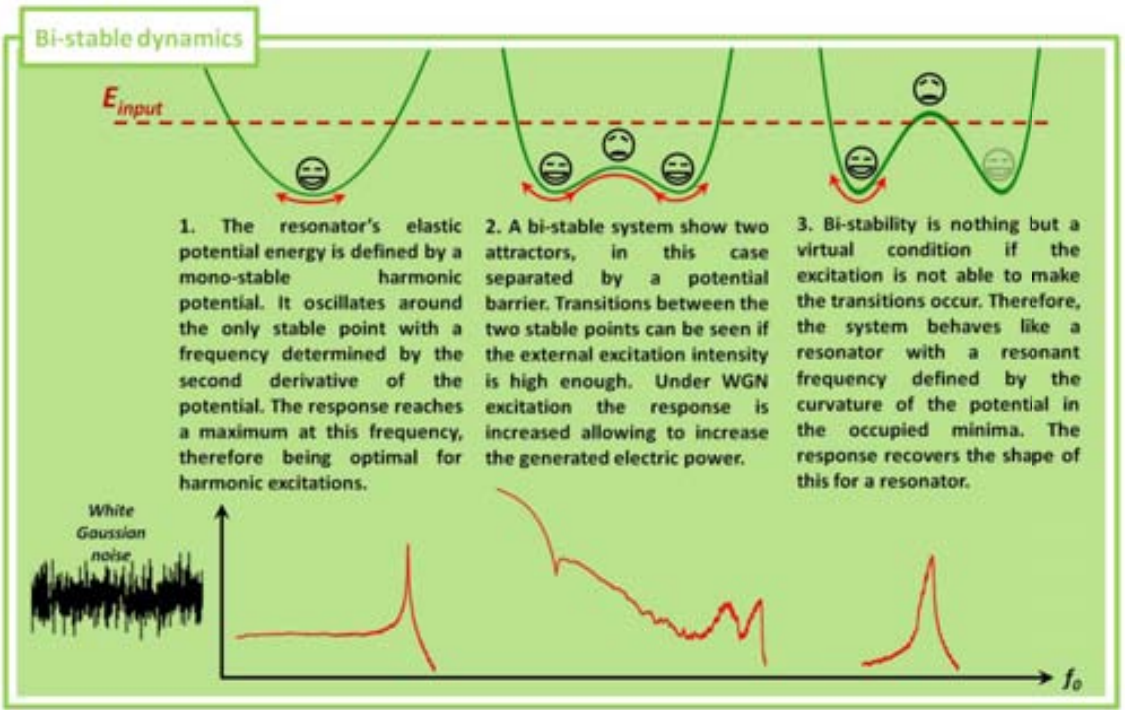

This work opened the door to the possibility of reducing the device dimensions without getting far away from the target input frequency.

Fig1.9 shows a scheme of the demonstrator. A permanent magnet of strength $|B|$ is placed at the free end of a pendulum. At the same time another magnet is placed in front of the first one, oriented in such a way that an anti-restoring force is added to the original system. Depending on the intensity of the magnetic repulsion, which is a function of $|B|$ and the distance between magnets, d, the system becomes bistable with the emergence of two new stable states together with the fade out of the original mono-

stable elastic potential energy. In this situation the original stable point becomes a saddle point.

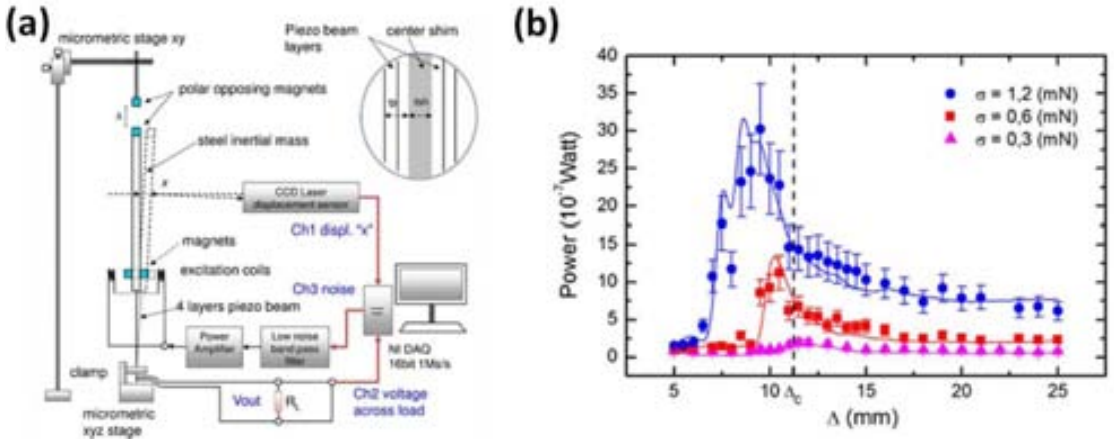

Fig.1. 9. (a) Scheme of the magnet-based demonstrator. Bi-stability is achieved by tuning the distance between magnets. Two extra magnets are placed near the clamped end of the pendulum in order to excite the structure. A piezoelectric transduction strategy is considered. (b) Generated power under three different WGN intensities achieving a maximum power of 3 mW for an excitation of 1.2 mN rms.

Bistability could be achieved by different means and some of these will be later discussed in this thesis dissertation, but there are some common characteristics. First, the potential energy barrier height between the two minima fixes a threshold value for the input noise or low frequency vibration to make the system to jump from one well to the other. Beneath this threshold value, the system behaves as a resonant one with its characteristic frequency determined by the potential curvature around the specific well where the system is confined. Therefore, it is worth to note that, in the resonating case, we deal with an accepted frequency window while in the bistable case this window is largely broadened. However, the required intensity for the input needs to overcome a certain value to operate at its maximum. This is shown in Table.1.6:

	Amplitude bandwidth	**Frequency bandwidth**
Resonating device	$[0, +\infty)$	$[f_0 - \delta f, f_0 + \delta f)$
Bi-stable device	$[A_{min}, +\infty)$	$(0, +\infty)$

Table 1. 6. Practical constraints for the resonator based and bistable based strategies.

Thereby, the bi-stable approach requires a precise tuning of the different parameters which tune the bistable configuration to be sensitive enough to a specific external excitation. If the example here commented is considered in a particular configuration to respond at its maximum under an excitation of 1.2mN, a reduction of this excitation intensity down to 0.6mN represents a reduction of the generated power of more than one order of magnitude.

1.4. Goals and outline of the thesis

The goal of this thesis dissertation is to explore the capability of bistable-based energy harvesting strategies to increase the performance of standard resonator-based harvesters, particularly at the micro and nano-scale. The following specific objectives are established:

i) Design, model, fabricate and test bi-stable MEMS for EH with a special effort on the agreement between model and experimental characterization in order to find a systematic way to achieve a rule of thumb for future fabrication, taking into account the particular specifications.

ii) Design and modeling of bi-stable NEMS for EH through atomistic description with special focus on 2D nano-structured materials. Piezoelectric effect is studied to be the mechanism for transduction. Fabrication of graphene devices is explored.

iii) Evaluate the benefits of the bistable approach and specify the conditions of operation.

iv) Investigate the feasibility of MEMS and NEMS as a main blocks for building EH devices.

Pursuing these objectives, the dissertation is divided in the following chapters (excluding the present one):

Chapter 2 This chapter is devoted to explain the framework within which this work has been carried out, with special emphasis on the spring-mass model and atomistic calculations.

Chapter 3 This chapter explains the results obtained in Paper A (appendix) and gives further information about the model, the fabrication process and the experimental realization.

Chapter 4 In this chapter a full description of 2D materials as graphene, h-BN and MoS_2 and their applicability for EH proposes is provided. It summarizes the results obtained in Paper B, C and D (appendix).

Chapter 5 The achievements concerning the attempts of fabricating graphene-based devices are presented also reported in Paper E (appendix).

Chapter 6 The main achievements explained in the previous chapters are summarized in this chapter.

References

[1] Perpetuum website: www.perpetuum.com

[2] Bampi, S., & Reis, R. (2011). Challenges and emerging technologies for system integration beyond the end of the roadmap of nano-CMOS. In *VLSI-SoC: Technologies for Systems Integration* (pp. 21-33). Springer Berlin Heidelberg.

[3] Declerck, G. (2005, June). A look into the future of nanoelectronics. In *VLSI Technology, 2005. Digest of Technical Papers. 2005 Symposium on* (pp. 6-10). IEEE.

[4] Starner, T. E. (2003). Powerful change part 1: batteries and possible alternatives for the mobile market. *Pervasive Computing, IEEE*, *2*(4), 86-88.

[5] Schaller, R. R. (1997). Moore's law: past, present and future. *Spectrum, IEEE*, *34*(6), 52-59.

[6] Thompson, S. E., & Parthasarathy, S. (2006). Moore's law: the future of Si microelectronics. *Materials Today*, *9*(6), 20-25.

[7] Ferry, David K. "Nanowires in nanoelectronics." *Science* 319.5863 (2008): 579-580.

[8] Denison, T., Consoer, K., Kelly, A., Hachenburg, A., & Santa, W. (2007, February). A 2.2µW 94nV/√ Hz, Chopper-Stabilized Instrumentation Amplifier for EEG Detection in Chronic Implants. In *Solid-State Circuits Conference, 2007. ISSCC 2007. Digest of Technical Papers. IEEE International* (pp. 162-594). IEEE.

[9] Shinagawa, M., Fukumoto, M., Ochiai, K., & Kyuragi, H. (2004). A near-field-sensing transceiver for intrabody communication based on the electrooptic effect. *Instrumentation and Measurement, IEEE Transactions on*, *53*(6), 1533-1538.

[10] Chandrakasan, A., Verma, N., Kwong, J., Daly, D., Ickes, N., Finchelstein, D., & Calhoun, B. (2006). Micropower wireless sensors. *Power*, *30*(35), 40.

[11] Roundy, Shad, Paul Kenneth Wright, and Jan M. Rabaey. *Energy scavenging for wireless sensor networks: with special focus on vibrations*. Springer, 2004.

[12] http://www.microstrain.com

[13] Tan, Y. K., & Panda, S. K. (2011). Energy harvesting from hybrid indoor ambient light and thermal energy sources for enhanced performance of wireless sensor nodes. *Industrial Electronics, IEEE Transactions on*, *58*(9), 4424-4435.

[14] Neri, I., Travasso, F., Mincigrucci, R., Vocca, H., Orfei, F., & Gammaitoni, L. (2012). A real vibration database for kinetic energy harvesting application. *Journal of Intelligent Material Systems and Structures*, *23*(18), 2095-2101.

[15] Roundy, S., Wright, P. K., & Rabaey, J. (2003). A study of low level vibrations as a power source for wireless sensor nodes. *Computer communications*, *26*(11), 1131-1144.

[16] White, N. M., Glynne-Jones, P., & Beeby, S. P. (2001). A novel thick-film piezoelectric micro-generator. *Smart Materials and Structures*, *10*(4), 850-852.

[17] Elfrink, R., Renaud, M., Kamel, T. M., De Nooijer, C., Jambunathan, M., Goedbloed, M. & Van Schaijk, R. (2010). Vacuum-packaged piezoelectric vibration energy harvesters: damping contributions and autonomy for a wireless sensor system. *Journal of Micromechanics and Microengineering*, *20*(10), 104001.

[18] Williams, C. B., Shearwood, C., Harradine, M. A., Mellor, P. H., Birch, T. S., & Yates, R. B. (2001, December). Development of an electromagnetic micro-generator. In *Circuits, Devices and Systems, IEE Proceedings*- (Vol. 148, No. 6, pp. 337-342). IET.

[19] Ching, N. N., Wong, H. Y., Li, W. J., Leong, P. H., & Wen, Z. (2002). A laser-micromachined vibrational to electrical power transducer for wireless sensing systems. *Sensors Actuators*, 97-98.

[20] Mitcheson, P. D., Stark, B. H., Miao, P., Yeatman, E. M., Holmes, A. S., & Green, T. C. (2003, September). Analysis and optimisation of MEMS electrostatic on-chip power supply for self-powering of slow-moving sensors. In *Proc. Eurosensors* (Vol. 3, pp. 492-495).

[21] Despesse, G., Jager, T., Chaillout, J. J., Leger, J. M., & Basrour, S. (2005, July). Design and fabrication of a new system for vibration energy harvesting. In *Research in Microelectronics and Electronics, 2005 PhD* (Vol. 1, pp. 225-228). IEEE.

[22] Roundy, S., Leland, E. S., Baker, J., Carleton, E., Reilly, E., Lai, E. & Sundararajan, V. (2005). Improving power output for vibration-based energy scavengers. *Pervasive Computing, IEEE*, *4*(1), 28-36.

[23] Beeby, S. P., Tudor, M. J., & White, N. M. (2006). Energy harvesting vibration sources for microsystems applications. *Measurement science and technology*, *17*(12), R175.

[24] Soliman, M., Abdel-Rahman, E. M., El-Saadany, E. F., & Mansour, R. R. (2009). A design procedure for wideband micropower generators. *Microelectromechanical Systems, Journal of*, *18*(6), 1288-1299.

[25] Murillo, G., Abadal, G., Torres, F., Lopez, J. L., Giner, J., Uranga, A., & Barniol, N. (2009). Harvester-on-chip: Design of a proof of concept prototype. *Microelectronic Engineering*, *86*(4), 1183-1186.

[26] Liu, J. Q., Fang, H. B., Xu, Z. Y., Mao, X. H., Shen, X. C., Chen, D. & Cai, B. C. (2008). A MEMS-based piezoelectric power generator array for vibration energy harvesting. *Microelectronics Journal*, *39*(5), 802-806.

[27] Longo, G., et al. "Rapid detection of bacterial resistance to antibiotics using AFM cantilevers as nanomechanical sensors." *Nature nanotechnology* 8.7 (2013): 522-526.

[28] Liu, Fei, et al. "Acoustic energy harvesting using an electromechanical Helmholtz resonator." *The Journal of the Acoustical Society of America* 123 (2008): 1983.

[29] Akaydin, Huseyin Dogus, Niell Elvin, and Yiannis Andreopoulos. "Energy harvesting from highly unsteady fluid flows using piezoelectric materials." *Journal of Intelligent Material Systems and Structures* 21.13 (2010): 1263-1278.

[30] Bouchouicha, D., et al. "Ambient RF energy harvesting." *IEEE Int. Conf. Renewable Energies Power Quality (ICREPQ'10)*. 2010.

[31] Radioactive: Duggirala, R., et al. "MEMS Radioisotope-Powered Piezoelectric μ-Power Generator (RPG)." *Micro Electro Mechanical Systems, 2006. MEMS 2006 Istanbul. 19th IEEE International Conference on*. IEEE, 2006.

[32] Cottone, F., Vocca, H., & Gammaitoni, L. (2009). Nonlinear energy harvesting. *Physical Review Letters*, *102*(8), 080601.

[33] López-Suárez, M., et al. "Inducing bistability with local electret technology in a microcantilever based non-linear vibration energy harvester." *Applied Physics Letters* 102.15 (2013): 153901-153901.

CHAPTER 2

WORKFRAME

The workframe of this dissertation is well defined within the limits of two different fields. In one hand, the modeling of electro-mechanical systems in an analytical form considering chunks of materials treated as a continuum that can be modeled with effective parameters within the spring-mass model [1]. In the other hand, atomistic description of structures in which the atomic scale details have an important role is carried out by *ab initio* calculations as implemented in the SIESTA package [2] within the Generalized Gradient Approximation, to be later discussed. Both allow the study of the dynamic and static characterization of the desired systems.
An important point is choosing the appropriate approach for each case. For instance, 2D crystals cannot be described through effective parameters, such the Young modulus, because they have no well-defined thickness, while standard MEMS and NEMS do.

In the two first sections of this chapter an overview of the static and dynamic behavior will be addressed without entering to the deepest details. In the third section the dynamic simulation and the electrical conversion model will be explained.

2.1. The spring-mass model

Mechanical structures have been widely studied from both static and dynamic points of view. As it was mentioned in chapter 1, MEMS and NEMS are widely used for applications in RF-communications, sensors and actuators. which demands a high control of the mechanical characteristics of the mobile part in terms of geometric parameters and material specifications. A first overview of the spring-mass model will be held in this section and will be taken up again in the first lines of the third section of this chapter.

Considering the bar depicted in Fig. 2.1, the arc defined by the angular differential, $d\theta$, can be expressed as a function of the coordinate z accomplishing that its length does not varies when the bar is bended along the dashed white line (neutral plane):

$$dl = (r - z)d\theta \qquad (2.1a)$$

$$dx = rd\theta \tag{2.1b}$$

Where *dl* stands for the length variation of the bar, *r* the radius of the bending, *z* is the position where the change in length is measured and *dx* is the projection of *dl* in the *x*-axis. Therefore, for *z>0* the bar is stretched while for *z<0* a compressive strain is produced.

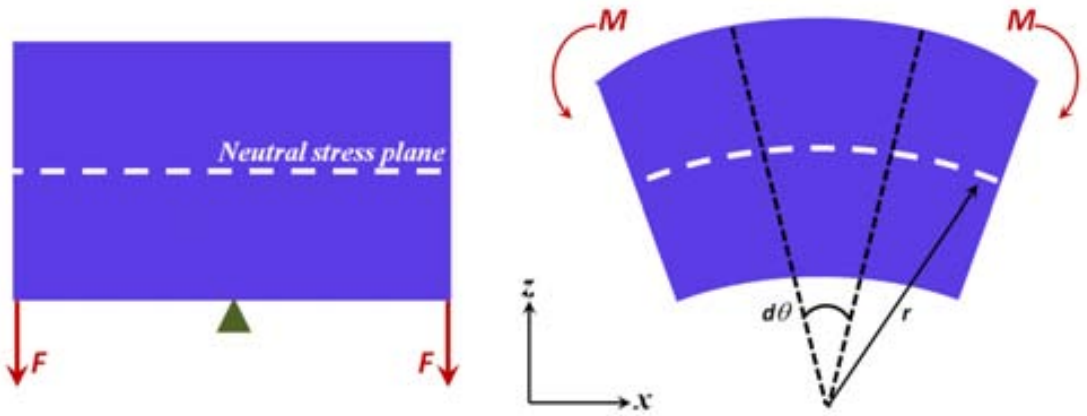

Fig. 2. 1. Segment of a beam under deformation caused by a force, *F*, provoking a bending moment, *M*. The neutral plane represented by a dashed white line is under no stress.

The slope of the beam at any point for a certain deformation defining an angle, θ, is given by:

$$\frac{du}{dx} = tan\theta \tag{2.2}$$

And the relation between the bending radius and the bending moment can be expressed as:

$$M = -\frac{t^3 wY}{12r} = -\frac{IY}{r} \tag{2.3}$$

Where *l*, *w* and *t* are defined in Fig. 2.2 and *Y* is de Young's modulus. The second moment of area is defined as $I=t^3w/12$. Both, *I* and *Y*, are normally assumed to be constant. Combining equations 2.1, 2.2 and 2.3 one can obtain the differential equation for a beam under deformation:

$$\frac{d^2u}{dx^2} = -\frac{M}{YI} \tag{2.4}$$

Once *M* is determined the deflection at any point is known integrating twice equation 2.4, taking into account particular boundary conditions.

The power of this theory is its ability of describing correctly the majority of the features of beams, regardless of the particular conditions, including composite structures and rare geometries. However, the interest of this work is focused on what is known as "clamped-free beams", or "cantilevers", and "clamped-clamped beams", or its abbreviation "cc-beam", with constant rectangular cross-section.

Therefore, if a cantilever of length, *l*, width, *w*, thick, *t*, with *u(0)=0* and $\frac{\partial u}{\partial x}\Big|_{x=0} = 0$ as boundary conditions is considered (Fig. 2.2), equation 2.4 can be solved directly to obtain:

$$u(x) = \frac{F}{YI}\left(\frac{lx^2}{2} - \frac{x^3}{6}\right) \tag{2.5}$$

where *u(x)* represents the deflection of the beam at some point *x*. Here the force, *F*, is assumed to be a point load acting at the free end of the cantilever and, therefore, the deflection of the free end can be expressed in a very compact manner as:

$$F = \frac{Y}{4}\frac{wt^3}{l^3}u(l) \tag{2.6}$$

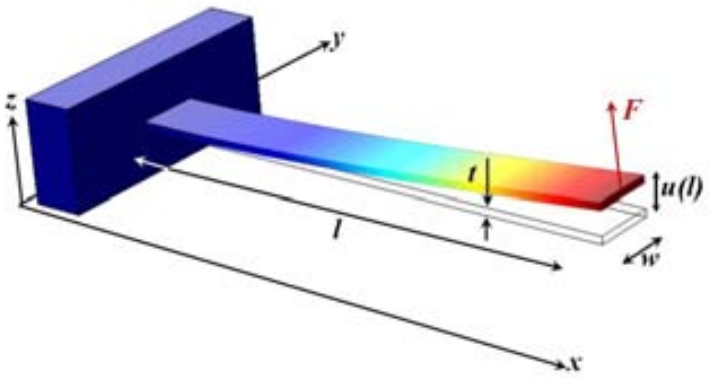

Fig. 2. 2. Representation of a point load, *F*, acting at the free end of a cantilever provoking a deformation, *u*.

The whole structure is treated as a system containing two elements: a spring governed by the Hook's law and a mass. If equation 2.6 is compared with the Hook's law, *F=kx*, it seems reasonable to state that the mechanical system behaves as a spring with elastic constant:

$$k_c = \frac{Y}{4}\frac{wt^3}{l^3} \tag{2.7}$$

The same development could be done in order to describe the deflection of a cc-beam (Fig. 2.3), which is the other structure concerning the present dissertation. In this case a point load acting on the center of the beam is considered, and boundary conditions described by $u(0)=u(l)=0$ and $\frac{\partial u}{\partial x}\Big|_{x=0} = \frac{\partial u}{\partial x}\Big|_{x=l} = 0$. This time the displacement of the center of the beam is expressed as:

$$F = \frac{16Ywt^3}{l^3}u(l/2) \tag{2.8}$$

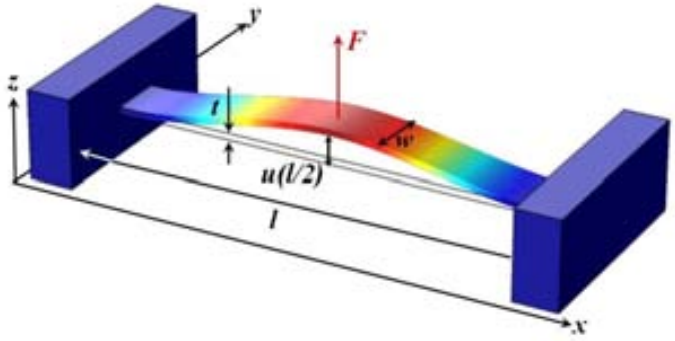

Fig. 2. 3. Representation of a point load, F, acting at the center of the structure, $x=l/2$, of a cc-beam provoking a deformation, u.

And the expression for its elastic constant may be written as:

$$k_c = \frac{16Ywt^3}{l^3} \tag{2.9}$$

Once the statics of these two cases have been determined in terms of material and geometric parameters, the next step is to determine the dynamics, that is, determining the natural frequency of the mode n, $\omega_n=2\pi f_n$. Considering the principle of minimum action, derived from the Hamilton principle [3], the governing equation is obtained for a dynamic deflection:

$$\left(YI\frac{\partial^4 u}{\partial x^4}\right) = -\mu\frac{\partial^2 u}{\partial t^2} + F \tag{2.10}$$

Where μ stands for the longitudinal mass density, ρS. Equation 2.10 can be solved assuming variable separation, $u(x,t) = \mathcal{U}(x)\cdot\Phi(t)$, with $\Phi(t) = cos(\omega_n t + \theta)$ and considering free vibrations, thus, no external force is applied, $F=0$. Therefore:

$$YI\frac{d^4\mathcal{U}(x)}{dx^4} + \rho A\omega_n^2\mathcal{U}(x) = 0 \qquad (2.11)$$

This equation has four solutions which can be written as:

$$S_1 = \left(\frac{\rho A\omega_n^2}{YI}\right)^{1/4} = k_n \qquad (2.12a)$$

$$S_2 = -S_1 \qquad (2.12b)$$

$$S_3 = iS_1 \qquad (2.12c)$$

$$S_4 = -iS_1 \qquad (2.12d)$$

These expressions determine the dependence of the resonant frequency for each mode of vibration in terms of a parameter, k_n:

$$f_n = \frac{k_n^2 w}{2\pi}\sqrt{\frac{Y}{12\rho}} \qquad (2.13)$$

In other words, the solution of equation 2.11 can be expressed as a sum of trigonometric functions as follows:

$$\mathcal{U}(x) = D_1^n \sin(k_n x) + D_2^n \cos(k_n x) + D_3^n \sinh(k_n x) + D_4^n \cosh(k_n x) \qquad (2.14)$$

Once again, the boundary conditions must be here applied in order to obtain the different coefficients showed on equation 2.14. For a cantilever beam, the D_i coefficients can be expressed as:

$$D_1^n = -D_3^n \qquad (2.15a)$$

$$D_2^n = -D_4^n \qquad (2.15b)$$

$$\frac{D_1^n}{D_2^n} = -\frac{cosh(k_n l) + cos(k_n l)}{sinh(k_n l) + sin(k_n l)} \qquad (2.15c)$$

$$\frac{D_1^n}{D_2^n} = -\frac{sinh(k_n l) - sin(k_n l)}{cosh(k_n l) + cos(k_n l)} \qquad (2.15d)$$

These equations lead to the transcendental equation for the cantilever beam which is:

$$cosh(k_n l) + cos(k_n l) = -1 \qquad (2.16)$$

For a cc-beam, as the boundary conditions are not the same than those for a cantilever beam, the equations for the coefficients are:

$$D_1^n = -D_3^n \qquad (2.17a)$$

$$D_2^n = -D_4^n \qquad (2.17b)$$

$$\frac{D_1^n}{D_2^n} = \frac{sin(k_n l) + sinh(k_n l)}{cos(k_n l) - cosh(k_n l)} \qquad (2.17c)$$

$$\frac{D_1^n}{D_2^n} = -\frac{cos(k_n l) - cosh(k_n l)}{sin(k_n l) + sinh(k_n l)} \qquad (2.17d)$$

For these kinds of structures, then, the transcendental equation becomes:

$$cosh(k_n l) + cos(k_n l) = 1 \qquad (2.18)$$

The valid solutions for k_n are listed in Table 2.1 for both kind of beams.

		Cantilever beam	Clamped-clamped beam
First mode	$k_1 \cdot l$	*1.87*	*4.73*
Second mode	$k_2 \cdot l$	*4.69*	*7.85*
Third mode	$k_3 \cdot l$	*7.85*	*10.99*

Table 2. 1. Solution parameters to the transcendental equations 2.13 and 2.15 for a rectangular cross-section cantilever and a cc-beam for the three first vibration modes.

Fig.2.4 plots the three first modes for both cantilever (a) and cc-beam (b). For the sake of simplicity the first mode is assumed to be the only relevant [4].

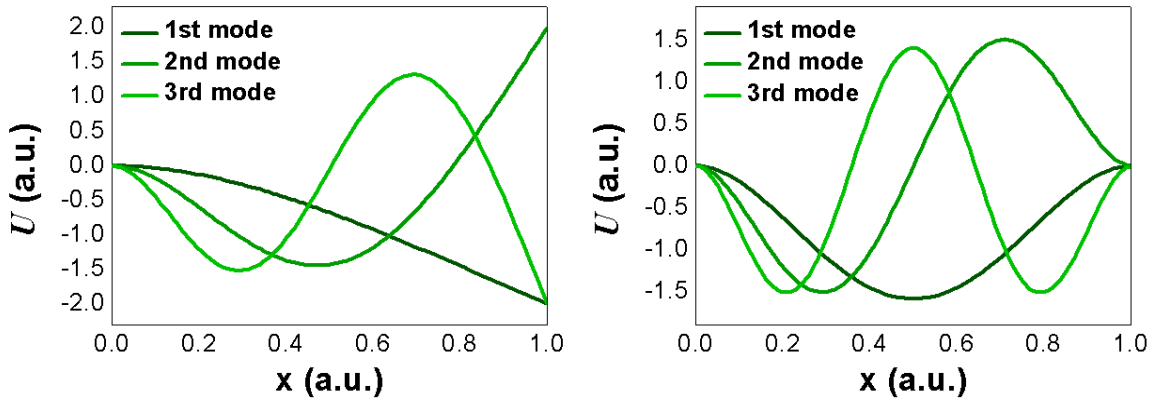

Fig. 2. 4. Shape for the three first modes, $\boldsymbol{U}$, for a (a) cantilever and (b) cc-beam. For a cantilever it presents 1, 2 and 3 nodes while for a cc-beam it has 2,3 and 4 nodes.

2.2. Atomistic calculations: DFT and the SIESTA code

Quantum mechanics has revealed to be a very powerful theory in order to describe the most intimate nature of matter. There are many situations where quantum effects become no negligible. One of the fields where a quantum description is required is condensed matter nano-physics. Unfortunately, the describing equations cannot be exactly solved for complex systems, and even for simple cases like the helium atom some approximations must be done in order to keep the problem at a manageable level.
The equations of a quantum mechanical many-body system are not possible to be solved even through numerical methods due to the high complexity of the related wave-function describing it, so one approach is to consider approximations to the exact theory, for instance treating the atoms as spheres whose interactions with the rest of atoms are described through effective potentials. However, the main objective of the Density Functional Theory (DFT) [5] is simplifying the Schrödinger equation to become a manageable problem without any approximation. DFT played a central role allowing a sound description of many-body systems achieving very accurate results, mainly for solid state physics. DFT belongs to a larger class of algorithms known as total energy methods, as the main output of the atomistic calculation is the estimation of the total energy and many other properties are obtained from it by mathematical derivations (forces on atoms by differentiation with respect to the strain tensor and so forth).
A detailed description of DFT is clearly beyond the scope of this Thesis. However, the main ideas and the capabilities of this powerful theoretical approach are quickly outlined in the following paragraphs. The interested reader is referred to Refs. [6-8].

The exact quantum mechanical description for a quantum system can be obtained solving the Schrödinger equation:

$$\widehat{H}\psi_i = E_i\psi_i \tag{2.19}$$

Assuming that the relativistic effects could be neglected, then the many-body Hamiltonian, $\widehat{H}$, can be expressed as follows:

$$\begin{aligned}\widehat{H} &= K + V_{nn} + V_{ee} + V_{ne} \\ &= \sum_I K_I + \sum_i K_i + \frac{e^2}{2}\sum_I \sum_{J\neq I} \frac{Z_I Z_J}{|R_I - R_J|} \\ &+ \frac{e^2}{2}\sum_i \sum_{j\neq i} \frac{1}{|r_i - r_j|} - e^2 \sum_I \sum_i \frac{Z_I}{|R_I - r_i|}\end{aligned} \tag{2.20}$$

Here, K stands for the kinetic energy contribution split into K_I for nuclei and K_i for electrons. The following three terms in this equation define, in order, the interaction energy between nuclei, between electrons and, finally, between each electron and the collection of atomic nuclei. A first way to simplify equation 2.20 comes from the observation that electrons move much quicker than nuclei, as their mass is much lower. Therefore, from the electronic density viewpoint nuclei can be considered to be static and the dynamics of nuclei consequently decoupled from that of the electron. This is the so-called Born-Oppenheimer approximation and it allows splitting the total wave-function solution to equation 2.19 into:

$$\psi(r, R; t) = \Theta(R; t)\phi(R, r) \tag{2.21}$$

Where $\phi(R,r)$ is the solution to the Schrödinger equation for the electronic Hamiltonian:

$$\hat{h}_e\phi_n(R, r) = \varepsilon_n\phi_n(R, r) \tag{2.22}$$

where $\hat{h}_e$ stands for:

$$\hat{h}_e = \sum_i K_i + \frac{e^2}{2}\sum_i \sum_{j\neq i} \frac{1}{|r_i - r_j|} - e^2 \sum_I \sum_i \frac{Z_I}{|R_I - r_i|} \tag{2.23}$$

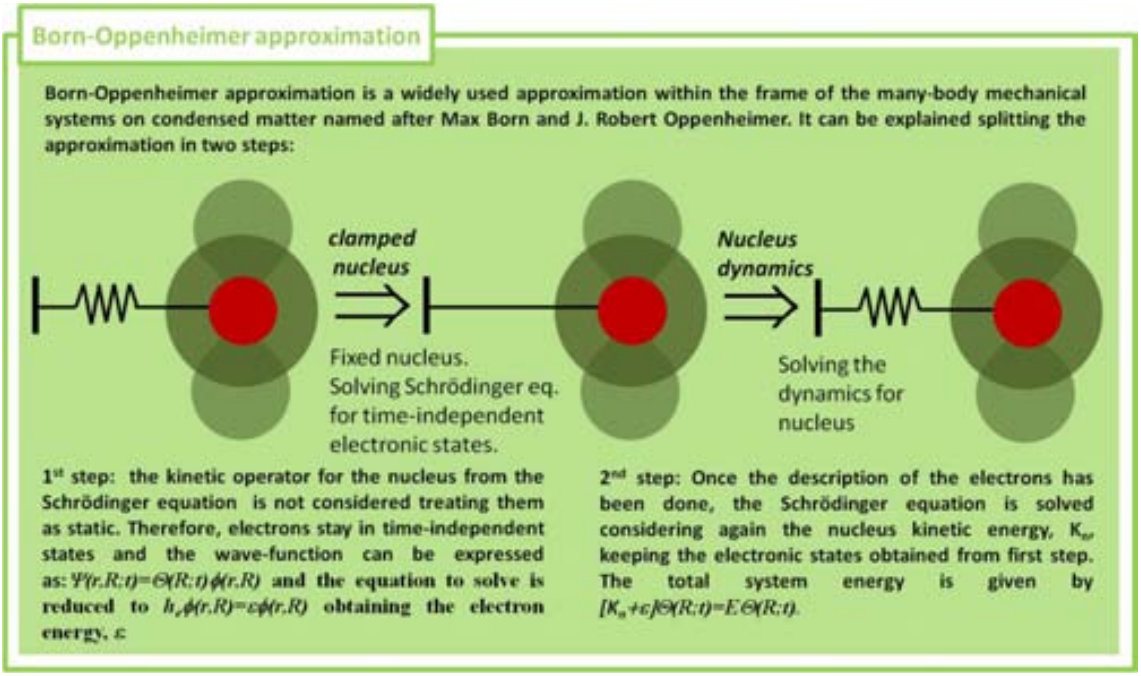

Notice that the simplification introduced with Born-Oppenheimer approximation is limited to the decoupling of electrons and nuclei and has, strictly speaking, nothing to do with DFT. Yet, it is nowadays used in most DFT codes, but not in all of them.

The fundamental theorem to formulate the DFT is the following:

> *"The electron density, n(r), of a bound system of interacting electrons under some external potential, V(r), determines this potential uniquely"*

Actually, it is the inverse formulation what sustains DFT and it can be written as:

> *"Given an electron density, n(r), there is a unique external potential, V(r), which can have determined it"*

The bijectivity of the relation between the electron density and the external potential leads us to the core of the DFT. Our starting point is the many-body system, made of interacting particles, that we cannot solve. However, if we can find a simpler system that we know how to solve, as long as it has the same electron density of the interacting system, we are guaranteed by the first theorem of DFT that the solution, i.e. the external potential, is the same. The trick consists in mapping the interacting-particle many-body system into a fictitious non-interacting particle ensemble, embedded into an effective potential. Thereby, considering equation 2.23, *V(r)* would represent the interaction between electrons and nuclei, and then the total energy of the system can be expressed as:

$$E[n(r)] = \int V(r)n(r)dr + K_i[n(r)] + E_{ee}[n(r)] \qquad (2.24)$$

The second basic theorem, due to Hohenberg and Khon, states that the true electron density is that which minimizes the functional *E[n]* being this last one the ground state energy always accomplishing $\int n(r)dr = N_e$ and $n(r) \geq 0$.

The Coulombian interaction between electrons can be reformulated in terms of the electron density, *n(r)*, as:

$$E_{ee} = \frac{1}{2}\int \frac{n(r)n(r')}{|r - r'|} drdr' = \int V_{ee}n(r')dr \qquad (2.25)$$

At this point the kinetic energy of the interacting electron system will be split into two terms: one regarding the kinetic energy of the fictitious system of non-interacting electrons with the same *n(r)*, and another term taking into account the difference of kinetic energy between the interacting and the non-interacting system and the exchange-correlation energy:

$$\begin{aligned} K_i[n(r)] &= K_{int}[n(r)] + \varepsilon_{XC}[n(r)] \\ &= K_{non-int}[n(r)] + \delta K[n(r)] + \varepsilon_{XC}[n(r)] \end{aligned} \qquad (2.26)$$

And then:

$$E[n(r)] = \int V(r)n(r)dr + K_{non-int}[n(r)] + E_{XC}[n(r)] + E_{ee}[n(r)] \qquad (2.27)$$

Back to equation 2. 23, the most critical term regards the electron-electron interactions: for a system with *N* electrons, a N^2-dimensional differential equation set must be solved. The main achievement of DFT is simplifying the problem to finding the right *n(r)* which can be expressed involving a single-electron equations set. This was done by Kohn and Sham showing that the DFT treatment is more simple.

Now, we can rewrite the Schrödinger equation acting on non-interacting states represented by ψ_i, as:

$$\left\{\frac{-\hbar^2}{2m}\nabla^2 + V(r) + V_{ee}[n(r)] + V_{XC}[n(r)]\right\}\psi_i(r) = \varepsilon_i\psi_i(r) \qquad (2.28)$$

This form a set of differential equations known as Kohn – Sham equations. Till this point the DFT is an exact theory. Unfortunately the exchange-correlation term of

equation 2. 28 remains unknown. A good approximation of $V_{XC}[n]$ is required in order to describe the main physical properties for a given system.

Until now we have simplified the problem to a non-interacting electron system with a exchange-correlation contribution yet to be determined. The Local Density Approximation (LDA) approach [9] the exact form of E_{XC} considering it to be close to that for an homogenous electron gas with the same $n(r)$ with energy density, ε_{XC}^{gas}:

$$E_{XC} \approx E_{XC}^{LDA} = \int \varepsilon_{XC}^{gas}[n(r)]n(r)dr \qquad (2.29)$$

A more complex functional comes from adding a correction to this E_{XC}^{LDA} considering the spatial distribution of $n(r)$ called Generalized Gradient Approximation (GGA) [10]:

$$E_{XC} \approx E_{XC}^{GGA} = E_{XC}^{LDA} + \int \varepsilon'_{XC}[n(r), \nabla n(r)]n(r)dr \qquad (2.30)$$

In the work presented in this thesis dissertation we have considered the GGA approach. Once the exchange-correlation energy density functional is determined equation 2.24 form a set of nonlinear coupled differential equations with a functional dependence on $n(r)$. At this point, it is worth to note there is something circular in the treatment of the problem: to solve the Kohn – Sham equations one must know V_{ee}, but to determine it the electron density is needed. Finaly, to know $n(r)$ the wave functions must be known but ψ_i are known once the Kohn – Sham equations are solved, and we are again at the beginning of this circle. Thus, the problem must be solved iterating until self-consistency is achieved.

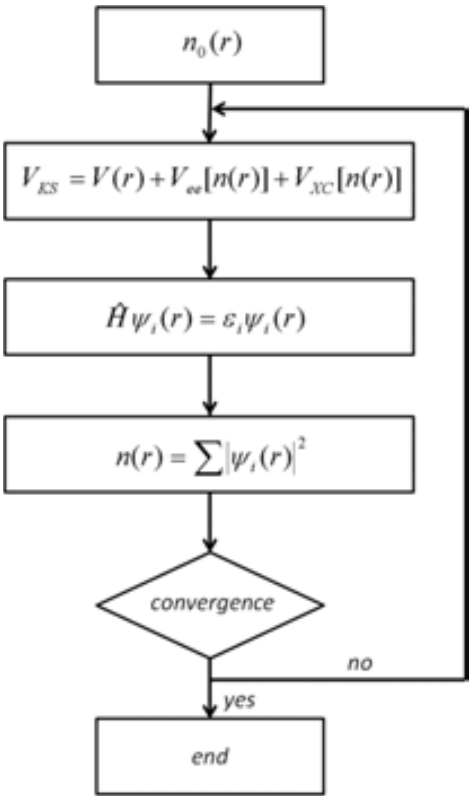

Fig. 2. 5. Flow diagram for a standard DFT based code. The buckling is iterated until self-consistency is achieved.

The flow-diagram of Fig. 2.5 shows the iteration path implemented in the most of the DFT based simulating codes:

1. Define an initial electron density, $n_0(r)$.
2. Build the potential related to this particular electron density.
3. Solve the Kohn – Sham equations to find the single-particle wave functions.
4. Calculate the resulting electron density.
5. Compare the obtained $n(r)$ with this used to solve the Kohn – Sham equations. If the two electron densities are the same within numerical accuracy, $n(r)$ is used to compute the total energy of the system, if not, the electron density is updated following a concrete protocol to begin again from point 2.

The calculation of the total energy of an infinite crystal is naturally approached by means of an expansion of $\psi_i(r)$ in terms of plane-waves. In this way one takes advantage of the periodicity of the potential, as showed by the Bloch's theorem. The number of plane-waves required to obtain converged values of energy and forces scales with the computational volume. However, the systems under study in this dissertation are two-dimensional (graphene, h-BN and MoS_2) and a large vacuum region is needed in the non-periodic direction[1]. This makes in principle plane-wave not an optimal

[1] For numerical reason, most DFT codes require the system to be periodic along all three coordinate directions. In this framework, the way of dealing with lack of periodicity is allowing a large vacuum

choice, as vacuum has to be described with the same accuracy of the space filled with atoms and, clearly, we are more interested in the latter.
For this reason a DFT code that uses localized basis function (which can be Gaussian functions, atomic orbitals…) seems in principle, more suited to this problem, as basis functions are centered on atoms and computational power is not wasted in the description of vacuum.

The results here presented are obtained using the SIESTA method [11]. It implements a self-consistent density functional method using standard norm-conserving pseudo-potentials of the Troullier-Martins type [12] and atomic orbitals as basis sets. The main advantage of this particular implementation relies in the use of numerical atomic orbitals (NAO), atomic orbitals that go smoothly to zero beyond a certain cutoff radius thus saving computational time [13]. Locality is needed for certain quantities to achieve linear scalability, meaning that perturbations at a distance sufficiently far do not affect substantially the system [14]. Moreover, this linear-scaling *ab-initio* method allows computing stresses and forces for structural relaxation and molecular dynamics analysis. In the following lines the main features and parameters of this particular code will be discussed.

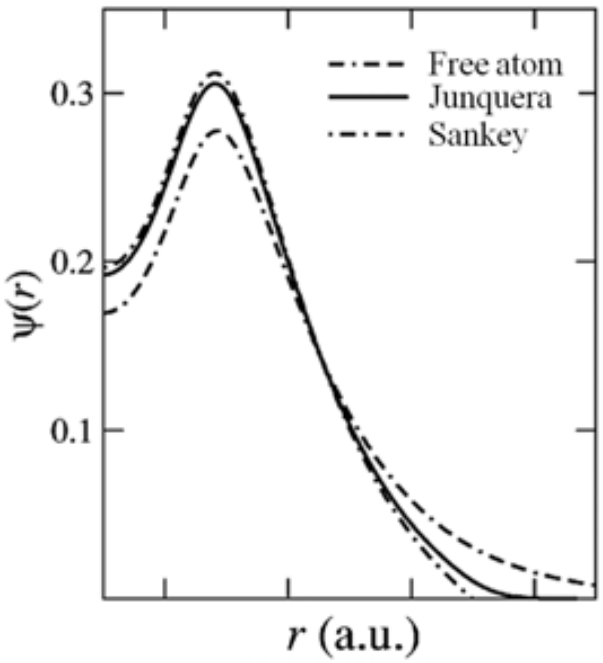

Fig. 2. 6. Comparison between radial harmonic contributions to the spherical harmonic for three different cases: *Sankey* [15], based on an *ab initio* thight-binding model for simulation of molecular dynamics, where a box-like potential is used. *Junquera* [16] considering a smoother potential and, thus, requiring a truncation of the radial function. Finally, the free atom is considered to use the respective orbitals as basis functions being extremely extended. Regarding condensed matter systems the effect of the truncated part is depreciable as their effect can be described by the basis orbitals of other atoms.

---

region. For instance, to deal with a zero-dimensional system such as a molecule, the atoms will be place into a very large cubic (the shape is really not important in this case) computational cell of side *a*. Now, the system *is* periodic, but the images of the molecule under study will be *a* faraway and the molecule in the computational cell, provided *a* is large enough, will behave as an isolated molecule.

Atomic orbitals are considered as basis functions. In Fig. 2. 6 the radial harmonic component for different examples are shown. As noted before, the main advantage of doing so is their efficiency in terms of number of orbitals needed for a similar precision than this for plane waves (PW). The main disadvantage is the lack of a rule for optimization. For linear scaling purposes it is important to obtain sparse Hamiltonian and overlap matrices. The traditional way to assure that condition is to neglect interactions with strength under a certain tolerance value. The approach considered here is using strictly localized basis, i.e. falling to zero beyond a cutoff radius [16]. Within this radius the atomic basis orbitals, NAO's are products of radial functions and spherical harmonics, as it was explained before. SIESTA counts with several automatic procedures to build a basis set, for example single-ζ or minimal basis set, but the generation of them as it happens with the pseudo-potentials is completely independent of the SIESTA method itself. Then, the user is free to use a basis set as complete as the user wants, keeping in mind that as more complete is the choice as higher will be in terms of computational time the cost. In addition to the atomic valence orbitals sometimes it is worth to consider polarization orbitals, i.e. extra pseudo-atomic orbitals with angular momentum $l_{max}+1$.

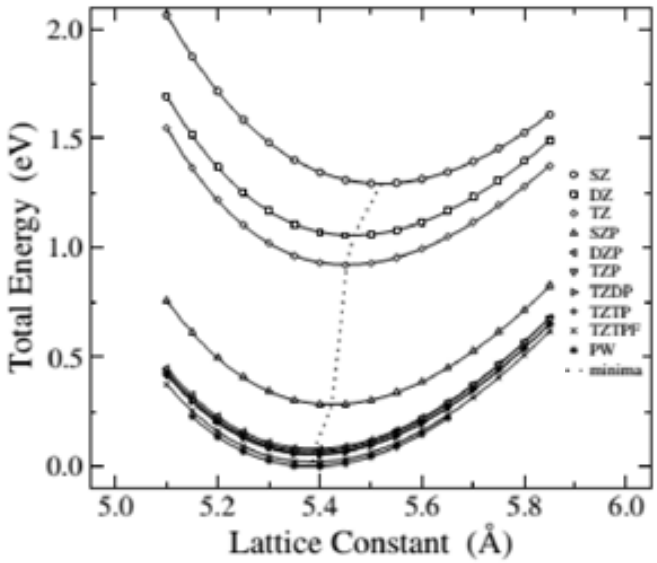

Fig. 2. 7. Total energy for bulk silicon for different basis sets starting from single-ζ to triple-ζ examples. The data obtained for a Plane Wave based basis is showed for comparison with atomic orbital based calculations.

Fig. 2. 7 show the total energy curve as a function of the lattice parameter of bulk silicon for different basis sets [16]. The dotted line follows the minima for each curve allowing to track the differences between the results for different choices.

As in the other DFT codes a variation of the Hellmann-Feynman method is used to compute the atomic forces [11]. The truncation of the basis functions affect the resulting forces which needs to be rearranged through Pulay-like corrections. Stresses are

computed by differentiation of the total energy *E[n]* with respect the atomic positions and the strain tensor directly:

$$\sigma_{\alpha\beta} = \frac{\partial E}{\partial \epsilon_{\alpha\beta}} \tag{2.34}$$

These quantities are continually calculated with the total energy in a real space grid. The related deformations needed to compute the derivatives are done in such a way that the shapes of the basis functions, KB projectors and atomic densities and potentials are not changed but only translated. Therefore, the stresses calculated are almost parallel to the forces, saving computational time.

2.3. Dynamic simulation

Once it is assumed that all the physics behind a mechanical structure can be described with a simplified linear model described by the Hook's law, the equation of motion can be expressed as:

$$m_{eff}\ddot{z} + \frac{\partial U}{\partial z} = 0 \tag{2.35}$$

Where the mass is considered to be concentrated at the end of the structure, for a cantilever, and at the center, for a cc-beam, with a value m_{eff}. This effective value takes into account that each mass element contributes to the inertial terms with different weight when performing a deformation. As it can be seen from Fig. 2.8, mass elements at x_1 and x_2 always fulfill $u(x_1)<u(x_2)$, therefore, the amplitude of deformation depends on the longitudinal coordinate. Hence, this allows reducing the system to a point-like system with mass m_{eff} [2]:

$$m_{eff} = \int \rho |\mathcal{U}_1(x)|^2 \, dV \tag{2.36}$$

greatly simplifying its analysis. The approach here is considering the mode shape, $\mathcal{U}_1$, to be normalized to 1. For a cantilever beam and a cc-beam the effective mass, in this picture, can be approximated to be:

$$m_{eff}^{cantilever} = 0.24\rho lwt \tag{2.37}$$

$$m_{eff}^{cc-beam} = 0.4\rho lwt \tag{2.38}$$

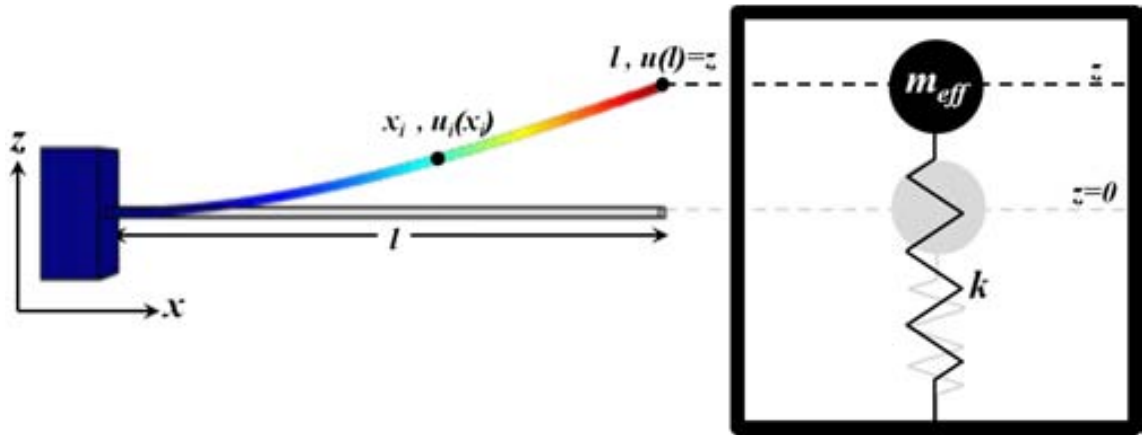

Fig. 2. 8. Approximation of the system through the spring-mass model: the real structure is replaced by a virtual system consisting on a punctual mass, m_{eff}, and a spring, k.

At this point another term must be added to equation 2.35 to take into account the mechanical damping, i.e. energy losses that are dissipated to the medium, which can be modeled through the quality factor, Q [17-21]. These energy losses can be related to internal friction effects on the structure or the interaction with the surroundings. For resonating systems, it is defined as the energy stored in the resonator, E_{stored}, divided by the energy delivered to the system to keep constant the amplitude of vibration, $E_{supplied}$, at a certain frequency, f_r:

$$Q = 2\pi f_r \times \frac{E_{stored}}{P_{supplied}} \tag{2.39}$$

It is assumed that the quality factor can be expanded in a sum of contributing terms as follows [19]:

$$\frac{1}{Q} = \sum_i \frac{1}{Q_i} \tag{2.40}$$

For the purpose of this thesis dissertation, Q will be experimentally measured, if possible, or left as a free parameter and introduced to the motion equation, assuming the damping term to be proportional to velocity, $\dot{z}$, as follows:

$$m_{eff}\ddot{z} + b_m\dot{z} + \frac{\partial U}{\partial z} = 0 \tag{2.41}$$

Where the relation between the proportional constant, b_m, and the quality factor is:

$$b_m = \frac{2\pi f_0 m_{eff}}{Q} \tag{2.42}$$

Where f_0 is the natural frequency of the system as it was defined on section 2.1. The higher the damping term in equation 2.41 is, the higher the wasted energy per cycle is. Thereby, oscillations vanish faster for low than for high Q values.

In order to measure Q experimentally, the standard procedure [22] is followed, which is based on considering the ratio between the resonance frequency of the structure, f_0, and the full width of the frequency response at half maximum (FWHM). Therefore, the quality factor can be computed from the following expression:

$$Q = \frac{f_0}{FWHM} \tag{2.43}$$

It is worth noting that, in this picture, the quality factor does not depend on any particular amplitude of vibration, neither the strength of the external excitation.

When actuated by an external driving force, F_{ext}, whatever its nature is, the dynamics of the system can be obtained solving the following second order differential equation:

$$m_{eff}\ddot{z} + b_m\dot{z} + \frac{\partial U}{\partial z} + F_{ext} = 0 \tag{2.44}$$

Troughout this thesis, F_{ext} will represent different stochastic processes related to WGN (White Gaussian Noise), pink noise or other broad-band signals in order to emulate a generic input containing the main characteristics of real vibrations or environmental made excitation processes as those described before (Fig. 1.6). Thus, due to the random nature of F_{ext}, equation 2.44 represents a Langevine-like equation which must be solved numerically as it does not accept analytical solutions. To carry out this task we have used MATLAB, implementing a 4th-order Runge-Kutta method [23]. During this work, the specific parameters for each simulation have been optimized till the obtained dynamics are stable under small changes of these parameters as shown in Fig.2.9.

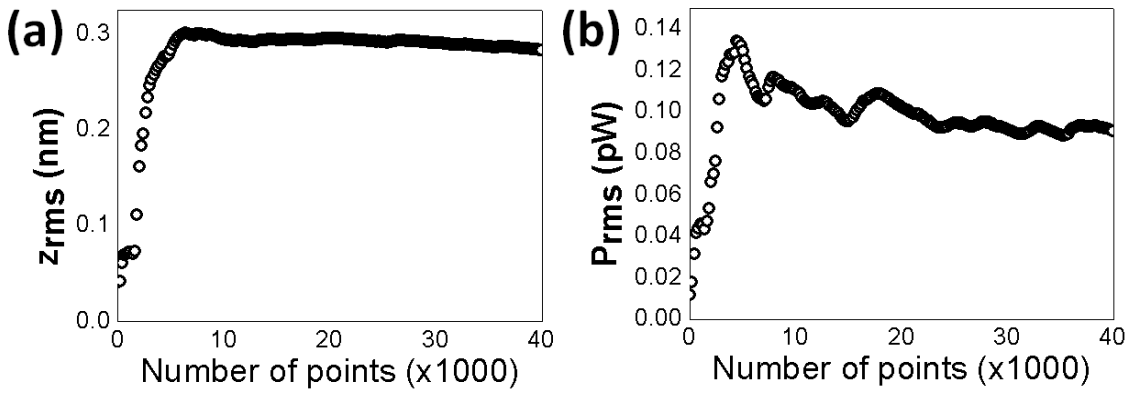

Fig. 2. 9. Results from a dynamic simulation for the system explained in chapter 3 (section 2): root mean square for (a) the displacement and (b) the generated electrical power as a function of the simulation length. The number of points needed to achieve the saturation for z_{rms} is around 10^4, while this for the P_{rms} is increased to $3Š10^4$. The more restrictive value is taken as the optimal.

Fig.2.9a show the obtained root mean square for the displacement of the system discussed in chapter 3. It can be seen that a minimum of 10000 points is required to obtain a stable value.

When performing electrical transduction the energy extracted and wasted in load impedance must be included in the model: the electrical damping. A piezoelectric method of transduction based on [24] is assumed. It is not the aim of this work to discuss the suitability of transducing with one method in particular. However, other works have demonstrated the good performances in terms of integration in microelectronics and high output power for the piezoelectric strategy [25]. Moreover, in the nanostructured materials study, that will be later shown, piezoelectric materials are contemplated to facilitate the fabrication and integration of the transducer.

Equation 2.44 is replaced by two coupled differential equations aggregating the voltage drop in the load, V, as a new variable:

$$m_{eff}\ddot{z} + b_m\dot{z} + \frac{\partial U}{\partial z} + \Gamma V + F_{ext} = 0 \qquad (2.45a)$$

$$\dot{V} = -\frac{I}{C} + \Gamma\dot{z} \qquad (2.45b)$$

Where the electrical damping has been added through the electromechanical coupling parameter, Γ, I is the current flowing through the load and C represents the capacitance of the piezoelectric element.
These equations still need numerical methods to obtain the trajectory, $z(t)$, and the voltage across the load, $V(t)$. The output of the numerical simulation are two vectors,

$\boldsymbol{z}=\{x_i(t_i)\}$ and $\boldsymbol{V}=\{V_i(t_i)\}$. Following the steps of [26] it is assumed that the generated power in a certain period of time can be evaluated by:

$$P = \frac{\langle \boldsymbol{V}^2 \rangle}{R} \qquad (2.46)$$

Due to the stochastic nature of the obtained dynamics, the numerical simulation period need to overcome a minimum value to achieve a stable output as it is shown on Fig.2.9b. Notice that the minimum number of points needed for output stabilization is not the same for z_{rms} (10000 approximately) and P_{rms} which needs 30000 points, at least. Moreover, the combination of stochastic forces and the random behavior of the obtained bistable dynamics demands a larger number of simulation points than this for a mono-stable system.

References

[1] Kaajakari, Ville. "Practical MEMS: Design of microsystems, accelerometers, gyroscopes, RF MEMS, optical MEMS, and microfluidic systems." *Las Vegas, NV: Small Gear Publishing* (2009).

[2] Soler, José M., et al. "The SIESTA method for ab initio order-N materials simulation." *Journal of Physics: Condensed Matter* 14.11 (2002): 2745.

[3] Marion, Jerry B., and Stephen T. Thornton. *Classical dynamics of particles and systems*. Saunders College Pub., 1995.

[4] Stark, Robert W., Tanja Drobek, and Wolfgang M. Heckl. "Thermomechanical noise of a free v-shaped cantilever for atomic-force microscopy." *Ultramicroscopy* 86.1 (2001): 207-215.

[5] Nogueira, Fernando, Alberto Castro, and Miguel A. Marques. "A tutorial on density functional theory." *A Primer in Density Functional Theory*. Springer Berlin Heidelberg, 2003. 218-256.

[6] Payne, Mike C., et al. "Iterative minimization techniques for ab initio total-energy calculations: molecular dynamics and conjugate gradients." *Reviews of Modern Physics* 64.4 (1992): 1045-1097.

[7] Jones, Robert O., and Olle Gunnarsson. "The density functional formalism, its applications and prospects." *Reviews of Modern Physics* 61.3 (1989): 689.

[8] Martin, Richard M. *Electronic structure: basic theory and practical methods*. Cambridge university press, 2004.

[9] Sham, L. J., and Walter Kohn. "One-particle properties of an inhomogeneous interacting electron gas." *Physical Review* 145.2 (1966): 561.

[10] Perdew, John P., Kieron Burke, and Matthias Ernzerhof. "Generalized gradient approximation made simple." *Physical review letters* 77.18 (1996): 3865.

[11] Ordejón, Pablo, Emilio Artacho, and José M. Soler. "Self-consistent order-N density-functional calculations for very large systems." *Physical Review B* 53.16 (1996): R10441.

[12] Troullier, Norman, and José Luriaas Martins. "Efficient pseudopotentials for plane-wave calculations." *Physical Review B* 43.3 (1991): 1993.

[13] Artacho, Emilio, et al. "Linear-scaling ab-initio calculations for large and complex systems." *arXiv preprint cond-mat/9904159* (1999).

[14] Kohn, Walter. "Density functional and density matrix method scaling linearly with the number of atoms." *Physical review letters* 76.17 (1996): 3168.

[15] Sankey, Otto F., and David J. Niklewski. "Ab initio multicenter tight-binding model for molecular-dynamics simulations and other applications in covalent systems." *Physical Review B* 40.6 (1989): 3979.

[16] Junquera, Javier, et al. "Numerical atomic orbitals for linear-scaling calculations." *Physical Review B* 64.23 (2001): 235111.

[17] Ekinci, K. L., Y. T. Yang, and M. L. Roukes. "Ultimate limits to inertial mass sensing based upon nanoelectromechanical systems." *Journal of applied physics* 95.5 (2004): 2682-2689.

[18] Lifshitz, Ron, and Michael L. Roukes. "Thermoelastic damping in micro-and nanomechanical systems." *Physical review B* 61.8 (2000): 5600.

[19] Blom, F. R., et al. "Dependence of the quality factor of micromachined silicon beam resonators on pressure and geometry." *Journal of Vacuum Science & Technology B: Microelectronics and Nanometer Structures* 10.1 (1992): 19-26.

[20] Yong, Y. K., and J. R. Vig. "Modeling resonator frequency fluctuations induced by adsorbing and desorbing surface molecules." *Ultrasonics, Ferroelectrics and Frequency Control, IEEE Transactions on* 37.6 (1990): 543-550.

[21] Vig, John R., and Yoonkee Kim. "Noise in microelectromechanical system resonators." *Ultrasonics, Ferroelectrics and Frequency Control, IEEE Transactions on* 46.6 (1999): 1558-1565.

[22] Vignola, Joseph F., et al. "Effect of viscous loss on mechanical resonators designed for mass detection." *Applied Physics Letters* 88.4 (2006): 041921-041921.

[23] http://en.wikipedia.org/wiki/Runge%E2%80%93Kutta_methods

[24] Beeby, S. P., M. J. Tudor, and N. M. White. "Energy harvesting vibration sources for microsystems applications." *Measurement science and technology* 17.12 (2006): R175.

[25] Cook-Chennault, K. A., N. Thambi, and A. M. Sastry. "Powering MEMS portable devices—a review of non-regenerative and regenerative power supply systems with special emphasis on piezoelectric energy harvesting systems." *Smart Materials and Structures* 17.4 (2008): 043001.

[26] Vocca, Helios, et al. "Kinetic energy harvesting with bistable oscillators." *Applied Energy* 97 (2012): 771-776.

CHAPTER 3

ELECTRET BASED BISTABLE MEMS

This chapter is devoted to report and extend the main results reported in paper A. Here, an electrostatic based bistable system for EH is proposed concerning both modeling and experimental realization. It represents a proof of concept of what was presented in section 1.3. at the micro-scale. No electric transduction is achieved, although the main results from [1] are reproduced with good agreement between modeling and experimental realization.
The content of this chapter splits in two parts: in one hand the modeling of the electro-mechanical structure, in the other, the details of the experimental realization and the data obtained in the laboratory, giving further information to what was published.

3.1. Modeling

The modeling of the system through the techniques presented on section 2.1 and 2.3 allows to obtain simple expressions describing the main characteristics of the device in terms of measurable parameters, i.e. k and q, and fabrication specifications, i.e. material and geometry. At the end of this section an evaluation of the possible achievable output power is given.

3.1.1. Potential calculation

In order to bring the bistable approach to the micro-scale, a commercial micro-cantilever from NANOWORLD [2] is considered: it is a typical Si_3N_4 tip-less AFM-micro-cantilever with a one-side gold coating to assure good laser beam reflection. The V-shape allows to achieve very low elastic constants (k~0.08N/m in the present case) for a given dimensions which is of great interest for our proposes as it will be discussed

later on. Fig. 3.1 shows an optical image of the cantilever, pointing out its dimensions and the material specifications.

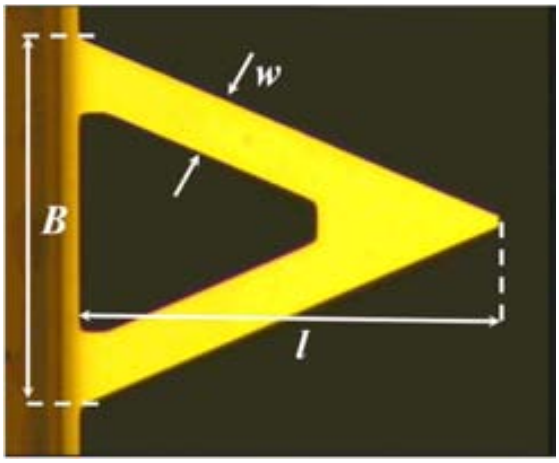

Fig. 3. 1. Optical image showing a top view of the V-shaped cantilever. The dimensions are $l=200$μm, $B=184$μm,$w=28$μm, $t=665$nm and the density is assumed to be $\rho=2300$Kg/m^3.

Following the description for cantilevers and its dynamic behavior presented in section 2.1. and 2.3. one can achieve a sound description of such a structure in terms of elastic potential energy, U, and effective mass, $meff\sim0.28\rho lwt$, within the Parallel Beam Approximation (PBA) [3].

Therefore, if electric charges, q_1 and q_2, are trapped at the tip of the cantilever and at the tip of a counter electrode (CE) respectively and brought close, as depicted in Fig. 3.2a, a bi-stable configuration can be achieved. For a given mechanical structure with stiffness k, the details of the bi-stable potential energy depend on the amount of charge $q=(q_1q_2)^{1/2}$ and the distance between them, d. The total potential energy concerning both the mechanical and electrostatic contribution can be expressed as:

$$U_T = U_{mech} + U_{elect} = \frac{1}{2}kx^2 + Kq^2(d^2 + x^2)^{-1/2} \qquad (3.1)$$

Where K stand for the Coulomb constant. Once the cantilever stiffness and the value for q are determined the resulting system has only one tuning parameter: d.

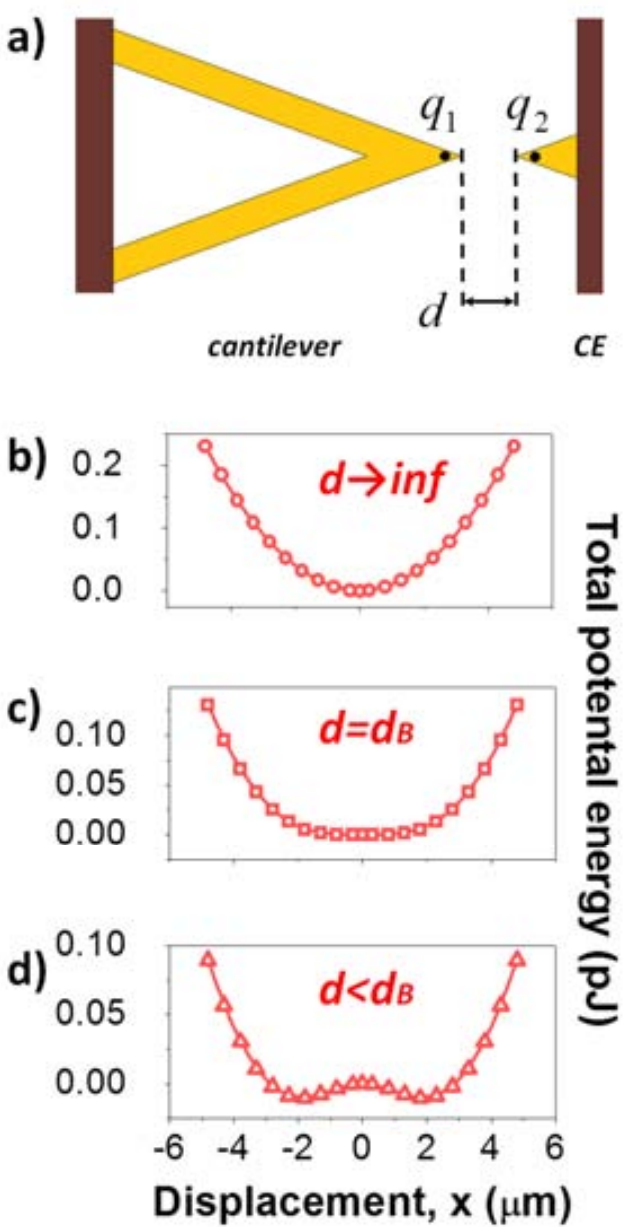

Fig. 3. 2. (a) Scheme of the prototype (top view) made of a cantilever and a CE: a distance d separates two electric charges, q_1 and q_2, which are ideally trapped at the free ends of both structures. The total potential energy as a function of the out-of-plane displacement, x, for three different distances, d, is showed: (b) the electrostatic interaction vanishes for large enough distances recovering the potential energy of a linear resonator, (c) bi-stability appears when the distance reaches $d=d_B$ which is determined by the elastic constant, k, and the average electric charges. (d) For $d<d_B$ two stable points appear separated by a potential barrier. All figures correspond to $q=10$fC.

Fig. 3.2 shows U_T considering $q=10$fC for three different distances: for large d (Fig. 3.2.b) the system behaves as a linear resonator with a frequency determined by equation 2.13. As electric charges get closer, the electrostatic interaction becomes not negligible and starts flatten U_T, making it less and less harmonic, but preserving the resonant behavior (Fig. 3.2.c). Below a threshold distance, which can be expressed by

$$d_B \leq \left(\frac{Kq^2}{k}\right)^{1/3} \qquad (3.2)$$

two potential wells start to be well defined. The distance between potential minima and the potential barrier height that defines the bistable behavior increases (Fig. 3.2.d) when d_B is decreased. These two can be analytically expressed as:

$$x_{\pm} = \pm\sqrt{\left(\frac{Kq^2}{k}\right)^{2/3} - d^2} \tag{3.3}$$

$$\Delta U_T = U_T(0) - U_T(x_{min}) = \frac{Kq^2}{d} - \frac{k}{2}\left(3\left(\frac{Kq^2}{k}\right)^{2/3} - d^2\right) \tag{3.4}$$

It is possible to find analytical expressions for the natural frequencies of the system for the different regimes it presents depending on the parameter *d*:

$$f_r^2 = \frac{1}{4\pi^2 m_{eff}}\left|\frac{d^2U_T}{dx^2}\right|_{x=x_{min}} \tag{3.5}$$

Here we have to differentiate two different cases: $d>d_B$ and $d<d_B$ as $x_{min}=0$ and $x_{min}=x_+=-x_-$ respectively. The different resonant frequencies can be expressed as:

$$f_r^0 = \frac{1}{2\pi}\sqrt{\frac{k - \left(\frac{Kq^2}{d^3}\right)}{m_{eff}}} \text{ for } d > d_B \tag{3.6}$$

$$f_r^{\pm} = \frac{1}{2\pi}\sqrt{\frac{3Kq^2\left(\frac{Kq^2}{k}\right)^{-5/3}\left[\left(\frac{Kq^2}{k}\right)^{2/3} - d^2\right]}{m_{eff}}} \text{ for } d < d_B \tag{3.7}$$

The trend of these two branches can be seen in Fig. 3.3 where f_0 represents the resonant frequency for the linear case as it was discussed in section 2.1.

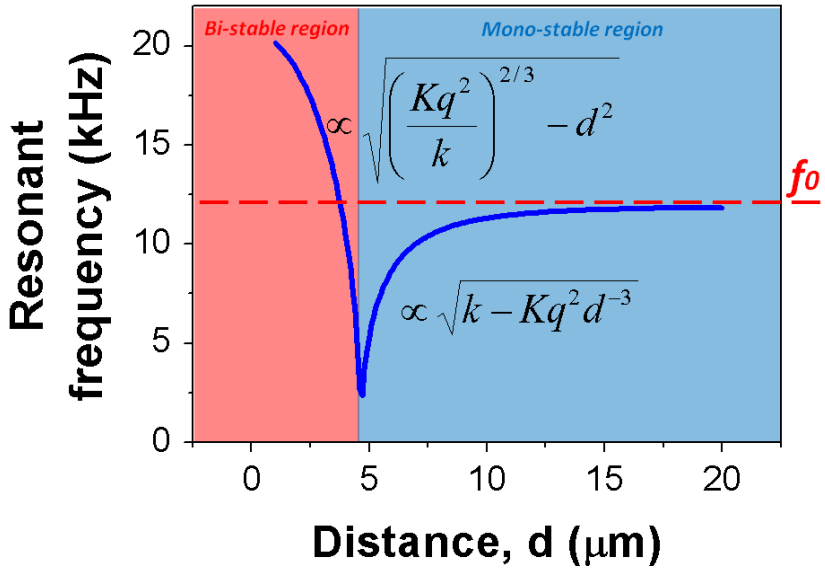

Fig. 3. 3. Natural frequency of the system as a function of the distance between charges, d. For $d>d_B$ the resonant frequency describes the oscillations around $x=0$, while for $d<d_B$ describes the oscillations around $x=x_+$. The natural resonant frequency of the mechanical structure is represented by the red dashed line.

It is clear that, starting at the mono-stable configuration (blue-shadowed region in Fig. 3. 3) from $d=20$μm, bringing near the electric charges softens the mechanical structure providing lower resonant frequencies. This fact suggests it could be used as a method to modify the resonant behavior of mechanical structures at the micro-scale. However, as the bi-stable region is approached, the resonant frequency becomes too sensitive to little variations of d. Once entered in the bi-stable configuration (red-shadowed region in Fig. 3. 3) the resonant frequency shifts its behavior increasing its value as d decreases. The limit for this phenomena regards the maximum achievable x_+ without meeting the rupture point of the mechanical structure.

3.1.2. Dynamics of the system

As specified in section 2.3, in order to obtain the dynamics of the system, the Langevine equation 2.44 must be numerically solved. Thus,

$$m_{eff}\ddot{z} + \frac{2\pi f_0 m_{eff}}{Q}\dot{z} + \frac{\partial U_T}{\partial z} = F^*_{ext} \qquad (3.8)$$

where f_0 and Q are measured experimentally as later will be showed. In order to be able to compare the results obtained from the model and the experiment the external force, F^*_{ext}, is set to match the real characteristics of the force measured during the experimental realization.

The dynamics of the system depends on the tuning parameter, d, and on the intensity of the external excitation, F^*_{ext}. Fig. 3.4a shows the root mean square of the displacement at the tip of the cantilever after numerical simulation under *1/f* noise excitation with F_{ext}^{rms}=*4*nN. The considered trapped charge is around *10*fC which determines the threshold distance value at *4.6μm* approximately.

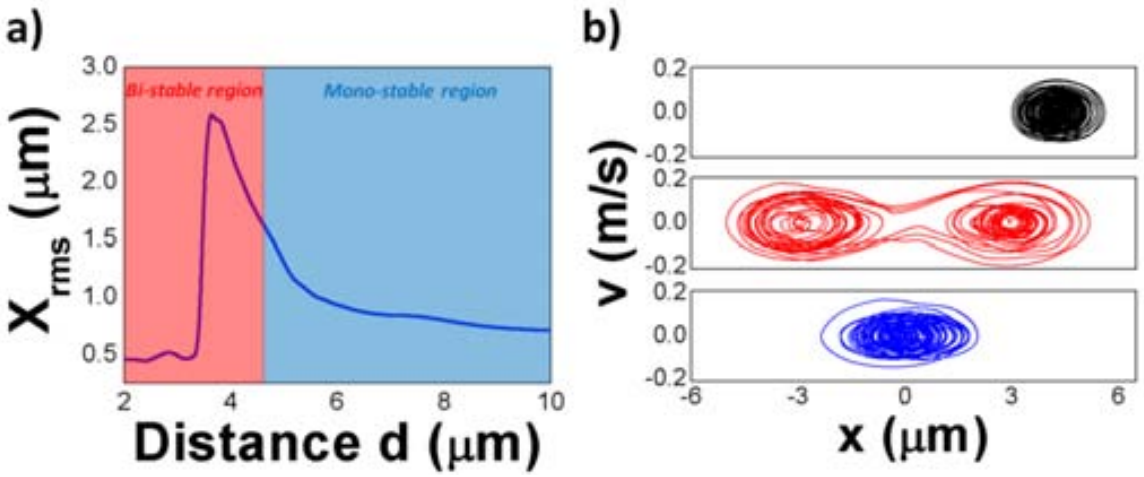

Fig. 3. 4. Results of numerical simulation. (a) Root mean square of the displacement, x_{rms}, as a function of the distance, d. The red and blue box separate the bi- and mono-stable regions. A peak can be observed once bi-stability is achieved. (b) Phase portrait for the three possible regimes. Lower panel: electrostatic interaction is not capable of inducing bistability and the system oscillates around $x=0$. Middle panel: Once bi-stability is achieved the system suffers transitions from one attractor to the other if an external force threshold is reached. Upper panel: electrostatic interaction is that intense that the system cannot overcome the potential barrier and the system gets confined in one of the two attractors.

The maximum x_{rms} value appears for distances below d_B which points out the benefit of bistability. It can be seen that even for the mono-stable configuration there is a sustained increase for decreasing distance between charges: although the bi-stable configuration is not achieved, the interaction between charges flatten the elastic potential energy, which leads to larger trajectories around $x=0$. Once the two minima appear there is an optimal value d_{opt} which combines the oscillations around the two minima and large excursions between and maximizes x_{rms}. If d is further decreased, after a certain point, the cantilever gets stuck in one of the two wells oscillating around x_+ or x_- with a characteristic frequency determined by the curvature of the total potential energy, U_T, at this point. These three different regimes are showed on Fig. 3.4b corresponding to d=*2*μm (upper), $d=d_{opt}$ (middle) and d=*10*μm (lower) in a phase-portrait representation. The evolution of the attractors can be followed as the bistable configuration is achieved.

3.1.3. Power guess

As it was pointed out in the introduction to this chapter no electric transduction was considered in the experimental realization. However, the maximum power achievable can be estimated based on the model discussed in sections 3.1.1 and 3.1.2, and

considering piezoelectric transduction. For this purpose a 20μm x 28μm x 150nm ZnO layer [4] placed at the clamped ends of the cantilever is considered, operating on the 31 mode with d_{31}=-5pm/V [5]. Regardless of the stiffening of the resulting structure, the consequent electric damping on the system is taken into account, as it was explained in section 2.3. In order to evaluate the generated power we computed the energy dissipated in a purely resistive load, R, by means of:

$$P_{rms} = \frac{V_{rms}^2}{R} \tag{3.9}$$

The optimal load corresponds to a resistance of R_{opt}=55kΩ providing a maximum output power of approximately P_{rms}^{max}=0.14pW when reaching d_{opt}~4.5μm as it can be seen from Fig. 3.5.

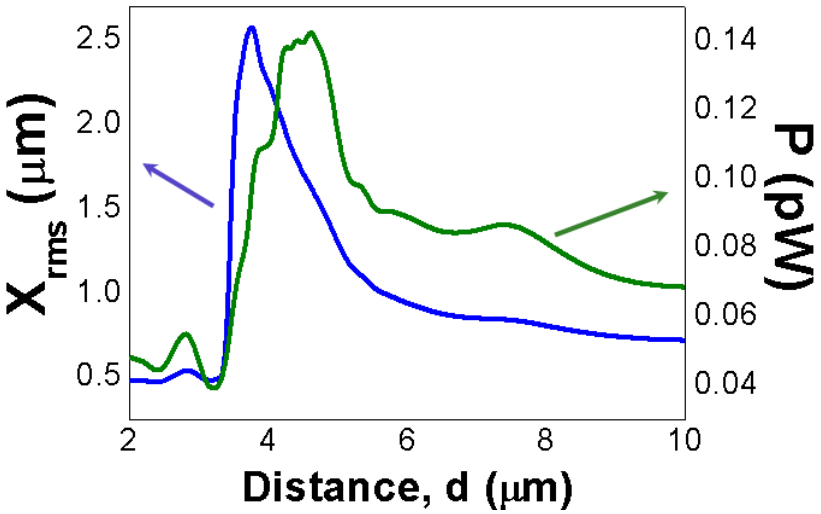

Fig. 3. 5. x_{rms}(blue line) and P_{rms} (green line) as a function of the distance, d, after numerical simulation.

The difference between the distances that maximizes the root mean square for the displacement and the generated electric power comes from the transduction process and the characteristics of the different elements. As a limit case if $RC>>1$ then integrating equation 2. 45b one can express the voltage across the load as:

$$V_{rms} = \frac{\Gamma}{C} x_{rms} \tag{3.10}$$

Therefore, the dissipated power becomes strictly proportional to the square of the root mean square of the position:

$$P_{rms} = \frac{\Gamma^2}{RC^2} x_{rms}^2 \tag{3.11}$$

allowing to estimate the generated output power by means of the performance of the mechanical transducer, i.e. x_{rms}, and the performance of the electro-mechanical transducer, i.e. Γ^2/RC^2. Out of this condition and supposing a certain value for Γ and C (which is determined by the considered materials and geometries), the optimization of the mechanical response through the distance parameter, d, and the optimization of the electro-mechanical coupling through the load impedance, R, cannot be done separately.

3.2. Experimental results

In this section the experimental data is reported not without previous description of the measurement set-up and the procedure followed in order of trapping electric charges in the cantilever's tip.

3.2.1.Electret fabrication

As explained in section 3.1., trapped electric charges are considered in order to add a repulsive force to the system. At this point we take advantage of the insulating nature of Si_3N_4 [6]: it is a well known fact the generation of electron and holes traps in the deep body or surface of an insulator when polarized [7] ruled by several mechanisms [8]. When polarized, these trapped charges assist the current through the insulator [9,10]. As a consequence, during the polarization of the capacitor-like structure formed by the polarization electrodes and the insulator itself, the characteristic *I(V)* curve presents an average increment revealing the presence of trapped charges in the body of the insulating material. The approach here presented is to consider the cantilever as a capacitor, as it is depicted in Fig. 3.6, which is polarized across the thickness of the structure, taking advantage of the *Au/Cr* coating of the cantilever which is used as an electrode. The cantilever is pushed against a gold substrate by a probe tip to achieve the capacitor configuration once it meets the substrate.

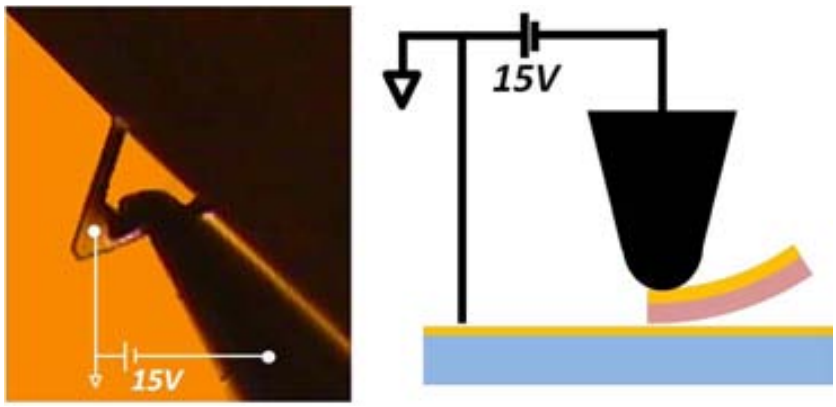

Fig. 3. 6. Optical image of the top view (left panel) and scheme of the lateral view (right panel) of the charging process considered to trap electric charge in the body of the cantilever. A voltage difference of $\mathbf{15}\boldsymbol{V}$ is applied between the gold coated top-side of the cantilever and a gold substrate. The cantilever is bended by the probe to assure good contact with the substrate.

Fig. 3.7a shows the current flowing through the capacitor-like structure when polarized at constant voltage. The variations in the measured current correspond to trapped or released charges into the insulator which assist or diminish the current through the capacitor respectively. The different *I-V* curves from Fig. 3.7b show the measured current when performing a voltage sweep after different stressing steps revealing the existence of electric charges in the body of the cantilever [11].

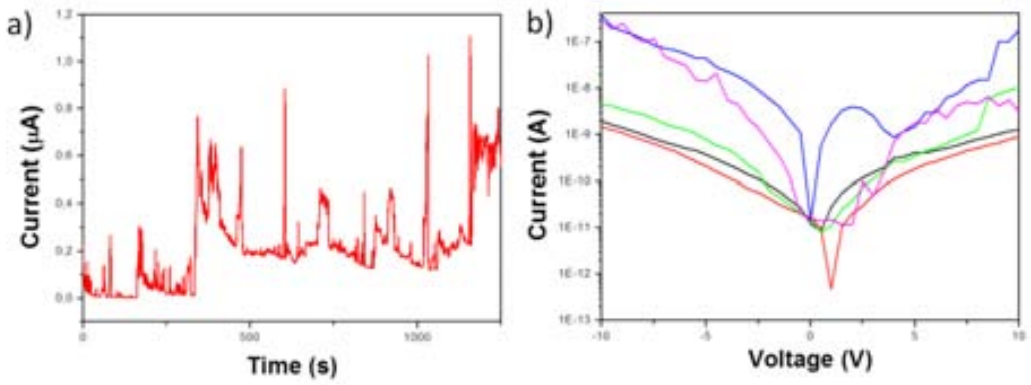

Fig. 3. 7. Evidence of the trapping process. (a) Measured electric current through the capacitor-like structure for a period of time of approximately 20min showing sparks that can be related to trapping and releasing processes. (b) *I-V* curves after electrical stress.

The data reported in Fig. 3. 7 evidences the existence of electric charges in the structure, although the exact value for the total trapped charge is unknown. The evaluation of the electric charge will be commented in following section.

3.2.2. Experimental set-up

Fig. 3.8 show a scheme of the experimental set-up considered to measure both static and dynamic deflection of the cantilever. It is based on a conventional AFM-like optical readout setup: a laser beam (HeNe, *632.8*nm, *15*mW) incident to the cantilever free end is reflected by the gold coating along a certain direction determined by the relative position between the cantilever and the laser. The reflected beam is detected by means of a Position Sensor Detector (PSD, New Focus 2930) which gives an electrical signal proportional to the cantilevers deflection, $V_{PSD} \propto x_{cant}$. The transduced signal is measured by an oscilloscope (Agilent InfiniiVision D50-X3054A).

In order to ensure the required alignment between the cantilever and the CE, they are attached to two manual 3D-positioners which also fix the initial distance, d_0, between them. Two CCD cameras giving top and lateral views of the whole system allow tracking the relative position of the different elements.

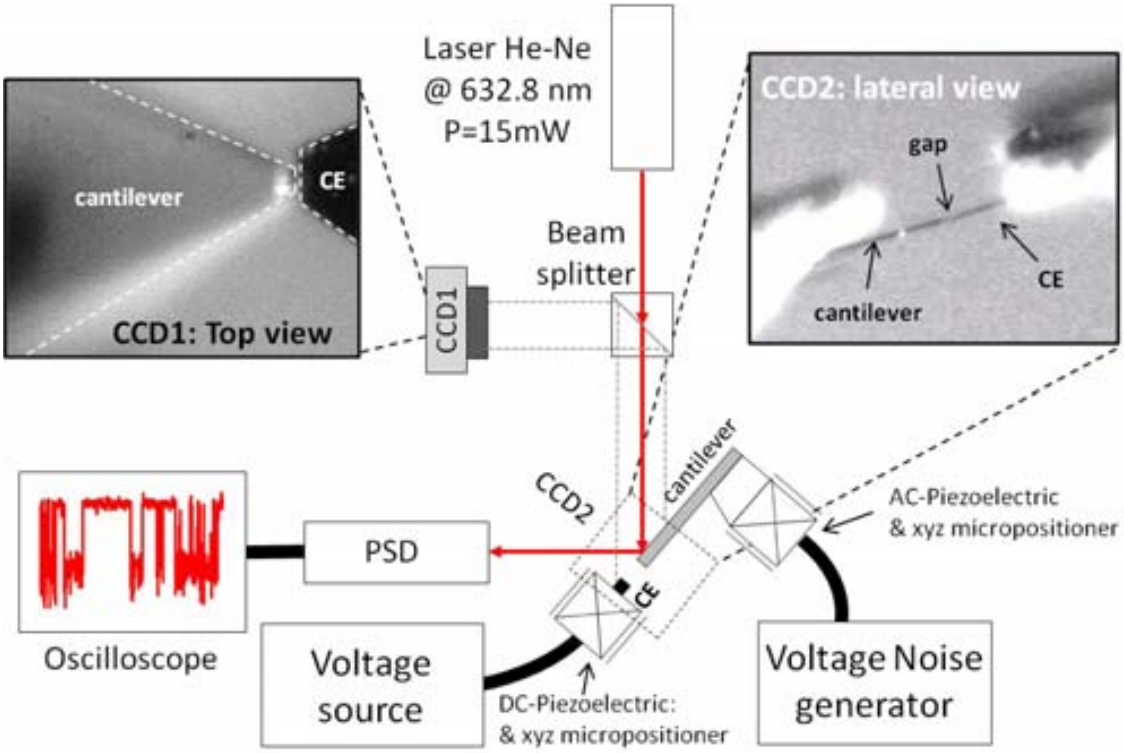

Fig. 3.8. Scheme of the optical read-out and excitation set-up.

The distance between the cantilever and the CE is tuned by a long range piezo-stack attached to the CE which produces a longitudinal displacement with a ratio of r_v~*0.1*µm/V, allowing to achieve a precise enough control of the gap between electric charges:

$$d = d_0 - r_V \cdot V_{stack} \qquad (3.12)$$

where d_0 stands for the initial distance between the cantilever and the CE and V_{stack} is the polarization across the piezoelectric stack.
In order to induce a mechanical excitation to the cantilever, a piezoelectric shaker is attached to the cantilever support and connected to a voltage generator.

3.2.3. Charge and Q-factor measurement

For our purposes the meaningful quantity to know is not the particular charge q_1 or q_2 but the geometric average expressed as $q=(q_1q_2)^{1/2}$. In order to evaluate q, we measure the static deflection of the cantilever when approaching frontally the CE. It is assumed that the measured static deflection corresponds to the position of one of the minima, x_+ and x_-, of the potential energy from equation 3. 1. Therefore, from equation 3.3. we obtain:

$$q = \sqrt{\frac{k}{K}\left(x_{\pm}^2 + d^2\right)^{3/2}} \qquad (3.13)$$

Fig. 3.9 shows the obtained data for the rest position, x_+, as a function of the distance d (squares) and the curve defined by equation 3.3 which allows estimating the electric charge to be approximately $q=10$fC by adjusting the theoretical curve to the experimental data.

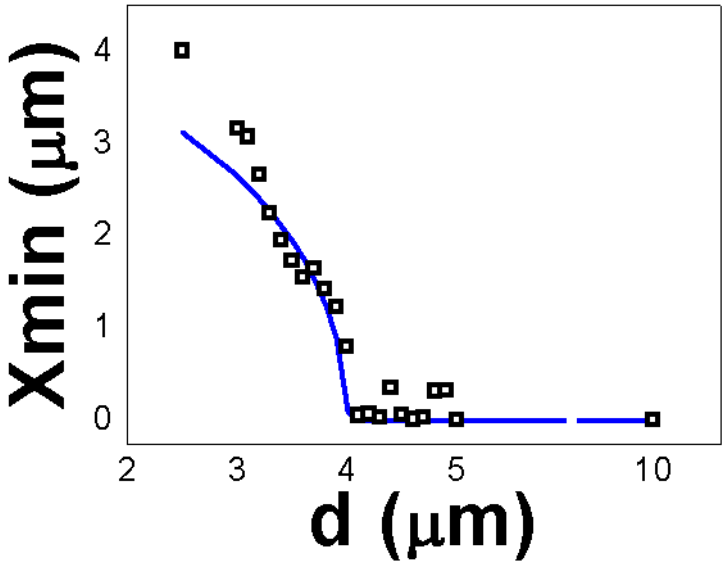

Fig. 3. 9. Measured rest position (squares) as a function of the distance, d. The blue line is a representation of equation 3.3: the average electric charge, q, is left as a free parameter which is determined by adjusting the blue line to the measured data. $q\sim10$fC is achieved.

On the other hand, as it was discussed in section 2.3. the quality factor could be measured from the resonance peak in the linear regime, as expressed on equation 2.43. Fig. 3.10 shows the measured resonance of the first mode of vibration around *11.3*kHz when mechanically excited by a force $F_{harm} \propto sin(\omega t)$.

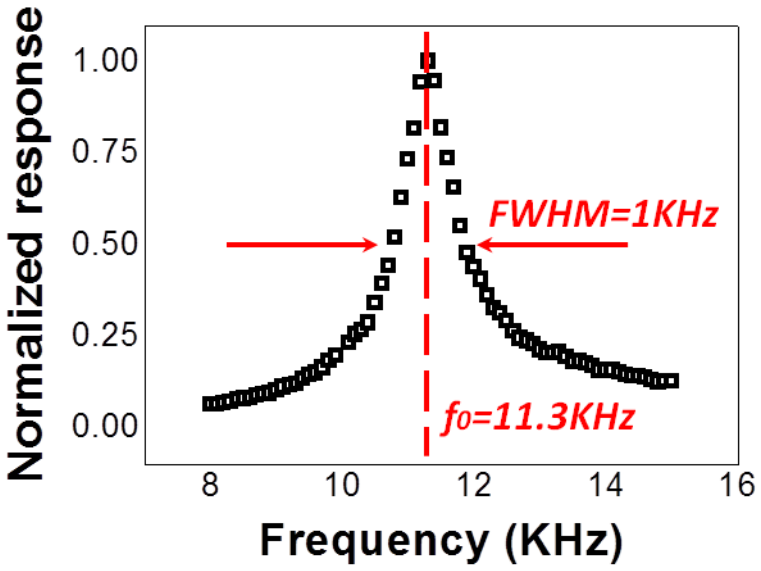

Fig. 3. 10. Measured response to harmonic excitation showing a resonance peak around *11.3*kHz and a FWHM of *1*kHz. The related quality factor is *Q~10*.

The measured FWHM is approximately *1*kHz which leads to a quality factor of *Q~10*, being considered along the following lines.

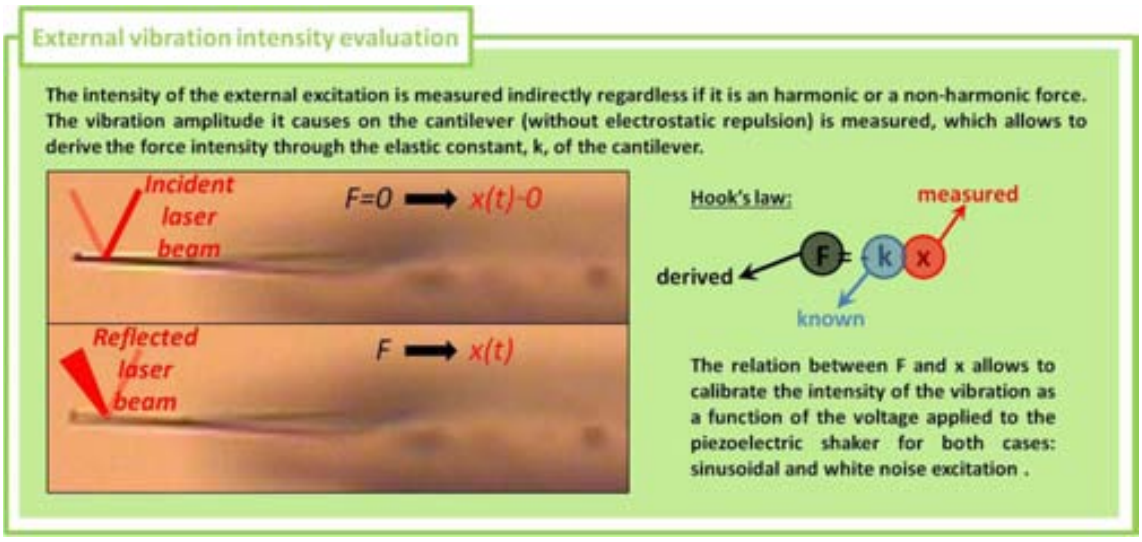

3.2.4. Dynamics measurement

With the aim of reproducing the results showed for the model, two different experimental realizations are carried out. In one hand, the noise intensity is kept constant at F_{rms}=4nN while the distance, d, is swept from 2.5 to 10μm. In the other hand, the distance is set to 3.6μm while the excitation intensity is increased starting from *2*nN up to *4*nN.

Fig. 3.11a it can be seen that the measured trajectories followed by the cantilever for the three different regimes: quasi-free oscillations around $x=0$ (lower panel), bistable regime combining oscillations around $x=x_+=-x_-$ and jumps between the two minima (middle panel) and oscillations stuck around one of the two minima where the system gets confined.

Fig. 3.11b show the root mean square of the displacement, x_{rms}, against the distance d when excited by *1/f* noise with intensity $Frms\sim4$nN. A good agreement between measured data (squares) and model (blue line) is achieved as it is shown by the very precise estimation of the optimal distance value that produces the maximum root mean square of x. Nevertheless, the model overestimates the width of the x_{rms} peak.

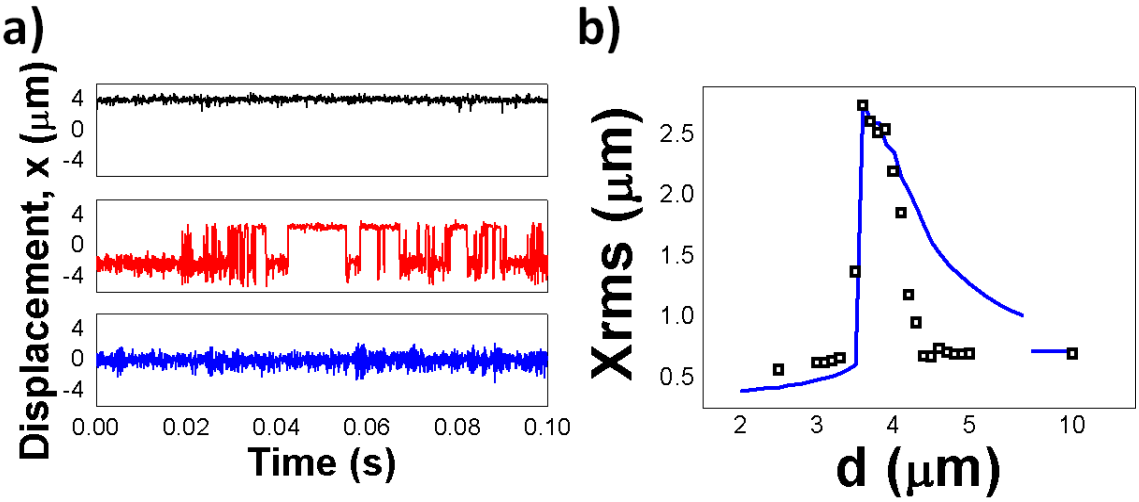

Fig. 3. 11. Measured data of the dynamics under noise excitation. (a) Displacement, x, as a function of time. Lower panel: oscillations around $x=0$. Middle panel: combined oscillations around $x=x_+$ and large excursions from one attractor to the other happening randomly. Upper panel: oscillations only around $x=x_+$ with no transitions between potential energy minima. (b) Measured x_{rms} (squares) as a function of the distance, d, compared to that from numerical simulation. A good agreement is achieved in terms of maximum x_{rms} and the related distance, d_{opt}.

As it was discussed before, d_{opt} depends on the statistics and intensity of the external excitation. Roughly speaking, the higher the F_{rms} is, and therefore more intense is the noise, the higher the potential barrier and the distance between minima should be in order to optimize the bistable condition. There is a practical constraint arising from the fabrication process: once the implanted electric charges and the distance between them are determined a threshold value for the external force needs to be overcome. Below this threshold the system will behave as a resonating one with a x_{rms} lower than this for the harmonic case with $q=0$. Well beyond this $F_{threshold}$, the benefit of the bi-stable

condition still applies. A comparison between model (blue line) and experiment (squares) of this step-like behavior can be seen in Fig. 3.12.

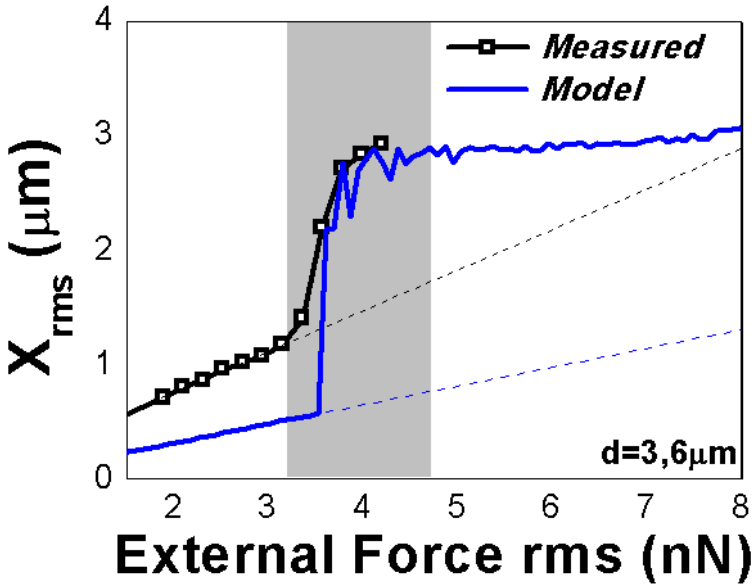

Fig. 3. 12. Measured x_{rms} (black line and squares) and simulated data (blue line) as a function of the intensity of the external force for a given distance between charges, $d=3.6\mu m$. An underestimation of the response can be seen for the numerical simulation results. The black and blue dashed lines represents the trend it would be followed if no transitions between attractors happens.

The model underestimates the x_{rms} for $F<F_{threshold}$ also providing a softer slope for their trends (dashed lines).

The increase of the response with respect to the resonating case extends for a range of external force intensity, ΔF. Unfortunately, from the data represented in Fig. 3. 12 it is not possible to determine the extension of ΔF as the experiment should be done also for $d>4$nN and this was the limit for practical issues. However, if the trend showed by the model is applicable to the experimental realization, the experimental slope of x_{rms} for $F>F_{threshold}$ should be softer than this for the model. Assuming that, it can be determined a minimum value of approximately $\Delta F=5$nN, corresponding to the meeting point between the simulated x_{rms} and the experimentally derived dashed line. Therefore, in a situation where the external force varies in intensity within a certain range the system should be tuned to be able to exploit the bi-stable condition for the lower value of the force.

3.3. Conclusions

In this chapter it has been demonstrated the feasibility of bringing electrostatic based bi-stable systems to the micro-scale. A proof-of-concept prototype based on a micro-cantilever and a CE with trapped electric charge at both ends has been modeled,

fabricated and tested with good agreement between modeling and experimental data allowing a systematic study and optimization for this kind of devices.

A maximum electric power of *0.14*pW is achieved assuming a piezoelectric transduction strategy based on ZnO layers attached at one side of the cantilever close to the clamped end of the moving part. This means a power density, PD, of approximately *12.7* $\mu W/cm^3$. The mechanical power of the structure, evaluated as $(F_{ext} \cdot v)_{rms}$ with $q=0$ and $R=inf$, is $P_{mech}=194$pW while this for $q=10$fC increases reaching a value of *250*pW for $d=2\mu m$.

The model allows to give an insight of what would be the situation for a system composed of a cantilever with different dimensions. If a scale factor of *10* is considered for all the dimensions and the electric charge, q, is also scaled in order to maintain constant the ratio between $x_{\pm}$ and the length of the structure, l, the $F_{threshold}$ decreases by a factor of *100* (*~0.04*nN). The electric power harvested in this case decreases to *3.5*fW which means *317.0* $\mu W/cm^3$ which is a considerable increase in terms of performance. The mechanical power is also reduced consistently to a value of *1.7*pW reaching a maximum of *3.7*pW for $d=0.43\mu m$ which implies that also the capability of harvesting mechanical energy is increased when scaling down the system.

Regarding the applicability of such a system, other materials should be taken into account to enlarge the average time the trapped charge remains in the body of the insulator. Other materials such Teflon provide extremely high performances in this direction. Even though, in the present case, where Si_3N_4 has been considered, the presence of the electric charge has been measured to remain for, at least, more than six months which make of it an optimal candidate for experimentation.

References

[1] Gammaitoni, Luca, et al. "Vibration Energy Harvesting: Linear and Nonlinear Oscillator Approaches." *Sustainable Energy Harvesting Technologies-Past, Present and Future (Dr. Yen Kheng Tan, Shanghai, 2011)* (2012): 169-188.

[2] NanoWorld^{TM} PirexNitride AFM probe: PNP-TR-TL

[3] Sader, John Elie. "Parallel beam approximation for V-shaped atomic force microscope cantilevers." *Review of Scientific Instruments* 66.9 (1995): 4583-4587.

[4] Wang, Zhong Lin, and Jinhui Song. "Piezoelectric nanogenerators based on zinc oxide nanowire arrays." *Science* 312.5771 (2006): 242-246.

[5] Gopal, Priya, and Nicola A. Spaldin. "Polarization, piezoelectric constants, and elastic constants of ZnO, MgO, and CdO." *Journal of electronic materials* 35.4 (2006): 538-542.

[6] Leonov, Vladimir, Paolo Fiorini, and Chris Van Hoof. "Stabilization of positive charge in SiO/sub 2//Si/sub 3/N/sub 4/electrets." *Dielectrics and Electrical Insulation, IEEE Transactions on* 13.5 (2006): 1049-1056.

[7] Wibbeler, Jürgen, Günter Pfeifer, and Michael Hietschold. "Parasitic charging of dielectric surfaces in capacitive microelectromechanical systems (MEMS)." *Sensors and Actuators A: Physical* 71.1 (1998): 74-80.

[8] Hori, Takashi. *Gate dielectrics and MOS ULSIs: principles, technologies, and applications*. Berlin: Springer, 1997.

[9] Houssa, Michel, et al. "Trap-assisted tunneling in high permittivity gate dielectric stacks." *Journal of Applied Physics* 87.12 (2000): 8615-8620.

[10] Rosenbaum, Elyse, and Leonard F. Register. "Mechanism of stress-induced leakage current in MOS capacitors." *Electron Devices, IEEE Transactions on* 44.2 (1997): 317-323.

[11] Buchanan, D. A., and D. J. DiMaria. "Interface and bulk trap generation in metal-oxide-semiconductor capacitors." *Journal of applied physics* 67.12 (1990): 7439-7452.

CHAPTER 4

2D-MATERIALS BASED NON-LINEAR NEMS

Along this fourth chapter the main results obtained from atomistic calculations for different 2D-materials based structures will be presented. Graphene, h-BN and MoS_2 are studied exploring the possibility to bring them to bi-stability. The object of study in all cases is a clamped-clamped ribbon under compressive strain. Generally, the static and dynamic behavior of the system is modified by the action of the compression.

4.1. Atomistic description

As described in section 2.2, the electro-mechanical characterization of the considered structures have been done using DFT as implemented within the SIESTA package [1] in order to have a purely atomistic description and an electronic structure calculated from first-principles. The diagram in Fig. 4. 1 shows the different steps followed in order to have a sound mechanical description of the system showing the main computed quantities and the approximations it has to be taken into account. First, the optimization of the unit cell, composed of n_0 atoms, which consists in determining the atomic coordinates minimizing the total energy of the system and the lattice vectors minimizing the stress tensor. Secondly, the "super-cell" construction consists on generating a structure made of n x m unit cells obtaining a system of $N=n_0 \cdot n \cdot m$ atoms. Finally, compressive strain, ε, and out-of-plane deformation, z, is applied to the super-cell conforming the studied system configurations. The compression is directly applied to the ribbon by means of a constant translation of the atoms at one of the ends of the structure. The bend is generated by means of sinusoidal out-of-plane changes on the atomic coordinates.

Periodic boundary conditions are assumed for all three spatial directions with a height for the out-of-plane direction falling between 15 and 35Å to prevent the interaction between periodic images. As it was pointed out in section 2.2, the electronic wave function is expanded in a numerical atomic orbital basis set. The sampling of the

Brillouin zone is done with a 1 x 10 Monkhorst-Pack mesh of *k*-points. The iterations for the self-consistency of the density matrix are done until an error, $\delta(\rho_i,\rho_{i-1})$, below $5\check{S}10^{-5}$ is achieved. For those calculations where relaxation of the structure is considered a threshold value for the atomic forces of 0.4 eV/nm is used.

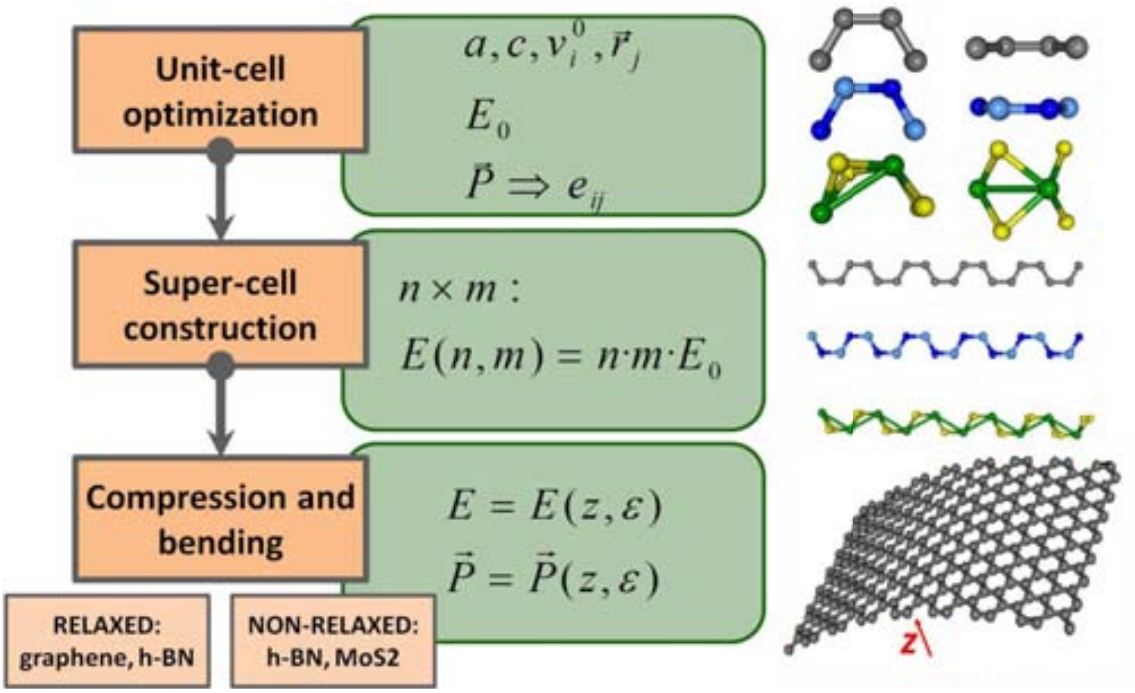

Fig. 4. 1. Block diagram of the steps followed for describing electromechanically the considered materials and specific geometries. Optimization of the unit-cell determines the lattice constants and the atomic coordinates. Little variations of these parameters allow to compute the piezoelectric coefficients. Here it is considered the extension of the two-dimensional material to the infinite by means of periodic images of the computational super-cell, which yields to the linear relation between the energy of the unit-cell and the energy for the super-cell. The computation of the total energy under compression and bending tracks the mechanical behavior of the suspended structure while the related macroscopic polarization describes the transduction capability of the system.

The unit-cell for graphene and h-BN consist in four atoms, and six atoms for MoS_2. A non-primitive rectangular unit-cell is considered which allows to simplify the construction of the super-cell. The initial atomic positions should not be far from the optimal final configuration. Moreover, an educated guess can save computational time. In Fig. 4. 2 the unit-cell for the three cases and the generation of the *n* x 1 super-cell are shown. To determine unequivocally the unit cell, the lattice constants *a* and *c* must be fixed together with the three lattice vectors, $\vec{v}_i^0$, and the atomic coordinates for all atoms, $\vec{r}_j$, once the system is relaxed.

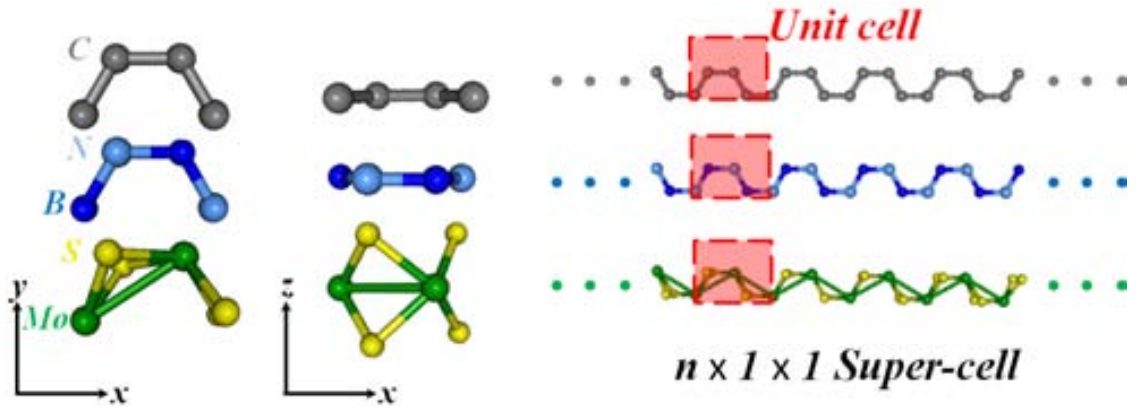

Fig. 4. 2. Representation of the unit-cells and the construction of the computational n x 1 x 1 cells for graphene (up), h-BN (middle) and MoS_2 (bottom). Graphene and h-BN are truly two-dimensional materials while the S atoms on the MoS_2 configuration present a dislocation respect the plane formed by the Mo atoms. Computational cells are formed by multiple unit-cells along the *x*-axis.

The piezoelectric properties are associated with ground electronic state changes under linear deformation giving changes in the total polarization of the system. Here we take advantage of the Berry Phase approach [2] implemented in SIESTA to compute the piezoelectric coefficients for h-BN and MoS_2. This means to calculate the polarization for each system configuration by evaluating the surface integral resulting of a 1D integral in the considered direction as follows:

$$P_{e,\parallel} = \frac{if\,q_e}{8\pi^3}\int_A d\vec{k}_\perp \sum_{n=1}^{M}\int_0^{|G_\parallel|} dk_\parallel \langle u_{\vec{k}n}|\delta/\delta k_\parallel|u_{\vec{k}n}\rangle \qquad (4.1)$$

Where f is the occupation number (2 for non-magnetic systems), M stands for the number of occupied bands implying the material has to be an insulator, $u_{\vec{k}n}$ are the periodic Bloch functions, q_e is the electron charge and $|G_\parallel|$ is the shortest reciprocal vector along the chosen direction.

Due to the discretization of the integrals of equation 4. 1 and the periodicity of the considered cell, it is possible that during the expansion or contraction of the unit-cell a quantum of polarization enters or exits the computational cell which can cause a shift of the value for the macroscopic polarization. Therefore, it must be subtracted or added respectively. The quantum of polarization along the i direction can be computed through:

$$\delta P_i = \frac{q_e}{V} v_i \; (C/m^2) \qquad (4.2)$$

where V is the total volume of the unit cell and v_i is the length of the unit cell vector along the i direction.

The related quantum of polarization for 2D materials can be expressed as:

$$\delta P_{2D,i} = \delta P_i \cdot t \ (C/m) \qquad (4.3)$$

Where t stands for the thickness of the considered computational cell. An offset of $2 \cdot \delta P_{2D}$ can be seen in Fig. 4. 3 corresponding to the calculation of the piezoelectric response of MoS_2 which is approximately $5.03 \cdot 10^{-10}$ C/m:

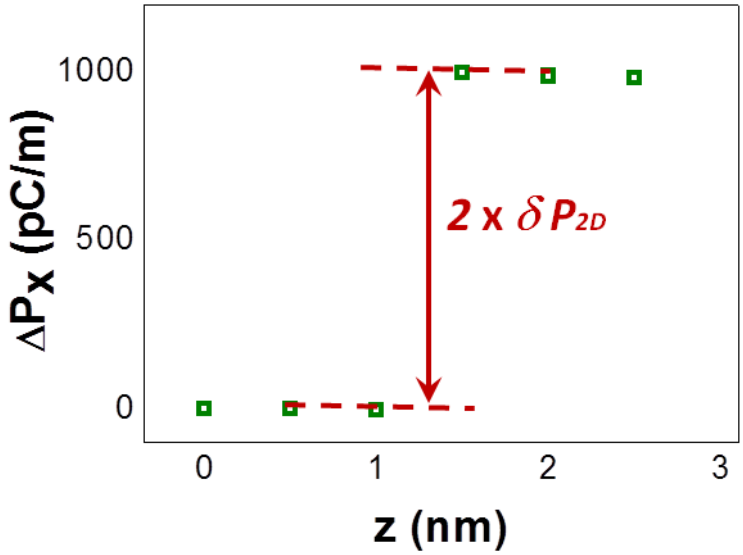

Fig. 4. 3. Polarization change under deformation of MoS_2. An abrupt step is shown related to the entrance of a pair of quantum of polarization.

With the aim of comparing the three different cases (graphene, h-BN and MoS_2) and, simultaneously, keeping the computational weight at a reasonable level, infinite graphene, h-BN and MoS_2 are considered rather than nanoribbons. Therefore, the structures are modeled by a n x 1 computational super-cell, thus, considering one single unit-cell along the y axis. Implicitly, it is assumed that the energy for a structure with a given width, W, can be calculated by rescaling the energy by a factor W/a. Within this approximation, edge effects [3] on the total energy and polarization are not considered since a infinite periodicity is considered along x and y directions. This is a reasonable approximation if the final structure is composed of several unit-cells in the perpendicular direction of the deformation, as expected for realistic devices [4-6], when the energy contribution from these free edges become negligible.

The followed strategy for bringing these mechanical structures into bi-stability is to apply a longitudinal compressive strain bringing closer the two clamped ends as it is depicted on Fig. 4. 4. Under these conditions, if the ribbon is suspended a buckled configuration is favored (not for all geometries as it will be shown later on) presenting two symmetric stable states around the plane defined by the uncompressed configuration. Only the deformations along the z-axis will be considered reducing the problem to compute the total energy, $E=E(z,\varepsilon)$, as a function of the applied compression and the z coordinate.

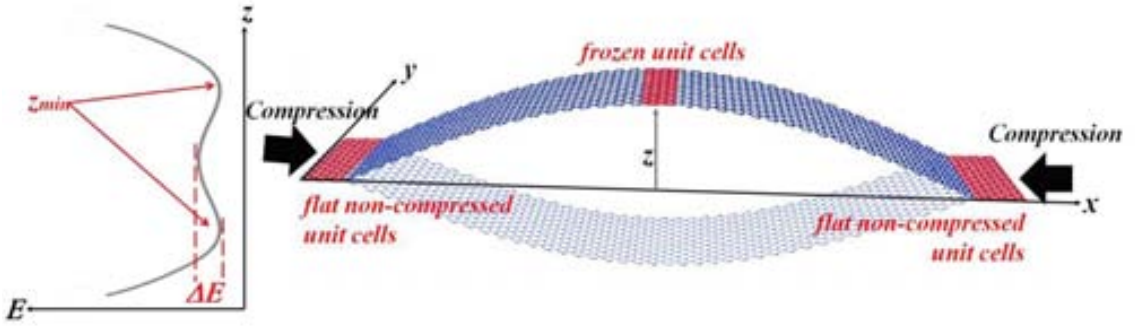

Fig. 4. 4. Scheme of the system: a 2D-material ribbon is compressed along the length direction favoring the appearance of two symetric stable points at z_{min}. The energy landscape defines the mechanical behavior of the system. Four unit-cells at each end are kept flat and uncompressed. One unit-cell at the center of the ribbon is frozen to prevent the structure to colapse to the ground state.

Notice that once the total energy, E, is known the simulation of the dynamics of the system can be done again in the frame of the spring-mass model. We assume only the first vibration mode to be of relevance which means considering $m_{eff} \sim 0.4m$ with $m=\rho S_{eff}$ where t_{eff} stands for the effective thickness of the structure which will be determined for each case in the following sections. The quality factor, Q, is left as a free parameter ranging from 10 to 10000 as it strongly depends on the specific conditions [4, 7].

To reproduce the shape of the ribbons under out-of-plane deformation a sinusoidal translation is applied to the atomic coordinates, z_i, of the kind of

$$\vec{r}_i: (x_i, y_i, 0) \rightarrow \vec{r}_i': (x_i, y_i, z'_i) \qquad (4.4a)$$

$$z_i' = z \cdot \sin(k_x x_i) = z \cdot \sin\left(\frac{2\pi}{(l/2)} x_i\right) \qquad (4.4b)$$

In this frame, z defines the amplitude of the sinusoidal deformation and represents the maximum displacement corresponding to the center of the suspended ribbon. Computing the total energy for different amplitudes allows achieving an expression for the elastic potential energy similar to this defined for the device presented in chapter 3, $U_T=U_T(x,d)$, with the difference that the tuning parameter that was represented by the distance d now is the strain, ε.

An intriguing issue concerns the type of calculations to carry out to define correctly the static and dynamic regimes of such devices: relaxing or not the atomic positions. In general the natural frequencies of NEMS are around the GHz range and it would represent a non-adiabatic process. Therefore, if it was possible to take an instant picture of the atomic positions during a free oscillation the x_i and y_i components are expected to keep unchanged. When a compression is applied the rest state is replaced by the above mentioned symmetric states changing these "in-plane" components of the position

vector for each atom in order to relax the forces seen by each atom. If relaxation is allowed then the expression for the change in the atomic coordinates becomes:

$$\vec{r}_i: (x_i, y_i, 0) \rightarrow \vec{r}_i': (x_i + \delta x_i, y_i, z'_i + \delta z_i) \qquad (4.5)$$

as depicted in Fig. 4. 5. For all cases, the frozen approach presents the advantage of saving computational time in comparison to the relaxed approach. The computation of the total energy after relaxation is carried out for graphene. For the MoS_2 ribbon only frozen configurations are considered. In order to evaluate the committed error both kind of calculations are performed for h-BN allowing a comparison in terms of the energies $E_{relaxed}$ and E_{frozen}.

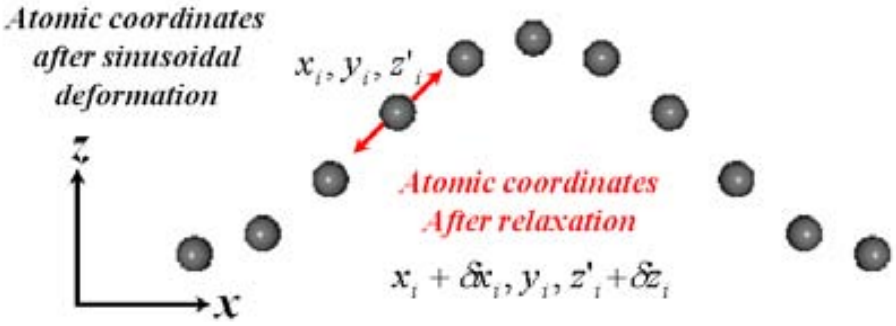

Fig. 4. 5. Scheme of the induced sinusoidal deformation to a one-dimensional atomic chain.

The clamped ends of the ribbons consist of four uncompressed and non-deformed unit-cells. In order to compute the total energy for the ribbons under deformation when relaxation is allowed, the central unit-cell (red lighted atoms from Fig. 4. 4) of the strip is frozen in order to prevent the collapsing into the ground state configuration, i.e. flat graphene for the non-compressed case.

The specific technical details of each case such as the used pseudo-potentials or basis sets will be discussed in the following subsections.

4.2. Graphene

Graphene is a carbon allotrope distributed in a hexagonal lattice forming a honey-comb structure one atom thick as illustrated in Fig. 4. 2. It presents outstanding electrical [8] and mechanical properties [9-11] such as the capacity to support high strains without breaking [12] (around ~10-20%) which makes of it an optimal material for the interest of this work. Moreover, it is a useful paradigm of 2D materials and perfectly illustrates the basic ideas behind our proposal. This seems to be a common property of all sp^2-bonded crystals [13]. The results here presented are mainly reported on the papers of

section 6.2 and 6.3 including also other relevant information for the completeness of this section.

A minimal basis set is considered (single-ζ) for the most time spending calculations, although for short graphene lattices satisfactory convergence tests have been carried out against a more reliable single-ζ polarized basis set.

Mechanical description── The considered graphene unit cell is a rectangular cell that consists of four carbon atoms as it is showed on Fig. 4. 2. The optimized lattice constant is a=2.479 Å in good agreement with other experimental value and DFT based calculations reported in other works [14, 15]. Computing the energy of the system under a linear deformation along the arm-chair direction allows to extract a Young's modulus of 0.85 TPa. If, when performing the deformation, a relaxation along the zig-zag direction is allowed the Poisson ratio is obtained giving 0.18. Both values are in good agreement with other reported values [9, 16].

These test results were obtained assuming an effective thick of 3.34 Å as it is done for all the simulations carried out during the present study. As a matter of fact, the thick of a 2D material is an ill defined quantity. Therefore, a thickness definition based on the separation between consecutive layers for bulk graphite is assumed [17].

The computational cell consists on a 40 x 1 super-cell (17nm length) along the arm-chair direction as the one represented on Fig. 4. 2.

Fig. 4. 6 show the energy, computed as $\Delta E=E-E_0^0$, as a function of the deformation amplitude, z, for non-compressed graphene. E_0^0 stands for the energy of flat graphene, i.e. $z=0$, $\varepsilon=0$.

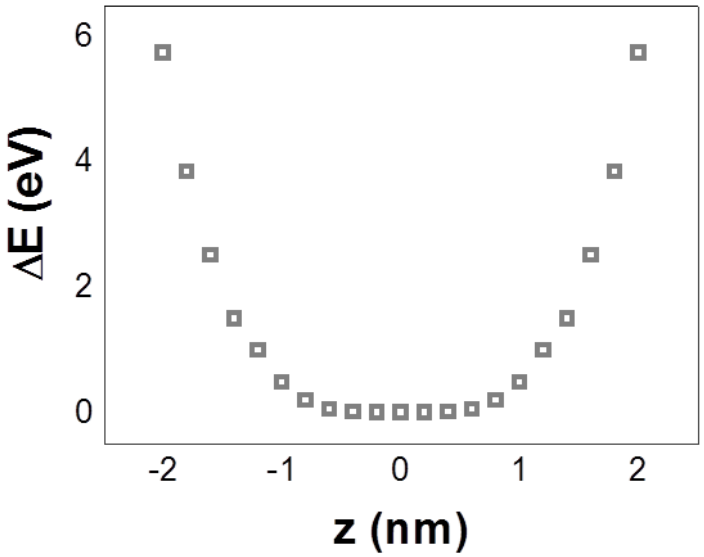

Fig. 4. 6. Elastic potential energy, ΔE, for a 40 x 1 graphene ribbon as a function of the out-of-plane displacement, z. An intrinsic non-linearity can be seen for small displacements flattening the potential: small forces are needed to provoke a large displacement.

A satisfactory fit to the obtained data is achieved by a 4th order polynomial setting to zero the coefficients for odd contributions. A strong non-harmonic behavior can be observed specially for little displacements where the curve presents a flat region. Therefore no natural frequency can be associated to the given geometry as $\partial^2 E/\partial z^2$ has a dependence on z. The fitting polynomial needs to be extended to 8th order to have a sound description for the energies with $\varepsilon \neq 0$ from Fig. 4. 7a, where a bi-stable configuration is induced by compression. Table 4. 1 shows the coefficients for the different studied cases:

$\boldsymbol{\varepsilon\,(\%)}$	$\boldsymbol{p_8(eV/\text{Å}^8)}$	$\boldsymbol{p_6(eV/\text{Å}^6)}$	$\boldsymbol{p_4(eV/\text{Å}^4)}$	$\boldsymbol{p_2(eV/\text{Å}^2)}$
0.00	$4.105 \cdot 10^{-11}$	$-3.582 \cdot 10^{-8}$	4.21010^{-5}	$5.993 \cdot 10^{-4}$
0.25	$8.115 \cdot 10^{-11}$	$-8.502 \cdot 10^{-8}$	$5.784 \cdot 10^{-5}$	$-2.284 \cdot 10^{-3}$
0.50	$1.577 \cdot 10^{-10}$	$-1.433 \cdot 10^{-7}$	$7.172 \cdot 10^{-5}$	$-4.885 \cdot 10^{-3}$
0.75	$1.725 \cdot 10^{-10}$	$-1.465 \cdot 10^{-7}$	$7.297 \cdot 10^{-5}$	$-6.991 \cdot 10^{-3}$
1.00	$2.432 \cdot 10^{-10}$	$-2.145 \cdot 10^{-7}$	$9.307 \cdot 10^{-5}$	$-1.032 \cdot 10^{-2}$

Table 4. 1. Coefficients of the 8th order fit of the elastic potential energy for different compression values.

These coefficients p_i follow a quite linear relation with the compression so a linear fit can be done in order to achieve a full description of the total energy in terms of displacement, z, and compression, c.

$$E = E(z,\varepsilon) = p_8(\varepsilon)\cdot z^8 + p_6(\varepsilon)\cdot z^6 + p_4(\varepsilon)\cdot z^4 + p_2(\varepsilon)\cdot z^2 \qquad (4.6a)$$

$$p_8(\varepsilon) = 1.983\cdot 10^{-10}\varepsilon + 3.999\cdot 10^{-11} \qquad (4.6b)$$

$$p_6(\varepsilon) = -1.675\cdot 10^{-7}\varepsilon - 4.127\cdot 10^{-8} \qquad (4.6c)$$

$$p_4(\varepsilon) = 4.683\cdot 10^{-5}\varepsilon + 4.413\cdot 10^{-5} \qquad (4.6d)$$

$$p_2(\varepsilon) = -1.062\cdot 10^{-2}\varepsilon + 5.325\cdot 10^{-4} \qquad (4.6e)$$

Notice that the only coefficient that change sign as a compression is applied to the system is p_2 and, as a matter of fact, this is what mainly describes the transition from the monostable potential with a minimum at z=0 to the corresponding saddle point at this coordinate as bistability is achieved. Then, from the analytical expression of this coefficient, one can say that bistability appears when it changes its sign, $\varepsilon_{bistable}$~0.05%, which indicates that below this $\varepsilon_{bistable}$ the structure prefer to absorb the stress incrementing the energy of the particular configuration rather than releasing this energy by buckling.

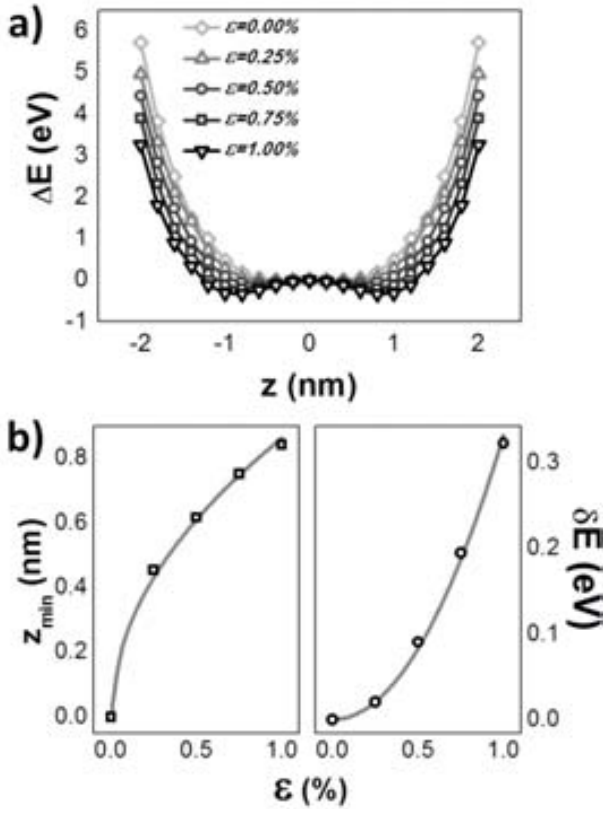

Fig. 4. 7. (a) Elastic potential energy, ΔE, as a function of the out-of-plane displacement, z, for a 17nm length ribbon (40 x 1 supercell) for five different compressive strains. Compression makes appear to symmetric stable points at ±zmin separated by a potential barrier of height δE. (b) Variation of z_{min} and δE with compressive strain. Higher compressions produce higher potential barriers and a great separation between minima.

As it was the case in the previous chapter, the two meaningful quantities are the position of the potential energy minima, z_{min}, and the barrier height between them, δE. Both increase by increasing the applied compression, as it can be seen from Fig. 4. 7b with the following dependence on the compression, ε:

$$z_{min} = 8.636\sqrt{\varepsilon}\ (\text{Å}) \tag{4.7}$$

$$\delta E = 0.332\varepsilon^2\ (eV) \tag{4.8}$$

Notice that, due to the assumption that the energy of the ribbon is strictly proportional to the number of unit cells taken into account in the *y*-direction, *m*, the barrier height can be expressed in a more general manner as $\delta E_m = m \cdot \delta E$ while the minima position remains invariable. Consequently, the ribbon width is an additional control parameter to tune bistability.

Dynamics and electric power—— Until this point the statics of the system in terms of energy has been described and a continuous modeling depending on the displacement and the applied compressive strain has been derived. With the aim of describing the dynamical behavior of the ribbon the following Langevine type equation of motion has to be solved:

$$m_{eff}\ddot{z} = -\frac{\partial E}{\partial z} - b\dot{z} + F_{ext} \tag{4.9}$$

where m_{eff} is the effective mass and *b* stands for a linear viscous damping term. As it was mentioned before, the quality factor remains as a free parameter to be determined. The external force, F_{ext}, is considered to be a white Gaussian noise,WGN, with zero mean and an intensity related to the level of the thermal fluctuations, as it is assumed to be the minimum level of noise for all systems [18]:

$$F_{rms} = \sqrt{4k_B T b B} = \sqrt{\frac{8\pi k_B T m_{eff} f_0 B}{Q}} \tag{4.10}$$

Where k_B is the Boltzmann constant, *T* is the temperature of the thermal bath and *B* stand for the bandwidth of the noise which is determined by the time-step of the numerical simulation. Due to the dependence of the damping coefficient, *b*, with the quality factor, *Q*, expressed in equation 2.42, the external force decreases as *Q* increases.

The randomness of F_{ext}, forces equation 4.7 to be solved by numeric methods as explained in subsection 2.3. The WGN to model the external force is defined by $F_{ext}=F_{rms}\check{\Xi}(t)$ where $\xi(t)$ is generated by the MATLAB function *randn*. An integration step of 5ps is used, which implies a noise bandwidth of 0.2THz, giving stable trajectories under bistable condition.

Fig. 4. 8 shows the response of the system to an external excitation of approximately F_{rms}~0.2 pN, corresponding to the force generated by thermal fluctuations (Q=100) of different compressions for a 17nm long and 1nm wide ribbon. As expected, for a certain range of compressions the system is able to suffer transitions from the two wells of the potential energy increasing the response to the external excitation. Fig. 4. 8a illustrates this increment in terms of frequency response. The lower panel corresponds to the non-compressed case where a quasi-harmonic behavior is showed presenting oscillations mainly around f~30 GHz. In the middle panel it can be seen that the frequency response for the bistable regime extends to the low frequency range presenting an average increment between 2 and 3 orders of magnitude compared to the other two cases. There is no preferred frequency as it is the case for the other two configurations. The upper panel corresponds to the situation where the graphene ribbon gets stuck in one of the two wells and the frequency recovers the shape of this for resonating systems with a clear peak around f~40 GHz.

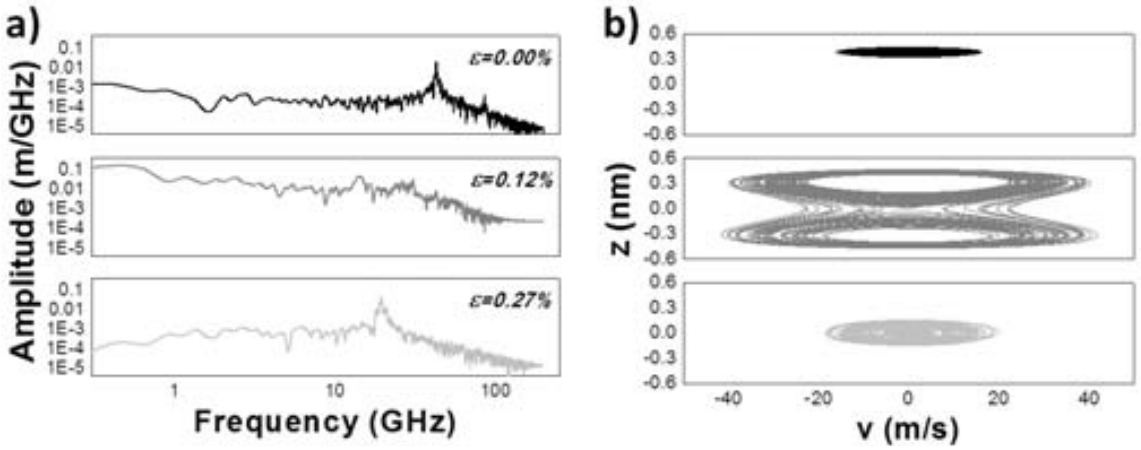

Fig. 4. 8. Dynamics of the three different regimes: uncompressed (lower panels), moderately compressed (middle panels) and overcompressed (upper panels). (a) Spectral response: zero or too large strains yields rather selective frequency responses while for an optimal compression value the response is broaded to the low frequency range. (b) The evolution of the different attractors of the system can be seen from the phase portrait. *Frms*=0.2 pN, Q=100, l x w = 17 nm x 1 nm.

From the phase portrait showed in Fig 4. 8b, the evolution of the attractors can be followed for the three different regimes. At this point it is worth to note that for non-linear systems the response at a given frequency range is not directly related to the excitation at this same frequency range, so it cannot be said that the middle panels correspond to a situation where the system responds better to the low frequency range as it will be discussed along the following lines.

In Fig. 4. 9 the root mean square for the out-of-plane displacement, z, is showed. An increase of the mechanical response is achieved for increasing compressive strains reaching the maximum at ε_{opt}~0.13%. Beyond this optimal value, the response is drastically reduced giving a z_{rms} even lower than this for the non-compressed configuration.

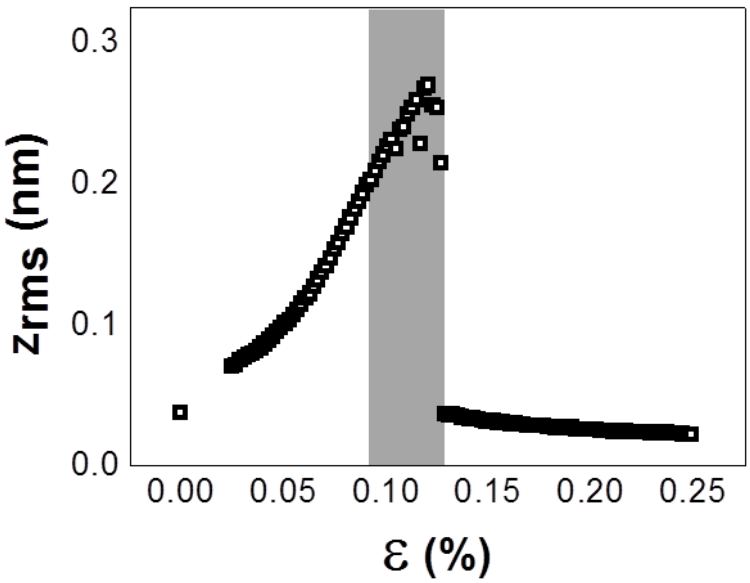

Fig. 4. 9. Root mean square of the out-of-plane displacement, z, as a function of the compressive strain, ε. As compression is increased and bi-stability is reached, the z_{rms} increases as well. The gray shadowed area represent the range of compressive strains giving the grater increment on z_{rms}. After ε_{opt}~0.13%, z_{rms} suddenly drops to values lower than that for ε=0. *Frms*=0.2 pN, Q=100, l x w = 17 nm x 1 nm.

At this point colored noise rather than WGN is considered in order to know in what extent the response depends on the kind of excitation. Fig. 4. 10 shows the root mean square of the displacement, z_{rms}, for low-pass and high-pass filtered noises respectively maintaining for all cases an standard deviation of 0.2pN. It can be observed that the maximum response is achieved at ε_{opt}~0.135% with z_{rms}~3 Ā for all cases independently of the kind of frequency distribution, which suggests the system response depends only on the excitation intensity, F_{rms}.

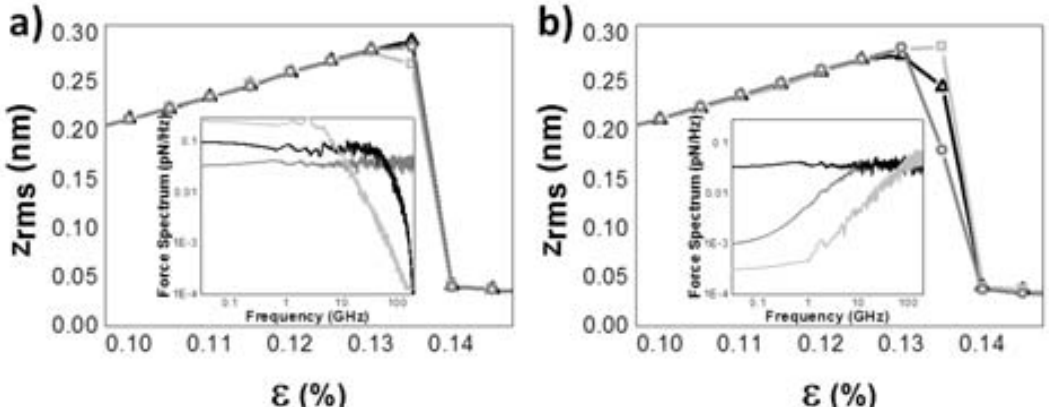

Fig. 4. 10. System response in terms of zrms under the action of colored external excitations (insets) with equal F_{rms} presenting a maximum at the same compressive strain, ε_{opt}, regardless of the filtering. (a) z_{rms} under low-pass filtered

noise. The maximum response is achieved around ε~0.13% for all cases. Inset: spectral charaxcterization of the force. The intensity increment in the low frequency band compensates the high frequency filtering. (b) z_{rms} under high-pass filtered noise also showing a maximum at ε_{opt}~0.13%. *Frms*=0.2 pN, Q=100, l x w = 17 nm x 1 nm.

As it can be seen from the inset on Fig. 4. 10a the response of the system is approximately the same even when the contribution of the external excitation around 30 GHz is decreased for more than one order of magnitude (clear grey line). As it was pointed out before, there is no relation between the response of the system at the low frequency range and the excitation at the same band. Therefore, the parameter determining the capacity of the ribbon to suffer intra-well transitions is the noise intensity and not the contribution of the external excitation at the high-frequency range.

The phase portrait of Fig. 4. 8b (middle panel) indicates that the increment in the low frequency range is related to the transitions between potential wells which would explain why, if the low frequency contribution is cut off, the dynamics keeps showing its characteristic peak as shown in Fig. 4. 10b.

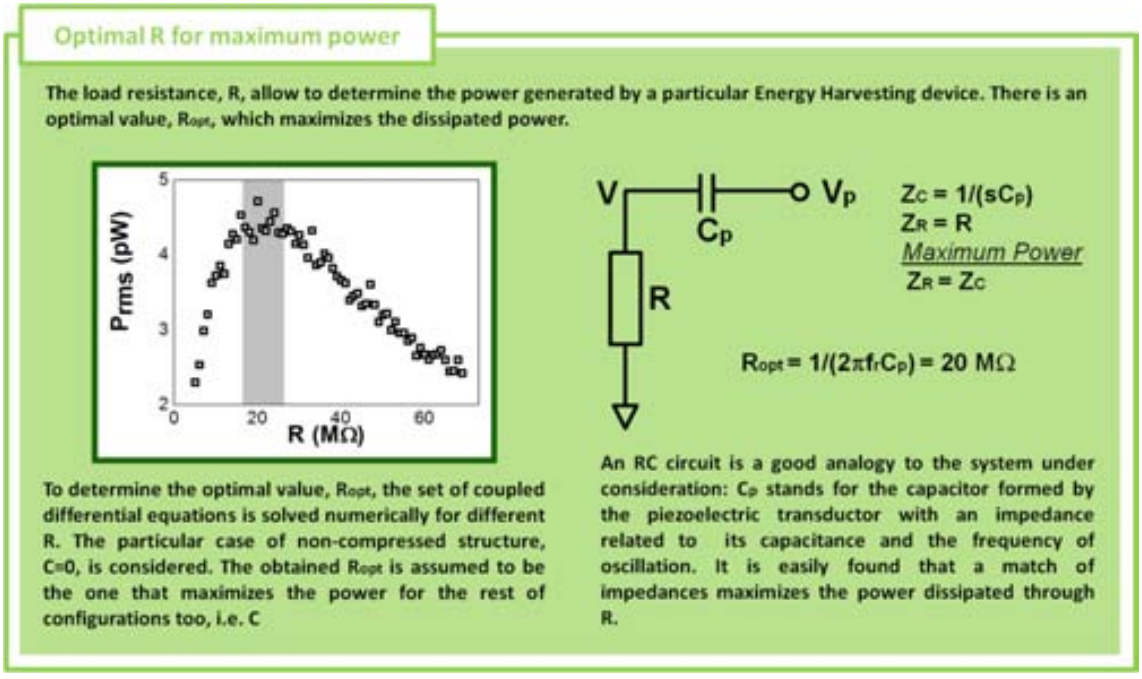

As it was said in the introduction to this chapter, graphene is a very promising material to be the future basis of electronics. Unfortunately piezoelectricity is not one of its outstanding properties. In order to transduce the energy from the mechanical to the electric domain it is considered a piezoelectric transduction strategy as it was done in chapter 3 consisting in two AlN layers 2 nm long with equal width that this for the graphene ribbon attached at both clamped-ends. The thickness of am AlN mono-layer is considered to be 0.3 nm [19]. The piezoelectric constant in the 31 mode is taken to be d_{31}= 1.73 pm/V [19]. The mechanical effects of the transducer on the system are not considered in the modeling although electro-mechanical coupling effects are. The

optimal resistive load value, R~10 MΩ, is obtained after numerical simulation for the non-compressed configuration.
The generated electric power for Q=100 and 10000 are represented on Fig. 4. 11 (green line) with the corresponding z_{rms} (grey solid line) and this for the case without transduction (grey dashed line).

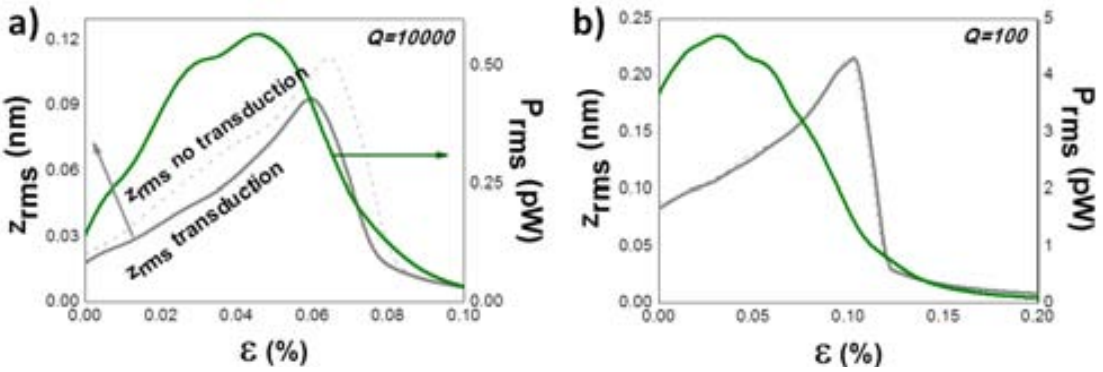

Fig. 4. 11. z_{rms} (grey line) and P_{rms} (green line) as a function of the compressive strain considering (a) Q=10000 and (b) Q=100. The grey dashed lines represent the z_{rms} when no transduction is performed. $Frms \propto Q^{-1/2}$, l x w = 17 nm x 1 nm.

There are two remarkable aspects in these two figures: first, the reduction of the power dissipated by R for higher Q values due to the reduction of the noise intensity as it varies with $Q^{-1/2}$. Second, the shift towards lower compression values of ε_{opt}. The maximum output power for Q=10000 is increased by a factor of 4 respect this for flat graphene, while for Q=100 the gain is reduced to a factor of 1.3. It is worth to keep in mind that the non-compressed graphene presents an intrinsic non-linear behavior so to reproduce the kind of curves achieved for the device presented on chapter 3 it would be necessary to consider not only compressive but also tensile stresses.

Now, if a constant external force of 2.2 pN independent of the quality factor is considered, i.e. the noise source is not due to thermal fluctuations, the dependence with Q can be better understood. In this case the optimal compression depends only on the external force intensity and then it remains approximately constant around 0.05% to achieve a maximum power of 9 pW for a quality factor of Q=10000 and of 2 pW for Q=10 as shown in Fig. 4. 12. This means that higher quality factors allows converting more efficiently the mechanical power into the electrical domain due to the reduction of the damping coefficient, b.

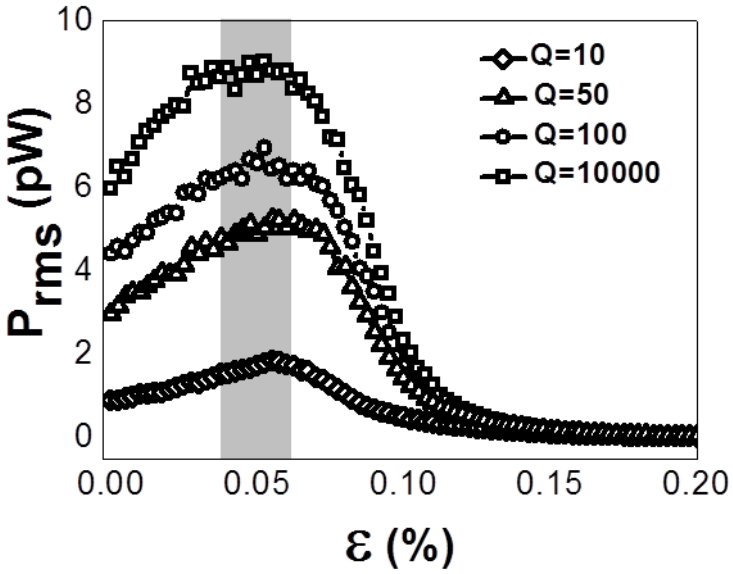

Fig. 4. 12. P_{rms} as a function of the compression for different quality factors, Q. The maximum value is achieved approximately for the same ε_{opt} though it is increased for increasing values of the quality factor indicating that more energy can be stored for low damping factors, b. $Frms$=2.2 pN, l x w = 17 nm x 1 nm.

Taking into account the results presented along this section regarding the electric power, it can be seen that a higher external force intensity is translated to an increment of the ε_{opt}, as it is expected since more energy is available to overcome the potential barrier.

4.3. h-BN

Despite the historical relevance of the graphene discovery and its 2D nature, it is by no means the only mono-layered material. Another material that allows isolating mono-layers is hexagonal Boron Nitride, h-BN. Like graphene, as it is a sp^2-bonded crystal, it can support huge out-of-plane deformations. h-BN, as other noncentrosymetric crystals, presents a macroscopic in-plane polarization under deformation stress due to the well-known piezoelectric effect. The use of a piezoelectric material not only as the mechanical-energy-to-electric-energy transducer, as considered for graphene, but also as the external-vibration-to-mechanical-energy transducer represents a simplification for the realization of such a device.

In this section the results obtained for h-BN will be presented following the structure of the previous section but focusing on characterizing the piezoelectric effect and its applicability for EH purposes.

A single-ζ polarized basis set is considered for all calculations, though a comparison against single-ζ and double-ζ polarized sets is carried out regarding the piezoelectric

characterization and the elastic potential energy calculation for the uncompressed case. Table 4. 2 shows a relation of the different calculations.

	$E_{relaxed}$ vs E_{frozen}	Elastic potential energy	Piezoelectric coefficient
Single-ζ	X	X	X
Single-ζ polarized	-	X	X
Double-ζ polarized	-	X	X

Table 4. 2. Summary of the different basis sets considered along the present subsection.

As a rule of thumb, the more complete the basis set is the higher the computational weight is. Double-ζ polarized based calculations are performed for several cases for checking the results from single-ζ polarized based results. The reason of comparing the the single-ζ polarized based results with those from the Single-ζ is to evaluate the committed error when comparing the energies from the relaxed and frozen approaches. The same motivation applies for the calculation of the piezoelectric coefficient.

Mechanical description—— Like in the case of graphene, for convenience we have used a rectangular unit-cell and that consists of two boron and two nitrogen atoms, as showed in Fig. 4. 2. The optimized lattice constant is a~2.508 Å which falls in the range of other publications [20].
Following the steps showed in the previous section, a 47 x 1 computational super-cell is considered upon which $E(z,\varepsilon)$ and $P(z,\varepsilon)$ will be computed. The results that follow are obtained assuming an effective thickness of 3.5 Å.

As mentioned in the first lines of this subsection, the total energy for the uncompressed case, $E(z,0)$, is computed for three different basis in order to evaluate the committed error. The error between the energies for single-ζ polarized and double-ζ polarized basis sets falls between 0.18 and 0.21% and this for single-ζ polarized and single-ζ is around 0.35%. Fig. 4. 13 shows the normalized energies $\Delta E=E(z,\varepsilon)-E(0,0)$ for the three cases commented before.

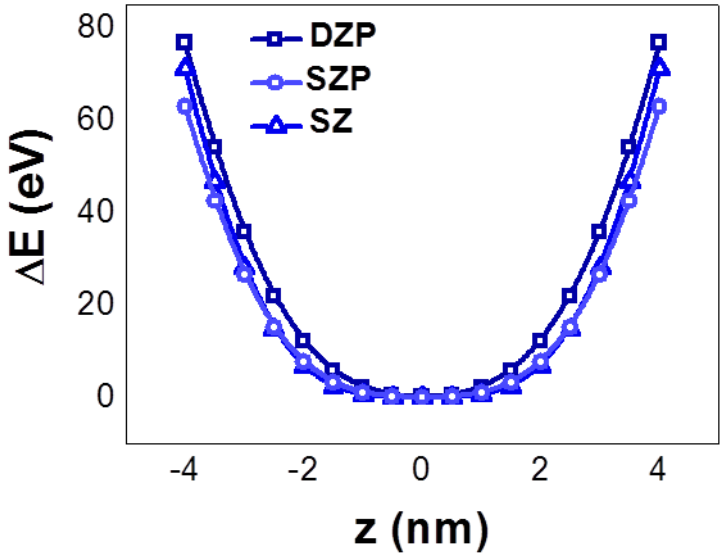

Fig. 4. 13. Elastic potential energy for a 47 x 1 computational-cell for three different basis. The comparison allows to evaluate the committed error considering a single-ζ polarized basis instead of a more reliable double-ζ polarized. As it happened with graphene an intrinsic non-linearity for small displacements can be seen in a form of a energy flattening.

As it was the case for the graphene ribbon, the uncompressed suspended ribbon presents an intrinsic non-linearity which can be fitted by a 4^{th} order polynomial curve, that needs to be extended to the 8^{th} to keep the track of the bi-stable regime once a compression is applied.

As it was pointed out before in this chapter, a comparison between relaxed and frozen calculations has been done. For the sake of minimizing the time of the relaxing calculations the single-ζ basis set is considered for this comparison. As it can be seen from Fig. 4. 14 there is a mismatch between the two curves: although the position of the minima is approximately the same, the potential barrier height is higher for the frozen calculation than for the relaxed one. Therefore, the following simulations, as they are performed in frozen conditions, will overestimate the barrier height around a ~50%.

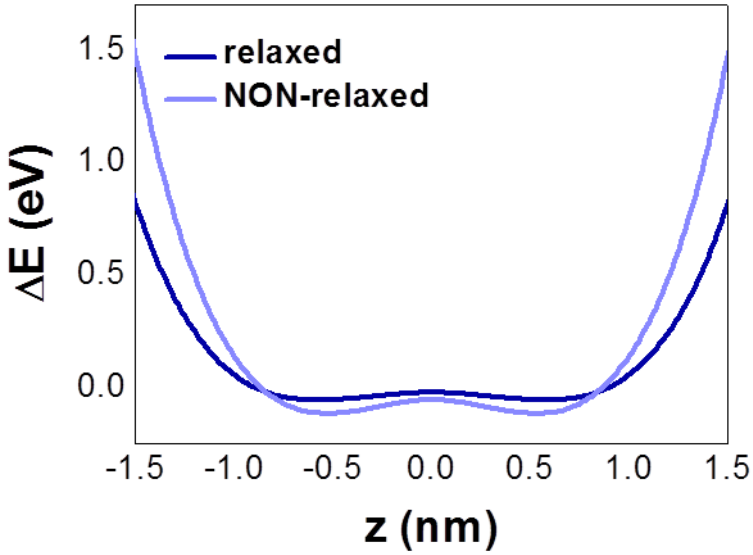

Fig. 4. 14. Elastic potential energy (ε=0.5%) comparison for the relaxed and frozen approaches showing a good agreement for the minima position and a overestimated potential barrier for the frozen case.

One of the main advantages of bi-stable harvesters is the generation of a greater separation of electric charges in the transducer element due to greater amplitude of movement. Thereby, the increasing of the barrier height, as long as the minima position remains unchanged, would fix the lower bound of the potentially achievable electric power.

The changes suffered by the potential energy curve are due to the rearrangement of the atomic positions that reduces the strain along the mode defined by *u(x)*. The normalized displacement, representing a measure of a kind of local-strain, is calculated for each atom labeled by an atomic index, *i*, by means of:

$$\varepsilon_i^{u(z)} = \frac{\sqrt{\left(\boldsymbol{r}_{i+n_0}^z - \boldsymbol{r}_i^z\right)^2} - \sqrt{\left(\boldsymbol{r}_{i+n_0}^0 - \boldsymbol{r}_i^0\right)^2}}{\sqrt{\left(\boldsymbol{r}_{i+n_0}^0 - \boldsymbol{r}_i^0\right)^2}} \qquad (4.11)$$

where $\boldsymbol{r}_i^z = (x_i, y_i, z_i)$ and the super index, z, stands for the amplitude of the deformation.

Fig. 4. 15 shows the trend of the computed strain for both type of calculations, relaxed (a and b) and frozen structures (c and d). The relaxation of the atomic positions trend to equal the distances between atomic periodic distances, $d_i^z = \sqrt{\left(\boldsymbol{r}_{i+n_0}^z - \boldsymbol{r}_i^z\right)^2}$, as it can be seen from Fig. 4. 15a and b regardless of the amount of compressive strain applied, while for the other cases from Fig. 4. 15c and d the strain follows the proper form of the function from equation 4.2. Due to the fact that the central unit-cell atomic positions are

kept frozen, as it was mentioned in the introduction of this chapter, the strain for these four atoms equals the value of the compression applied to the whole structure.

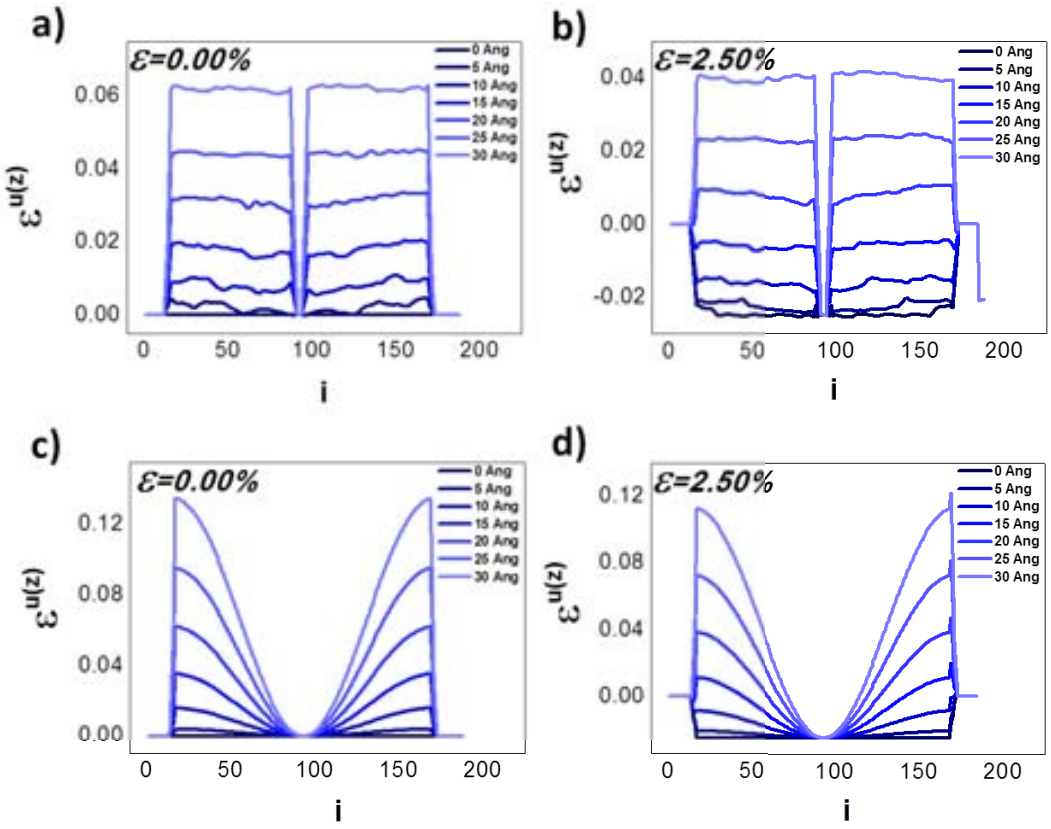

Fig. 4. 15. Strain profiles along the ribbon's length for the relaxed (a and b) and frozen approaches (c and d).

Regarding the curves from the relaxed calculations, a change on the strain sign can be appreciated for the compressed configuration: for z=0 the computed strain is negative in accordance with the fact that the ribbon is compressed. As z increases the average value of the strain decreases and at a certain amplitude value, z_0, it starts to be positive in a similar way it happens with the first derivative of the energy although there is a mismatch between the corresponding z_0. Fig. 4. 16 plots the average strain for four different configurations in front of the out-of-plane displacement, z.

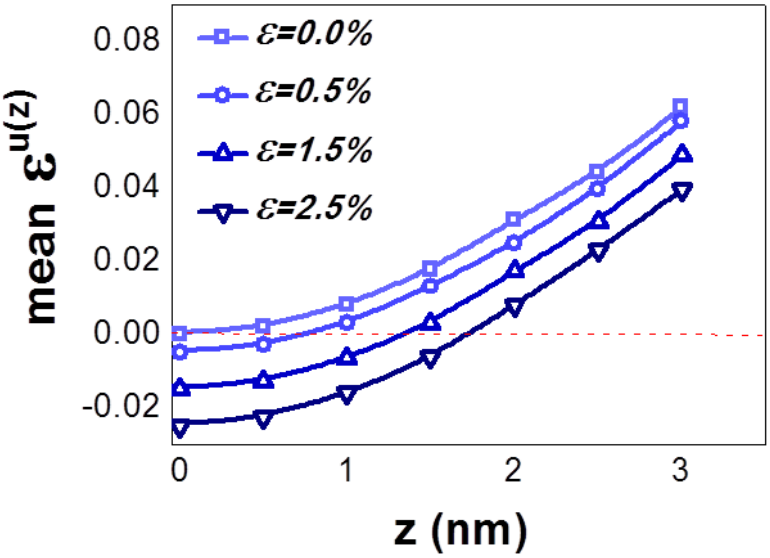

Fig. 4. 16. Mean strain along the ribbon's length for different compression values. The red dashed line represents ε=0.

As it was done for the graphene ribbon, the elastic potential energy is computed as a function of the out-of-plane displacement, z, and the applied compression ranging from 0 to 2%. Fig. 4. 17 shows the obtained data in terms of the energy difference, ΔE.

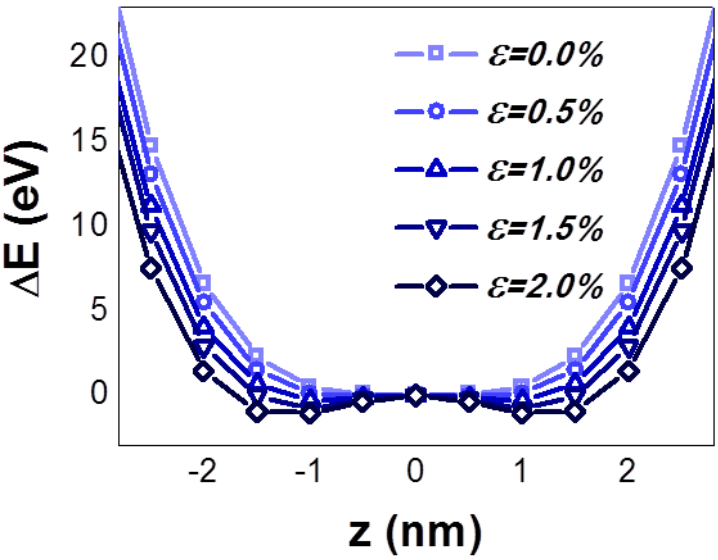

Fig. 4. 17. Elastic potential energy as a function of the out-of-plane displacement, z. A buckled configuration is favored for compressed h-BN.

The compression applied to the ribbon flattens the potential energy provoking at certain point the buckling of the ribbon as it was the case for the graphene ribbon.

Table 4. 3 lists the coefficients of the 8th order polynomial fit of the energies for the different considered compressions. In contrast to what happens with graphene, p_8 and p_6 are considered to be almost constant while p_4 and p_2 have a linear dependence with the compressive strain, ε, with very similar behavior to what was reported for graphene. Also, the only coefficient that change sign as compression increases is p_2, giving a value

for the transition strain of $\varepsilon_{bistable}$~0.08%, very close to what was reported for graphene, $\varepsilon_{bistable}$~0.05%.

ε (%)	$p_8(eV/Å^8)$	$p_6(eV/Å^6)$	$p_4(eV/Å^4)$	$p_2(eV/Å^2)$
0.00	$2.253 \cdot 10^{-12}$	$-1.472 \cdot 10^{-8}$	$4.522 \cdot 10^{-5}$	$6.246 \cdot 10^{-4}$
0.50	$2.910 \cdot 10^{-12}$	$-1.703 \cdot 10^{-8}$	$4.849 \cdot 10^{-5}$	$-3.310 \cdot 10^{-3}$
1.00	$3.258 \cdot 10^{-12}$	$-1.846 \cdot 10^{-8}$	$5.109 \cdot 10^{-5}$	$-7.568 \cdot 10^{-3}$
1.50	$2.997 \cdot 10^{-12}$	$-1.832 \cdot 10^{-8}$	$5.348 \cdot 10^{-5}$	$-1.131 \cdot 10^{-2}$
2.00	$2.989 \cdot 10^{-12}$	$-1.861 \cdot 10^{-8}$	$5.479 \cdot 10^{-5}$	$-1.557 \cdot 10^{-2}$

Table 4. 3. Coefficients of the 8th order fit of the elastic potential energy for different compression values.

$$E = E(z, \varepsilon) = p_8(\varepsilon) \cdot z^8 + p_6(\varepsilon) \cdot z^6 + p_4(\varepsilon) \cdot z^4 + p_2(\varepsilon) \cdot z^2 \quad (4.12a)$$

$$p_8 = 2.990 \cdot 10^{-12} \quad (4.12b)$$

$$p_6 = -1.782 \cdot 10^{-8} \quad (4.12c)$$

$$p_4(\varepsilon) = 6.442 \cdot 10^{-6}\varepsilon + 4.517 \cdot 10^{-5} \quad (4.12d)$$

$$p_2(\varepsilon) = -0.830 \cdot 10^{-2}\varepsilon + 6.830 \cdot 10^{-4} \quad (4.12e)$$

The trend of the minima separation, z_{min}, and the potential barrier height, δE, is similar to those for graphene:

$$z_{min} = 8.784\sqrt{\varepsilon}\ (Å) \quad (4.13)$$

$$\delta E = 0.297\varepsilon^2\ (eV) \quad (4.14)$$

In the frame of z=0, the variation of the energy due to the compressive strain is related to the Young Modulus, Y. It is defined as a measure of the stiffness for an elastic material in terms of stress and strain along a certain direction for soft deformations, when the Hook's law applies:

$$Y = \frac{\sigma_i}{\varepsilon_i} \quad (4.15)$$

Where σ_i is the stress along the *i*-direction produced by a strain along the same direction, ε_i. From a variational point of view, equation 4. 15 can be rewritten as:

$$Y = \frac{\partial \sigma}{\partial \varepsilon} \sim \frac{\partial \left(\frac{F}{S}\right)}{\partial \varepsilon} = \frac{1}{S}\frac{\partial F}{\partial \varepsilon} \tag{4.16}$$

Where F stands for the force related to the stress. The force can be expressed in terms of elastic potential energy as:

$$F = -\frac{\partial E}{\partial x} = \frac{\partial E}{\partial \varepsilon}\frac{\partial \varepsilon}{\partial x} = \frac{1}{l_0}\frac{\partial E}{\partial \varepsilon} \tag{4.17}$$

Rearranging equation 4. 17, the relation between the changes in the elastic energy, E, and the compressive strain, ε, can be expressed as:

$$Y = \frac{1}{S}\frac{\partial F}{\partial \varepsilon} = \frac{1}{S}\frac{\partial}{\partial \varepsilon}\left(\frac{1}{l_0}\frac{\partial E}{\partial \varepsilon}\right) = \frac{1}{V}\frac{\partial^2 E}{\partial \varepsilon^2} \tag{4.18}$$

As it was the case when computing the piezoelectric coefficients, an approximated thickness for the material should be considered in order to evaluate the volume, V. It is assumed a thickness of 0.35Ā as it was done before.
Fig. 4. 18 shows the energy variation which shows a quadratic dependence with compressive strain:

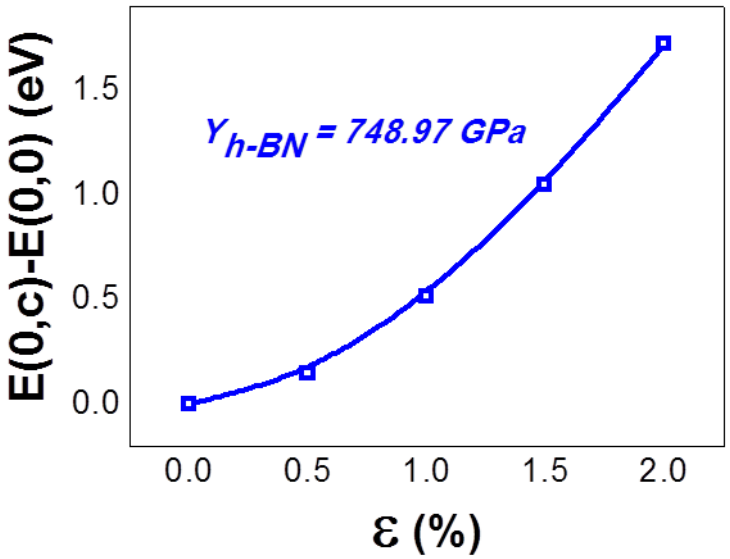

Fig. 4. 18. The Young's modulus, Y, can be computed from $E(0,\varepsilon)$ by differenciating respect the strain, ε. Considering an effective thicness of 0.35 Ā the obtained value for h-BN is around 749 GPa.

$$\Delta E_0 = E(0,\varepsilon) - E(0,0) = 0.44 \cdot \varepsilon^2 \ (eV) \tag{4.19}$$

$$Y_{h-BN} = 748.97 \ GPa \tag{4.20}$$

The derived value for the Young modulus, $Y_{h\text{-}BN}$~750 GPa, is similar to other theoretically calculated values [21].

Piezoelectric and flexoelectric description── Standard e_{11} piezoelectric coefficient is also computed applying straining and stretching in-plane stresses and reading the generated polarization within the Berry Phase approach as mentioned before in the introduction to this chapter.

The related piezoelectric coefficient can be calculated through:

$$e_{ij} = \frac{1}{Volume}\left(\frac{\partial P_i}{\partial \varepsilon_j}\right) \rightarrow e_{11} = \frac{1}{Volume}\left(\frac{\partial P_x}{\partial \varepsilon_x}\right) \tag{4.21}$$

Due to the difficulty to define the thickness of layered materials it is usual to define the piezoelectric response in terms of a 2D piezoelectric coefficient labeled e^{2D} which consists on replacing the "volume" divinding in equation 4. 21 by the in-plane area, *S*, as follow:

$$e_{11}^{2D} = \frac{1}{S}\left(\frac{\partial P_x}{\partial \varepsilon_x}\right) \tag{4.22}$$

The change in the *x*-polarization is shown in Fig. 4. 19 for all the three considered basis sets, i.e. single-ζ, single-ζ polarized and double-ζ polarized corresponding to the relaxed-ion approach:

.

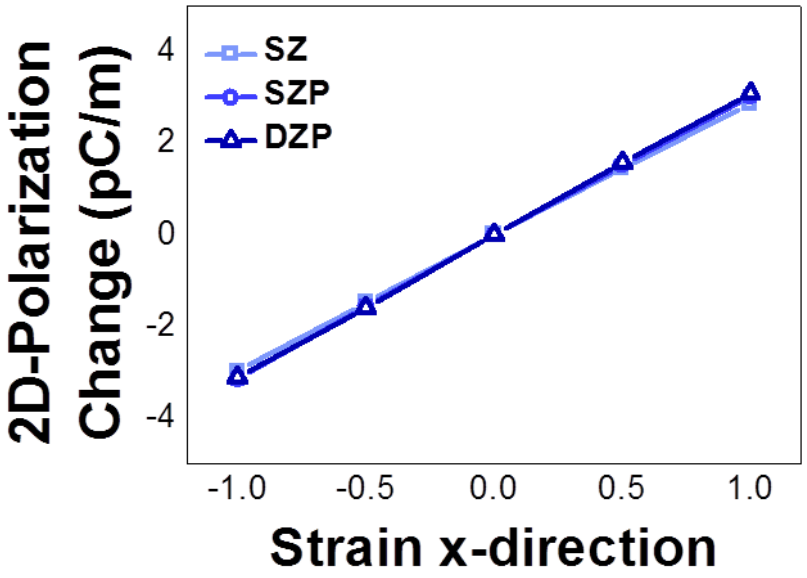

Fig. 4. 19. Polarization change under compressive and tensile stress along the *x*-direction (arm chair) for three different basis sets. Piezoelectric coefficients are directly derived from the slope of $\Delta P(\varepsilon)$. For the proposes of this work only the 11 mode is considered.

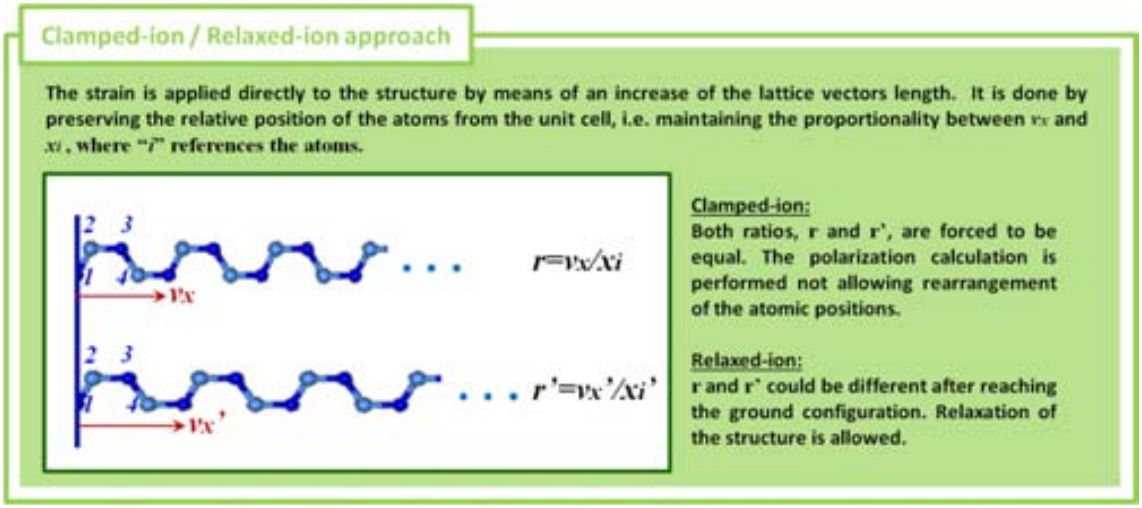

The resulting piezoelectric coefficients are listed in Table 4. 4 together with the deviation with respect to the values from [22] for the relaxed-ion approach.

	Relaxed-ion		Clamped-ion
Basis set	e_{11} $(10^{-10}\ C/m)$	**Error (%) [22]**	e_{11} $(10^{-10}\ C/m)$
single-ζ	*2.920*	*18.2*	*2.717*
single-ζ polarized	*3.085*	*13.6*	*2.885*
double-ζ polarized	*3.138*	*12.1*	*-*

Table 4. 4. Calculated piezoelectric coefficients within the relaxed- and clamped-ion approaches for basis sets considered in this subsection and the error for the relaxed-ion approach compared to 3.57pC/cm from [22].

Before studying the dynamics of the system we have computed the macroscopic polarization for each state. The longitudinal strain profile is not constant, as it is clear from Fig. 4. 15, due to the constraint imposed to all atomic coordinates. The polarization change is computed taking as a reference value the polarization for the non-compressed and flat case. Fig. 4. 20 shows the polarization change, ΔP_x, for the five different compressive strains considered in Fig. 4. 17:

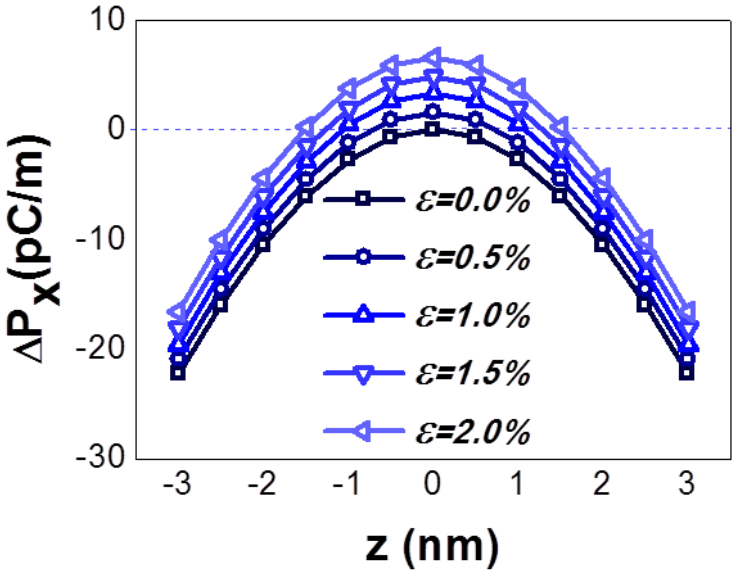

Fig. 4. 20. Polarization change along the *x*-direction as a function of the out-of-plane displacement, *z*. The effect of compressing seems to affect mainly in a shift towards higher ΔP. The capability of transducing the mechanical energy to a electrical domain depends on the polarization variations, $d(\Delta P)/dz$, thus, shifting the polarization curve does not affect the transduction capability.

The macroscopic polarization is computed for all considered out-of-plane displacements, *z*. The different curves corresponding to each compressive strain fits in a bi-quadratic adjustment allowing to achieve an analytic expression for ΔP_x in terms of compression, ε, and displacement, *z*. All data are listed in Table 4. 5:

ε (%)	$P_4(C/m/Å^4)$	$P_2(C/m/Å^2)$	$P_0(C/m)$
0.00	$3.090 \cdot 10^{-18}$	$-2.751 \cdot 10^{-14}$	0.0
0.50	$3.165 \cdot 10^{-18}$	$-2.782 \cdot 10^{-14}$	$1.593 \cdot 10^{-12}$
1.00	$3.205 \cdot 10^{-18}$	$-2.824 \cdot 10^{-14}$	$3.277 \cdot 10^{-12}$
1.50	$3.345 \cdot 10^{-18}$	$-2.842 \cdot 10^{-14}$	$4.791 \cdot 10^{-12}$
2.00	$3.399 \cdot 10^{-18}$	$-2.878 \cdot 10^{-14}$	$6.616 \cdot 10^{-12}$

Table 4. 5. Coefficients of the bi-quadratic fit of the macroscopic polarization for different compression values.

The bi-quadratic fit allows to track the dependence of the three coefficients P_4, P_2 and P_0, with the applied compressive strain as follows:

$$P_x^{2D} = P_x^{2D}(z, \varepsilon) = P_4(\varepsilon) \cdot z^4 + P_2(\varepsilon) \cdot z^2 + P_0(\varepsilon) \quad (4.23a)$$

$$P_4(\varepsilon) = 1.596 \cdot 10^{-19}\varepsilon + 3.081 \cdot 10^{-18} \quad (4.23b)$$

$$P_2(\varepsilon) = -6.280 \cdot 10^{-16}\varepsilon - 2.753 \cdot 10^{-14} \quad (4.23c)$$

$$P_0(\varepsilon) = 3.286 \cdot 10^{-12}\varepsilon \quad (4.23d)$$

The functional dependence with the compression only applies a linear shift to P_x^{2D}.

To validate the obtained macroscopic polarizations, a comparison with the results from [22] is carried out. The target of the publication is to characterize an unusual flexoelectric effect on h-BN under certain conditions concerning the chosen chirality of the particular ribbon under study. The main achievement is a characterization of the generated macroscopic polarization of a *l*-long h-BN sheet under sinusoidal deformation along the *z*-axis with amplitude *A* of the kind of:

$$u_z(\vec{r}) = A \cdot sin\left(\vec{k} \cdot \vec{r} + \varphi\right) \quad (4.24)$$

Similar to the deformation expressed on equation 4. 24 where *A* is related to the out-of-plane displacement, *z*, and φ=0. $\vec{k}$ is the undulation wave vector and $\vec{r}$ the in-plane vector. In its most general expression u_z expresses the deformation profile for deformations along whatever direction from arm-chair to zigzag chirality. θ=0 corresponds to a wave vector parallel to an arm-chair chirality and for this case, which is the one of interest for this work, the polarization is demonstrated to be well fitted with the following expression:

$$\vec{P}_k = \alpha\varepsilon_{\parallel}\left[\vec{e}_{\parallel}\left(1-\frac{3}{2}\varepsilon_{\parallel}\right)\right] \tag{4.25}$$

Where α is the piezoelectric constan, $\varepsilon_{\parallel} = \frac{A^2k^2}{4}$ the net film stretching along $\vec{k}$ due to the deformation and $\vec{e}_{\parallel}$ stands for the director vector parallel to $\vec{k}$. For the particular case of the h-BN ribbons considered along this thesis we set $\vec{e}_{\parallel} = \vec{e}_x$. Then the polarization is reduced to have only a component different to zero along the *x*-axis with no unusual flexoelectric contribution:

$$P_x = \alpha\frac{A^2k^2}{4}\left(1-\frac{3}{2}\frac{A^2k^2}{4}\right) \tag{4.26}$$

With the aim of comparing the present results with these from [22] a $|\vec{k}| = \pi/l$ is considered and $\Delta P_x/2$ is calculated for different amplitudes, A. Fig. 4. 21 shows a graphic comparison between the data from [22] and the polarization obtained in this work considering zero compressive strain, ε=0.

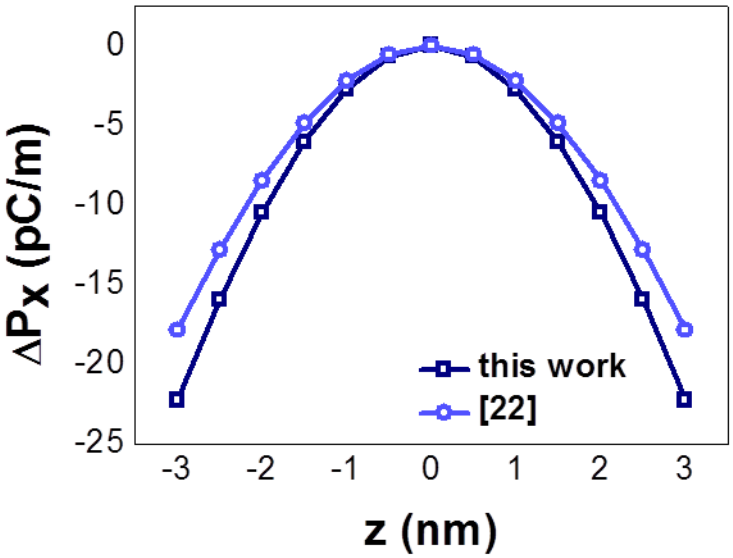

Fig. 4. 21. A good agreement is achieved between the calculated polarization change and the phenomenological expression from [22].

Comparing the coefficients accompanying the amplitude of the deformation, A, of equation 4. 26 with the coefficients P_2 and P_4 from Table 4. 5 for the case where no compression is applied we can extract the related piezoelectric coefficient:

$$\frac{\pi^2}{\lambda^2}\cdot e_{11}^{(2nd\ order)} = 2.753\cdot 10^{-14} \Rightarrow e_{11}^{(2nd\ order)} \sim 3.224\cdot 10^{-10}\ (C/m) \quad (4.27)$$

$$\frac{3}{2}\frac{\pi^4}{\lambda^4}\cdot e_{11}^{(4th\ order)} = 3.081\cdot 10^{-18} \Rightarrow e_{11}^{(4th\ order)} \sim 3.208\cdot 10^{-10}\ (C/m) \quad (4.28)$$

Almost a perfect match is achieved although the value is higher than the reported in Table 4. 4 for the clamped-ion approach, e_{11}=2.885·10^{-10} C/m, however both values coincide with this extracted from considering the polarization values from Fig. 4. 20 corresponding to a zero out-of-plane displacement, *z*:

ε (%)	***strain***	$\Delta \boldsymbol{P}_{\boldsymbol{x}}^{(\mathbf{0})}(\boldsymbol{C/m})$
0.00	**0.000**	$\mathbf{0.000}$
0.50	**0.005**	$\mathbf{1.61\cdot 10^{-12}}$
1.00	**0.010**	$\mathbf{3.29\cdot 10^{-12}}$
1.50	**0.015**	$\mathbf{4.81\cdot 10^{-12}}$
2.00	**0.020**	$\mathbf{6.63\cdot 10^{-12}}$

Table 4. 6. Macroscopic polarization for the flat configurations (zero out-of-plain deformation) for different compression values.

From the data shown in Table 4.6 the piezoelectric coefficient can be computed by considering only zero out-of-plane configurations: e_{11}~3.26·10^{-10}C/m, very close to this from equation 4. 27 and 4. 28. The mismatch (~10%) is attributed to the effects of the clamped ends of the suspended structure.

Therefore, the standard approach of computing the generated voltage across the piezoelectric material through the standard piezoelectric constants does not apply as it is defined as the derivative of the polarization respect the strain: in the present situation we are dealing with a strain gradient. The following lines aim to explain the approach followed in this work.

Dynamics and electric power—— The second coupled equation of 2. 45 relates the time evolution of the voltage across the resistive load, *R*, with the time evolution of the voltage across the piezoelectric itself. The piezoelectric voltage was considered to be

proportional to the displacement of the center of the ribbon, z, and the piezoelectric constant, e_{11}.

$$V_p = const \times e_{11} \cdot z \Longrightarrow \frac{dV_p}{dt} \propto \left(\frac{\partial P_z}{\partial \varepsilon_x}\right) \cdot \dot{z} \qquad (4.29)$$

In the present case these expressions cannot be applied due to the non-linear contributions of the polarization of equation 4. 27a and then we introduce directly the polarization across the piezoelectric into the dynamic equation treating the h-BN structure as a capacitor. Therefore, taking into account that $Q=C_p \cdot V_p$ and $P=Q/w$, the ribbon is electrically compared to an infinity parallel wire capacitor with capacitance equal to:

$$C_p = \frac{\pi\epsilon\epsilon_0}{Ln\left(l_q/r_q\right)} \cdot w \qquad (4.30)$$

Where l_q is the separation between the charged edges (the length of the ribbon), r_q is the effective radius of those states that can be approximated to be $r_q \sim a$, ϵ and ϵ_0 stand for the BN and vacuum electric permittivity respectively and w is the width of the ribbon. Therefore, the dependence of the voltage, V, and the 2D macroscopic polarization, P_x^{2D}, can be expressed as follows:

$$V_p = \frac{Ln\left(l_q/r_q\right)}{\pi\epsilon\epsilon_0} P_x^{2D} \qquad (4.31)$$

Then, the time derivative of equation 4. 29 is replaced by:

$$\dot{V_p} = \frac{Ln\left(l_q/r_q\right)}{\pi\epsilon\epsilon_0}\left(\frac{dP_x^{2D}}{dt}\right) = \frac{Ln\left(l_q/r_q\right)}{\pi\epsilon\epsilon_0}(4P_4(\varepsilon) \cdot z^3 + 2P_2(\varepsilon) \cdot z) \cdot \dot{z} \qquad (4.32)$$

And the second coupled equation 4. 45 can be expressed as:

$$\dot{V} = \frac{Ln\left(l_q/r_q\right)}{\pi\epsilon\epsilon_0}(4P_4(\varepsilon) \cdot z^3 + 2P_2(\varepsilon) \cdot z) \cdot \dot{z} - \frac{V}{RC} \qquad (4.33)$$

In order to evaluate the power dissipated through the resistor R, numerical simulations are carried out. As it was the case for graphene, the quality factor determining the viscous damping of the system is left as a free parameter. The main results from the simulations are shown in the following figures considering Q=100 and R=0.24 MΩ,

which is the calculated optimal value that maximizes the output power. The external force is described again by a WGN with F_{rms}=5 pN.

Fig. 4. 22 shows the dynamics of the structure for a period of time of 2 ns for three different compression values. As it was expected, there is a range of compressions that makes the system jump from one well to the other maximizing the amplitude of the trajectory implying an improvement of the generated polarization.

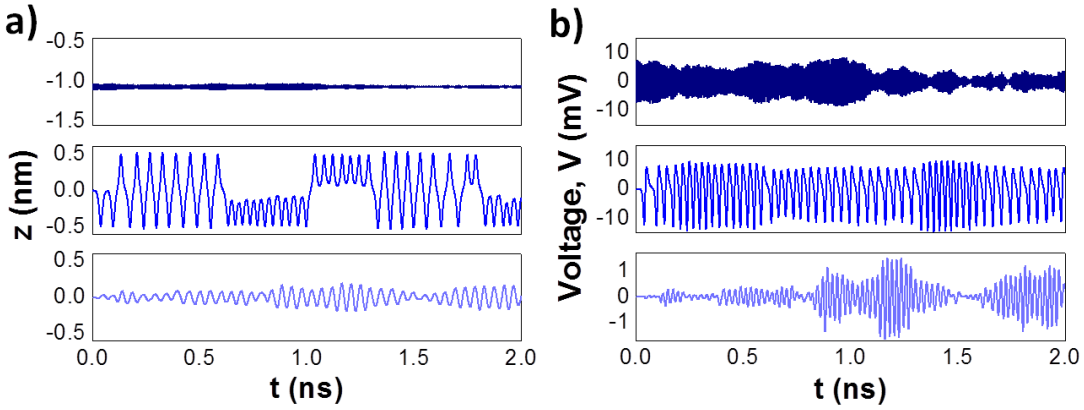

Fig. 4. 22. Obtained dynamics after solving the corresponding coupled stochastic differential equations. For ε=0 (bottom panels) show oscillations around z=0 generating a voltage of 1 mV at maximum. For moderate strains (middle panels) oscillations around minima combined with large excursions from one well to the other can be observed. The output voltage is increased almost in an order of magnitude (~10 mV) in comparison to the non-compressed configuration. For over-compressed configurations (upper panel) the system stuck in one of the two wells reducing drastically the amplitude of the oscillations. However, the generated voltage still shows a high value due to the bi-quadratic shape of ΔP_x showed on Fig. 4. 18. *Frms*=5 pN, Q=100, l x w = 17 nm x 1 nm.

The voltage across the load R corresponding to the trajectories of Fig. 4. 22a is shown in Fig. 4. 22b. A remarkable phenomena happens for the over-compressed case: although the system becomes confined in one of the two potential wells and its amplitude of movement is reduced in comparison to the case of optimal compression, the voltage amplitude keeps showing a high value that can be compared to that for the optimal compressed case. This is due to the bi-quadratic behavior of the macroscopic polarization, P_x^{2D}, shown before: a displacement amplitude of 5 Å around z=10 Å induces a polarization change of 2.7 pC/m approximately, while to achieve the same amount of polarization around z=0 an amplitude of 14 Å is needed. An amplitude almost three times larger is needed to generate the same output voltage.

The obtained output power as a function of the applied compression can be seen from Fig. 4. 23. The positions for the z_{rms} and P_{rms} peaks present almost a perfect match around ε~0.3%. The non-linear dependence of the macroscopic polarization with the out-of-plane displacement, z, makes the slope of the P_{rms} for $\varepsilon>\varepsilon_{opt}$ much softer than it was for the case of graphene or the system presented on chapter 3 and this broads significantly the range of compressions that lead an improvement in terms of electric power with respect to the non-compressed case. It is worth to note that the model for the piezoelectric transduction for graphene was extremely simple and, possibly, not

realistic. For the present case, the range of compressions that improves the response in terms of z_{rms} is around 0.2% while in terms of power it is extended to more than a 1%.

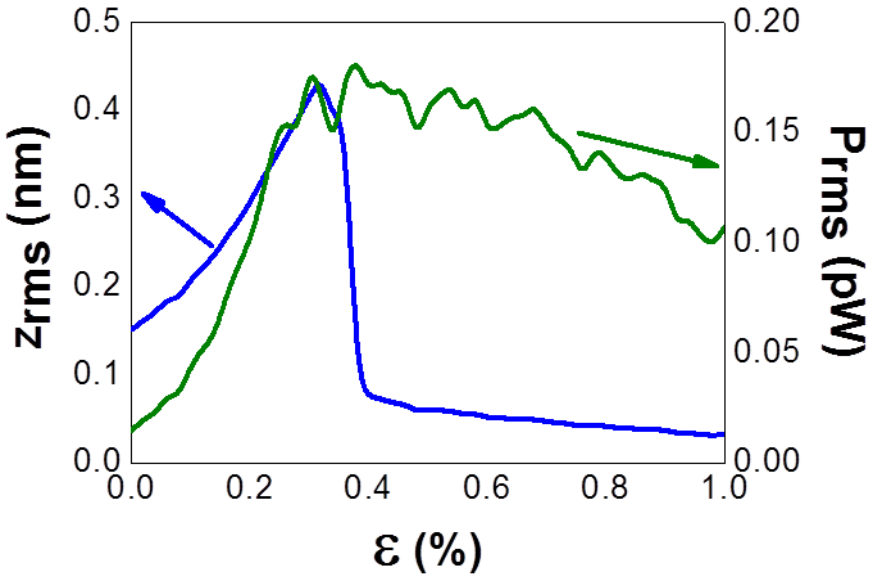

Fig. 4. 23. z_{rms} and P_{rms} as a function of the applied compressive strain. It can be seen a clear peak for z_{rms} around ε=0.3%. The maximum for the electric power is also reached around this strain value but the decreasing trend followed by P_{rms} after reaching the maximum is softer than this for the x_{rms}.

Thus, considering h-BN operating in the 11 mode not only makes easier the implementation of the transduction mechanism but also makes the system more robust and versatile. The lack of control in the tuning parameter (the distance d for the device studied in chapter 3, and the compressive strain ε during the present) is one of the drawbacks for the bi-stable strategy as it was pointed out during chapter 1. The results shown in Fig. 4. 23 paves the way to avoid the tuning problem, which seems to be not that dramatic as it was in previous reported cases.

4.4. MoS_2

Among other piezoelectric materials, MoS_2 is a very promising one due to the possibility of exfoliation for transferring to arbitrary substrates [23] forming mono-layered devices as the one here discussed. It is worth to note that this is not a one-atom thick material as the sulphur atoms, S, are displaced from the plane formed by the molybdenum atoms, Mo. The interest for this material has tremendously increased lately [24, 25] and a complete mechanical description is required. The mechanical and piezoelectric characterization for a 17 nm long cc-beam like structure is provided in this section.

As it was done for h-BN, a single-ζ polarized basis set is used for all calculations during this section including piezoelectric behavior which is also computed for a double-ζ polarized set.

Mechanical description—— For this material 6 atoms conform the rectangular unit cell. It consists of two molybdenum atoms and four sulphur atoms as it is showed on Fig. 4. 2. The optimized lattice constants are a~3.182 Ā and c~1.612 Ā, in good agreement with publications [26].

Fig. 4. 24 show the elastic potential energy for the ribbon as a function of the out-of-plane displacement, z, for different compression values, ε, ranging from 0 up to 2%. As it is clear from these curves compressive strain does not favor a buckled configuration for MoS_2 even for the maximum compression value. This means that a mono-layer of this material prefers to absorb the stress rather than relax it modifying the non-compressed rest state. Moreover, the only effect of compression is a soft stiffening of the mechanical response which is a non-intuitive feature not sheared by the other two studied cases where a softening of the structure was observed. The energies calculated for small displacements, from 0 to 20 Ā, are surprisingly similar for all compressions.

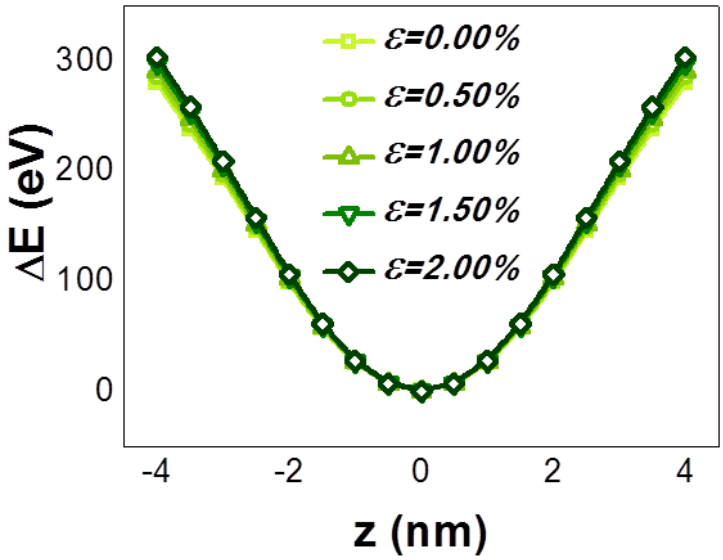

Fig. 4. 24. Elastic potential energy as a function of the out-of-plane displacement, z. No buckling is achieved for this particular geometry even for the larger compression values.

In contrast to what happens with graphene and h-BN, the potential energy for small displacements can be adjusted by a second order polynomial function recovering the linear resonator-like shape. However, a bi-quadratic description is required to fit well the data for all the displacement range. Table 4. 7 lists the value of the polynomial coefficients:

$\varepsilon\,(\%)$	$p_4(eV/Å^4)$	$p_2(eV/Å^2)$
0.00	$-5.796 \cdot 10^{-5}$	**0.2669**
0.50	$-5.879 \cdot 10^{-5}$	**0.2718**
1.00	$-5.991 \cdot 10^{-5}$	**0.2773**
1.50	$-6.100 \cdot 10^{-5}$	**0.2830**
2.00	$-6.203 \cdot 10^{-5}$	**0.2886**

Table 4. 7. Coefficients of the bi-quadratic fit of the elastic potential energy for different compression values.

$$E = E(z,\varepsilon) = p_4(\varepsilon)\cdot z^4 + p_2(\varepsilon)\cdot z^2 \qquad (4.34a)$$

$$p_4(\varepsilon) = -0.207\cdot 10^{-5}\varepsilon - 5.787\cdot 10^{-5} \qquad (4.34b)$$

$$p_2(\varepsilon) = 1.092\cdot 10^{-2}\varepsilon + 0.267 \qquad (4.34c)$$

Following the same procedure reported on subsection 4.1.2, the energies for flat configurations allow to obtain the Young modulus, *Y*, as shown in Fig. 4. 25.

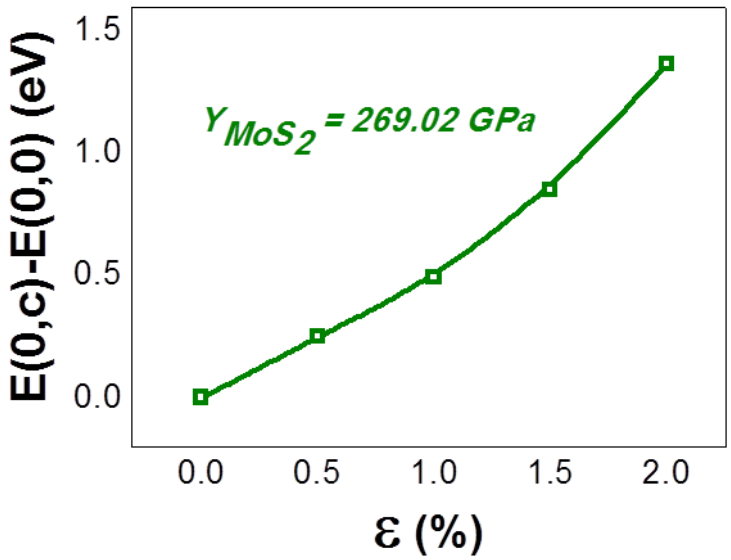

Fig. 4. 25. Calculation of the Young's modulus, *Y*, from *E(0,ε)* curve by direct differentiation respect the strain, *ε*. Considering an effective thicness of 3.2 Å the obtained value for MoS_2 is around 270 GPa.

The curve can be adjusted by an expression like $E=E_2\check{\varepsilon}^2+E_1\check{\varepsilon}$. Using equation 4. 18 we obtain an effective value for the Young modulus for MoS_2 of Y_{MoS_2}=269 GPa in very good agreement with previous publications [27]:

$$\Delta E_0 = E(0,\varepsilon) - E(0,0) = 3702.1828 \cdot \varepsilon^2 \ (eV) \qquad (4.35)$$

$$Y_{MoS_2} = 269.019 \ GPa \qquad (4.36)$$

Piezoelectric and flexoelectric description— Standard e_{11} piezoelectric coefficient is computed following the same procedure it is considered for the h-BN study, i.e. computing the generated polarization change under compressive and tensile in-plane stress. The obtained results for the two basis sets corresponding to the relaxed-ion approach are shown in Fig. 4. 26.

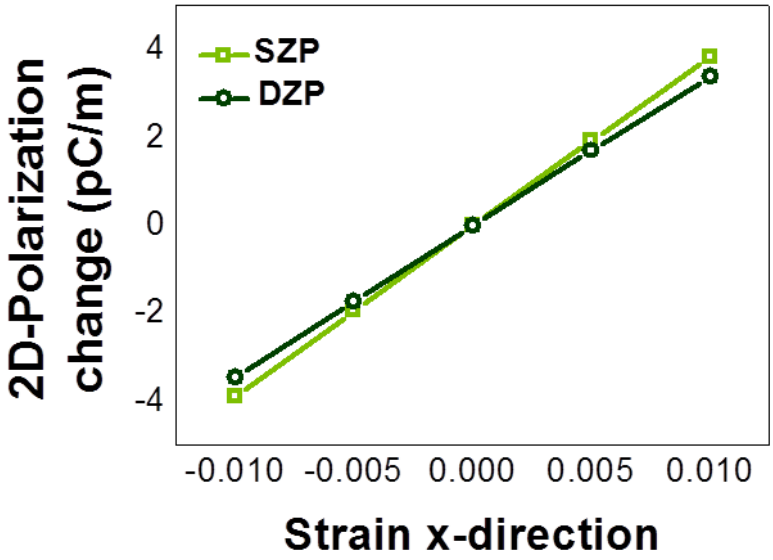

Fig. 4. 26. Polarization change under compressive and tensile stress along the *x*-direction (arm chair) for two different basis sets. Piezoelectric coefficients are directly derived from the slope of $\Delta P(\varepsilon)$. For the purposes of this work only the 11 mode is considered.

In Table 4. 8 the piezoelectric coefficients for the two basis sets considering the clamped and relaxed-ion approaches are listed. The obtained results are compared to those obtained in [26]:

	Relaxed-ion		Clamped-ion	
Basis set	e_{11} $(10^{-10}\ C/m)$	**Error (%) [26]**	e_{11} $(10^{-10}\ C/m)$	**Error (%)**
single-ζ polarized	*3.87*	*6.3*	*3.81*	*24.5*
double-ζ polarized	*3.43*	*5.7*	*3.47*	*13.4*

Table 4. 8. Calculated piezoelectric coefficients within the relaxed- and clamped-ion approaches for the basis sets considered in this subsection and the error compared to 3.64 pC/cm and 3.06 pC/cm respectively from [26].

As it was done in the two previous cases, h-BN and graphene, a computational super-cell of 39 x 1 is considered giving a ribbon of approximately 215 Ā total length. Considering the clamped ends of the suspended structure formed by 4 unit cells each gives a 17 nm long suspended ribbon.

The polarization along the *x*-direction has been computed for all considered configurations as it was done for h-BN. The resulting macroscopic polarizations can be seen from Fig. 4. 27 where a similar behavior to what was achieved for h-BN is observed:

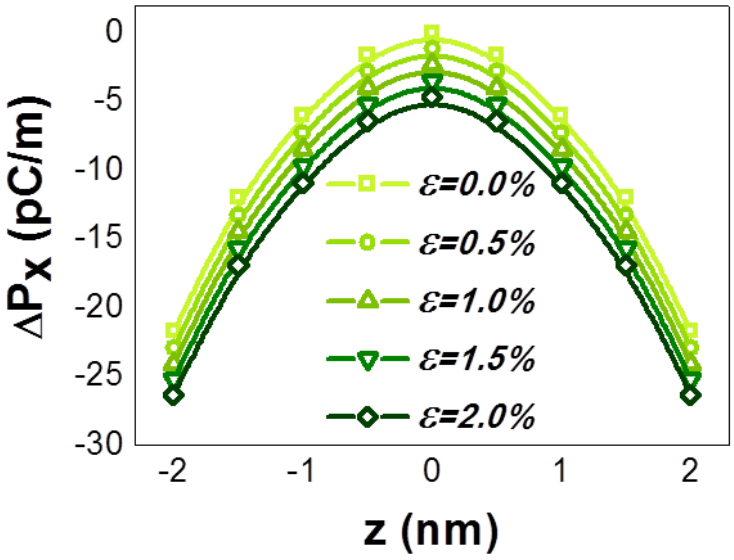

Fig. 4. 27. Polarization change along the *x*-direction as a function of the out-of-plane displacement, *z*. The effect of compressing seems to affect mainly, as it was the case for h-BN, in a shift towards lower *ΔP*.

The main difference with respect to the results previously reported is the higher slopes the curves present. As it was presented before, MoS_2 has a greater piezoelectric constants and this leads to greater changes in the polarization under a certain deformation, *z*.

ε (%)	$P_4(C/m/Å^4)$	$P_2(C/m/Å^2)$	$P_0(C/m)$
0.00	$6.057 \cdot 10^{-18}$	$-5.442 \cdot 10^{-14}$	0.0
0.50	$4.456 \cdot 10^{-18}$	$-5.543 \cdot 10^{-14}$	$-1.367 \cdot 10^{-12}$
1.00	$5.197 \cdot 10^{-18}$	$-5.578 \cdot 10^{-14}$	$-2.541 \cdot 10^{-12}$
1.50	$7.078 \cdot 10^{-18}$	$-5.633 \cdot 10^{-14}$	$-3.722 \cdot 10^{-12}$
2.00	$8.304 \cdot 10^{-18}$	$-5.659 \cdot 10^{-14}$	$-4.915 \cdot 10^{-12}$

Table 4. 9. Coefficients of the bi-quadratic fit of the macroscopic polarization for different compression values.

Following the steps done for the h-BN case, data listed in Table 4.9 can be well described through a polynomial fit. The macroscopic polarization is expressed as a function of the compression and the out-of-plane displacement as:

$$P_x^{2D} = P_x^{2D}(z, \varepsilon) = P_4(\varepsilon) \cdot z^4 + P_2(\varepsilon) \cdot z^2 + P_0(\varepsilon) \quad (4.37a)$$

$$P_4(\varepsilon) = 1.423 \cdot 10^{-18}\varepsilon - 4.795 \cdot 10^{-18} \quad (4.37b)$$

$$P_2(\varepsilon) = -1.048 \cdot 10^{-15}\varepsilon - 5.466 \cdot 10^{-14} \quad (4.37c)$$

$$P_0(\varepsilon) = -2.437 \cdot 10^{-12}\varepsilon \quad (4.37d)$$

The same treatment it was done on section 4.1.2 with the polarization change for a h-BN ribbon (see equation 4. 26) is here applied comparing the results the model from [22] would achieve and the curves here presented for the MoS_2 ribbon. This is shown in Fig. 4. 28.

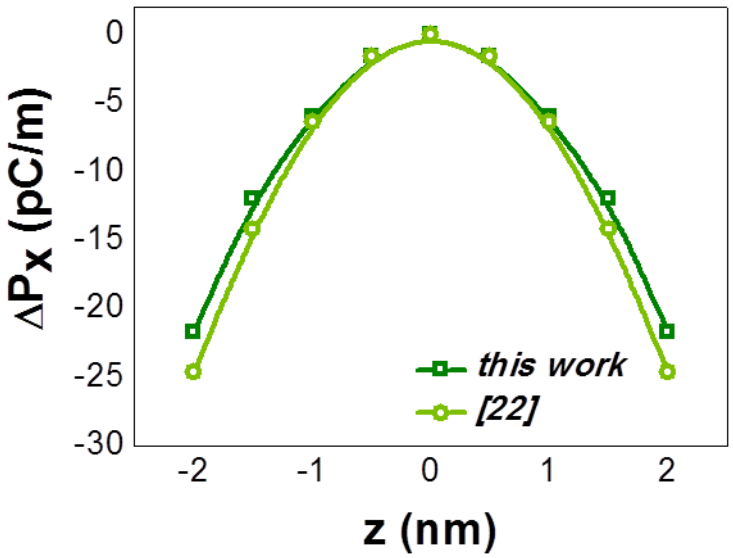

Fig. 4. 28. A good agreement is achieved between the calculated polarization change and the phenomenological expression from ref [22] applied to MoS_2.

A good agreement is achieved even fo11.r this material. Equations 4. 27 and 4. 28 are written in this case as:

$$\frac{\pi^2}{\lambda^2}\cdot e_{11}^{(2nd\ order)} = 5.466\cdot 10^{-14} \Rightarrow e_{11}^{(2nd\ order)} \sim 6.402\cdot 10^{-10}\ (C/m) \qquad (4.38)$$

$$\frac{3}{2}\frac{\pi^4}{\lambda^4}\cdot e_{11}^{(4th\ order)} = 4.795\cdot 10^{-18} \Rightarrow e_{11}^{(4th\ order)} \sim 4.385\cdot 10^{-10}\ (C/m) \qquad (4.39)$$

Dynamics and electric power— Bi-stability allows to achieve higher displacements when the optimal compression value, ε_{opt}, is reached. However, for MoS_2 it seems that a buckled induced bi-stable configuration is not achievable, at least for the considered dimensions, so it is not possible to produce oscillations around a z providing greater polarization changes traduced to higher output power. Instead of that an intrinsic higher slope for the ΔP_x curves can be explored to be an advantage respect other materials under certain conditions. Comparing equations 4. 23d and 4. 37d it can be seen that for a given variation in the out-of-plane displacement would generate a greater polarization variation for MoS_2, which is quite intuitive taking into account that the piezoelectric effect is stronger for MoS_2 than for h-BN. However, due to the stiffness of the MoS_2 ribbon it is easier to induce a given deformation to the h-BN ribbon.

Fig. 4. 29 shows an extract of the dynamics for a MoS_2 ribbon under the action of an external force equal to which was considered for the dynamics study for h-BN, i.e. F_{rms}=5 pN:

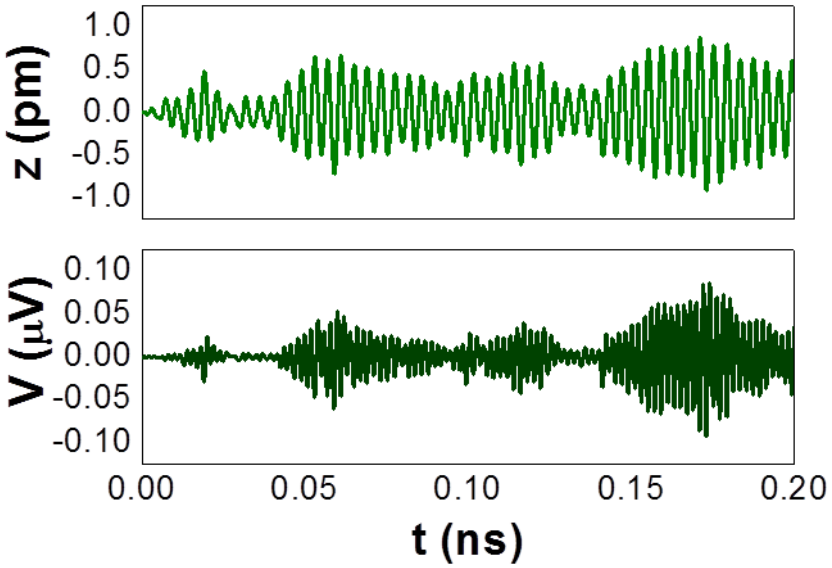

Fig. 4. 29. Obtained dynamics after solving the corresponding coupled stochastic differential equations. Only ε=0 is considered showing oscillations around z=0 with a maximum amplitude of 0.5 pm. A voltage of 0.1 μV at maximum is achieved which means that the higher piezoelectric response of MoS_2 compared to this for h-BN does not compensates the rigidity of the structure. *Frms*=5 pN, Q=100, l x w = 17 nm x 1 nm.

The maximum amplitude of vibration achieved is around 0.5 pm, largely below the 2 Ā afforded in the h-BN study for the non-compressed configuration. A reduction in two orders of magnitude of the displacement is translated into a decrease in the output voltage of more than four orders of magnitude due to the nonlinear dependence between the voltage, V, and the displacement, z.

It is worth to note that a greater piezoelectric effect as it is shown by MoS_2 in comparison to h-BN is an advantage even in the light of the results reported in this work. It is assumed that the impossibility of inducing bi-stability to the structure and the extreme stiffness of the system are due to the particular size it has been considered. Further calculations with large structures (beyond the computational capabilities of a DFT-based approach) should be taken into account in order to compare the throughput between different materials using, for instance, an empiric potential approach. At this point many parameters play an important role such as the specific dimensions or the piezoelectric response, and each one need to be analyzed to find the best strategy for each specific application.

4.5. Conclusions

In this chapter a full description of 2D-materials based bi-stable NEMS has been provided regarding graphene, h-BN and MoS_2. The computation of the elastic potential energy allows to describe the systems in terms of a punctual-mass system with coordinate *z*. The piezoelectric and flexoelectric description is carried out to include the possibility of using these materials as transducers. This fact would simplify the fabrication procedure as the structure acts as mechanical and electric transducer at the same time. Moreover, the flexoelectric effect some materials present enhances the throughput as the range of compressions that increases the output power is notably broadened.

From the experimental point of view, the procedure followed for the fabrication of suspended graphene ribbons is reported although further work must be done in order to reproduce the results obtained along this chapter. However, the fabrication procedure represents a novel approach to obtain sets of identical graphene resonators.

References

[1] Soler, José M., et al. "The SIESTA method for ab initio order-N materials simulation." *Journal of Physics: Condensed Matter* 14.11 (2002): 2745.

[2] King-Smith, R. D., and David Vanderbilt. "Theory of polarization of crystalline solids." *Physical Review B* 47.3 (1993): 1651.

[3] Hod, Oded, Juan E. Peralta, and Gustavo E. Scuseria. "Edge effects in finite elongated graphene nanoribbons." *Physical Review B* 76.23 (2007): 233401.

[4] Bunch, J. Scott, et al. "Electromechanical resonators from graphene sheets." *Science* 315.5811 (2007): 490-493.

[5] Garcia-Sanchez, Daniel, et al. "Imaging mechanical vibrations in suspended graphene sheets." *Nano letters* 8.5 (2008): 1399-1403.

[6] Shivaraman, Shriram, et al. "Free-standing epitaxial graphene." *Nano letters* 9.9 (2009): 3100-3105.

[7] Eichler, A., et al. "Nonlinear damping in mechanical resonators made from carbon nanotubes and graphene." *Nature nanotechnology* 6.6 (2011): 339-342.

[8] Neto, AH Castro, et al. "The electronic properties of graphene." *Reviews of modern physics* 81.1 (2009): 109.

[9] Lee, Changgu, et al. "Measurement of the elastic properties and intrinsic strength of monolayer graphene." *science* 321.5887 (2008): 385-388.

[10] Hod, Oded, and Gustavo E. Scuseria. "Electromechanical properties of suspended graphene nanoribbons." *Nano letters* 9.7 (2009): 2619-2622.

[11] Traversi, Floriano, et al. "Elastic properties of graphene suspended on a polymer substrate by e-beam exposure." *New Journal of Physics* 12.2 (2010): 023034.

[12] Ni, Zhonghua, et al. "Anisotropic mechanical properties of graphene sheets from molecular dynamics." *Physica B: Condensed Matter* 405.5 (2010): 1301-1306.

[13] Naumov, Ivan, Alexander M. Bratkovsky, and V. Ranjan. "Unusual Flexoelectric Effect in Two-Dimensional Noncentrosymmetric sp^{2}-Bonded Crystals." *Physical review letters* 102.21 (2009): 217601.

[14] Reich, Stephanie, et al. "Tight-binding description of graphene." *Physical Review B* 66.3 (2002): 035412.

[15] Pozzo, Monica, et al. "Thermal expansion of supported and freestanding graphene: lattice constant versus interatomic distance." *Physical Review Letters* 106.13 (2011): 135501.

[16] Van Lier, Gregory, et al. "Ab initio study of the elastic properties of single-walled carbon nanotubes and graphene." *Chemical Physics Letters* 326.1 (2000): 181-185.

[17] Allen, Matthew J., Vincent C. Tung, and Richard B. Kaner. "Honeycomb carbon: a review of graphene." *Chemical reviews* 110.1 (2009): 132-145.

[18] Leland, Robert P. "Mechanical-thermal noise in MEMS gyroscopes." *Sensors Journal, IEEE* 5.3 (2005): 493-500.

[19] Bernardini, Fabio, Vincenzo Fiorentini, and David Vanderbilt. "Spontaneous polarization and piezoelectric constants of III-V nitrides." *Physical Review B* 56.16 (1997): R10024.

[20] Kern, G., G. Kresse, and J. Hafner. "Ab initio calculation of the lattice dynamics and phase diagram of boron nitride." *Physical Review B* 59.13 (1999): 8551.

[21] Song, Li, et al. "Large scale growth and characterization of atomic hexagonal boron nitride layers." *Nano letters* 10.8 (2010): 3209-3215.

[22] Naumov, Ivan, Alexander M. Bratkovsky, and V. Ranjan. "Unusual Flexoelectric Effect in Two-Dimensional Noncentrosymmetric sp^{2}-Bonded Crystals." *Physical review letters* 102.21 (2009): 217601.

[23] Liu, Keng-Ku, et al. "Growth of large-area and highly crystalline MoS2 thin layers on insulating substrates." *Nano letters* 12.3 (2012): 1538-1544.

[24] Radisavljevic, B., et al. "Single-layer MoS2 transistors." *Nature nanotechnology* 6.3 (2011): 147-150.

[25] Castellanos-Gomez, Andres, et al. "Single-Layer MoS2 Mechanical Resonators." *Advanced Materials* 25.46 (2013): 6719-6723.

[26] Duerloo, Karel-Alexander N., Mitchell T. Ong, and Evan J. Reed. "Intrinsic Piezoelectricity in Two-Dimensional Materials." *The Journal of Physical Chemistry Letters* 3.19 (2012): 2871-2876.

[27] Bertolazzi, Simone, Jacopo Brivio, and Andras Kis. "Stretching and breaking of ultrathin MoS2." *ACS nano* 5.12 (2011): 9703-9709.

CHAPTER 5

GRAPHENE NEMS FABRICATION

The fabrication of graphene-based electro-mechanical devices is a very active area nowadays as graphene is called to be the basis material for future electronics. Particularly, a lot of efforts have been done in order to fabricate and characterize graphene-based NEMS. Two different approaches represent the main strategies to achieve mono and bi-layer graphene structures: chemical-growth [1,2] and mechanical exfoliation [3], very common due to its simplicity. The work here presented is focused on the second approach, following standard exfoliation procedures from a primary graphite stack. A well-known drawback of this method is the low probability of achieving single-layer graphene flakes and the high shape variability they present from flake to flake. However, its simplicity makes it the most suitable approach for demonstrating proofs-of-concepts.

In the following lines it is presented the results achieved in the attempts to fabricate the device presented in section 4.2. The long term goal would be fabricating nanostructures able to validate the results discussed earlier. Although no results validating the dynamics obtained from the combination of atomistic calculations and numerical simulations have been achieved, it has been possible to develop a simple fabrication method capable to obtain large arrays of very regular and identical suspended graphene ribbons without requiring multiple post-processing steps. A characterization of the structures is also provided along this section.

5.1. Fabrication process

Very often, graphene flakes are deposited directly over a Si substrate with a SiO_2 layer. It is possible to determine the number of layers conforming a particular graphene flake by means of the color it presents under optical inspection. This was not achievable in the laboratory and, therefore, a different approach is considered.

The starting point is a standard p-type silicon substrate of 500 μm thick with a 20 nm/100 nm thick layer of chromium/gold. 950 K molecular weight PMMA (2% dissolved in anisole) is spun at 1500 rpm for 1 minute. After spinning the anisole solvent is removed by baking the sample at 180°C for 1 minute. The process is iterated three times in order to achieve a final PMMA thick of 300 nm. PMMA will be used as a sacrificial material as it will be explained below. The scheme of the resulting stack is showed in Fig. 5. 1a.

Mechanical exfoliation from a graphite stack is done following the standard procedure [3] peeling repeatedly to allow leaving thinner layers on one side of the scotch tape to be transferred. Usually the peeling process is repeated until few layers remain attached to the scotch tape to increase the relative number of mono and bi-layer graphene flakes transferred to a SiO_2 substrate: doing it this way some regions of the tape loss all the rests of graphene then exposing some adhesive parts. As PMMA is the outermost layer in the present case rather than SiO_2, the adhesive would pull out part of the Cr + Au + PMMA stack. Therefore, the peeling process is done in a manner that prevents to expose any adhesive part. Product of that is that some thick amorphous flakes are present in the sample. At this point the method used to transfer the graphene to the sample consists on putting the scotch tape against the PMMA surface dragging a spatula along a certain direction as it is depicted in Fig. 5. 1b. As it will be commented later on the dragging direction represents an important parameter in order to maximize the quality of the obtained graphene flakes.

A simple optical inspection of the sample on Fig. 5. 1c allows to determine the areas with higher density of graphene flakes.

In order to release the structures the PMMA is selectively exposed to a EBL process. Thanks to the well defined orientation of the transferred graphene flakes (see section 5.5) it is possible to perform the EBL process patterning the trenches perpendicular to the length direction of the obtained structures as shown in Fig. 5. 1d. Dipping the sample into a standard methyl isobutyl ketone/isopropyl alcohol developer allows to erase the exposed PMMA and obtaining suspended graphene structures of the type of a cc-beam. As it is shown in Fig. 5. 1e after releasing the PMMA the underlying gold layer becomes visible allowing the good contrast needed for SEM imaging.

Because of the direction of the EBL process, the trenches width determines the length of the suspended structures. Different trench widths have been considered, i.e. 100, 300, 500 and 600 nm.

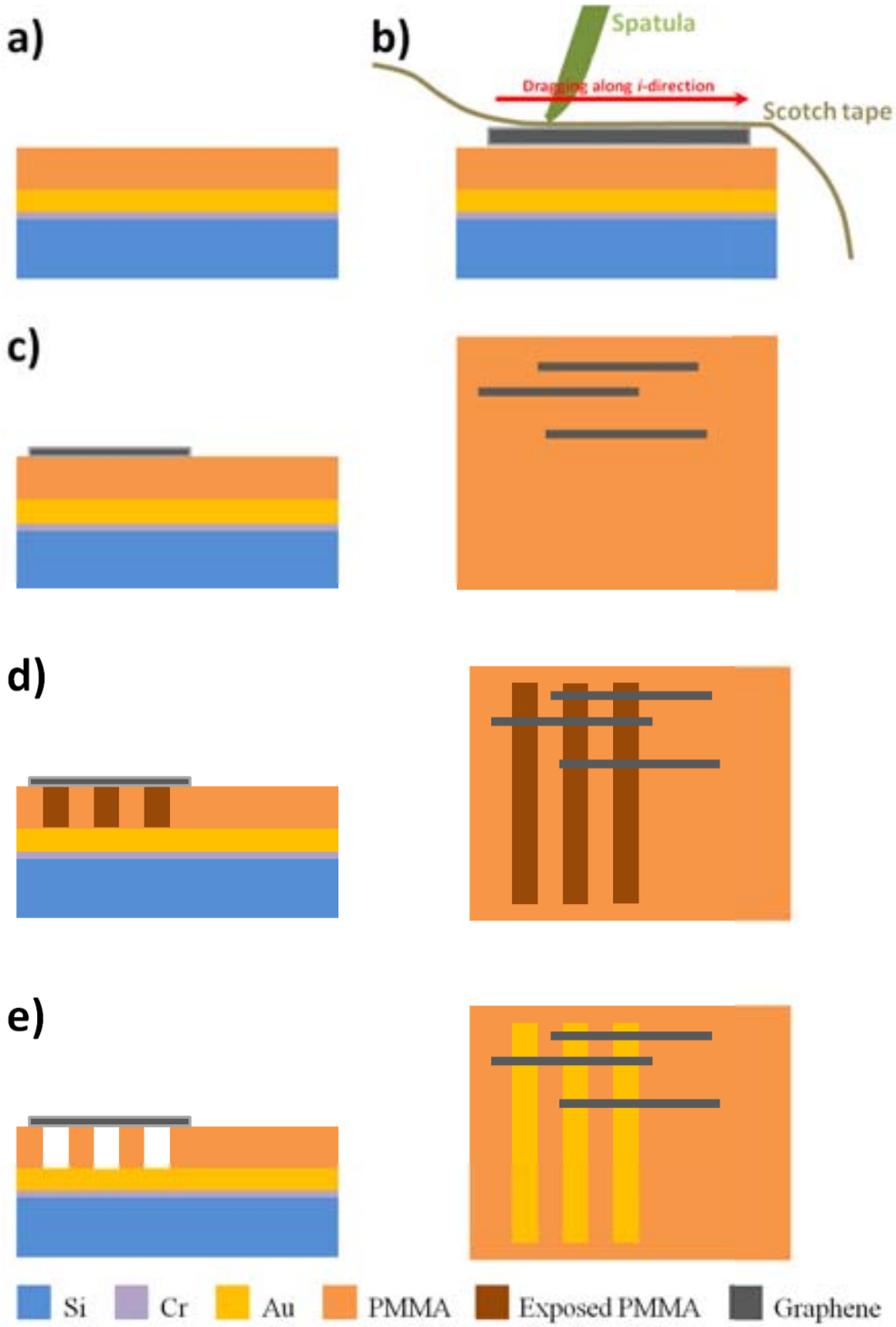

Fig. 5. 1. Scheme of the fabrication steps. (a) Initial Si/Cr/Au/PMMA stack. (b) graphene transfer by means of dragging a spatula in a certain *i*-direction. (c) Spacial disposition of the graphene flakes in the substrate. (d) EBL step exposing selectively some areas of PMMA. (e) After developing the exposed PMMA the graphene structures are suspended.

5.2. SEM characterization

The first step once graphene is transferred is to locate where the interesting ribbons are. Unfortunately, mono-layers are often difficult to see optically and SEM imaging is required for catch the detail. At any rate, optical inspection could be useful to localize non mono-layer graphene expecting mono-layer graphene to be around.
Fig. 5. 2 shows two SEM images of different samples with trenches (vertical strips) presenting widths of 500 nm, Fig. 5. 2a, and 100, 300 and 600 nm, Fig. 5. 2b. Different ribbons (defined as primary ribbons) containing each several suspended devices (defined as secondary ribbons) can be seen (horizontal structures). Therefore, graphene resonators have a length equal to the dug trenches. Both images were taken with a 60 deg tilting that provokes only the center of the image to be totally focused.

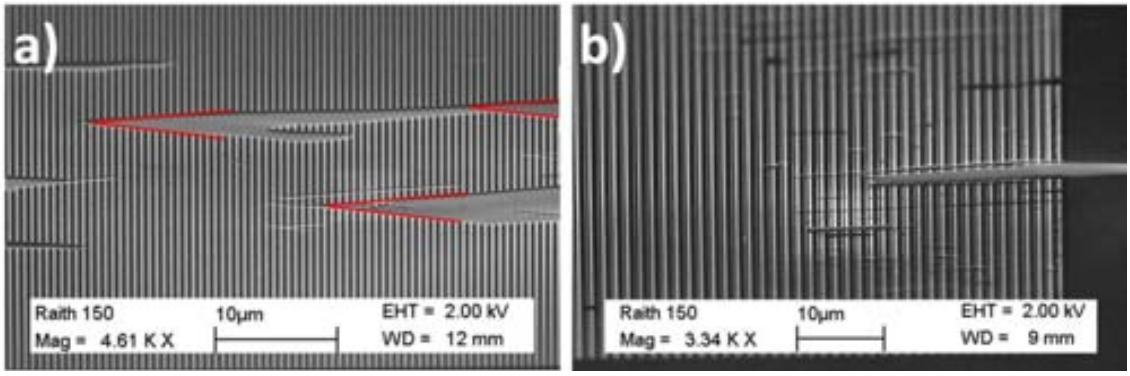

Fig. 5. 2. SEM images of two samples: (a) trenches of 500 nm width (vertical strips) define the length of the suspended graphene devices (horizontal structures). (b) trenches of 100, 300 and 600 nm are patterned achieving suspended ribbons with different lengths.

From Fig. 5. 2a several flakes can be seen with very varying shapes although there are some recurrent angles the edge of the flakes follow (30 deg approx.) which are highlighted with red solid lines. Around the lower highlighted angle a clearer square zone can be seen. It is due to the statically charging effect the SEM image at high energies provokes, as it was the case for the commented squared area. In Fig. 5. 2b it is shown at the right side a edge of the exposed area. Contrary to what happens in Fig. 5. 2a, the thinner ribbons are most and only one comparably larger flake is observed. Although from this it cannot be seen their edges it can be appreciated how all ribbons follow a certain direction which is taken as a reference for the orientation of the trenches in order to achieve a perpendicular position between them.

A more detailed SEM image of the suspended structures can be seen in Fig. 5. 3 corresponding to the same samples of Fig. 5. 2 showing a remarkably high shape regularity between secondary ribbons with almost constant width, w~[0.5 µm, 1.0 µm], and length, $l=w_{trench}$. Inevitably they differ between primary ribbons as a result from the transfer process.

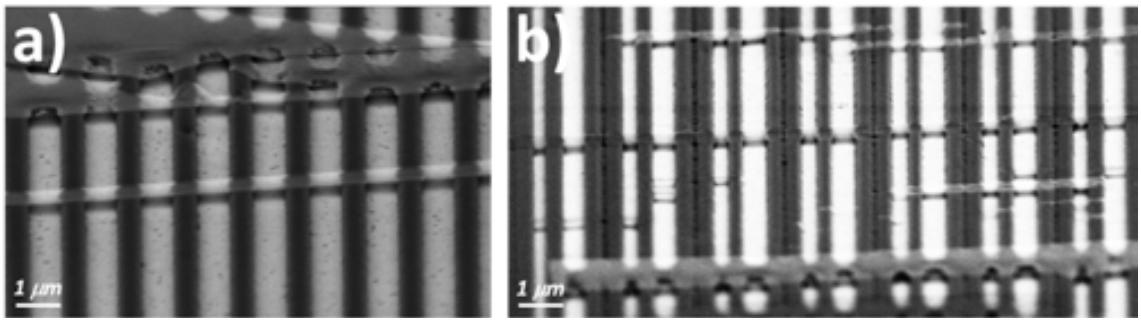

Fig. 5. 3. Detailed SEM image from the samples showed on Fig. 5. 2. (a) A primary ribbon containing a minimum of 9 secondary ribbons can be appreciated. Regardless of the inerent variability of shape between primary ribbons, a very regular shape can be seen for all secondary ribbons. (b) Several ribbons containing many secondary ribbons with different lengths can be seen.

Moreover, a single primary ribbon can contain from 2 up to 50 secondary ribbons, paving the way to a systematic study of graphene properties due to their high regularity. Looking at the larger structures commented before it can be seen that the wider the structure is the worse is the developing of PMMA under it. It prevents the ribbons to be released indicating there is a ratio between length and width which has to be overcome in order to achieve totally suspended structures. Dipping the sample in the developer alcohol for a longer period of time will probably solve the undercut problem; nevertheless it would provoke an ill defined shape of the PMMA walls.

Fig. 5. 4 shows a detail of the fabricated suspended ribbons with different lengths, where it can be seen that the structures are fully suspended: 500 nm for Fig. 5. 4a, 300 nm and 600 nm for those from Fig. 5. 4b. A narrower trench was patterned in the sample from Fig. 5. 4b but unfortunately they were not totally removed and no good contrast was achievable.

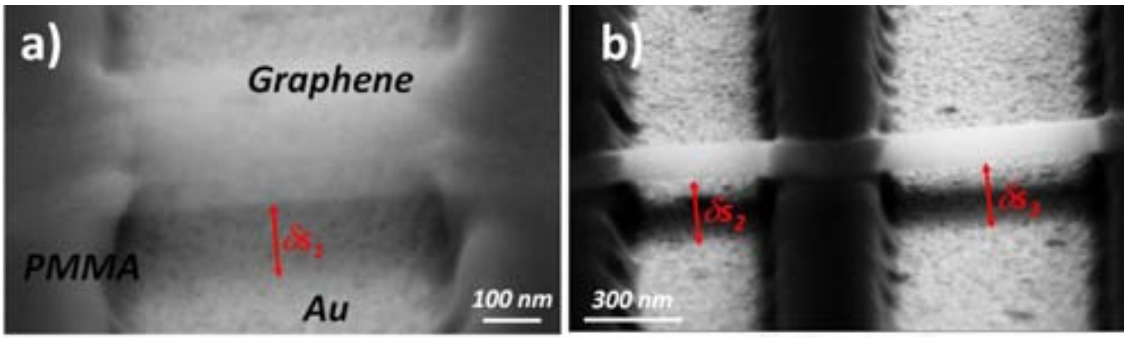

Fig. 5. 4. Detailed SEM image of the three different length devices.

In the introduction to this section the nominal value for the trenches height was said to be around 300 nm. Taking advantage of the 60 deg tilting of the sample and the electronic shadow it provokes, it is possible to measure approximately through geometric considerations the real height for the PMMA trenches. The procedure is depicted in Fig. 5. 5:

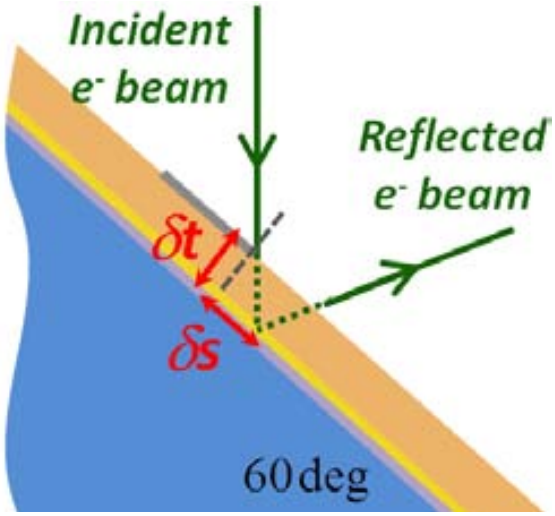

Fig. 5. 5. Scheme of the 60 deg tilted sample. δs can be measured from the SEM images showed in Fig. 5.4.

Hence, it follows that:

$$\delta t = \frac{\delta s}{tan(60)} \sim 0.577 \cdot \delta s \qquad (5.1)$$

Table 5. 1 lists the measured values for δs and the derived value for δt.

# ribbon	$\boldsymbol{\delta s}$ $(\boldsymbol{nm})$	$\boldsymbol{\delta t}$ $(\boldsymbol{nm})$
1	151	87
2	200	113
3	196	115

Table 5. 10. Deduced trenches height obtained from equation 5.1

The measured trench heights are considerably below the expected value. This fact could be ascribed to many causes, such as a lost of purity in the PMMA which seems to be the most probable. The objective of depositing a 300 nm thick PMMA layer is to prevent the collapse of the graphene devices over the gold layer due to superficial tension or van der Waals interactions. Although this mismatch between the measured and expected values, the structures are fully suspended and only a negligible reduction of the distance between the structures and the gold layer is achieved.

5.3. Raman spectroscopy characterization

Raman spectroscopy has been successfully utilized as a convenient technique for identifying and counting graphene layers on different substrates [4,5]. It was shown that the evolution of the 2D-band Raman signatures with the addition of each extra layer of graphene can be used to accurately count the number of layers [4] together with the position of G peak, which up-shifts with the increasing $1/n$, where n is the number of graphene layers [6].

The quality and number of layers of the suspended graphene ribbons were evaluated by Micro-Raman spectroscopy using a Jobin-Yvon T64000 with a liquid N_2-cooled CCD detector and the 514 nm excitation wavelength at low power levels to avoid laser heating and subsequent degradation of PMMA and graphene.

Fig. 5. 6a shows the Raman spectra for graphite (dark gray line), mono- and bi-layer graphene (light grey and blue lines respectively) and PMMA (orange line). The laser spot used for this study was around 1 μm diameter and, because of the width of the explored mono- and bi-layer ribbons, some contribution from the gold layer exposed in the deep of the trenches can distort the results for these two cases. For the single layer case the G band peak, ω_G^{1L}=1584±2 cm^{-1}, is less intense than this for the bi-layer, ω_G^{1L}=2182±2 cm^{-1} as it is expected with a ratio of around $\frac{i_G^{1L}}{i_G^{2L}}$~0.9. Fig. 5. 6b show the detail of the 2D peaks which represent the most used characteristic to discern from mono- and multi-layered graphene: mono-layered graphene show a simple peak while bi-layered graphene, as it happens with the rest of multi-layered cases, show a multiple peak.

Number of layers	**G band intensity, i_G (a.u.)**	**2D band intensity, i_G (a.u.)**
1	***1465***	***1846***
2	***1591***	***1379***

Table 5. 2. Measured peaks height for the G and 2D band expressed in arbitrary units.

Moreover, the 2D peak is more intense for a mono-layer than that for a bi-layer ribbon as discussed in the literature. The concrete values of the intensities of both peaks for the two reported cases can be seen from Table 5. 2.

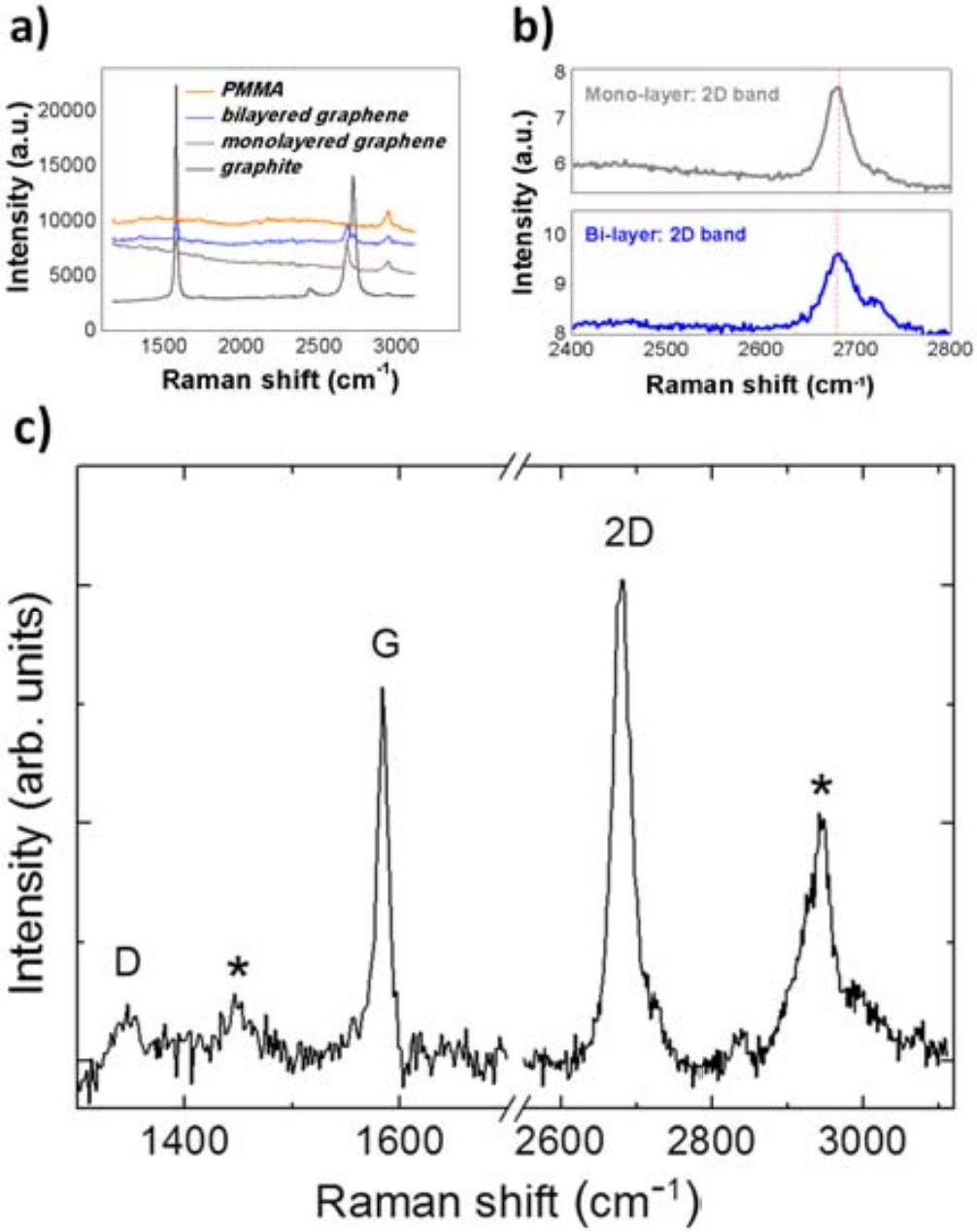

Fig. 5. 6. Raman spectrums of: (a) PMMA (orange line), bi-layered graphene (blue line), mono-layered graphene (light gray line) and graphite (dark grey line), (b) the 2D band comparing the contribution to this for a mono-layered ribbon (top panel) and a bi-layered ribbon (bottom panel), (c) a mono-layered ribbon showing a higher peak height for the 2D band than this for the G band. The marked peaks (*) are Raman modes from the PMMA layer.

Fig. 5. 6 show the results of a suspended monolayer graphene with a sharp G band (~1584 cm^{-1}) and 2D band (~2690 cm^{-1}) peaks and a low G/2D ratio. The single layer nature of the graphene ribbon is further confirmed by the full with at half maximum (FWHM) of the Lorentz fit of the 2D band being ~30 cm^{-1}. The small D peak (~1350 cm^{-1}) intensity indicates that the graphene has low defect density. The peaks marked with a star (*) are originated in the PMMA layer [7] also excited with the incident laser radiation.

5.4. AFM characterization

A AFM study has been carried out in order to have a deeper knowledge of the topography of the fabricated devices. Non-contact mode is considered to avoid sample damaging.

Fig. 5. 7a shows a topography image of the devices previously studied by SEM on Fig. 5. 2 (a) 5. 3 (a) and 5. 4 (a). As it can be appreciated, the primary ribbon contains more than 20 secondary ribbons with very sharp and regular widths.

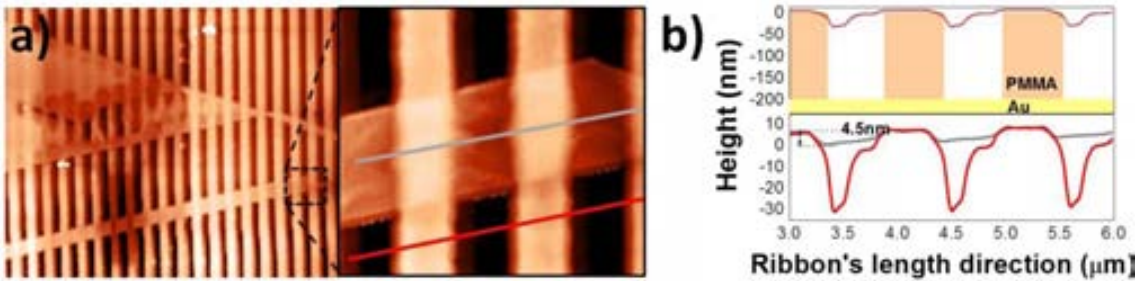

Fig 5. 7. (a) Topographic AFM images of the 500 nm long secondary ribbons. (b) Upper panel: height profile along the red line from (a) superposed to the expected PMMA trench profile. Lower panel: height profiles for both red and grey lines from (a) showing the suspension of the fabricated devices. Graphene adhesion to the walls can be appreciated.

The zoom showed on the right side of Fig. 5. 7a shows a more detailed topographic image revealing some corrugations on the suspended parts. These corrugations are in the range of less than 1 nm. Fig. 5. 7b show the height profile along the grey and red solid lines drawed on Fig. 5. 7a. In the upper panel the measured trenches profile (red line) can be seen compared to the expected height revealing a strong mismatch between them. Moreover, the measure show some irregularities in the shape of the walls. Both fenomena can be regarded to a lack of vertical resolution due to the dimensions of the AFM-cantilever's tip. The lower panel shows the profile along the studied primary ribbon superimposed to this for the trenches. It also shows an approximately 4.5 nm deep nanoindentation to the PMMA walls, which is a very low value compared to the device length.

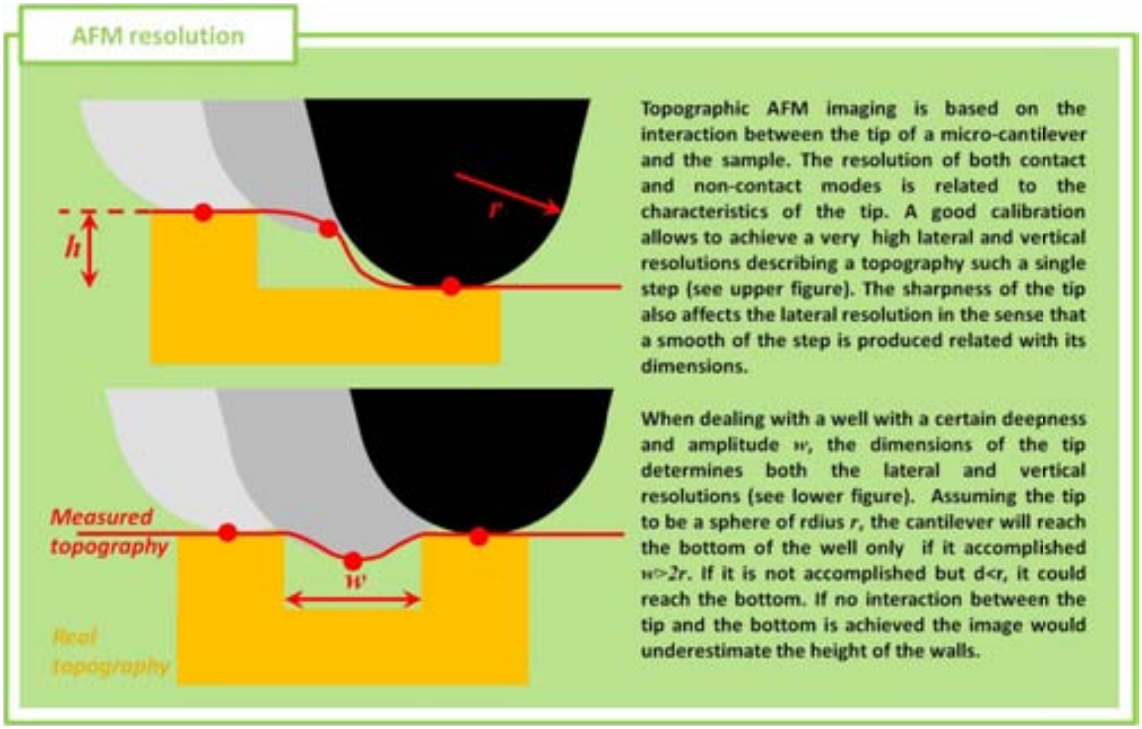

Fig. 5. 8a shows a topography image of the from Fig. 5. 2 (b) 5. 3 (b) and 5. 4 (b). In this case the suspended structures have different lengths, i.e. 100, 300 and 600 nm. As it is done with the devices from Fig. 5. 7 the height profile along an area clean of graphene ribbons (red line) and along the graphene primary ribbon (grey line) is showed on Fig. 5. 8b. The grey shadowed rectangles remarks the free PMMA areas. As it was shown in Fig. 5. 7 an underestimation of the trench deepness can be appreciated. This is more pronounced for trenches with small widths which reinforces the argument of the over-dimensioned AFM-cantilever tip. Besides the indentation of graphene on the PMMA walls also seen in the sample from Fig. 5. 7, an apparent buckling can be seen with an amplitude of less than 1 nm. This can be explained by residual stresses generated after the exposed PMMA removal.

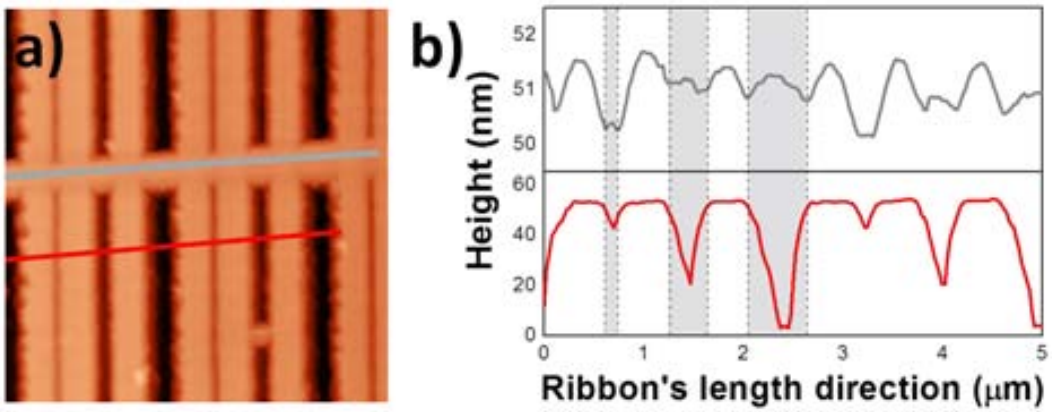

Fig 5. 8. (a) Topographic AFM images of the 100, 300 and 600 nm long ribbons. (b) Upper panel: graphene height profile along the grey line from (a). Lower panel: height profile along the red line from (a). Grey bars indicate the dimensions of the 100, 300 and 600 nm wide trenches.

In the other hand, AFM allow to evaluate the thickness of graphene on PMMA. Obviously, the measured height does not represent the real thick of this material but it can provide a measure comparable to findings from other works. It has been measured to be 1.44 nm approximately, in good agreement with ref. [8] reporting 1.6 nm for mono-layer graphene on PMMA.

5.5. Dragging direction study

As it was commented in the first lines of this section, graphene is obtained from a primary HOPG stack and the transfer is done by means of dragging a spatula along a certain direction. Although the number of graphene ribbons obtained by this method is the same reported by other methods [8], 0.13mm^2 per square centimeter of exposed area, the novel feature here is the highly oriented set of graphene samples it is obtained and their shape regularity.
HOPG is formed by multiple graphene platelets with no spatial coherence between them. A scheme of the appearance of the HOPG surface can be seen on Fig. 5. 9.

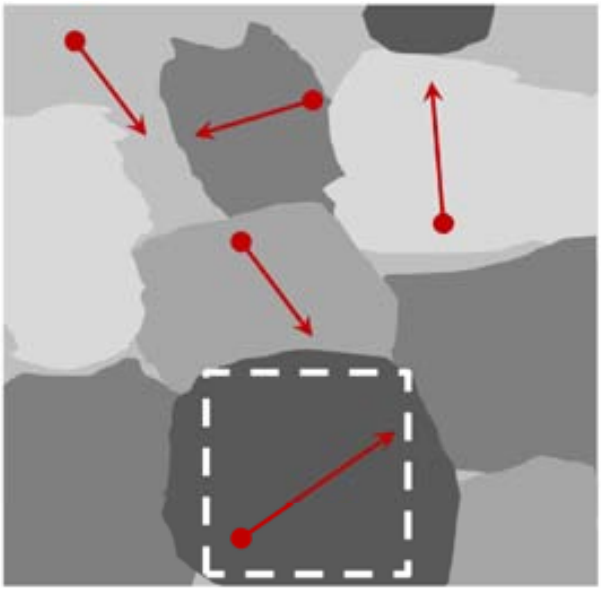

Fig 5. 9. Schematic of the platelets composing the exfoliated layers from the graphite stack. The red arrows represent the random orientation of a certain direction, for instance the arm-chair direction, without indicating their periodic images at 60deg.

The red arrows represent a certain arbitrary crystallographic direction (arm chair for instance). Each platelet show or may show different orientation. The approach followed here is to reduce the area under the action of the spatula to an area as the remarked by the dashed white square, trying to expose a single platelet.

A study on the dependence of the total achieved graphene area with the dragging direction is carried out. The possibility of avoiding the previous optical inspection needed to pattern the trenches perpendicularly to the graphene ribbons would simplify even more the fabrication procedure. In order to do so the occupied area by graphene is computed for different dragging directions from 0 to 90 deg in a 15 deg step. The 0 deg direction corresponds to one of the sample edges. Fig. 5. 10 shows the result in terms of total ribbon area in μm^2 reaching a maximum for α=60 deg approximately. A Gaussian fit (black line) can be also seen.

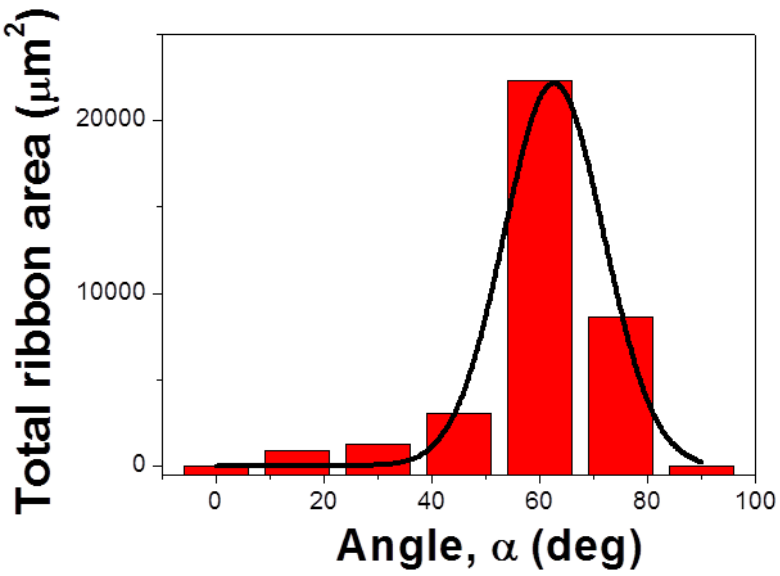

Fig 5. 10. Ribbon's occupied area for different dragging direction from 0 to 90 degrees, relative to the (001) Si cut.

The results here presented indicate that if the right direction is considered the transference of graphene is maximized. In the light of the devices presented along this section, the match of the dragging direction with the "preferred direction" of the considered platelet will produce a set of highly oriented ribbons along the same direction. In this sense, knowing a priori the exact orientation of each part of the HOPG stack would allow to reduce the fabrication to a one single EBL step after transferring the graphene on the PMMA.

5.6. Conclusions

In this chapter a full description of 2D-materials based bi-stable NEMS has been provided regarding graphene, h-BN and MoS_2. The computation of the elastic potential energy allows to describe the systems in terms of a lumped-mass system with coordinate z. The piezoelectric and flexoelectric description is carried out to include the possibility of using these materials as transducers. This fact would simplify the

fabrication procedure as the structure acts as mechanical and electric transducer at the same time. Moreover, the flexoelectric effect some materials present enhances the throughput as the range of compressions that increases the output power is notably broadened.

From the experimental point of view, the procedure followed for the fabrication of suspended graphene ribbons is reported although further work must be done in order to validate experimentally the results obtained along this chapter. However, the fabrication procedure represents a novel approach to obtain sets of identical graphene resonators.

References

[1] Garcia, Jorge M., et al. "Graphene growth on h-BN by molecular beam epitaxy." *Solid State Communications* 152.12 (2012): 975-978.

[2] Reina, Alfonso, et al. "Large area, few-layer graphene films on arbitrary substrates by chemical vapor deposition." *Nano letters* 9.1 (2008): 30-35.

[3] Chang, You Min, et al. "Multilayered graphene efficiently formed by mechanical exfoliation for nonlinear saturable absorbers in fiber mode-locked lasers." *Applied Physics Letters* 97.21 (2010): 211102-211102.

[4] Ferrari, A. C., et al. "Raman spectrum of graphene and graphene layers." *Physical review letters* 97.18 (2006): 187401.

[5] Calizo, Irene, et al. "The effect of substrates on the Raman spectrum of graphene: Graphene-on-sapphire and graphene-on-glass." *Applied Physics Letters* 91.20 (2007): 201904-201904.

[6] Gupta A, Chen G, Joshi P, Tadigadapa S and Eklund P C "Raman Scattering from High-Frequency Phonons in Supported n-Graphene Layer Films" *Nano Letters* **6** (2006) 2667

[7] Sumit Kumar, Anshu Sharma, Balram Tripathi, Subodh Srivastava, Shweta Agrawal, M. Singh, Kamlendra Awasthi, Y.K. Vijay "Enhancement of hydrogen gas permeability in electrically aligned MWCNT-PMMA composite membranes", *Micron* **41** (2010) 909–914

[8] , Floriano, et al. "Elastic properties of graphene suspended on a polymer substrate by e-beam exposure." *New Journal of Physics* 12.2 (2010): 023034.

CHAPTER 6

RESULTS SUMMARY AND FUTURE WORK

This thesis is devoted to study the suitability of bistable energy harvesting devices for scavenging energy from vibration sources for ultra-low power ICT technologies. The fact that low intensity vibrations generally show broad frequency spectra and the difficulty of matching the natural frequency of resonators to this of the target source makes unpractical the use of MEMS and NEMS for energy harvesting purposes. Bistable systems open the door to avoid the problem of the frequency match and to bring these kinds of mechanics down to the micro and nano-scale. Two different strategies, based on electrostatic interaction and compression, are proposed to bring mechanical structures to a bistable configuration. An incursion to an experimental characterization of such systems has been done attempting to reproduce the theoretical results obtained from modeling and numerical simulations. Due to the difficulty for establishing a common metrics for quantifying the performance of energy harvesting devices, it is not possible to directly compare the results here obtained with results reported by other authors. Moreover, the miniaturization of these devices allows considering new low-intensity vibration sources described in this thesis dissertation as non-inertial forces, i.e. bacteria movement or structure-medium interaction. These kinds of vibrations contain much more power than vibrations based on inertial mechanisms, i.e. machinery and building vibrations.

The main conclusions as well as possible lines of future work extension of this thesis are summarized as foolows:

In **chapter 1** an extended introduction to the objectives and achievements of the Energy Harvesting community is given: starting from the well-known green energies based technologies for energy generation and moving to the applicability of self-powering for ultra-low power consumption ICT devices. The state of the art is reviewed focusing on harvesting from mechanical vibrations and introducing the bistable approach.

In **chapter 2** the different approaches for modeling the systems under consideration in chapter 3 and 4 are provided. In one hand, a continuum description of mechanical structures based on effective parameters is used to describe the static behavior of

cantilevers and cc-beams. In the other hand, an *ab-initio* approach allows to find expressions to achieve a sound description of 2D-crystals regarding mechanical, piezoelectric and flexoelectric characteristics. For both cases the dynamical response under the action of different mechanical vibrations is obtained by means of solving numerically the corresponding Langevine equation considering, when needed, the transduction mechanism used to convert the mechanical energy into the electric domain.

In **chapter 3** a MEMS based bistable system prototype is presented where the bistable condition is achieved by means of electrostatic repulsion. A commercial V-shaped cantilever and a counter electrode are polarized across their thickness in order to provoke permanent charge trapping allowing to tune the potential energy of the cantilever in terms of the distance between the electric charges. The model is checked experimentally presenting a good agreement for both static and dynamical behavior.
The model foresee a maximum output power of 0.14pW when the system is excited by a 1/f noise with root mean square 4nN. This represents a PD of 12.7$\mu W/cm^3$, although no optimization of the transduction mechanism is carried out, which is comparable to other values found in the literature. The performance of the device is increased when downscaled: for a linear dimension shrinking of a factor 10 gives a PD more than 20 times higher. Moreover, although the benefit of the bistable configuration is reduced to a certain value of the distance between electric charges, it allows having a good performance for a wide range of force intensities.
No transduction mechanism is included in the experimental realization. A verification of the output power achieved by numerical simulations would be the following milestone for this part of the present work. Regarding the charge trapping procedure, the consideration of other materials with improved trapping lifetime must be addressed to assure the functionality at long term, which represent a basic characteristic for energy harvesting devices. Also regarding the optimization of the prototype, the different key parameters of the model must be adjusted to maximize the performance under specific excitation conditions.

In **chapter 4** *ab initio* calculations based on a DFT code are performed to study 2D materials such graphene, h-BN and MoS_2. A suspended nano-ribbon is studied to be the main block of an energy harvester. The bistable condition is achieved by applying a compressive strain along the length of the structure which allows to tune the response of the system to reach its maximum.
In order to evaluate the capability of harvesting energy from noisy vibrations of a graphene-based device, two piezoelectric AlN layers placed at the clamped ends of the structure are included in the model during the simulation of the dynamics. A maximum output power of 5pW is achieved considering a quality factor of Q=100 and setting the external force to match the intensity of thermal noise which has an explicit dependence on Q. This value is reduced to 0.5 if Q=10000.
For h-BN and MoS_2 is the mechanical transducer itself that act as electromechanical transduction element, thanks to the piezoelectric effect this materials show. Flexoelectric effects observed during simulation also provide a higher generation of

electric power even when the external excitation is not capable of producing the transitions between the two potential energy minima. This enlarges the range of compressive strains providing high output electric power. A maximum value of 0.18pW is achieved for the h-BN case, considering a force described by a white Gaussian noise with a root mean square of 5pN.
No bistability was seen for MoS_2 for the particular dimensions considered in this work.
The fabrication of a real device verifying the present characterization, which is treated in chapter 5, and the generalization of the obtained results to other geometries and dimensions represent the main goal to achieve in the near future.

In **chapter 5** the first steps in order to fabricate the graphene device discussed in chapter 4 are reported. A novel approach to maximize the number of obtained suspended graphene ribbons is presented. It is supposed to allow a systematic study of the characteristics of graphene resonators thanks to the possibility of obtaining quasi-identical suspended structures.
The bistabilization of the device and the verification of the results reported on chapter 4 represent the most ambitious goals to pursue although, as it is shown in chapter 4, other 2D crystals with piezoelectric effect will facilitate the fabrication of a prototype with harvesting capabilities.

PAPERS

In this appendix the papers already published or accepted for publication are summarized. This dissertation is presented as a compendium of publications although only two of these items are part of the official compendium. However, for completeness, all the papers representing an important contribution to the present dissertation are included.

Paper A

López-Suárez, M.; Agustí, J.; Torres, F.; Rurali, R.; Abadal, G. "Inducing bistability with local electret technology in a microcantilever based non-linear vibration energy harvester". A: Applied Physics Letters (2013).

Paper B

López-Suárez, Miquel, et al. "Nanostructured graphene for energy harvesting". Physical Review B 84.16 (2011): 161401.

Paper C

López-Suárez, M.; Rurali, R.; Abadal, G. "Buckling suspended grahene nanoribbons to harvest energy from noisy vibrations". A: Microelectronic Engineering (2013).

Paper D

López-Suárez, M.; Pruneda, M,; Abadal, G.; Rurali, R. "Piezoelectric layered materials for energy harvesting". Accepted for Nanotechnology (2014).

Paper E

M. López-Suárez, F. Torres, N. Mestres, R. Rurali, G. Abadal. "Fabrication of highly regular suspended graphene nanoribbons through a one-step EBL process". Submitted.

APPLIED PHYSICS LETTERS **102**, 153901 (2013)

Inducing bistability with local electret technology in a microcantilever based non-linear vibration energy harvester

M. López-Suárez,[1,a)] J. Agustí,[1] F. Torres,[1] R. Rurali,[2] and G. Abadal[1]
[1]*Departament d'Enginyeria Electrònica, Universitat Autònoma de Barcelona, Bellaterra 08193, Spain*
[2]*Institut de Ciència de Materials de Barcelona (ICMAB-CSIC), Campus de Bellaterra, Bellaterra 08193, Spain*

(Received 22 January 2013; accepted 21 March 2013; published online 16 April 2013)

A micro-electro-mechanical system based vibration energy harvester is studied exploring the benefits of bistable non linear dynamics in terms of energy conversion. An electrostatic based approach to achieve bistability, which consists in the repulsive interaction between two electrets locally charged in both tip free ends of an atomic force microscope cantilever and a counter electrode, is experimentally demonstrated. A simple model allows the prediction of the measured dynamics of the system, which shows an optimal distance between the cantilever and the counter electrode in terms of the root mean square vibration response to a colored Gaussian excitation noise. © *2013 American Institute of Physics*. [http://dx.doi.org/10.1063/1.4800926]

Among all the explored alternatives to improve the performance characteristics in vibration energy harvesting (VEH) schemes, those based on the non-linear mechanical properties of the transducer element have demonstrated to be one of the most promising options.[1–3] In particular, two main issues make these systems to perform better than traditional linear ones. First, they are able to harvest energy from wide band non-harmonic vibration sources; consequently, they do not require complex tuning strategies in the transducer to match the characteristic frequency of the energy source.[4] Second, they can extract energy from low frequency sources in a non-resonant way. Therefore large inertial masses and large volume realizations are not strictly needed.[5]

On the one hand, bistable implementations have become one of the most reported non-linear vibration energy harvesting (NLVEH) choices. Several ways to induce bistability in NLVEH have been demonstrated so far: magnetic repulsion,[2] inverted cantilever,[6] induced or residual stress.[7]

On the other hand, it has been demonstrated that micro-electro-mechanical systems (MEMS) technology can provide solutions for NLVEH with improvements in the energy level sensitivity,[8] according to their extremely high mechanical compliance.

However, in most of the previous cases, a physical realization of the transducer at the nano or even at the microscale becomes technologically difficult, due to the low control of the bistability parameter during the fabrication process (stress) or due to material non-compatibility (magnetic materials).

In this paper, we demonstrate an alternative based on local electret technology to induce bistability in the mechanical behavior of a triangular tipless AFM-like microcantilever. A simple method based on the capacitance constant voltage stress is used to locally charge the free end of a silicon nitride cantilever. A counter electrode (CE), having the same geometry and material as the cantilever, is also locally charged by the same procedure and brought in close proximity to the cantilever. Repulsive electrostatic interaction between both electrets combined with the restoring force of the cantilever gives rise to a bistable potential for a certain cantilever-electrode distance, which is used as the parameter to control the bistability. A detailed study of the cantilever dynamics when it is excited with a colored vibration noise is presented for different bistability and noise intensity conditions.

We consider a commercial 600 nm thick silicon nitride (Si_3N_4) V-shaped cantilever,[9] as the one depicted in the top side of Figure 1(a) with a 65 nm thick Cr/Au layer coating the backside of the structure.

The AFM-like cantilever has a nominal resonance frequency and a spring constant of 17 kHz and 0.08 N/m, respectively. The same kind of triangular structure, but having a length short enough to prevent any significant displacement, is used to define a counter electrode (see bottom side of Figure 3(a)).

The tip of the cantilever or the counter electrode are independently charged by applying a voltage (15 V typically during 30 min) between the Cr/Au coated top side and the back sides through a contacting gold coated sample, as shown in Figure 2(a). During this process, some charges overcome the barrier at the metal-insulator junction and end up trapped at the surface or deep in the body of the cantilever/electrode.[10] To detect the dynamics of the system we use a conventional AFM optical readout setup, as described in Figure 2(b). The alignment of the cantilever and the counter electrode is achieved by moving both elements with one each 3D micropositioners. Top and lateral views are obtained by means of two CCD cameras which provide an optical feedback during the whole process. A precise control of the cantilever-CE gap distance, d, is achieved with a long range piezo-stack which produces a longitudinal displacement of the CE at a 0.1 μm/V ratio. The deflection of a reflected HeNe laser beam (632.8 nm, 15 mW) on the cantilever surface is detected by means of a position sensitive detector (PSD, New Focus 2930). The transduced electrical signal is captured and stored through an oscilloscope. The mechanical excitation of the cantilever is done through a piezoelectric shaker connected to a voltage noise generator. We have

[a)]Author to whom correspondence should be addressed. Electronic mail: miquel.lopez@uab.cat

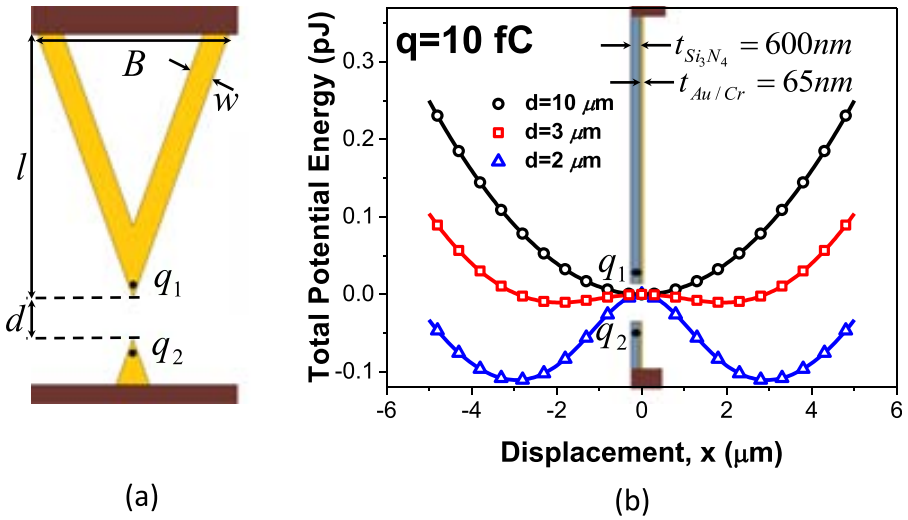

FIG. 1. (a) Scheme of the experimental system. A V-shaped cantilever (top) ($l = 200\,\mu m$; $w = 28\,\mu m$; $B = 184\,\mu m$) and a counter electrode (bottom) are permanent and locally charged with q_1 and q_2, respectively, at their free ends and separated by a distance d. (b) Total potential energy for different d values showing the transition from monostability to bistability as this distance is reduced. For the sake of simplicity an effective electric charge is defined as $q = (q_1 \cdot q_2)^{1/2}$. Inset in (b) is a view of the system indicating the thickness of the composite structure.

verified that the noise used to excite the device is a pink noise, with the intensity inversely proportional to the frequency, as expected in 1/f noise.

We assume a simple elastic restoring force, $F_{el} = -k \cdot x$, for the cantilever, where k and x are the stiffness and the out-of-plane displacement, respectively. A nominal value of $k = 0.08$ N/m is considered.

We assume that the electric charges, q_1 and q_2, have the same sign and that they are trapped at the tip end of the cantilever and CE. Facing them as shown in Figure 1, we can compute the total potential energy of the system as

$$V(x) = 1/2 \cdot k \cdot x^2 + K \cdot q^2/(d^2 + x^2)^{1/2}, \quad (1)$$

where K is the Coulomb constant and $q = (q_1 \cdot q_2)^{1/2}$. This defines a bistable potential for certain values of the parameters k, q, and d as it can be seen in Figure 1(b). Deriving and solving the equation $dV/dx = 0$, the position of the stable points can be found as well as the potential barrier height in terms of these three parameters

$$x_{min} = ((Kq^2/k)^{2/3} - d^2)^{1/2}, \quad (2)$$

$$\Delta V = V(0) - V(x_{min}). \quad (3)$$

It is clear that to achieve the bistability condition, expression (2) must give a real number and, then, one can express this condition as $d < (Kq^2/k)^{1/3}$. As it is expected, this range of values assure a real value for the barrier height as well. For the experimental purposes, the nonlinearizing parameter will be the distance between electric charges as both q and k will be determined before displaying the experiment while d will be a tunable quantity.

Figure 3(a) (bottom) shows the trajectory followed by the system when driven by a Colored Gaussian noise for three different values of the distance between charges, d,

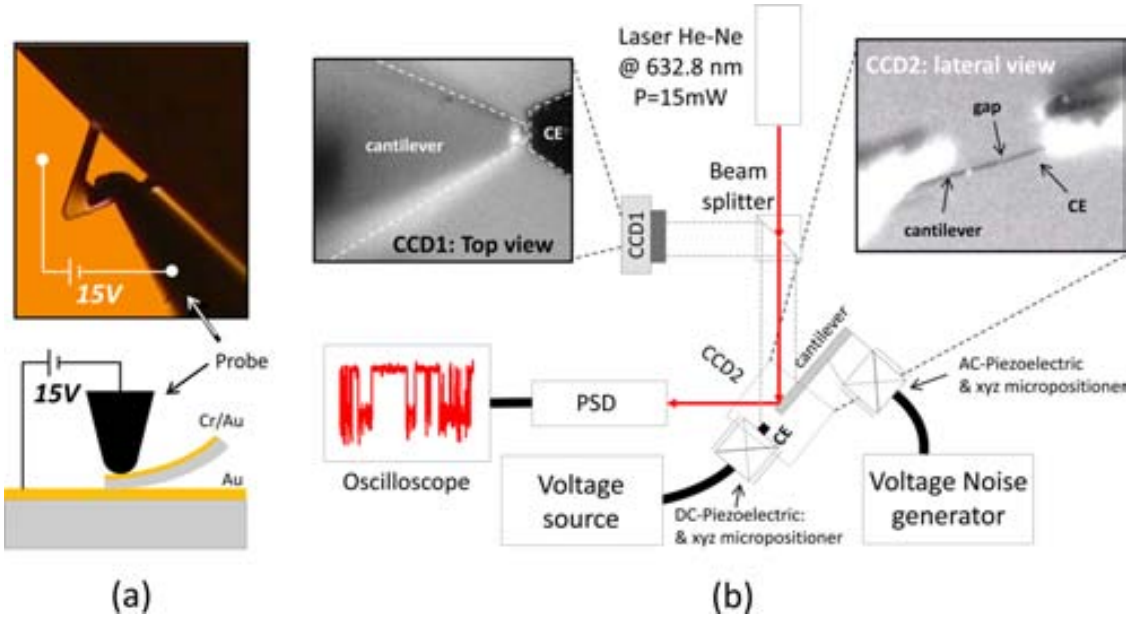

FIG. 2. (a) Optical image (top) and scheme (bottom) of the electrets charging setup/procedure. A probe is used to apply a voltage to the Cr/Au-Si_3N_4-Au capacitor formed by a gold coated sample and the cantilever (or counter electrode). (b) Measurement setup: the deflection of a laser beam incident to the cantilever surface is detected by a PSD in terms of voltage. Two optical images of the system show the captures of the two CCD's which allow the cantilever-CE alignment through two 3D micro-positioners. The finer control of d is carried out through a DC piezoelectric stack with a characteristic ratio of 0.1 μm/V.

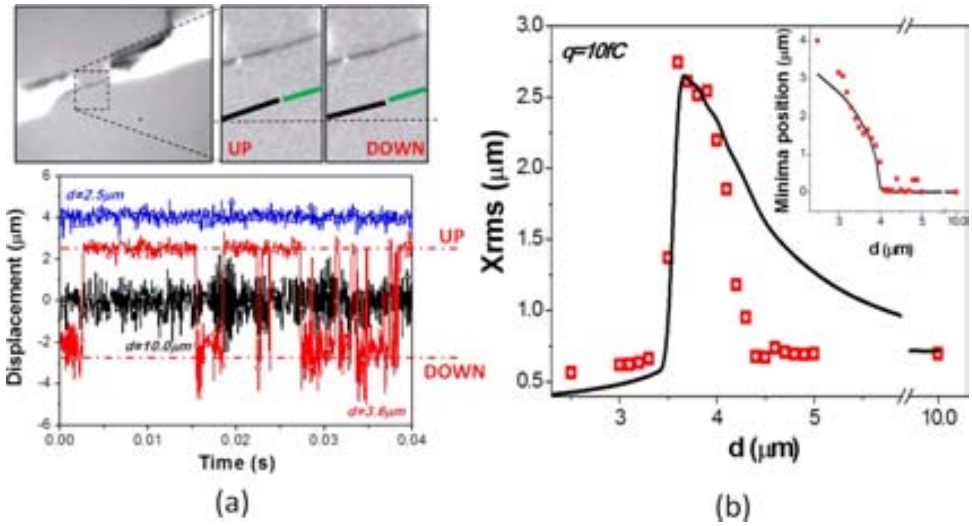

FIG. 3. (a) Upper side: lateral optical image and drawing showing the "up" and "down" states of the cantilever (left, black) movement, with respect to the fixed CE (right, green). Lower side: different regimes of the dynamical response of the system for three different values of the distance between the charges, d: monostability around $x = 0$ (black squares), bistability (red circles), and monostability around $x = x_+$ (blue triangles). (b) Experimental (symbols) and simulated (lines) results for the x_{rms} and potential minima position $x_{min} = x_+$ as a function of d. The dynamics of the system is obtained solving $m_{eff} \cdot d^2x/dt^2 = -b \cdot dx/dt - dV/dx + F_{ext}x(t)$, where x stands for the displacement, b represents the energy losses of the system, and $F_{ext}x(t)$ represents the external force as a stochastic process with intensity F_{ext}. The noise intensity is given by $F_{rms} = 4$ nN (enhanced online) [URL: http://dx.doi.org/10.1063/1.4800926.1].

representative of the three characteristic dynamical regimes. (i) For large d, the system responds as a linear resonant system oscillating around $x = 0$ (black line). (ii) As d decreases and charges get closer, the bistability appears and the cantilever is able to jump from one potential minimum to the other in a random sequence (red line). (iii) Finally, when charges are too close, the potential barrier is too high and the dynamics gets stuck in one of the two wells: the cantilever oscillates around one of its equilibrium positions, but lower-frequency swings to the other minimum are hindered by the barrier height (blue line). An optical image of the system is shown in the upper panel of Figure 3(a), where magnified images slightly allow differentiating the up and down states of the bistable regime. This can be seen more clearly in the video provided (see link in Fig. 3 caption). Besides, note that in top Figure 3(a) images, the optical resolution and the lack of perfect perpendicularity of the view avoid to solve both the 600 nm thickness of the cantilever (or of the CE) and the gap distance. In Figure 3(b) we plot the displacement root mean square, x_{rms}, obtained experimentally (red symbols) for different values of the distance d, while keeping fixed the noise intensity. These results are in good agreement with the predictions of the model (continuous lines). Clearly, there is an optimal cantilever-CE gap, $d_{opt} = 3.6\ \mu$m, that maximizes the system response in terms of x_{rms}, which is closely related to the capability of transducing kinetic energy into electric energy.[7] The position of the potential energy minima as a function of d (inset of Figure 3(b)), obtained by measuring the average position, also shows a good agreement between experimental data and model (Eq. (2)).

Thus far, we have considered a given noise intensity and optimized the separation between charges, achieving the bistability and maximizing the root mean square of the cantilever displacement. Now we consider the case of a given value of d, and we show that, as expected, there is always a value for the noise intensity from which the system again becomes strongly non-linear, jumping from one well to the other, while below this threshold the cantilever gets stuck in one of the two wells. This behavior is shown in Figure 4, pointing out that the benefits of bistability can be extended to all F_{rms} below the rupture limit when overcoming a threshold value. Furthermore, even beneath this threshold value, when the external noise is not able to provoke transitions over the potential barrier, the response seems to be of the same order of that for the resonating case.

In summary, we have modeled, fabricated, and tested a bistable NLVEH where a strategy based on local electrets technology is used to engineer the non-linearity of the system. The harvester, consisting in a 0.08 N/m Si_3N_4 microcantilever faced to a counter electrode, is driven into bistable regime by controlling the distance between the tip end of both elements, where two electric charges of the same sign have been implanted, thus tuning their electrostatic repulsion. A good agreement between the predictions of a simple

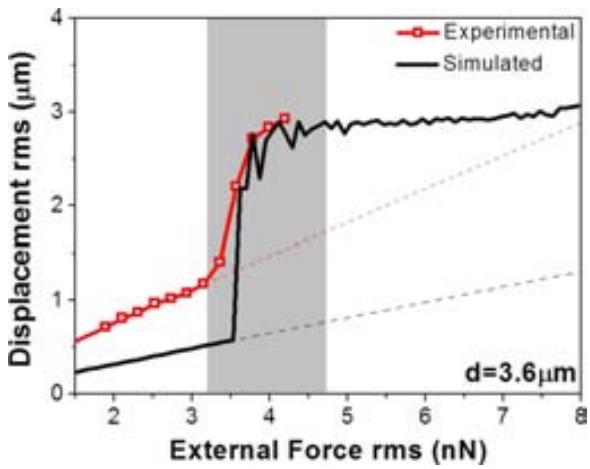

FIG. 4. Experimental (red line-symbols) and simulated (black line) results for the x_{rms} for a given distance d as the noise intensity is swept showing an abrupt increment when a threshold value is overcome. The dashed line represents the trend of this quantity if no bistability is considered, i.e., $q = 0$.

model and the experimental data is achieved reproducing all the main features of the expected dynamics. The proof-of-concept demonstrated in this letter should now be followed by a careful optimization of the device parameters, including the material of choice. While here we have used commercial Si_3N_4 cantilevers, other materials such as Teflon should be preferred for the much longer decay times of the trapped charge.[11,12]

The authors would like to thank the Spanish "Ministerio de Ciencia y Innovación" for financially supporting this research under the projects OPACMEMS Nos. ENE2009-1430-CO2-02, FIS2009-12721-C04-03, and FIS2012-37549-C05-05.

[1]L. Gammaitoni, H. Vocca, I. Neri, F. Travasso, and F. Orfei, *Vibration Energy Harvesting: Linear and Nonlinear Oscillator Approaches, Sustainable Energy Harvesting Technologies - Past, Present and Future* (Dr. Yen Kheng Tan, Shanghai, 2011), pp. 169–188.
[2]F. Cottone, H. Vocca, and L. Gammaitoni, Phys. Rev. Lett. **102**, 080601 (2009).
[3]L. Gammaitoni, I. Neri, and H. Vocca, Appl. Phys. Lett. **94**, 164102 (2009).
[4]M. Lallart, S. R. Anton, and D. J. Inman, J. Intell. Mater. Syst. Struct. **21**, 897–906 (2010).
[5]G. Murillo, G. Abadal, F. Torres, J. L. López, J. Giner, A. Uranga, and N. Barniol, Microelectron. Eng. **86**, 1183 (2009).
[6]M. I. Friswell, S. F. Ali, O. Bilgen, S. Adhikari, A. W. Lees, and G. Litak, J. Intell. Mater. Syst. Struct. **23**(13), 1505 (2012).
[7]F. Cottone, L. Gammaitoni, H. Vocca, M. Ferrari, and V. Ferrari, Smart Mater. Struct. **21**, 035021 (2012).
[8]M. López-Suárez, R. Rurali, and G. Abadal, Phys. Rev. B **84**, 161401(R) (2011).
[9]NanoWorld™ Pirex Nitride AFM probe: PNP-TR-TL.
[10]J. Wibbeler, G. Pfeifer, and M. Hietschold, Sens. Actuators, A **71**, 74 (1998).
[11]P. W. Chudleigh, R. E. Collins, and G. D. Hancock, Appl. Phys. Lett. **23**, 211 (1973).
[12]J. A. Małecki, Phys. Rev. B **59**, 9954 (1999).

PHYSICAL REVIEW B **84**, 161401(R) (2011)

Nanostructured graphene for energy harvesting

Miquel López-Suárez,[1] Riccardo Rurali,[2,*] Luca Gammaitoni,[3] and Gabriel Abadal[1]

[1]*Departament d'Enginyeria Electrònica, Universitat Autònoma de Barcelona, E-08193 Bellaterra, Barcelona, Spain*

[2]*Institut de Ciència de Materials de Barcelona (ICMAB–CSIC), Campus de Bellterra, E-08193 Bellaterra, Barcelona, Spain*

[3]*NiPS Laboratory, Dipartimento di Fisica, Universitá di Perugia, and Istituto Nazionale di Fisica Nucleare, Sezione di Perugia, I-06100 Perugia, Italy*

(Received 1 August 2011; revised manuscript received 12 September 2011; published 6 October 2011)

Engineered nonlinearities have been shown to play an important role in increasing the efficiency of energy harvesting devices. Macroscopic prototypes using this approach have been demonstrated recently [F. Cottone, H. Vocca, and L. Gammaitoni, Phys. Rev. Lett. **102**, 080601 (2009).] Here, in order to implement such a scheme at the nanoscale, we propose a simple device which is based on strained nanostructured graphene and discuss how it can respond to many energy sources that, although having a low intensity, are freely available, such as ambient vibrations or thermal noise. We discuss in some detail the case of thermal fluctuations harvesting in the steady-state nonequilibrium regime and of ambient vibrations.

DOI: 10.1103/PhysRevB.84.161401 PACS number(s): 61.48.Gh, 05.40.Ca, 05.10.Gg, 81.05.ue

An efficient power supply for increasingly small electronic devices is a challenging task that could prevent prototype nanocircuitry to move to mass production. On the other hand, as the size of devices shrinks, their power requirements also diminish.[1] Hence, energy sources that are freely available, such as ambient vibrations or thermal energy, become important and allow envisaging a batteryless world of self-powered devices.[2–5] For this reason, and to pursue clean energy sources compatible with a sustainable development, energy harvesting and energy conversion have become a very intense field of research.[6–9]

Linear mechanical resonators are the most common solution to convert vibrational into electrical energy[10,11] exploiting piezoelectric[7] or capacitive transduction.[12] Unfortunately, it is not always possible to tune their resonant frequency in the spectral region of ambient vibrations and, even when such tuning is possible, their efficiency rapidly decreases when moving away from the resonant frequency, which is an important limitation especially for broad spectral densities such as those of ambient vibrations. Cottone *et al.*[13] have demonstrated the role of engineered nonlinearity to improve significantly the efficiency of noise harvesting devices. Their macroscopic toy model consists of an inverted pendulum with a magnet attached to its tip. The approach of an external magnet is used to control the pendulum dynamics, pushing its tip away from its equilibrium position and making it oscillate around two unique and symmetric equilibrium positions. The magnetic repulsion can be tuned in a way that the pendulum operates as a bistable device, combining high-frequency oscillations around one of the two equilibrium positions—where it spends most of the time—with low-frequency, large excursions from one to the other.

In this Rapid Communication we show that a compressed graphene sheet can be used to implement such a bistable device to harvest thermal fluctuations and ambient vibrations at the nanoscale. The degree of compression ϵ is the only control parameter and allows switching among three possible regimes: (a) single-well potential ($\epsilon \sim 0$), (b) double-well potential with allowed swings from one minimum to the other (intermediate ϵ), i.e., the bistable device, and (c) double-well potential with no commutation between the two equilibrium positions (large ϵ). Yet, we show that graphene possesses an intrinsic nonlinearity[14] and can harvest thermal fluctuations and other kinds of nonequilibrium noise, outperforming any comparable linear oscillator, even when it is not compressed (see, for instance, Ref. 15 for general nonlinear potentials).

Thermal fluctuations are ubiquitously present in every dissipative system at a finite temperature. In principle, random fluctuations in equilibrium with their surroundings cannot be harvested without violating the second law of thermodynamics. However, it has been argued that equilibrium, a concept derived from macroscopic physics, is elusive when applied to the atomic scale and fluctuations become important.[16] Nevertheless, to avoid formal problems related to the definition of thermodynamical equilibrium of a nanoscale system, we restrict our discussion to the case of open systems in the steady-state nonequilibrium regime or systems under slowly varying local equilibrium conditions.

To calculate the deformation potential of graphene, we perform first-principles electronic structure calculations within density-functional theory (DFT). We use the SIESTA package,[17] norm-conserving pseudopotentials, and the generalized gradient approximation[18] to the exchange-correlation energy. Given the very large number of atoms necessary to describe the deformation that oscillating graphene undergoes, we use a minimal basis set, though for short graphene strips satisfactory convergence tests have been carried out against a more reliable single-ζ polarized basis. We obtain a Young's modulus of 0.85 TPa (assuming an effective thickness of the graphene sheet of 3.34 Å) and a Poisson ratio of 0.18. The structures were relaxed until all the forces were lower than 0.04 eV/Å, except for those atoms that need to be constrained to sample the transition states. To keep the computational load at a manageable level, rather than nanoribbons, we consider infinite graphene, which can be modeled by one single primitive cell along the y axis, the direction perpendicular to the deformation (see Fig. 1). The energy of a device with a given width W is obtained by rescaling the calculated energy by a factor W/w, w being the width of the primitive cell. It should be stressed that within this approximation, where a linear scaling of the

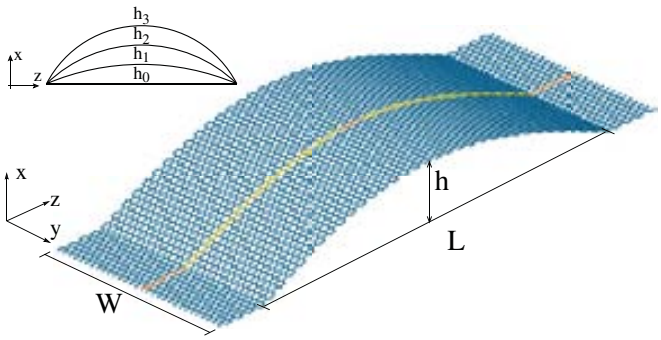

FIG. 1. (Color online) Buckled ground-state configuration of a graphene sheet under compressive strain. The atoms of the primitive cell explicitly introduced in the calculation within periodic boundary conditions are shown in light yellow (light gray). Atoms of the computational cell that need to be constrained to sample transition states (at the apex and at the clamped ends) are displayed with a darker color (gray). The potential profile is obtained by performing a series of calculations of sinusoidal deformations with increasing amplitudes h_i, as shown schematically in the inset.

energy with W is assumed, edge effects are neglected. Edges can generate stress fields, induce the formation of ripples and, in general, will affect the overall dynamic behavior of the system. These effects are not accounted for in our model. However, for the width of ribbons to be used in realistic devices the energetics and the dynamic response of the system is not expected to qualitatively change.

We start from a flat graphene sheet with a compressive strain ϵ [defined as $(L_0 - L)/L_0$, where L is the length of the graphene sheet and L_0 its equilibrium value in absence of compression; see also Fig. 1] ranging from 0% to 0.1%. For each value of ϵ we generate several sinusoidal deformations with an increasing amplitude h_i (see the inset of Fig. 1). Previous tests indicated that sinuslike profiles are close to the minimum energy configurations, and thus are good initial guesses. Next, we carry out a geometric optimization of each structure. Small regions at the beginning and at the end of the strip are kept flat to mimic typical nanoindentation experiments. As our purpose is mapping the potential landscape, the apex of each of the deformed strip is kept fixed to prevent all the structures from relaxing to their atomic ground state.

As illustrated in Fig. 2, the potential has a minimum at $h = 0$ in the case of uncompressed graphene, while for $\epsilon > 0$ two symmetric minima appear, indicating that graphene favors a buckled configuration such as the one sketched in Fig. 1. As ϵ increases, the minima move apart and the transition barrier grows, making the commutation between wells less likely.

The dynamics of the system is described by the equation of motion

$$m\ddot{x} = -\frac{\partial E_p}{\partial x} - b\dot{x} + F_0\xi(T), \tag{1}$$

where E_p is the elastic (potential) energy as obtained by the electronic structure calculations and reported in Fig. 2. As customary in the study of beam deflection or cantilever vibrations, we reduce the dynamics of the clamped graphene sheet of total mass M to the equivalent dynamics of a free pointlike mass $m = 0.4M$.[19] Here we assume a simple phenomenological viscous damping term[20] with a damping coefficient that in the harmonic potential case can be expressed as $b = m\omega_0/Q$, taking $Q = 100$ for the quality factor of a graphene sheet in air. In general the mechanical dissipation in the graphene dynamics is due to a number of different phenomena[21,22] and can be more properly expressed in terms of a dissipation function that takes into account generalized memory effects as in the expression $\int_{-\infty}^{t} b(t-\tau)\dot{x}(\tau)d\tau$.

$F_0\xi(T)$ represents the random force [$\xi(T)$ is a flat spectrum stochastic process, Gaussian distributed, with zero mean and unitary standard deviation] accounting for the thermal noise-induced stochastic dynamics of the graphene sheet. When the potential is harmonic ($E_p = 1/2kx^2$) and the system is at thermal equilibrium, the fluctuation-dissipation theorem links the magnitude of the thermal fluctuation to the damping coefficient via $\hat{F}_0^2 = 4k_BTb$, where k_B is the Boltzmann

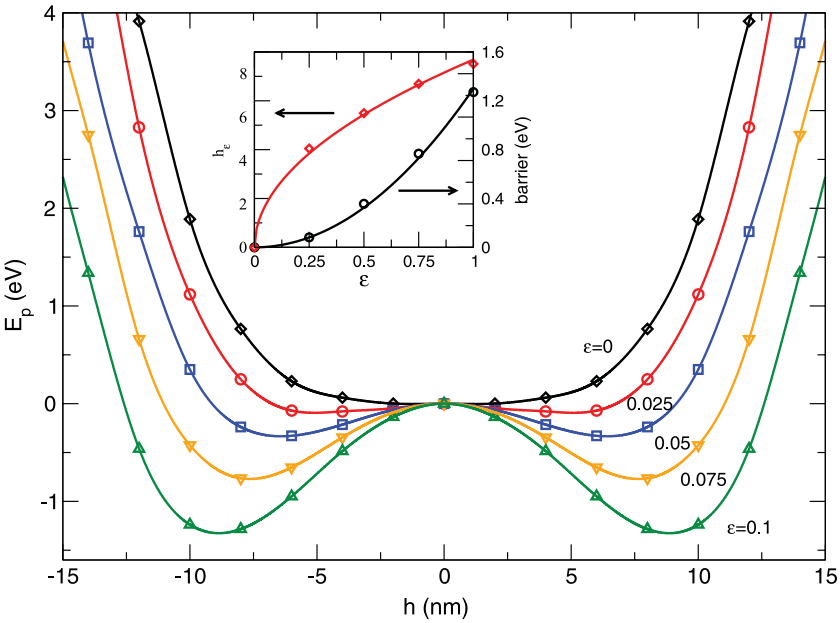

FIG. 2. (Color online) Potential as a function of the out-of-plane coordinate h for compressions ϵ ranging from 0% to 0.1%. Finite values of ϵ favor buckling of the graphene sheet, with two symmetric minima at $h \neq 0$. The inset displays the separation between the minima and the transition barrier as a function of ϵ, together with fits to ϵ^2 and $\sqrt{\epsilon}$, respectively.

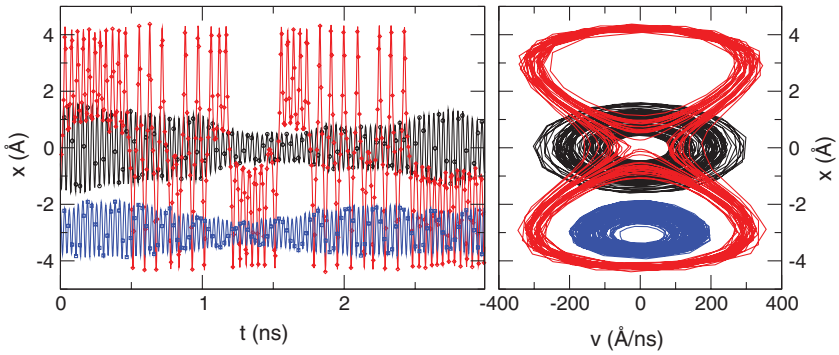

FIG. 3. (Color online) Evolution of the position x in the three possible regimes: (i) At low applied compressions the system oscillates in a single-well potential at approximately $x = 0$ (black circles); (ii) at the optimal compression a bistable behavior is clearly observed, with long swings from one well to the other (red diamonds); (iii) at large compressions the buckled graphene gets trapped in one of the minima (blue squares). The left-hand panel shows the time evolution $x = x(t)$; the right-hand panel is the attractor diagram $x = x(v)$.

constant and T is the temperature. In this case the root mean square (rms) of the displacement amounts to $x_{\rm rms} = \sqrt{k_B T/k}$.

The potential that we obtained from the DFT calculations, however, is strongly nonharmonic, even in the simple case of uncompressed graphene, where a satisfactory fit is achieved only with the order-4 polynomial $c_4x^4 + c_2x^2$ (we obtain $c_4 = 0.12$ meV Å^{-4} and $c_2 = 6.59$ meV Å^{-2} for the nanoribbon of Fig. 2). Hence a useful prediction from the stochastic differential equation (1) can only be obtained numerically. Here we used the well-known Euler-Maruyama method, where the stochastic force intensity is set arbitrarily at $\hat{F}_0^2 = 4k_BTb$ with a flat spectral distribution (white noise approximation) and $T = 300$ K, to mimic a nonequilibrium thermal noise acting on the graphene sheet.

Solutions of Eq. (1) for a graphene nanoribbon of 1×17 nm are shown in Fig. 3 for the different working regimes. This graph illustrates how the dynamics of the system can be controlled by tuning the level of compression. At high values of ϵ the trajectory is confined around one of the two attractors, in a buckled configuration, whereas for low ϵ the barrier is not effective and the system is swinging in a perturbed, single-well potential around zero. It is at intermediate compressions that the system can jump from one well to the other, increasing the rms of the position vector. This optimal compression range

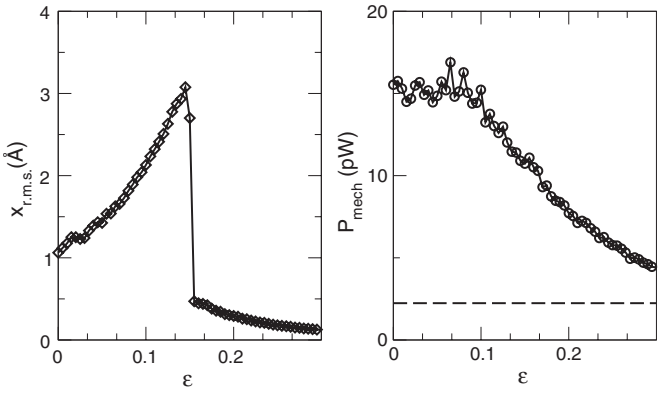

FIG. 4. Root mean square (rms) of the position vector x (left-hand side) and mechanical power (right-hand side) as a function of the compressive strain ϵ. The optimal compression that maximizes $x_{\rm rms}$ is $\epsilon \sim 0.17$. This value of ϵ also maximizes the piezoelectrically generated voltage in the transduction circuit described in the text. The dashed line in the right-hand panel gives an estimation of the mechanical power accumulated by a linear oscillator of comparable size to the one discussed.

depends on the geometrical parameters of the graphene device and the temperature of the noise that has to be harvested.[13]

The dependence of $x_{\rm rms}$ on the compression level is shown in Fig. 4(a). Here the $x(t)$ time series has been averaged to zero before computing the $x_{\rm rms}$ in order to filter out any dc component that cannot be considered interesting for energy harvesting purposes as in Ref. 13. Increasing ϵ leads to an increase of the rms of the position: The two attractors of the dynamics have appeared, but the barrier still allows low-frequency swings from one well to the other. At approximately $\bar{\epsilon} = 0.17$, $x_{\rm rms}$ gets to a maximum and then drops dramatically, indicating that the barrier has reached a critical value and the dynamics is trapped in one of the two attractors.

The mechanical power, defined as $P_{\rm mech} = \langle F_0\xi(T)\dot{x}\rangle$, on the other hand, is slowly decaying and does not present a maximum at $\bar{\epsilon}$ [see Fig. 4(b)]. This happens because, although the graphene sheet on average moves *more*, as shown in Fig. 4(a), it also moves *slower*, yielding a decrease in the mechanical power.[23]

Figure 4(b) seems to suggest that it is pointless to pursue the double-well potential of the buckled graphene, because the maximum mechanical power is accumulated by flat graphene. However, as it will be clear in the following, in order to harvest electrical energy we need a conversion mechanism that is capable of transforming the available mechanical energy into this final form of energy. Before dealing with the conversion mechanism, we further note that another energy source that could be scavenged is represented by ambient vibrations, such as mechanical vibrations and acoustic energy,[3,4,24] that are not intrinsic to the system as is the thermal noise considered so far. The main limitation of conventional linear nano-oscillators with respect to these kinds of environmental vibrations is the poor flexibility of their frequency sensitivity: Not only is the spectral response usually very narrow, but it is also difficult to shift it toward the low-frequency domain, which is where most of the ambient vibration energy is located.

The spectral response of the proposed graphene device, expressed by the vector $X(\omega) = \mathcal{F}\{x(t)\}$, is shown in Fig. 5. The output spectrum shown represents the amplitude of movement in response to each frequency component of the incident noise. Indeed, the larger average mechanical power is harvested by the flat graphene [Fig. 4(b)], but responds only to frequencies close to a resonance frequency of ~30 GHz, with an approximate bandwidth of 10 GHz. On the other hand, close to the optimal compression, when the system is allowed to swing from one well to the other, a very broad range of

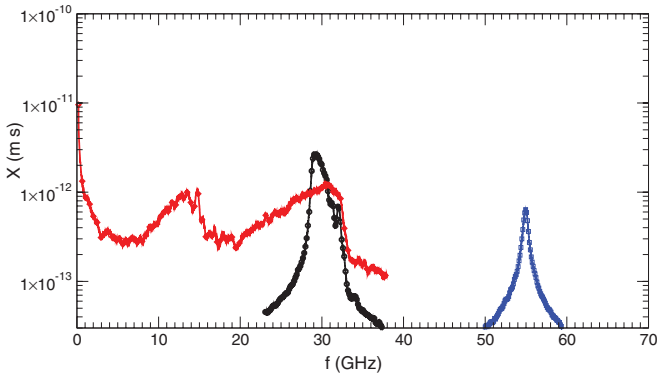

FIG. 5. (Color online) Spectral response in the three operating regimes. Zero or too large compressive strains yields rather selective frequency responses (black circles and blue squares, respectively). Around the optimal compression, on the other hand, the spectral response is much broader and extends significantly to the low-frequency domain (red diamonds). The spectral response is defined as the Fourier transform of the position vector as follows: $X(\omega) = \mathcal{F}\{x(t)\} = \frac{1}{\sqrt{2\pi}} \int_{-\infty}^{+\infty} x(t) e^{-i\omega t}\, dt$.

frequencies can be harvested, with a noticeable extension to low frequencies. This means that even if the maximum power is higher in the uncompressed case [$P(\bar{\epsilon})$ is 2/3 of the maximum power $P(0)$], the device becomes sensitive to a much broader frequency spectrum, with an integrated power that exceeds significantly the linear case, especially in the case of harvesting ambient vibrations. It should be noticed that when the optimal compression is exceeded and the system gets stuck in one of the two wells, the spectral response gets significantly worse, resulting in a narrower and higher-frequency distribution, even with respect to the case of flat graphene. This fact suggests that certain caution should be paid when choosing the value of ϵ, especially in view of the experimental difficulties to control it with accuracy.

The energy harvested by the vibrating graphene device, however, cannot be stored in a simple way, as mechanical energy storing is an elusive task and a very intense research field. Yet, the harvested thermomechanical energy needs to be converted to electrical energy and used immediately or stored with known storing procedures, namely, through electrical capacitors. As we discuss below, such a conversion provides an argument in favor of the buckled configuration.

Devising and engineering an efficient transduction scheme is subjected to the optimization of many parameters. Here we assume a simplified piezoelectric conversion model consisting of two ZnO transducers placed at the clamped ends of the suspended sheet. The behavior of the piezoelectric material is modeled as a capacitance with a deformation-dependent charge density $d_{31} = -5.1 \times 10^{-12}$ m/V,[25,26] coupled to a load resistance. Following Roundy and Wright,[11] the whole dynamics of the graphene harvester can be described by

$$m\ddot{x} = -\frac{\partial E_p}{\partial x} - b\dot{x} - \Gamma_1 V + F_0 \xi(T), \tag{2}$$

$$\dot{V} = \Gamma_2 \dot{x} - \frac{V}{RC}, \tag{3}$$

where the motion equation is modified by the inclusion of a piezoelectric term [Eq. (3)], which accounts for the forces associated with the transduction mechanism and which couples motion and the transduction equations [Eq. (3)]. Taking a large enough value of the time constant RC of the transducing circuit (low cut-on frequency $\omega_{hp} = 1/RC$), the second equation provides $V = \Gamma_2 x$, where V is the generated voltage and Γ_2 is the electromechanical coupling coefficient as defined in Ref. 11. Therefore, the piezoelectric rms voltage V is simply the rms of the position vector rescaled by a factor Γ_2—taken to be 5.8 V/m from Ref. 11. Now the maximum harvested electrical power $P_{\rm el} = V^2/R$ no longer corresponds to the unstrained graphene sheet and the optimal compression is $\bar{\epsilon}$, the one that gives the larger $x_{\rm rms}$ (see Fig. 4), as previously observed in Ref. 13. This piezoelectric model is admittedly a simple one, and it should be taken into account that the specific transduction scheme implemented will also affect the overall dynamics of the system.

In conclusion, we have shown that a nanostructured graphene device can harvest ambient noise thanks to its intrinsically anharmonic deformation potential, outperforming conventional linear oscillators. A linear oscillator of a size comparable to our device is estimated to harvest 2.2 pW of mechanical power, almost one order of magnitude less than flat graphene. Under an appropriate compressive strain the graphene sheet assumes a buckled configuration and behave as a bistable device. Such an engineered nonlinearity is shown to broaden the spectral response, extending it toward the low-frequency domain, where most of the ambient energy source is typically available. Mechanical-to-electrical energy conversion through a model piezoelectric transduction scheme is briefly discussed.

L.G. acknowledges financial support of the Future and Emerging Technologies (FET) programme of the European Commission (FPVII, Grant Agreement No. 256959, NANOPOWER and Grant Agreement No. 270005, ZEROPOWER). Funding under Contract Nos. TEC2009-06986, FIS2009-12721-C04-03, CSD2007-00041, and ENE2009-14340-C02-02 are greatly acknowledged.

*rrurali@icmab.es

[1] E. Pop, Nano Rese. **3**, 147 (2010).
[2] J. Song, J. Zhou, and Z. L. Wang, Nano Lett. **6**, 1656 (2006).
[3] X. Wang, J. Song, J. Liu, and Z. L. Wang, Science **316**, 102 (2007).
[4] S. P. Beeby, M. J. Tudor, and N. M. White, Meas. Sci. Technol. **17**, R175 (2006).
[5] S. Roundy, J. Intell. Mater. Syst. Struct. **16**, 809 (2005).
[6] J. Paradiso and T. Starner, IEEE Pervasive Comput. **4**, 18 (2005).
[7] Z. L. Wang and J. Song, Science **312**, 242 (2006).
[8] K. A. Cook-Chennault, N. Thambi, M. A. Bitetto, and E. Hameyie, Bull. Sci. Technol. Soc. **28**, 496 (2008).

[9]V. Balzani, A. Credi, and M. Venturi, Chem. Soc. Rev. **38**, 1542 (2009).

[10]S. Meninger, J. Mur-Miranda, R. Amirtharajah, A. Chandrakasan, and J. Lang, IEEE Trans. Very Large Scale Integration (VLSI) Syst. **9**, 64 (2001).

[11]S. Roundy and P. K. Wright, Smart Mater. Struct. **13**, 1131 (2004).

[12]P. A. Truitt, J. B. Hertzberg, C. C. Huang, K. L. Ekinci, and K. C. Schwab, Nano Lett. **7**, 120 (2007).

[13]F. Cottone, H. Vocca, and L. Gammaitoni, Phys. Rev. Lett. **102**, 080601 (2009).

[14]E. Cadelano, P. L. Palla, S. Giordano, and L. Colombo, Phys. Rev. Lett. **102**, 235502 (2009).

[15]L. Gammaitoni, I. Neri, and H. Vocca, Appl. Phys. Lett. **94**, 164102 (2009).

[16]C. Jarzynski, Séminaire Poincaré XV Le Temps, p. 77 (2010).

[17]J. M. Soler, E. Artacho, J. D. Gale, A. García, J. Junquera, P. Ordejón, and D. Sánchez-Portal, J. Phys. Condens. Matter **14**, 2745 (2002).

[18]J. P. Perdew, K. Burke, and M. Ernzerhof, Phys. Rev. Lett. **77**, 3865 (1996).

[19]V. Kaajakari, *Practical MEMS* (Small Grid Publishing, Las Vegas, NV, 2009).

[20]J. Atalaya, A. Isacsson, and J. M. Kinaret, Nano Lett. **8**, 4196 (2008).

[21]J. S. Bunch, A. M. van der Zande, S. S. Verbridge, I. W. Frank, D. M. Tanenbaum, J. M. Parpia, H. G. Craighead, and P. L. McEuen, Science **315**, 490 (2007).

[22]C. Seoánez, F. Guinea, and A. H. Castro Neto, Phys. Rev. B **76**, 125427 (2007).

[23]Upon compression the potential energy of the graphene sheet grows, thus its kinetic energy has to decrease.

[24]T. Galchev, H. Kim, and K. Najafi, Procedia Chem. **1**, 1439 (2009).

[25]F. Bernardini, V. Fiorentini, and D. Vanderbilt, Phys. Rev. B **56**, R10024 (1997).

[26]M.-H. Zhao, Z.-L. Wang, and S. X. Mao, Nano Lett. **4**, 587 (2004).

Paper C

Microelectronic Engineering 111 (2013) 122–125

Contents lists available at SciVerse ScienceDirect

Microelectronic Engineering

journal homepage: www.elsevier.com/locate/mee

Buckling suspended graphene nanoribbons to harvest energy from noisy vibrations

M. López-Suárez [a,*], R. Rurali [b], G. Abadal [a]

[a] Departament d'Enginyeria Electrònica, Universitat Autònoma de Barcelona, E-08193 Bellaterra, Barcelona, Spain
[b] Institut de Ciència de Materials de Barcelona (ICMAB-CSIC), Campus de Bellaterra, E-08193 Bellaterra, Barcelona, Spain

ARTICLE INFO

Article history:
Available online 26 February 2013

Keywords:
Energy harvesting
Energy scavenging
Bistable systems
Non-linear systems
Graphene
Micro/nanoelectromechanical systems (M/NEMS)

ABSTRACT

Most mechanical vibrations in our environment can be classified as noisy vibrations, since they have no preferred frequency and a spectrum that spreads to the low frequency range. Bistable systems have shown to be a solution to the existing frequency mismatch between the energy source and the harvester device. In this work a parametric study is carried out in order to show the dependence of these improvements with the quality factor Q of a vibrating beam and the different responses when driven by different types of model noise. Specifically, we studied Colored Gaussian Noise instead of the much more common White Gaussian Noise, considered as a reference in most studies.

1. Introduction

Mechanical vibration harvesters are mostly based on resonators capable of transducing the energy from the mechanical to the electrical domain through piezoelectric, electromagnetic or capacitive strategies [1]. The need to deal with low intensity vibrations makes the use of MEMS/NEMS suitable in order to improve the response of the device in terms of the ratio between input and output power. The reduction of the dimensions of such a resonator increases dramatically their resonant frequency [2,3]. This feature and the typical frequency selectivity of these devices make them not optimal to harvest energy from broad band noises, particularly when it extends to the low frequency range.

2. Modeling

In order to address the problems described above we propose a bistable device based on a suspended graphene nanoribbon: bistability has been demonstrated to improve the response in comparison with that of resonators when driven by noise [4]. The bistability is achieved by applying compression as it is shown in Fig. 1. Once the compression is applied the resonating behavior is broken and two new attractors appear symmetrically positioned with respect to the initial stable point ($x = 0$). The description of the graphene nanoribbon is done through the determination of the elastic potential energy through *ab initio* calculations as it is explained in [5]. Fig. 2 shows different potential energy curves that highlight the role of the compressive strain, i.e. the larger the compression, the larger the separation of the two attractors and the higher the barrier are. The inset shows the dependence of the barrier height and the minima position with the compression, which is the non-linearizing parameter. It is worth noting the strong non-harmonic shape the uncompressed case shows. Therefore, even when the system is not strained it shows a non-resonating behavior.

In this work we extend our previous report [5] by studying the response to different types of noise. Specifically, we start with a White Gaussian Noise (WGN) and then filter it to selectively eliminate the contributions of certain frequency range, as discussed below. Additionally, we focus on the dependence of the performances of the harvesting device on the quality factor Q, which is a highly variable parameter and might vary significantly from realization to realization of the device.

3. Simulation and results

To characterize the dynamics of this kind of system a Langevine differential equation of motion must be solved numerically:

$$m_{eff} \cdot x'' = -dE_p/dx - b \cdot x' + F_n(t) \quad (1)$$

where m_{eff} stands for the effective mass as it is defined in the frame of the spring-mass model [6] and x, x' and x'' are the position vector and its first and second time derivatives, respectively. The constant b accounts for the losses in the system which we assume to be dominated by friction processes, and can be expressed in terms of the quality factor as follows:

$$b = m_{eff} \cdot \omega_0/Q \quad (2)$$

* Corresponding author. Tel.: +34 93 581 35 24.
E-mail address: miquel.lopez@uab.cat (M. López-Suárez).

0167-9317/$ - see front matter © 2013 Elsevier B.V. All rights reserved.
http://dx.doi.org/10.1016/j.mee.2013.02.053

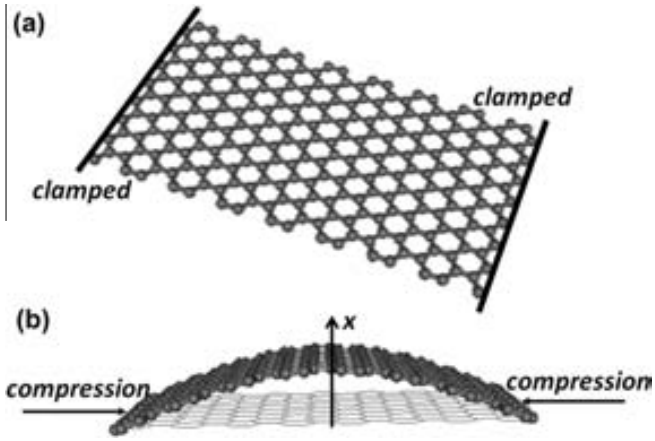

Fig. 1. (a) Scheme of the structure showing the two clamped ends and the *arm-chair* configuration along the longitudinal axis it has been considered. (b) Illustration of the compression applied in the *arm-chair* direction in order to produce the bistability. The *x*-coordinate is shown and it is considered as the only displacement direction of the mechanical system in the dynamical regime.

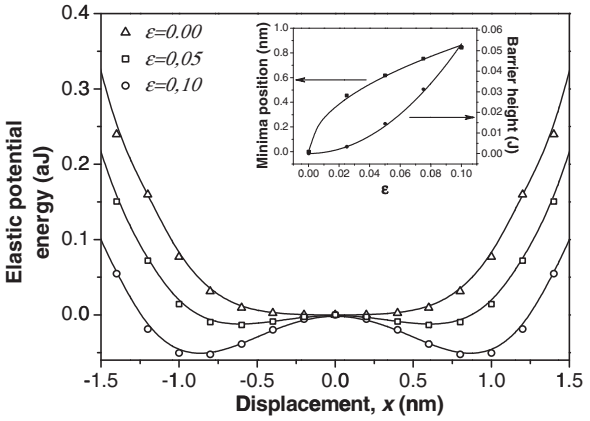

Fig. 2. Elastic potential energy for three different compressions starting from the non-stressed configuration. The inset shows the dependence of the well position and the potential barrier height between minima with the compression: $x_{\pm} = 8.64\sqrt{\varepsilon}$ Å; $\Delta V = 0.05\ \varepsilon^2 aJ$.

F_n describes the force suffered by the oscillator when it is driven by a mechanical vibration and it will have a root mean square value of 2.2 pN from now on, which corresponds to a sound pressure of approximately 200 dB.

In order to describe the dynamics of the system we considered a WGN excitation. Although real vibrations are better approximated by a colored noise, we first analyze this reference case due to its relevance to previous literature. Fig. 3 shows the dynamics in terms of trajectory and phase portrait. Three different working regimes, corresponding to different compression values, are displayed. For a non-stressed graphene system the dynamics is that of a resonator with a single attractor i.e. it oscillates around $x = 0$. For larger values of ε the trajectory shows oscillations around just one of the two wells. However, at intermediate compressions the system can suffer transitions from one attractor to the other, then increasing the root mean square of the position vector as it is shown in Fig. 4. The increase of x_{rms} is understood as an improvement with respect to the non-stressed case and it is very closely related to the capability of generating electric power when allowing the transduction [4]. In order to compute the generated power, a piezoelectric method of transduction is considered, as previously proposed in [5]. Fig. 4 shows a shift of the peak towards smaller compression values between the x_{rms} computed when no transduction is considered and when it is. It can be easily understood in terms of available energy: during transduction some of the energy is extracted, thus leaving less energy to overcome the potential barrier. Notice that there is also a difference between the optimal compression for the x_{rms} and this for the P_{rms}. Under certain conditions there can be an absolute match [7], though these cannot be applied in our particular case due to the very high time constant $\tau = RC$ of the electromechanical system [5].

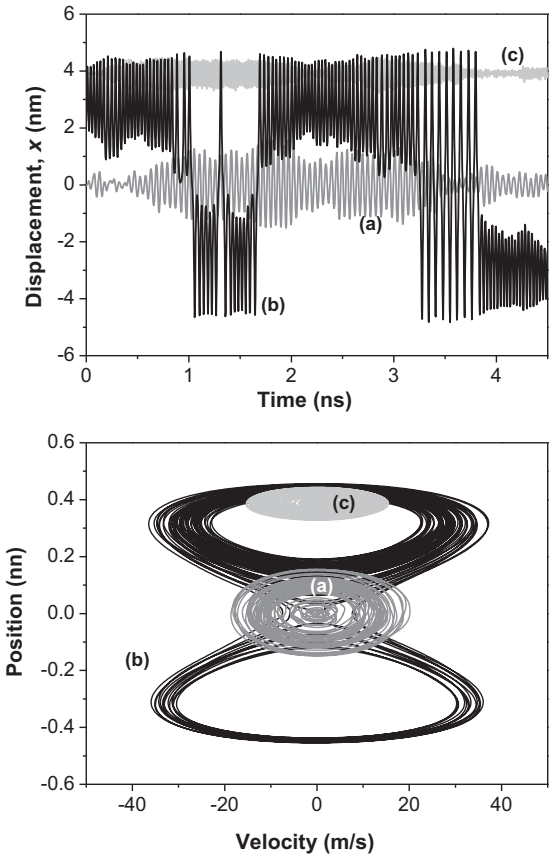

Fig. 3. Displacement vs time and phase portrait for the three different regimes: (a) non compressed case. The system oscillates around the attractor positioned at $x = 0$. (b) Medium compression applied. The excitation makes the system to cross from one well to the other. (c) Large compression. The system gets stuck in one of the two minima.

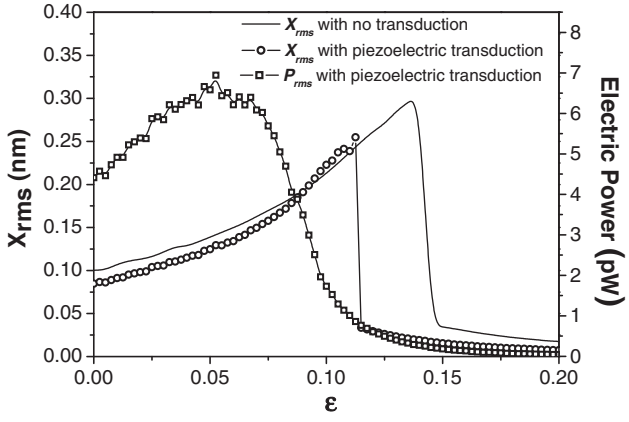

Fig. 4. Root mean square of the displacement *x* and the generated electric power as a function of the applied compression.

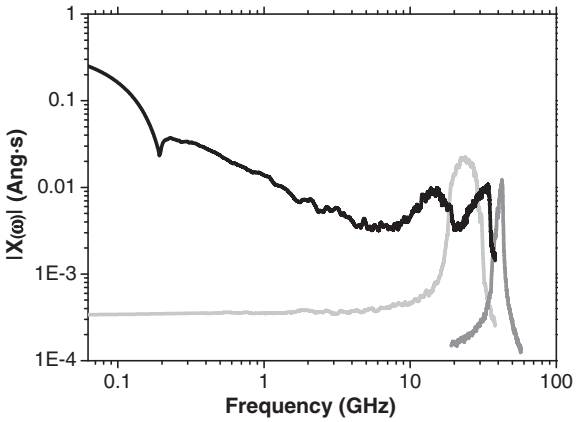

Fig. 5. Frequency response for the three different regimes of the purely mechanical case. The black line related to the bistable condition spreads towards the low frequency range while the other two curves present a well defined peak related to a preferred range of frequencies centered at the high frequency range that maximizes the response.

The value of the optimal compression to be applied depends on the kind of vibration taken into account and its intensity as later will be discussed. Generally one can argue that more energy leads to larger values for the optimal compression.

In Fig. 5 the spectra for the three purely mechanical regimes showed in Fig. 3 are shown. The optimal compression spreads the spectrum to the low frequency range increasing the area under the curve indicating an increase of the response in that domain. The other two curves show preferred frequencies specified by the curvature of the elastic potential energy around the minima where the system is stuck thus lowering the amount of harvested energy.

3.1. Noise issues

The broadening of the spectrum in the low frequency range must not be understood as a larger response to the components of the driving force at that frequency range. This is just applicable to linear systems. In the next lines the responses of the system to different kinds of noise will be discussed in order to justify the previous affirmation.

We start again from a WGN and then we follow by different filtering of this first case as it is showed in the corresponding insets of Fig. 6. Although the spectra of these noisy vibrations are very different among them, they preserve their root mean square value. It seems clear that no remarkable change is induced in the x_{rms} curves not even for the value of the optimal compression to be applied.

This points out that the response in the low frequency range is not due to excitations at that particular interval as it has been said before. Bistability improves the features of resonating systems not just for those drift by WGN but also for different broad band excitations.

3.2. The importance of the quality factor

It has been reported that graphene resonators can have a very high quality factor Q [8]. However, as Q is very hard to control,

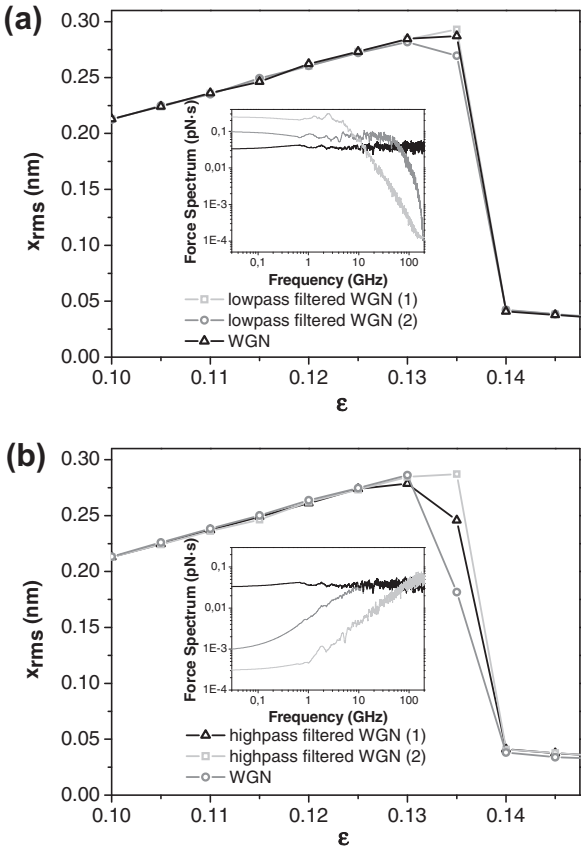

Fig. 6. Root mean square of the displacement x for two different kinds of noise: Low pass (a) and High pass (b) filtered noises maintaining constant the root mean square of these driving forces.

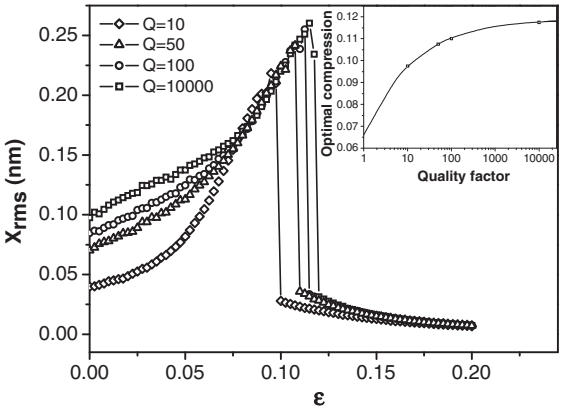

Fig. 7. $x_{\rm rms}$ vs compression for different Q factors from 10 to 10000 showing the increase of both the optimal compression value, $\bar{\epsilon}$, and the peak height. The inset displays this change of $\bar{\epsilon}$ together with fits to $1/\epsilon^4$.

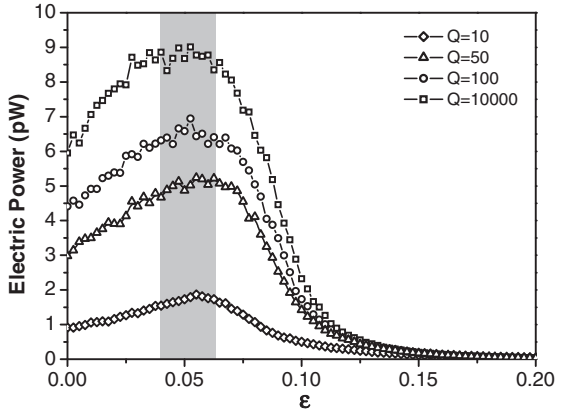

Fig. 8. P_{rms} vs compression for different Q factors showing no big differences of the range of compressions that maximizes the output power. The shadowed area remarks those optimal values.

especially considering its strong dependence on the environmental conditions, it is reasonable to consider it as a main parameter of the system and to study to what extent it affects the dynamics of the system, while keeping the WGN intensity constant. We take Q to vary from 10 to 10,000, which is a common range for this parameter according to the values reported in the literature [8].

As it can be seen from Eq. (2) friction losses, i.e. the damping parameter, b are inversely proportional to the quality factor: large values of Q leads to small losses, thus more energy can be in principle harvested. Indeed, this is what can be observed in Fig. 7: the reduction of the friction is expressed as an increment of both the optimal compression and the corresponding x_{rms} peak. There is a slight difference between the dependence with Q of x_{rms} and P_{rms} as it can be seen in Fig. 8.

There is no appreciable shift of the optimal compression that stands around 0.05 for all quality factors values. An increase of the harvested power can be observed as well.

4. Conclusions

A theoretical work has been done in order to put some light on the possibility of using mechanical graphene resonators as energy harvesters. The atomistic computations show some peculiarities which are characteristics of these kinds of systems and allow a well-grounded description of the device. We also show how bistable systems are not just interesting when driven by WGN but also for different spectral kinds of noisy inputs. A piezoelectric method of transduction has been considered in order to give concrete electric power values taking into account the dependence with the quality factor associated to a mechanical structure of this kind: the maximum generated power for the device considering $Q = 10{,}000$ is around 9 pW, which drops to 2 pW for $Q = 10$.

Acknowledgements

The authors would like to thank the Ministerio de Ciencia y Innovación de España for financially supporting this research under the project OPACMEMS No. ENE2009-1430-CO2-02.

References

[1] S. Beeby, M. Tudor, et al., Measurement Science and Technology 17 (12) (2006) R175.
[2] A.N. Cleland, M.L. Roukes, Applied Physics Letters 69 (18) (1996) 2653–2655.
[3] D. García-Sánchez, A. San Paulo, et al., Physical Review Letters 99 (8) (2007) 85501.
[4] F. Cottone, H. Vocca, et al., Physical Review Letters 102 (8) (2009) 80601.
[5] M. López-Suárez, R. Rurali, et al., Physical Review B 84 (16) (2011) 161401.
[6] V. Kaajakari, Practical MEMS: Design of Microsystems, Accelerometers, Gyroscopes, RF MEMS, Optical MEMS, and Microfluidic Systems, Small Gear, Estados Unidos, 2009.
[7] L. Gammaitoni, I. Neri, et al., Applied Physics Letters 94 (16) (2009) 164102–164103.
[8] A. Eichler, J. Moser, et al., Nature Nanotechnology 6 (6) (2011) 339–342.

Paper D

Piezoelectric monolayers for energy harvesting

Miquel López-Suárez
Departament d'Enginyeria Electrònica, Universitat Autònoma de Barcelona, 08193 Bellaterra, Barcelona, Spain

Miguel Pruneda
ICN2 - Institut Catala de Nanociencia i Nanotecnologia, Campus UAB, 08193 Bellaterra (Barcelona), Spain and CSIC - Consejo Superior de Investigaciones Cientificas, ICN2 Building , Campus UAB ,08193 Bellaterra (Barcelona), Spain

Gabriel Abadal
Departament d'Enginyeria Electrònica, Universitat Autònoma de Barcelona, 08193 Bellaterra, Barcelona, Spain

Riccardo Rurali
*Institut de Ciència de Materials de Barcelona (ICMAB–CSIC) Campus de Bellterra, 08193 Bellaterra, Barcelona, Spain**
(Dated: November 6, 2013)

We study the dynamics of h-BN monolayers by first performing *ab-initio* calculations of the deformation potential energy and then solving numerically a Langevine type equation to explore their use in vibration energy harvesting devices. Similarly to our previous proposal for a graphene-based harvester [López-Suárez et al., Phys. Rev. B **84**, 161401(R) (2011)], an applied compressive strain is used to drive the system into a bistable regime, where quasi-harmonic vibrations are combined with low frequency swings between the minima of a double-well potential. Due to its intrinsic piezoelectric response, the mechanical harvester naturally provides an electrical power that is readily available or can be stored by simply contacting the monolayer at its ends. Engineering the induced non-linearity, a 20 nm^2 device is predicted to harvest an electrical power of up to 0.18 pW for a noisy vibration of 5 pN.

Two-dimensional materials, such as graphene and other monolayer systems [1] exhibit many properties that render them promising candidates for electromechanical actuation [2]. Suspended nanostructures that combine a low mass density and relatively large areas seem to be ideally suited for the harvesting of mechanical vibrations and other energy sources that are freely available [3, 4]. Harmonic oscillators are, in most of the cases, very good approximations of the dynamical behavior of these systems. Nevertheless, a harmonic oscillator is very sensitive around a set of frequencies its resonant frequencies but responds poorly otherwise. Unfortunately, ambient vibrations and thermo-mechanical noise have normally a very broad frequency spectrum that extends into the very low frequency region (typically below 100 Hz). Harmonic oscillators that respond in such frequency range, besides being intrinsically inefficient, would be extremely large, making their use in self-powering of small devices impractical. To overcome this limitation, mechanical harvesters with non-linear potentials have been analyzed and compared to linear resonators [5] as optimal alternatives when the energy sources are stochastic and characterized by a wideband spectrum [6 8].

Following the ground-breaking work of Cottone *et al.* [9], in a previous study we have shown how engineered non-linearities can increase the efficiency of ambient vibration harvesting of a suspended graphene nanoribbon [10]. By compressively straining it, the graphene sheet is driven into a bistable regime that maximizes the root mean square (rms) of the displacement, thus the mechanical power. However, harvested mechanical power is difficult to use and it is desirable to convert it into electrical energy, which can be straightforwardly stored. Although piezoelectricity the electrical response to applied mechanical stress is not one of the many outstanding properties of graphene, non-centrosymmetric monolayers have been predicted to have remarkable intrinsic piezoelectric coefficients [11].

In this work we discuss the nanoscale implementation of a bistable device based on piezoelectric h-BN capable of harvesting thermo-mechanical noise and low frequency vibrations from the environment, yielding an electrical voltage due to the intrinsic electromechanical response of these materials. Remarkably, the generated voltage is mostly independent of the degree of strain, as long as the resonator operates in the bistable regime.

Our device consists of a 20 nm long (17 nm suspended) single-layer h-BN subjected to compressive strains ranging from 0 to 2 %. Upon compression the monolayer favors two buckled ground states, symmetric with respect to the plain defined by the ideal flat layer. A sketch of the system is shown in Fig. 1. As in our previous work[10], we calculated the deformation potential of the vibrating system, and the changes in induced polarization due to the mechanical deformation by means of atomistic first-principles calculations within density-functional theory (DFT) as implemented in the Siesta package [12].

To reduce the computational load, we consider the two-

*rrurali@icmab.es

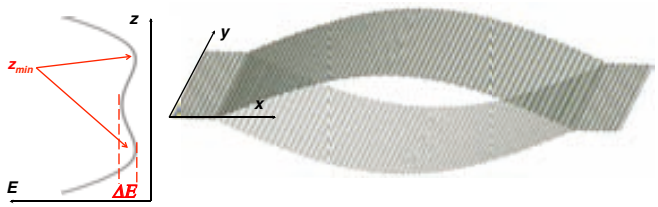

FIG. 1. Sketch of the h-BN structure studied, highlighting the two symmetric equilibrium configurations under compressive strain. The double-well potential is shown on the left-hand side.

dimensional material, rather than a nanoribbon with finite width. The energies quoted in the text have been obtained by rescaling the results obtained for the computational cell and thus neglect edge effects. which can generate stress fields and ripples. These effects are not accounted for in our model. However, the dynamic response of the system is not expected to qualitatively change.

Changes in polarization are calculated using the standard Berry's phase approach [13]. The Brillouin zone was sampled with a grid of 1 × 14 × 1 k-points. We used norm-conserving pseudopotentials to account for the core electrons and the generalized gradient approximation (GGA) for the exchange-correlation functional [14]. We used a carefully optimized single-ζ polarized basis set to expand the one-electron wave function [15]. This lighter basis set allowed us to deal efficiently with the large number of structures involved and with the computationally intensive calculations of the polarization, maintaining a very good accuracy (tests against a high-quality optimized double-ζ basis set gave lattice parameter and piezoelectric constant of h-BN within 3 and 2 %, respectively).

The two minimum energy configurations that appear under compressive strain are separated by a barrier whose maximum corresponds to the strained, flat layer (see Fig. 2). Increasing the compression leads to higher barriers and larger separation between the minima, as shown in the left inset (see also Ref. [10]). Notice that $E_s(\epsilon) = E(\epsilon)|_{z=0} - E(0)|_{z=0}$ is the energy cost of sustaining a strain ϵ. By performing a similar set of calculation for tensile strains the uniaxial Young modulus can be estimated as $Y = \frac{1}{V_0}\frac{\partial^2 E_s}{\partial \epsilon^2}|_{\epsilon=0}$, where V_0 is the equilibrium volume [16] (right inset of Fig. 2). We obtain a value of 0.85 TPa, in good agreement with previous results [17].

Non-centrosymmetric planar BN sheet develops an electric dipole moment either by (i) the applied uniaxial strain (*direct piezoelectric effect*, $z = 0$ and $\epsilon > 0$), (ii) the elastic deformation induced by the vibrating mode (*flexoelectric effect*, $z \neq 0$ and $\epsilon = 0$) or (iii) a combination of the two ($z \neq 0$ and $\epsilon > 0$). The uniaxial strain is the simplest of these cases: it yields an electrical polarization aligned with the straining direction which depends linearly on the strain through the piezoelectric constant of the material, $P = \alpha\epsilon$. We have estimated this parameter by applying increasingly higher uniaxial strains

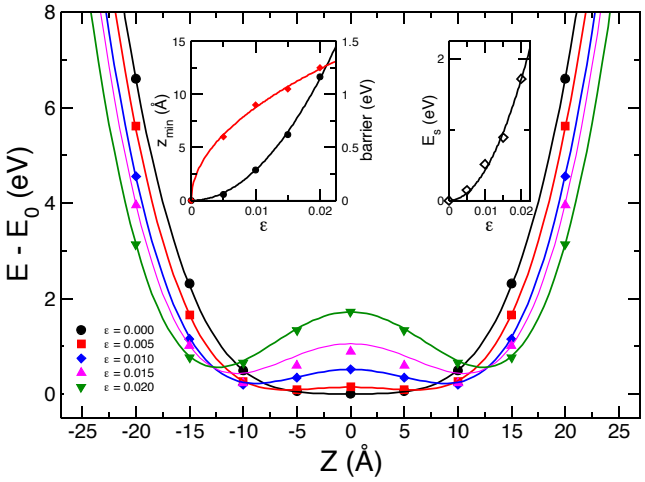

FIG. 2. Potential energy as a function of the amplitude of the sinusoidal deformation for different values of the compressive strain ϵ. The position of the minima and the height of the barrier between them are plotted in the left inset (symbols). Fits (continuous line) reveal the $\sqrt{\epsilon}$ and ϵ^2 dependence of these two quantities. Energies of the main panel are referred to the energy of the flat and unstrained h-BN sheet. The right inset show how the energy increases upon straining, i.e. the strain energy. Its dependence on the strain ϵ is used to extract the Young's modulus (see text).

to the BN sheet and calculating the polarization, obtaining a value of $3.085{\cdot}10^{-10}$ C/m in good agreement with previously published results [18]. The situation becomes considerably more intricate when out of plane displacements are involved. As discussed in detail by Naumov *et al.* [18], these configurations feature not only a finite strain, but also a strain gradient. Therefore the polarization also includes a flexoelectric term, beside the conventional piezoelectric response. Our numerical results are in excellent agreement with the phenomenological expression of P induced by a sinusoidal out-of-plane displacement of Ref. [18] (circles and continuous line in the inset of Fig. 3, respectively). The calculated values of the polarization as a function of the applied strain and of the amplitude of the sinusoidal vibration (symbols in Fig. 3) can be satisfactorily fitted to a biquartic polynomial (continuous lines in Fig. 3).

We now move to the study of the dynamical behavior of the device, which is described by the equation of motion:

$$m\ddot{z} = -\frac{\partial E}{\partial z} - b\dot{z} + F_0\xi(T) \qquad (1)$$

where E is the elastic (potential) energy as obtained by the *ab initio* calculations and reported in Fig. 2, m is the effective mass (taken to be 0.4 times the total mass [19]), and b is a viscous damping coefficient [20] related to the quality factor Q through $b = 2\pi f_0 m/Q$. We have considered $Q = 100$ throughout all this work [21, 22]. $F_0\xi(T)$ represents a random force with flat spectrum that reproduces the main characteristics of most kinds of environmental vibrations. We take a noise intensity of

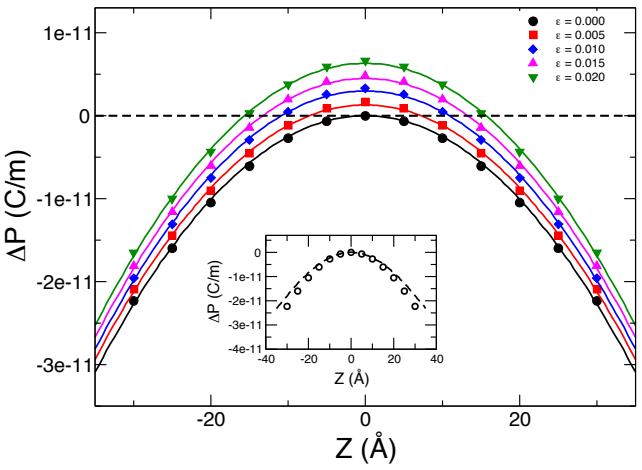

FIG. 3. Electrical polarization as a function of the amplitude of the sinusoidal deformation for different values of the compressive strain ϵ. The continuous lines are fits of the *ab-initio* data to a biquartic polynomial. The inset shows the good agreement between our calculated data (symbols) for $\epsilon = 0$ and the phenomenological relation given in Naumov *et al.* [18] (dashed line), where the polarization is related to the amplitude of the sinusoidal deformation.

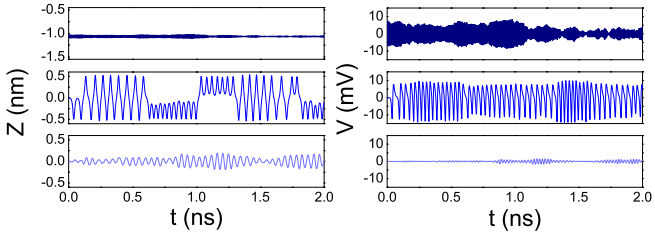

FIG. 4. Time evolution of the generalized coordinate z (left) and the generated voltage V (right) in the three characteristic regimes: (i) at no compression the single-well potential is quasi-harmonic (bottom); (ii) a moderate strain induces the bistable dynamics (middle); (iii) at large strains the dynamics is trapped in one of the minima of the double-well potential (top). These simulations correspond to a 200 Å × 10 Åh-BN monolayer.

5 pN, which suits most vibrational ambient noise [23] (for comparison, 1 pN corresponds to room temperature pure thermo-mechanical noise).

Notice that having fitted the calculated polarizations for arbitrary compressions, together with the generalized position z, we can also trace the dynamical evolution of the polarization and, consequently, of the generated voltage across a load R_L by solving [24]

$$m\ddot{z} = -\frac{E}{z} - bz - \Gamma_1 \frac{P_x^{2D}}{z} z + F_0 \xi(T) \qquad (2)$$

$$V = \Gamma_2 \frac{P_x^{2D}}{z} \dot{z} - \frac{1}{R_L C_p} V \qquad (3)$$

where P_x^{2D} is the 2D polarization along x, C_p is the capacity of an infinite parallel wire capacitor analogous to our system [25], $\Gamma_2 = w\ C_p$, w being the layer thickness, is the electromechanical coupling coefficient [26] and $\Gamma_1 = \Gamma_2\ C_p$. R_L is taken to be 2.4 GΩ, which is the impedance matched value that maximizes the electrical power (see below).

The device exhibit three distinct modes of operation that are summarized in Fig. 4, where we plot z and V as a function of time (left and right column, respectively). (i) At moderate compressive strains the BN sheet vibrate around the equilibrium position of the unstrained system, i.e. the flat sheet, and a voltage of at most 1 mV is generated (bottom panels). (ii) As the strain increases the two potential wells appear: the system will vibrate around the equilibrium position of one of them, but if the barrier is not too high it will be able to stochastically swing to the other well. When bistability kicks in the greatly increased z_{rms} results in a voltage which is almost one order of magnitude larger (middle panels). (iii) Finally, for high values of the strain, the barrier will be high enough for the system to remain trapped in one of the two minima (top panels). Interestingly, although z_{rms} is reduced and is even smaller than for the uncompressed sheet, the generated voltage is of the same order of the purely bistable case (top panels).

To further investigate the evolution of the dynamics with stress, Fig. 5 shows the rms of the generalized coordinate z and the harvested electrical power [9], $P_{rms} = V_{rms}^2\ R_L$, are plotted as a function of the applied strain. Increasing the strain drives progressively the vibrating sheet into the bistable regime, z_{rms} goes through a steep increase and the harvested power follows it. At $\epsilon \sim 0\,3$ z_{rms} is maximum and features a sharp peak: slightly larger strains trap the system in one of the minima of the double-well potential. In this regime, nonetheless, the harvested power starts to be dominated by the polarization, which experiences very large changes even for small variations of the amplitude of the vibrating mode. This increase of $\frac{P_x^{2D}}{z}$ almost entirely balances the reduction in z_{rms}.

This fact has important consequences from the device design viewpoint, because one can pursue the optimal compression $\epsilon \sim 0\,3$ without risking that small errors can suddenly drive the system into an operation regime where the efficiency is even lower than with the unstrained sheet. When the optimal strain is exceeded, the device progressively recovers a quasi-linear behavior with an harvested electrical power that is still within 85% its maximum value.

We conclude by observing that the overall performance in term of energy harvesting has two components: (i) the intrinsic properties of the material, such as the piezoelectric coefficient or the Young s modulus and (ii) the way the device is engineered. Although these two components are not independent (the optimal strain, for instance, depends on the material compressibility), it seems that other 2D materials with a larger piezoelectric response would in principle result in more

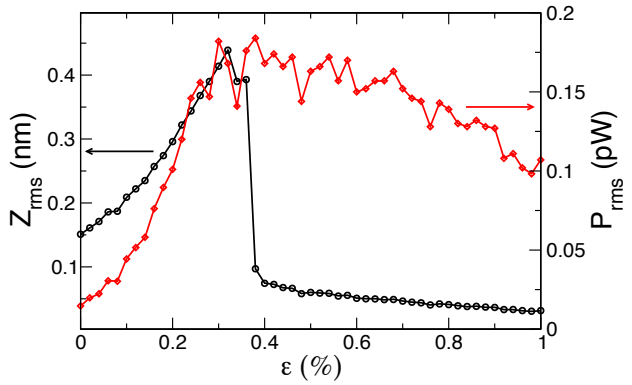

FIG. 5. Root mean squares of z and of the harvested electrical power as a function of the compressive strain ϵ. The sudden drop of z_{rms} at large values of ϵ is balanced by the increase in P_x^{2D}, thus the harvested power decreases gently after its maximum for the optimal compression. These simulations correspond to a 200 Å × 10 Åh-BN monolayer.

efficient harvesting. A good candidate is MoS_2, which has larger piezoelectric coefficients (in good agreement with previous studies [11], we have obtained values of $3.87{\cdot}10^{-10}$ and $3.81{\cdot}10^{-10}$ C/m in the relaxed-ion and clamped-ion frameworks, respectively, to be compared with $3.085{\cdot}10^{-10}$ and $2.855{\cdot}10^{-10}$ C/m for h-BN). Unfortunately, we could not observe buckling of the MoS_2 sheet, as it is much stiffer than one atom thick h-BN concerning out-of-plane displacements. The larger piezoelectric coefficients do not compensate the lack of bistability and at this size the choice of h-BN still pays off. For longer ribbons, currently beyond our computational capabilities, buckling should be observed and the overall performances of a MoS_2-based harvester could probably exceed those of h-BN. More work in this direction is needed.

In conclusions, we have shown that engineered nonlinearities in piezoelectric two-dimensional system such as monolayer h-BN can lead to sizeable energy harvesting of ambient vibrations, thermo-mechanical and other broad band energy source freely available. In particular, a 20 nm × 1 nm h-BN monolayer under a compressive strain $\epsilon = 0.3$ % can harvest up to 0.18 pW from a 5 pN vibration. Finally, the combination of piezoelectric and mechanical bistability properties of the suspended BN structures can pave the way for the future development of beyond CMOS devices that could perform sensing, computing and transmission functions at the nanoscale in a selfpowered way.

ACKNOWLEDGMENTS

Funding from the Ministerio de Ciencia e Innovación under contract No ENE2009-14340-CO2-02 (OPACMEMS) and FIS2012-37549, and from the EU-FP7 FET-Proactive Coordination Action, Project no. 270005 (ZEROPOWER), are greatly acknowledged. We thank the Centro de Supercomputación de Galicia (CESGA) for the use of their computational resources.

[1] K. S. Novoselov, J. D., S. F., B. T. J., K. V. V., M. S. V., and A. K. Geim, Proc. Natl. Acad. Sci. USA **102**, 10451 (2005).
[2] Y. Huang, J. Liang, and Y. Chen, J. Mater. Chem. **22**, 3671 (2012).
[3] D. Garcia-Sanchez, A. M. van der Zande, A. San Paulo, B. Lassagne, P. L. McEuen, and A. Bachtold, Nano Lett. **8**, 1399 (2008).
[4] A. M. van der Zande, R. A. Barton, J. S. Alden, C. S. Ruiz-Vargas, W. S. Whitney, P. H. Q. Pham, J. Park, J. M. Parpia, H. G. Craighead, and P. L. McEuen, Nano Lett. **10**, 4869 (2010).
[5] V. Méndez, D. Campos, and W. Horsthemke, Phys. Rev. E **88**, 022124 (2013).
[6] N. A. Khovanova and I. A. Khovanov, Appl. Phys. Lett. **99**, 144101 (2011).
[7] E. Halvorsen, J. Microelectromech. Syst. **17**, 1061 (2008).
[8] E. Halvorsen, Phys. Rev. E **87**, 042129 (2013).
[9] F. Cottone, H. Vocca, and L. Gammaitoni, Phys. Rev. Lett. **102**, 080601 (2009).
[10] M. López-Suárez, R. Rurali, L. Gammaitoni, and G. Abadal, Phys. Rev. B **84**, 161401 (2011).
[11] K.-A. N. Duerloo, M. T. Ong, and E. J. Reed, J. Phys. Chem. Lett. **3**, 2871 (2012).
[12] J. M. Soler, E. Artacho, J. D. Gale, A. García, J. Junquera, P. Ordejón, and D. Sánchez-Portal, J. Phys.: Condens. Matter **14**, 2745 (2002).
[13] R. D. King-Smith and D. Vanderbilt, Phys. Rev. B **47**, 1651 (1993).
[14] J. P. Perdew, K. Burke, and M. Ernzerhof, Phys. Rev. Lett. **77**, 3865 (1996).
[15] E. Anglada, J. M. Soler, J. Junquera, and E. Artacho, Phys. Rev. B **66**, 205101 (2002).
[16] The equilibrium volume is defined by taking an effective thickness of 3.5 Å, which is the layer-to-layer separation in bulk h-BN.
[17] Q. Peng, W. Ji, and S. De, Comput. Mater. Sci. **56**, 11 (2012).
[18] I. Naumov, A. M. Bratkovsky, and V. Ranjan, Phys. Rev. Lett. **102**, 217601 (2009).
[19] V. Kaajakari, *Practical MEMS* (Small Grid Publishing, Las Vegas, Nevada, 2009).
[20] J. Atalaya, A. Isacsson, and J. M. Kinaret, Nano Lett. **8**, 4196 (2008).
[21] J. S. Bunch, A. M. van der Zande, S. S. Verbridge, I. W. Frank, D. M. Tanenbaum, J. M. Parpia, H. G. Craighead, and P. L. McEuen, Science **315**, 490 (2007).
[22] R. A. Barton, B. Ilic, A. M. van der Zande, W. S. Whitney, P. L. McEuen, J. M. Parpia, and H. G. Craighead, Nano Lett. **11**, 1232 (2011).
[23] M. López-Suárez, R. Rurali, L. Gammaitoni, and G. Abadal, Microelectronic Engineering **111**, 122 (2013).

[24] S. P. Beeby, M. J. Tudor, and N. M. White, Measurement Science and Technology **17**, R175 (2006), ISSN 0957-0233.

[25] A parallel wire capacitor has capacitance $C = \frac{\pi \epsilon w}{Ln(l_q/r_q)}$, where l_q is the separation between the charged edges, i.e. the length of the suspended ribbon, and r_q is the effective radius of the edge states, which can be approximated to be one lattice parameter [18].

[26] S. Roundy and P. K. Wright, Smart Materials and Structures **13**, 1131 (2004).

Paper E

Fabrication of highly regular suspended graphene nanoribbons through a one-step EBL process

[1]M. López-Suárez, [1]F. Torres, [2]N. Mestres, [2]R. Rurali, [1]G. Abadal

[1]Departament d'Enginyeria Electrònica, Universitat Autònoma de Barcelona, E-08193 Bellaterra, Barcelona, Spain
[2]Institut de Ciència de Materials de Barcelona (ICMAB-CSIC), Campus de Bellaterra, E-08193 Bellaterra, Barcelona, Spain

E-mail: Miquel.Lopez@uab.cat

Abstract
A method to obtain pre-oriented large 1-D arrays of identical suspended graphene nanoribbons is presented. Mechanical exfoliation from graphite was done in order to deposit single- and multiple-layered graphene over a Polymethyl-Methacrylate (PMMA) substrate, which is used as a sacrificial material. Electron Beam Lithography (EBL) is used to define the anchors and the suspended part of the structures. The method allows to achieve a high number of graphene suspended nanoribbons with a very regular width and length. The main advantage of the method, from the process point of view, with respect to other standard procedures is that only one EBL step is needed in the whole sequence, so that the overall process is extremely simplified.

1. Introduction

Graphene, among other 2D-structured materials, has attracted the attention for the last years of both experimental and theoretical researchers due to its outstanding mechanical [1-3] and electrical [4] properties. In particular, a lot of efforts have been devoted to the fabrication and characterization of graphene-based-nanoelectromechanical systems (NEMS) [5-9]. Graphene sheets can be obtained through chemical growth [10,11] or mechanical exfoliation of a primary graphite stack [12]. The latter is very common thanks to its simplicity, though its drawbacks are the low probability of obtaining single-layer graphene ribbons and the high shape variability they present from flake to flake, hindering the achievement of reproducible results for different ribbons and the systematic study of the properties of graphene-based NEMS.
Here we present a simple fabrication method that maximizes the probability of obtaining mono and bi-layered graphene (usually around 0.13%, or a total graphene area of 0.13 mm^2 per square centimeter of exposed area) and to largely reduce their geometric variability, controlling the orientation and increasing the shape regularity of the ribbons. The proposed method simply requires a standard mechanical exfoliation and the transfer of graphene flakes on a Si/Cr/Au/PMMA substrate as initial step,

followed by an EBL-based definition of large areas of nanotrenches on the PMMA layer at the flakes zone, to achieve suspended ribbons.

2. Fabrication process

A 20nm/100nm thick layer of chromium/gold is deposited on a p-type (100) silicon substrate 500μm thick. 950k molecular weight Polymethyl-Methacrylate (PMMA), 2% dissolved in anisole, is spun at 1500 rpm for 1 min. After spinning, the sample is baked in a hot plate to evaporate the anisole solvent at 180ºC for 1 min. The spinning/baking sequence is repeated 3 times in order to achieve a total PMMA layer 300 nm thick. Such a thickness will assure the suspension of the graphene structure once the sacrificial PMMA layer is removed. A scheme of the resultant stack can be seen in Fig. 1(a).
Mechanical exfoliation is done following a pseudo-standard procedure [12]. Once the multilayered graphene flake is attached to the scotch tape, the transfer is done pressing it onto the substrate and dragging a spatula following a certain *i*-direction, as represented on Fig.1(b and c). As it will be later discussed, the probability of obtaining a high density of graphene ribbons depends on the chosen dragging direction.

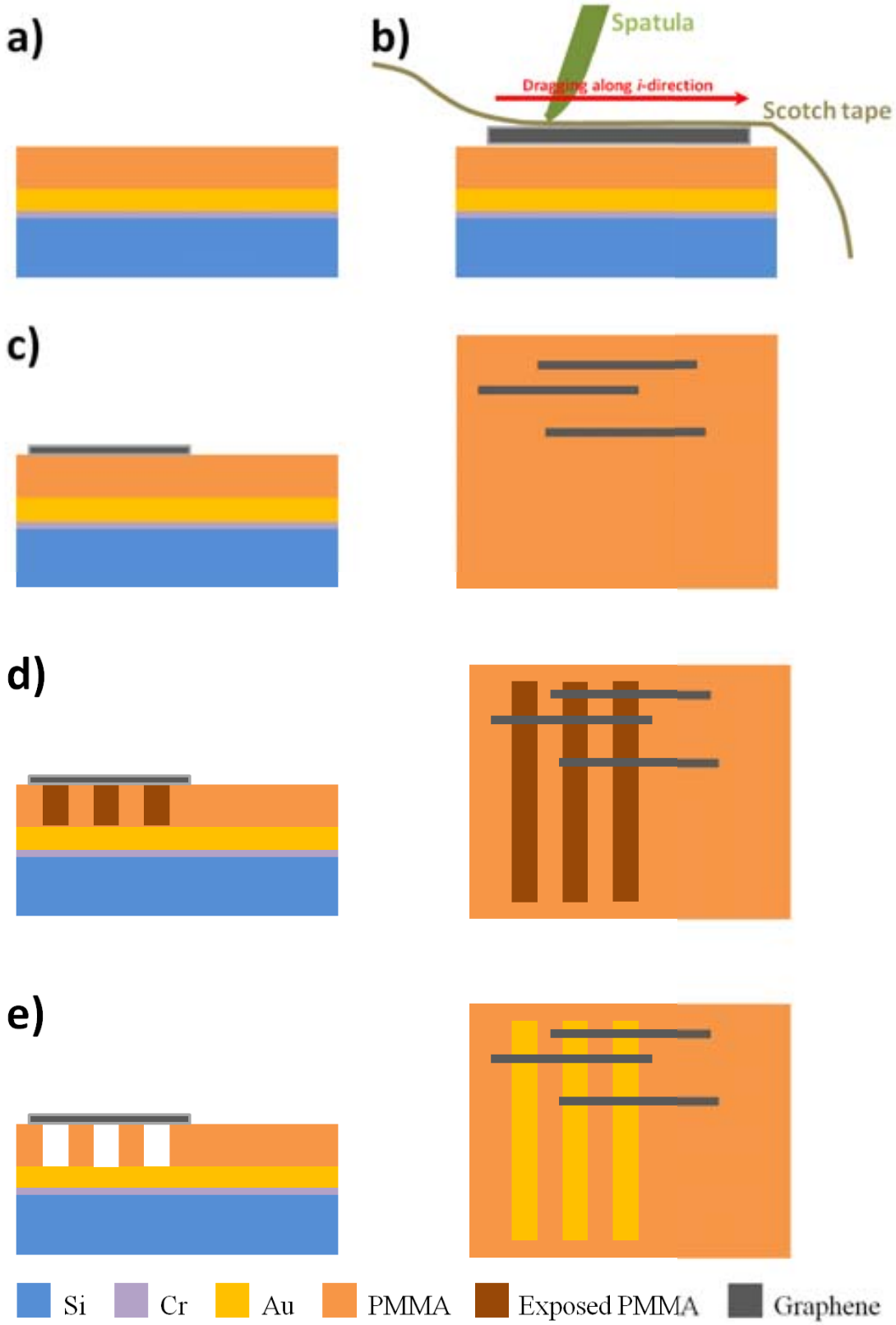

Fig. 1: Schematic representation of the fabrication process. (a) A stack of silicon (0.5 mm), chromium (20 nm), gold (100 nm) and PMMA (300 nm) is used as a substrate. (b) A non-abrasive spatula is used to favor the transfer along a certain direction. (c) A set of pre-oriented graphene ribbons are transferred onto the substrate. (d) The sample is exposed selectively to an EBL process to pattern the trenches. (e) The exposed PMMA is removed achieving the suspended devices. From (c) to (e), left and right figures correspond to cross-section and top-view of the sample, respectively.

Trenches are dug under graphene by exposing the PMMA selectively to Electron Beam Lithography (EBL) (Fig.1.d) and dipping the sample into a standard methyl isobutyl ketone/isopropyl alcohol developer (Fig.1.e). After removing the exposed PMMA, the graphene ribbons get released and the underlying Au film becomes visible, allowing a good contrast for SEM imaging. Different trench widths, that in turn determine the length of the suspended ribbons, are considered, i.e. 100, 300, 500 and 600 nm.

3. Characterization of the devices

3.1 Scanning Electron Microscopy inspection

Fig. 2 shows SEM images of a processed sample, where some graphene flakes (horizontal structures) on the trench patterned PMMA surface (vertical strips) are visible. Trenches have been defined with different widths depending on the sample, but those in Fig. 2(a) present only one single width value of 500nm. The trench widths determine the length of the suspended devices, yielding a high-degree of reproducibility of this dimension from ribbon to ribbon. All SEM images were performed with a tilt in the sample of 60 deg that provokes that only the center of the image is totally focused.

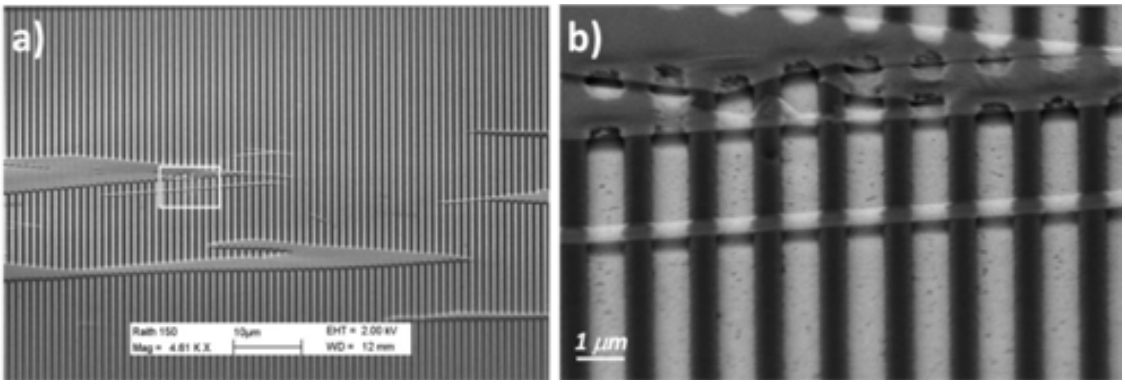

Fig. 2: SEM images of the sample with 500nm length suspended nanoribbons. (a) Shows a part of the area exposed to EBL. (b) Shows the detail of the white rectangle remarked in (a). A very straight primary ribbon can be seen presenting nine secondary ribbons with identic dimensions.

Different ribbons (defined as primary ribbons) containing each one several suspended devices (defined as secondary ribbons) can be seen. Fig. 2(b), in particular, shows a magnified SEM image of the obtained suspended graphene. As it can be seen, primary ribbons are remarkably straight, although they inevitably differ from one to another as a result of the exfoliation and transfer process. On the other hand, the secondary ribbons, i.e. the suspended devices, have very high shape regularity, with a constant width, w, and length, l. The obtained structures have a width between 0.5 and 1μm. Each primary ribbon can contain from 2 to up to 50 secondary ribbons, paving the way to a systematic study of their properties, due to their high regularity.

Fig. 3 shows a high resolution SEM image of three devices with different lengths, where it can be seen that the structure is fully suspended and all the PMMA under the

graphene ribbon has been removed. A narrower 100 nm trench was patterned in the sample of Fig. 3(b), besides those of 300 and 600 nm shown, but unfortunately they were not fully developed and we could not achieve the contrast exhibited by the other devices.

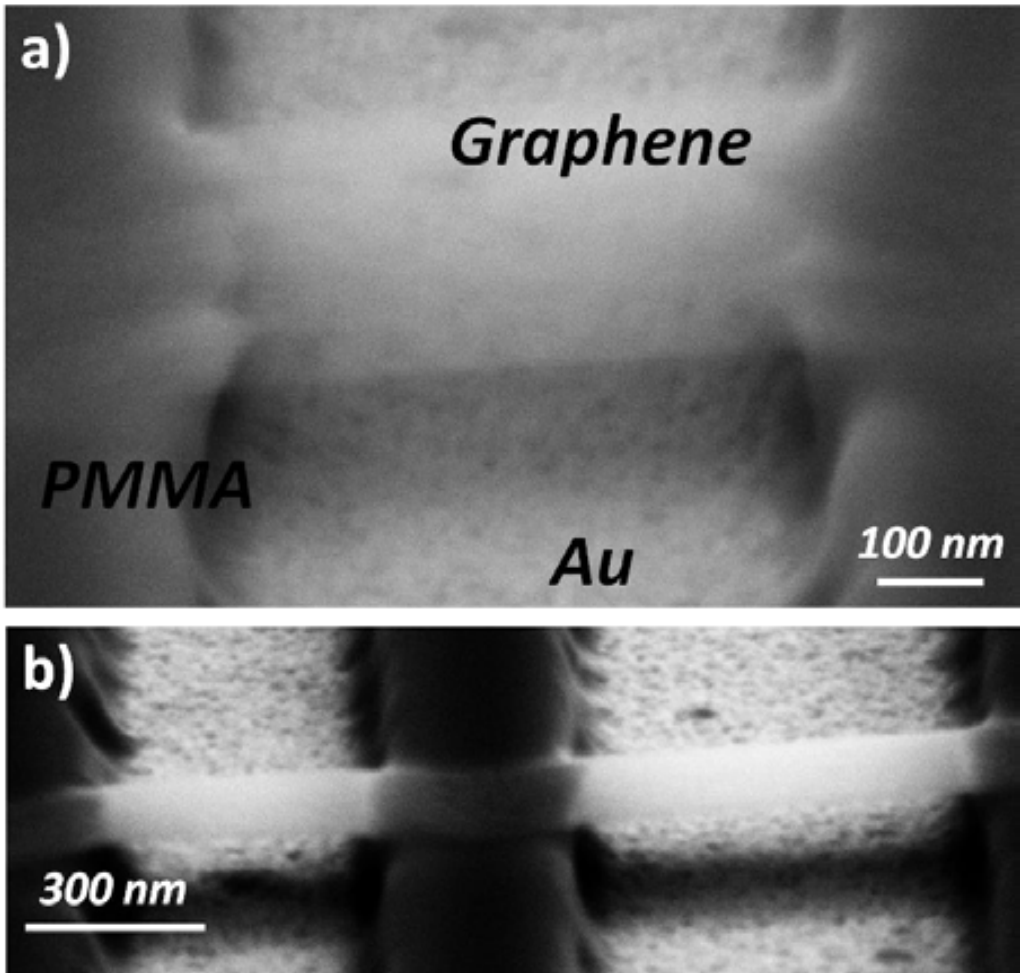

Fig. 3: High resolution SEM image for three different length suspended ribbons. (a) 500nm and (b) 300nm (left), 600nm (right).

3.2 Raman spectroscopy

Raman spectroscopy has been successfully utilized as a convenient technique for identifying and counting graphene layers on different substrates [13-14]. It was shown that the evolution of the 2D-band Raman signatures with the addition of each extra layer of graphene can be used to accurately count the number of layers [13] together with the position of G peak, which up-shifts with the increasing $1/n$, where n is the number of graphene layers [15].

The quality and number of layers of the suspended graphene ribbons were evaluated by Micro-Raman spectroscopy using a Jobin-Yvon T64000 with a liquid N_2-cooled CCD detector and the 514 nm excitation wavelength at low power levels to avoid laser heating and subsequent degradation of PMMA and graphene. Figure 4 shows the typical Raman spectra of a suspended monolayer graphene with a sharp G band (~1584 cm^{-1})

and 2D band (~2690 cm^{-1}) and a low G/2D ratio. The single layer nature of the graphene ribbon is further confirmed by the full with at half maximum (FWHM) of the Lorentz fit of the 2D band being ~30 cm^{-1}. The small D peak (~1350 cm^{-1}) intensity indicates that the graphene has low defect density. The peaks marked with a star (*) are originated in the PMMA layer [16] also exited with the incident laser radiation.

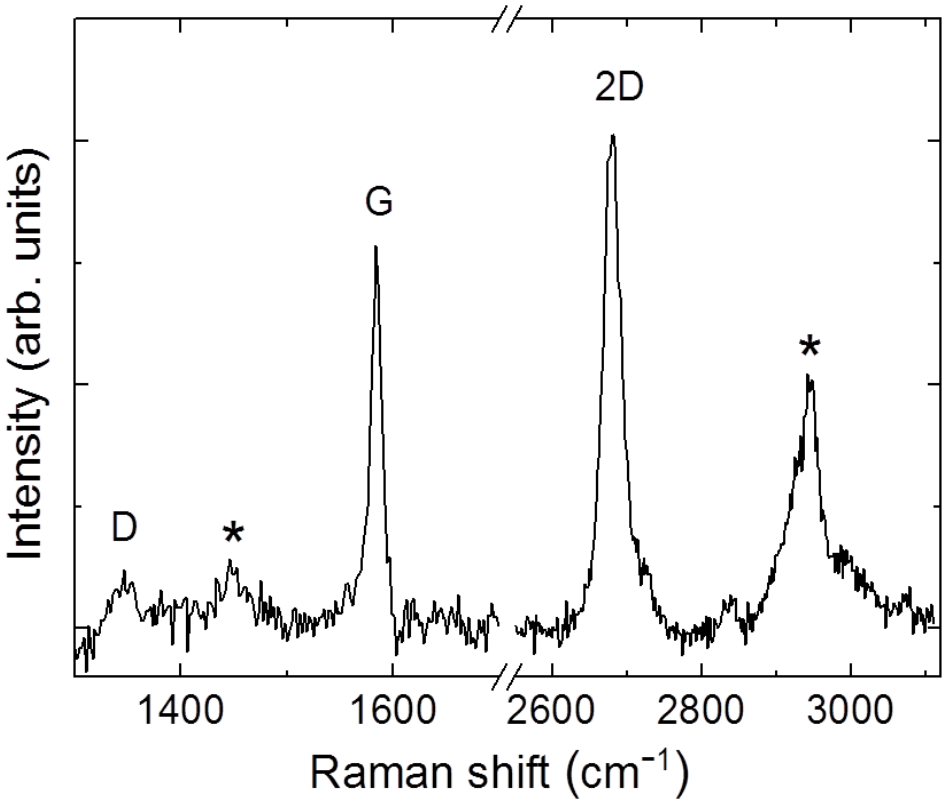

Fig. 4: Raman spectrum of a suspended single layer graphene flake. The marked peaks (*) are Raman modes from the PMMA layer.

3.3 Atomic Force Microscopy high resolution topography

In order to have a higher resolution topography characterization of the suspended devices, we also performed AFM images. Non-contact mode has been used in order to avoid damaging of the samples. In Fig 5(a), different lateral range AFM images of the area previously studied by SEM (Fig.2 and Fig. 3.a) are shown. As it can be appreciated, fig. 5(a) shows the topographic image of a graphene primary ribbon containing more than 20 equal suspended 500 nm long secondary ribbons.

In the upper side of Fig. 5(b) the estimated height of the PMMA walls is represented by colored vertical bars. The red line indicates the height profile measured with the AFM in a scan performed in an area free of graphene nanoribbons (red line in Fig.5.a). The difference between the estimated and the measured height of the trenches is attributed to the lack of sharpness of the AFM cantilever tip, whose cone angle should be smaller than the width of the trenches in order to allow the tip to penetrate and reach their bottom [17].

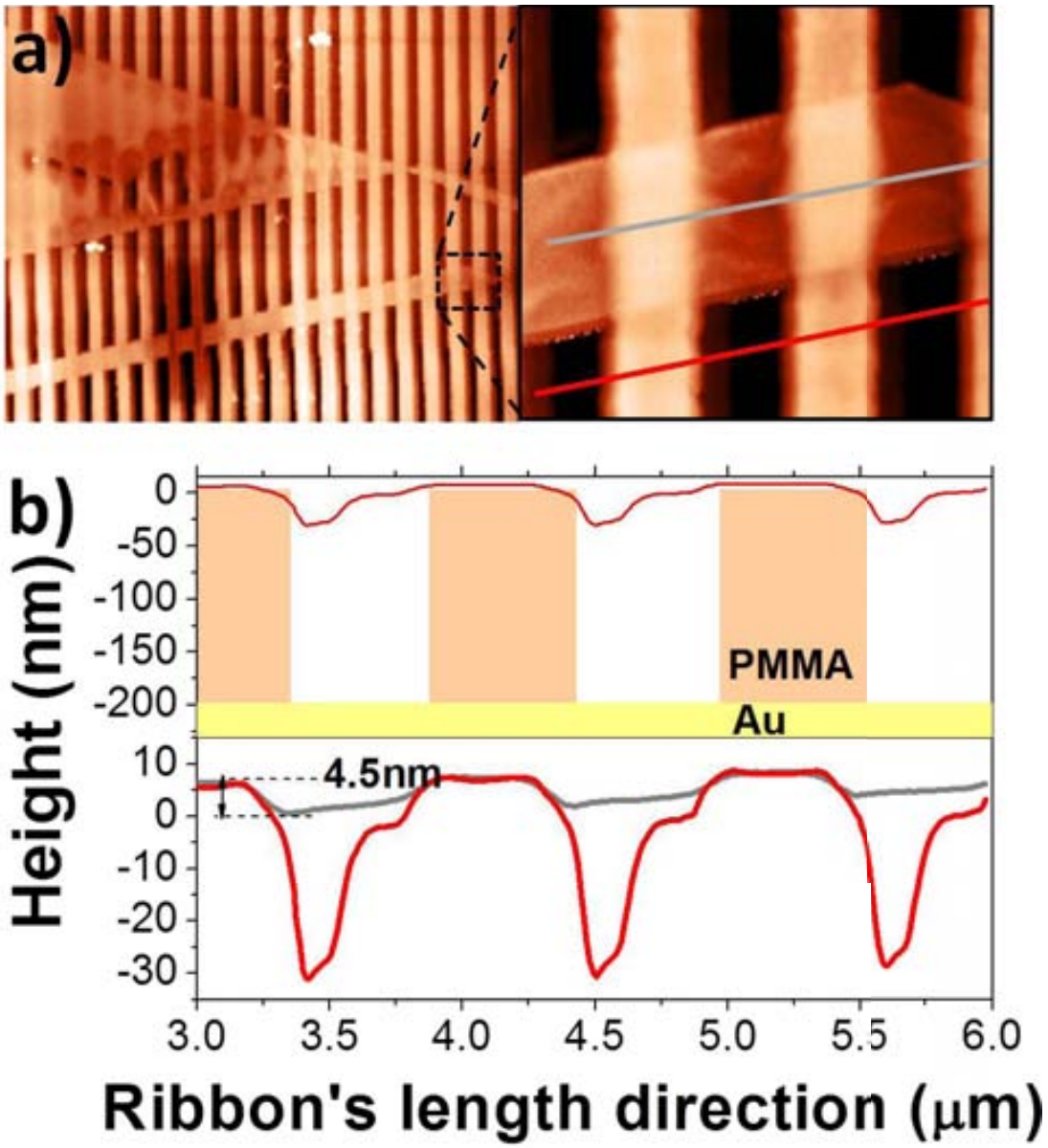

Fig. 5: (a) Topographic AFM images of the 500 nm long secondary ribbons. (b) Upper panel: height profile along the red line from (a) superposed to the expected PMMA trench profile. Lower panel: height profiles for both red and grey lines from (a) showing the suspension of the fabricated devices. Graphene adhesion to the walls can be appreciated.

The difference between the height profile along the graphene ribbon (grey line) and trenches (red line) indicated in Fig. 5(a) that can be appreciated in the lower panel of fig. 5(b), demonstrates that the secondary graphene ribbons are suspended after the last releasing step. The lower panel of fig.5(b) also shows a 4.5nm deep indentation close to the walls of the dug trenches, which is a very low value compared to the device length.

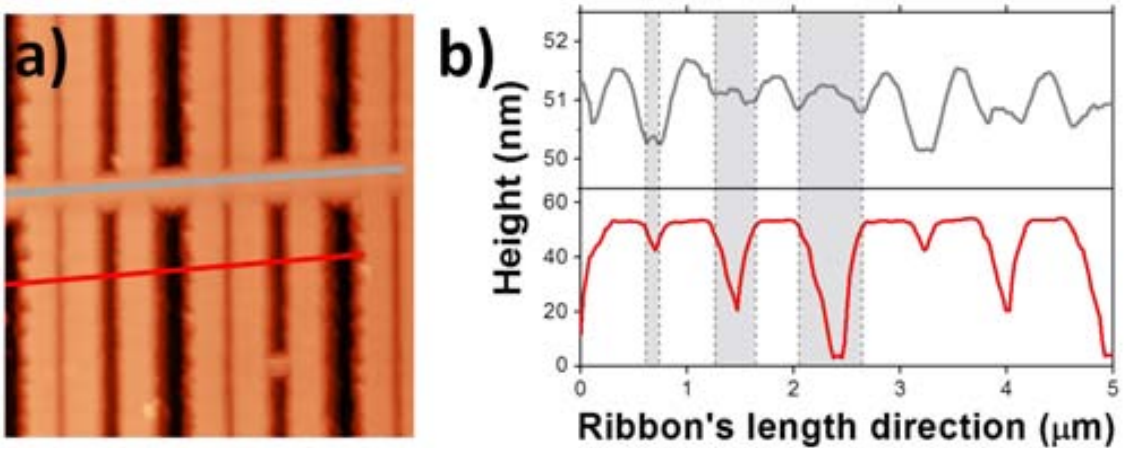

Fig. 6: (a) Topographic AFM images of the 100, 300 and 600 nm long ribbons. (b) Upper panel: graphene height profile along the grey line from (a). Lower panel: height profile along the red line from (a). Grey bars indicate the dimensions of the 100, 300 and 600 nm wide trenches.

Fig. 6 shows the results of the AFM topography of a sample with trenches of different widths, i.e. 100, 300 and 600 nm. In Fig. 6(a) it is shown a detail of a primary ribbon containing seven suspended structures with the corresponding 100, 300 and 600 nm lengths. The upper panel of fig. 6(a) shows that the graphene structure is apparently buckled with an amplitude of less than 1nm. Such a buckling can be explained as being produced by the residual stress difference between the two materials, PMMA and graphene. The lower panel shows the AFM measured profile of 100, 300 and 600nm wide trenches. The same mismatch between the measured and nominal heights of the PMMA columns is reproduced. Besides, in this case the difference in penetration of the AFM tip through the trenches with different widths (the wider the trench the deeper the penetration is) confirms that this effect is due to the lack of probe sharpness. On the other hand, small lateral range topographic AFM images reveal an apparent thickness of the graphene ribbons around 1.44 nm, which is in good agreement with previous works [3] reporting 1.6 nm for mono-layer graphene on PMMA.

3.4 Dragging direction dependence

Although the number of mono-layer graphene ribbons obtained by this method is comparable to what is reported in previous works [3], here we obtain a highly oriented set of graphene samples. This fact represents a considerable advantage to pattern the trenches, because previous imaging can be avoided, thus simplifying the e-beam step.

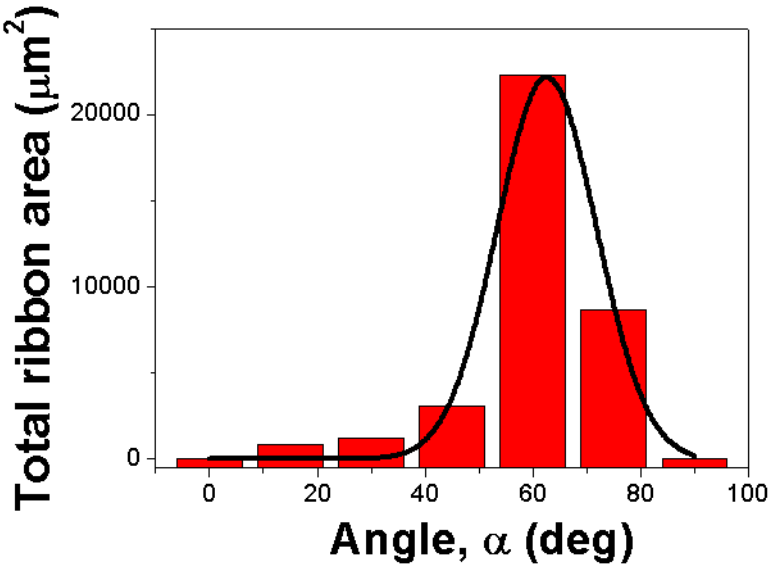

Fig. 7: Ribbon's occupied area for different dragging direction from 0 to 90 degrees, relative to the (001) Si cut.

As mentioned before, the dragging *i*-direction plays an important role in terms of the number of achieved graphene ribbons. In Fig. 7 the statistics of the obtained graphene flakes as a function of the dragging direction in terms of the total ribbon area over the same substrate area of approximately 0.2 cm^2 is shown, extracted from optical inspection. A maximum density of graphene structures is achieved around $\alpha_0 \sim 60$ deg with respect the initial dragging direction corresponding to one of the edges of the Si substrate. Other works reported that both armchair and zig-zag chirality are preferred directions for the mechanical rupture of the honey-comb lattice (with a larger probability for the first), suggesting that α_0 is related in some way to the armchair direction. Additionally, as it can be seen from Fig. 5(a), the ribbons trend to break during the transfer step showing a recurrent angle of 30 deg between their non-parallel edges, which is the angle between the armchair and zigzag directions. This seems to support the idea of having armchair boundaries in the suspended ribbons. However, beyond the origin of the observed dependence of the nanoribbon population on the dragging direction, from the nanoengineering point of view of graphene–based NEMS devices the dragging angle becomes an extremely useful process parameter to optimize the fabrication yield. The control provided by the dragging angle, combined with the simplicity of a single e–beam lithography step and the uniformity in length and width of the obtained secondary suspended nanoribbons, turn this method in a very promising way for NEMS prototyping.

4. Conclusions

Tens of suspended highly regular single-layer and few-layer graphene nanoribbons have been fabricated by mechanical exfoliation of graphite and transfer to a Si-Au-PMMA stack. The polymer is used as a sacrificial layer to release the graphene structures by means of a single e-beam lithography step consisting on the patterning of trenches

perpendicular to the graphene ribbons. A preferred dragging direction in the transfer step has been found, which increases the probability of obtaining graphene ribbons. The control of this dragging angle allows predicting the directions of the ribbons so that the releasing trenches can be patterned with a minimum previous inspection for flakes region location.

5. Acknowledgments

The authors wants to thank the Spanish "Ministerio de Ciencia y Innovación" for financially supporting this research under the projects Nos. ENE2009-1430-CO2-02 (OPACMEMS), FIS2009-12721-C04-03, FIS2012-37549-C05-05 and to the EU for the support through the FP-7 FET-Proactive Coordination Action Pr.No. 270005 (ZEROPOWER).

References

[1] Lee, Changgu, et al. "Measurement of the elastic properties and intrinsic strength of monolayer graphene." *science* 321.5887 (2008): 385-388.
[2] Hod, Oded, and Gustavo E. Scuseria. "Electromechanical properties of suspended graphene nanoribbons." *Nano letters* 9.7 (2009): 2619-2622.
[3] Traversi, Floriano, et al. "Elastic properties of graphene suspended on a polymer substrate by e-beam exposure." *New Journal of Physics* 12.2 (2010): 023034.
[4] Neto, AH Castro, et al. "The electronic properties of graphene." *Reviews of modern physics* 81.1 (2009): 109.
[5] Ekinci, K. L., and M. L. Roukes. "Nanoelectromechanical systems." *Review of scientific instruments* 76.6 (2005): 061101-061101.
[6] Bunch, J. Scott, et al. "Impermeable atomic membranes from graphene sheets." *Nano letters* 8.8 (2008): 2458-2462.
[7] Liu, Xinghui, et al. "Observation of Pull-in Instability in Graphene Membranes under Interfacial Forces." *Nano letters* (2013).
[8] Bunch, J. Scott, et al. "Electromechanical resonators from graphene sheets." *Science* 315.5811 (2007): 490-493.
[9] Frank, I. W., et al. "Mechanical properties of suspended graphene sheets." *Journal of Vacuum Science & Technology B: Microelectronics and Nanometer Structures* 25.6 (2007): 2558-2561.
[10] Garcia, Jorge M., et al. "Graphene growth on h-BN by molecular beam epitaxy." *Solid State Communications* 152.12 (2012): 975-978.
[11] Reina, Alfonso, et al. "Large area, few-layer graphene films on arbitrary substrates by chemical vapor deposition." *Nano letters* 9.1 (2008): 30-35.
[12] Chang, You Min, et al. "Multilayered graphene efficiently formed by mechanical exfoliation for nonlinear saturable absorbers in fiber mode-locked lasers." *Applied Physics Letters* 97.21 (2010): 211102-211102.
[13] Ferrari, A. C., et al. "Raman spectrum of graphene and graphene layers." *Physical review letters* 97.18 (2006): 187401.
[14] Calizo I, Bao W, Miao F, Lau C N and Balandin A A "The effect of substrates on the Raman spectrum of graphene: Graphene-on-sapphire and graphene-on-glass" *Appl. Phys. Lett.* **91** (2007) 201904
[15] Gupta A, Chen G, Joshi P, Tadigadapa S and Eklund P C "Raman Scattering from High-Frequency Phonons in Supported n-Graphene Layer Films" *Nano Letters* **6** (2006) 2667
[16] Sumit Kumar, Anshu Sharma, Balram Tripathi, Subodh Srivastava, Shweta Agrawal, M. Singh, Kamlendra Awasthi, Y.K. Vijay "Enhancement of hydrogen gas permeability in electrically aligned MWCNT-PMMA composite membranes", *Micron* **41** (2010) 909–914
[17] Tranchida, D., S. Piccarolo, and R. A. C. Deblieck. "Some experimental issues of AFM tip blind estimation: the effect of noise and resolution." *Measurement Science and Technology* 17.10 (2006): 2630.

SUMMARY

Information and Communication Technologies (ICTs) are ubiquitous and experience a growth of a 5% every year with applications in very different areas ranging from cell-phones to healthcare control. ICT's are responsible of the extraordinary increment in the amount of information exchange all around the world and also represents a considerable contribution to what is known as CO_2-footprint. A huge effort is nowadays devoted to decrease more and more the power needed to switch a bit trying to reach Landauer's limit which states an energy requirement of at least 2.85 zJ: this is the physical limit for a unit of information. The fast developing of low-power consumption electronics and its miniaturization opened the door to the possibility of self-powered and autonomy for these kinds of technologies. Moreover, the development of self-powered devices is a key point in order to avoid the issue of battery replacing or recharging. Vibrations based Energy Harvesting (EH) represents a very attractive possibility to power such devices in terms of availability and power density.

The objective of this Thesis is to provide an outlook of the state of the art and to find new strategies to increase the performance of vibration-based EH technologies. A bistable approach at the micro and nano-scale is explored to increase the generated power when dealing with broad-band and low-intensity vibrations in comparison to the throughput of resonator-based approaches.